

**HOW SEA ICE MICROSTRUCTURE INFLUENCES THE POLAR TRANSPORT
OF SALTS FROM THE OCEAN INTO THE ATMOSPHERE**

A Thesis
Submitted to the Faculty
in partial fulfillment of the requirements for the
degree of

Doctor of Philosophy

by

Ross Lieb-Lappen

Thayer School of Engineering
Dartmouth College
Hanover, New Hampshire

January 2016

Examining Committee:

Chair _____
Rachel W. Obbard

Member _____
Donald K. Perovich

Member _____
Erland M. Schulson

Member _____
Scott D. Pauls

Member _____
Howard K. Roscoe

Member _____
Mark L. Rivers

F. Jon Kull
Dean of Graduate Studies

ABSTRACT

Sea ice appears to form an impenetrable boundary at the ocean-atmosphere interface in polar regions, yet in fact its porous structure provides critical pathways for the exchange of heat, gases, salts, and other chemical species impacting the global climate. It is a complex media composed of ice, liquid brine, air pockets, and salt precipitates. The importance of microstructure on bulk properties of sea ice (e.g., albedo, permeability, conductivity) is becoming increasingly more relevant in a changing climate. A primary importance of permeability and the corresponding brine channel network is for providing a mechanism for transporting salts to the surface snow and atmosphere interface. Once exposed to air, bromide and other salts are photochemically activated into reactive halogen species, and play a role in many atmospheric chemical interactions, such as tropospheric ozone depletion.

By combining measurements from ion chromatography (IC), x-ray micro-fluorescence (XRF), and x-ray micro-computed tomography (μ CT), it was possible to trace the transport of salts from the ocean, through brine channels, and into the surface snow. IC was used to analyze the chemical signature of blowing snow, surface snow, and sea ice collected from the Ross Sea, Antarctica. Differences in ionic ratios provided insight into the role of blowing snow in the activation of bromine. Since salts originate in the ocean and are transported through the ice, it was critical to have a precise description of the location of salts within sea ice. XRF added to the understanding of microstructural and stratigraphic location by providing elemental maps for each salt. This illustrated that salts are located primarily in tubular channels and between grain boundaries of the ice crystal lattice. In order to more completely elucidate brine transport through sea ice, this information was augmented with a quantitative description of the brine network measured using μ CT. From these measurements, a topological network was constructed, allowing for the analysis of brine channel geometry and connectivity. This 3-D characterization of the shape and structure of pathways transporting salts through sea ice provided detailed insight into how sea salts can mobilize through sea ice and later play critical roles in tropospheric chemical reactions.

ACKNOWLEDGEMENTS

This work would not have been possible without the support and guidance from a large number of people. First of all, I would like to thank my advisor Rachel Obbard for taking me aboard this wild and venturesome journey spanning both poles of the earth. We have had quite a large number of adventures together, creating memories that will last a lifetime. I would like to thank Don Perovich, who first sent me to the Arctic on my first polar field expedition, helping to instill my love of sea ice and my polar fever. I still expect to find M&M's every time I reach into the pockets of my parka. Thank you to Scott Pauls for the guidance in developing a mathematical brine network model and answering all of my ignorant questions on topology and networks. I would like to thank Howard Roscoe for help on a variety of thesis (and non-thesis) related topics, particularly in regards to tropospheric chemistry and snow interactions. Thank you to Erland Schulson with whom I spent the most amount of class time at Thayer and introduced me to the basic concepts of engineering, while I questioned why I was pursuing a doctorate in a degree in which I had little background. I would also like to thank Mark Rivers as my external committee member, who welcomed and helped me at Argonne National Laboratory's Advanced Photon Source (APS) during my undergraduate degree and once again during my Ph.D. Together Rachel, Don, Scott, Howard, Erland, and Mark formed an academically diverse committee that was invaluable in completing this thesis.

I have been fortunate to have spent a lot of time working closely with many undergraduate students (some of who are now graduate students) throughout my time at Dartmouth, many through the Women in Science Project (WISP). Thank you to Katie Nordick, Gunnar Pope, Natalie Afonina, George Boateng, Anna Miller, Ellen Kim, Sarah McGowan, Silvia Arora, Jeremiah Leonard, Taringana Guranungo, and Leina McDermott. I would like to give a special thanks to Ellyn Golden, who has been like a little sister to me over the multiple years of working together, including an epic two month field expedition to Barrow. I think we kept each other "mostly" sane during the long nights with constant bantering.

Completing field work, particularly in extreme environments such as Barrow, AK and Antarctica, requires an immense amount of logistical support. I would like to thank the United States Antarctic Program (USAP), the US Army Corps of Engineers' Cold Regions Research and Engineering Laboratory (CRREL), CH2M Hill Polar Services (CPS), *Ukpeajvik Iñupiat Corporation* (UIC), and the United States Naval Academy Polar Science Program (USNA PSP). I would especially like to thank the Barrow bear guards Michael Thomas, Raymond Lambrecht, and Nelson Nungasak for keeping us alive, as well as all of the support staff. These field campaigns would not have been as enjoyable without the friends and collaborators who provided scientific advice, an extra set of hands, companionship, and many many laughs. Thank you to Son Nghiem, Tom Douglas, and all of the "Bromexicans" during my first trip to the Arctic, to Lars Kalnajs, Tim Hay, and Thomas Reese during my trip to Antarctica, and to John Woods, Johannes Zielcke, Denis Pöhler, and Udo Frieß during both expeditions. I would also like to thank Austin Kovacs, Elijah Keib, Dirk Notz, Karl Twelker, Anthony Faiia, and Marc Oggier for help in preparation and during these trips.

This work required a lot of laboratory work as well, both here at Dartmouth and at Argonne National Laboratory. Thank you to Josh Landis, Dave Ferris, and Dartmouth's Earth Science Department for adopting me and helping with all of the ion chromatography. I would like to thank the Thayer Machine Shop, the Thayer Instrument Room, and the rest of the staff at the Thayer School of Engineering for all of the support over the last five years. For the work at APS, I would like to thank Matt Newville, Tony Lanzirotti, and all of the staff at GSECARS, Sector 13.

Most importantly, thank you to all of my family and friends. Your love, friendship, and support have shaped who I am today. Thank you to a great snow and ice lab group of friends including Alden Adolph, Amber Whelsky, Alex Arntsen, Kaitlin Keegan, Xuan Wang, Carolyn Stwertka, Cameron Planck, Nick Wright, Ben Kopec, Stephen Nodder, Scott Snyder, and Kevin Hammonds. Thank you mom, dad, Mia, Mike, Beverly, Brianna,

and all of my grandparents for your continual love throughout my life. Thank you to Altai and Lily for always taking me on adventures and showering me with licks. And thank you Steph, my best friend and partner, supporting me and watching each other's back as we wander through this journey of life.

This research was funded by the National Science Foundation through grants NSF-ANT 1043145 and NSF-PLR 1304134. Thanks for additional support from the Mathematics and Climate Research Network (MCRN).

In loving memory of my father

Edward N. Lappen (Jan. 18, 1950 - Dec. 31, 2010)

CONTENTS

Abstract	ii
Acknowledgements	iii
List of Tables	ix
List of Figures	x
1 Introduction and Background	1
1.1 Microstructure	2
1.2 Sea Ice Growth	6
1.3 Salts	12
1.4 Brine Channels and Transport	17
1.5 Atmospheric Interactions	20
1.6 Purpose of this Work	25
2 Methods	26
2.1 Sample Collection and Preparation	26
2.2 Ion Chromatography	29
2.3 X-Ray Micro-Fluorescence Spectroscopy	33
2.4 X-Ray Micro-Computed Tomography	37
3 The Role of Blowing Snow in the Activation of Bromine over Sea Ice	46
3.1 Abstract	46
3.2 Introduction	47
3.3 Methods	50
3.4 Results	52
3.5 Discussion	55

3.6	Conclusion	60
3.7	Supplement	61
4	Microstructural Location of Salts in Sea Ice	64
4.1	Introduction	64
4.2	Methods	65
4.3	Results and Discussion	68
4.3.1	Elemental Maps	68
4.3.2	Correlation Between Different Salts	76
4.3.3	Trends with Depth	80
4.3.4	Comparison to Thin Sections	82
4.4	Conclusion	86
5	Analyzing Brine Channel Morphology Using μCT	90
5.1	Abstract	90
5.2	Introduction	91
5.3	Methods	92
5.3.1	Sample Preparation	92
5.3.2	Scanning	93
5.3.3	Reconstruction	94
5.4	Metrics for Microstructural Analysis	97
5.5	Results	100
5.5.1	Brine	100
5.5.2	Air	101
5.5.3	Ice	102
5.5.4	Spatial Variability	103
5.5.5	Temperature Sensitivity	107
5.6	Discussion	108

5.7	Conclusions	109
6	Characterizing Brine Channels	110
6.1	Introduction	110
6.2	Methods	111
6.3	Results from Scanning Sea Ice at In-Situ Temperatures	115
6.4	Brine Network Model for Sea Ice	124
6.5	Conclusions	147
7	Conclusion and Future Work	149
Appendices		
A	Additional Sea Ice Ion Concentrations and Correlation Plots	152
B	XRF Metal Elemental Maps	157
C	Additional Throat Size Distributions	159
D	Probability Distributions of Statistics for Directed Paths	166
	Literature Cited	173

LIST OF TABLES

3.1	Raw anion concentrations of blowing snow samples	61
3.2	Raw anion concentrations of surface snow samples	62
3.3	Raw anion concentrations of sea ice core samples	63
4.1	Matrix of mean correlation values for relative amounts of each element . . .	79

LIST OF FIGURES

1.1	September Arctic sea ice extent	2
1.2	September Antarctic sea ice extent	2
1.3	Freezing point depression and maximum density	4
1.4	Crystal structure of ice 1h	5
1.5	Constitutional supercooling	8
1.6	Schematic of the cellular structure of sea ice	10
1.7	Sea ice phase diagram	16
1.8	Sea ice salinity profiles	17
1.9	Schematic of percolation threshold in two dimensions	19
1.10	Numerical model of sea ice permeability	20
2.1	Map of the full study region	27
2.2	Snow depth maps for Butter Point Site and Iceberg Site	27
2.3	Vertical thin sections of all six ice cores	30
2.4	Representative IC chromatogram	31
2.5	IC standard calibration curves	32
2.6	Example XRF spectrum	36
2.7	Schematic of cone-beam μ CT	38
2.8	Example μ CT projection radiograph	39
2.9	Thresholding a trinary image of sea ice	42
2.10	Histogram for thresholding μ CT images	44
3.1	Anion concentrations for sea ice cores	53
3.2	Br^-/Cl^- mass ratios for sea ice, surface snow, and blowing snow	55
3.3	$\text{SO}_4^{2-}/\text{Cl}^-$ mass ratios for sea ice, surface snow, and blowing snow	56

4.1	Representative XRF spectra	69
4.2	Br XRF maps for Butter Point ice core	70
4.3	Br XRF maps for Iceberg Site ice core	70
4.4	Br XRF maps for Scott Base ice core	70
4.5	Sketches of the pore structure in frazil ice and columnar ice	71
4.6	μ CT images of the brine phase in frazil ice and columnar ice	72
4.7	Representative Br XRF map scaled for concentration	73
4.8	XRF elemental maps for Br, Cl, K, Ca, and Sr for the Butter Point ice core .	74
4.9	XRF elemental maps for Br, Cl, K, Ca, and Sr for the Iceberg Site ice core .	75
4.10	XRF replicate maps for Br, Cl, K, Ca, and Sr	76
4.11	XRF elemental overlay maps showing Br, Cl, and Sr	78
4.12	XRF elemental overlay maps showing Br, Cl, and K	78
4.13	Pair-wise correlation values of different elements for all samples	79
4.14	Principal component analysis of XRF maps	81
4.15	Maximum and mean intensities for XRF elemental Br maps	82
4.16	Metrics for quantifying the Br-concentrated regions of XRF maps	83
4.17	Horizontal thin sections from the Butter Point ice core	84
4.18	Horizontal thin sections from the Iceberg Site ice core	85
4.19	Horizontal thin sections from the Scott Base ice core	85
4.20	Comparison of XRF elemental maps to a horizontal thin section	87
4.21	Two features of interest from the Cl XRF map	88
4.22	XRF x-ray spectra for features of interest	88
5.1	Three-dimensional visualization of sea ice with brine channels	98
5.2	μ CT metrics for analyzing the definition and shape of brine channels	102
5.3	The degree of anisotropy for the air, ice, and brine phases.	103
5.4	The Euler number and degree of connectivity of the brine channels	104
5.5	μ CT metrics for analyzing the definition and shape of air pockets	105

5.6	μ CT metrics for analyzing the definition and shape of the ice phase	106
5.7	Analysis for calculating the representative elementary volume	107
6.1	Temperature profiles of Antarctic sea ice cores	112
6.2	Sketch illustrating how the brine channel network is defined	114
6.3	Definition and shape of brine channels scanned at in-situ temperatures	115
6.4	Histogram for thresholding μ CT images of warmer ice	117
6.5	Comparison of brine phases scanned at -20 °C and at in-situ temperatures	117
6.6	Definition and shape of air pockets scanned at in-situ temperatures	118
6.7	Definition and shape of the ice phase scanned at in-situ temperatures	120
6.8	The degree of anisotropy for μ CT scans at in-situ temperatures	121
6.9	The degree of connectivity for μ CT scans at in-situ temperatures	121
6.10	Comparing measured and expected brine volume fractions	122
6.11	Brine phase for sample scanned at varying temperatures	123
6.12	$\{\bar{r}_{z_i}\}$ for five largest brine channels, Butter Point core	125
6.13	$\{\bar{r}_{z_i}\}$ for five largest brine channels, Iceberg Site core	126
6.14	$\{\bar{r}_{z_i}\}$ for largest brine channels of each sample, Butter Point core	127
6.15	$\{\bar{r}_{z_i}\}$ for largest brine channels of each sample, Iceberg Site core	128
6.16	Degree of branching for 15 channels in 70-cm sample, Butter Point	128
6.17	r_i of each node for the largest channel in the Butter Point core	130
6.18	r_i of each node for the largest channel in the Iceberg Site core	131
6.19	Cumulative distribution function for total number of pixels in the channel	132
6.20	Cumulative distribution function for summed throat size in the channel	133
6.21	Histogram of nodes having different degree of edge counts	135
6.22	$\{r_i\}$ probability distribution for branching and non-branching nodes	136
6.23	Topological complexity of the five largest brine channels, Butter Point	137
6.24	Topological complexity of the five largest brine channels, Iceberg Site	138
6.25	Largest brine channel at 70 cm, Butter Point ice core	140

6.26	Probability distribution of r^{min} of paths connecting top to bottom	142
6.27	Probability distribution of r^{max} of paths connecting top to bottom	144
6.28	Probability distribution of summed throat size of connecting paths	146
A.1	Anion concentrations for the multi-year ice core collected near Scott Base	152
A.2	Cations concentrations of Ca, K, Mg, S, Sr, and Na for sea ice cores	153
A.3	Correlation plots of all measured ions versus Cl	155
A.4	Correlation plots of all measured ions versus Na	156
B.1	XRF elemental maps for Fe, Cu, and Zn for the Butter Point ice core	157
B.2	XRF elemental maps for Fe, Cu, and Zn for the Iceberg ice core	158
C.3	r_i of each node for largest channel of all samples in the Butter Point core	162
C.6	r_i of each node for largest channel of all samples in the Iceberg Site core	165
D.2	Probability distribution of r^{min} of longest directed path	168
D.3	Probability distribution of r^{max} of paths connecting top to bottom	170
D.4	Probability distribution of summed throat size of connecting paths	172

INTRODUCTION AND BACKGROUND

Sea ice appears to form an impenetrable boundary at the ocean-atmosphere interface in polar regions, yet in fact its porous structure provides critical pathways for the exchange of heat, gases, salts, and other chemical species impacting the global climate. About 71% of Earth's surface is covered by water, of which approximately 7% is covered by sea ice. This represents two-thirds of the ice-covered area on Earth, but less than 1% of the total volume of ice (Maykut, 1985). Since sea ice is generally less than 1 – 2 m thick, it is incredibly sensitive to environmental changes, and thus is often used as an indicator for climate change.

Although sea ice appears quite uniform, it is in fact a very variable and dynamic system. In the Arctic, sea ice coverage varies from approximately 6 million km² in the summer to 15 million km² in the winter (Fetterer et al., 2002, updated daily). However, these numbers are changing rapidly as the Arctic sea ice is becoming increasingly thinner with a higher percentage of first-year ice (Perovich and Richter-Menge, 2009). Over the past 30 years, September Arctic sea ice coverage has decreased at an average rate of 9% per decade, with that number increasing to 15% per decade over the last decade (e.g., Stroeve et al., 2007, 2012). In the Antarctic, sea ice forms a ring around the continent, varying in area from 3 – 4 million km² in the austral summer to 19 million km² in the winter, with less decadal fluctuation than the Arctic (Fetterer et al., 2002, updated daily). September sea ice extents comparing the change from 1980 to 2012 are shown for the Arctic in Fig. 1.1 and for the Antarctic in Fig. 1.2 (Fetterer et al., 2002, updated daily). As the climate continues to change, understanding the response of the sea ice is paramount to understanding the response of the entire Earth climate system.

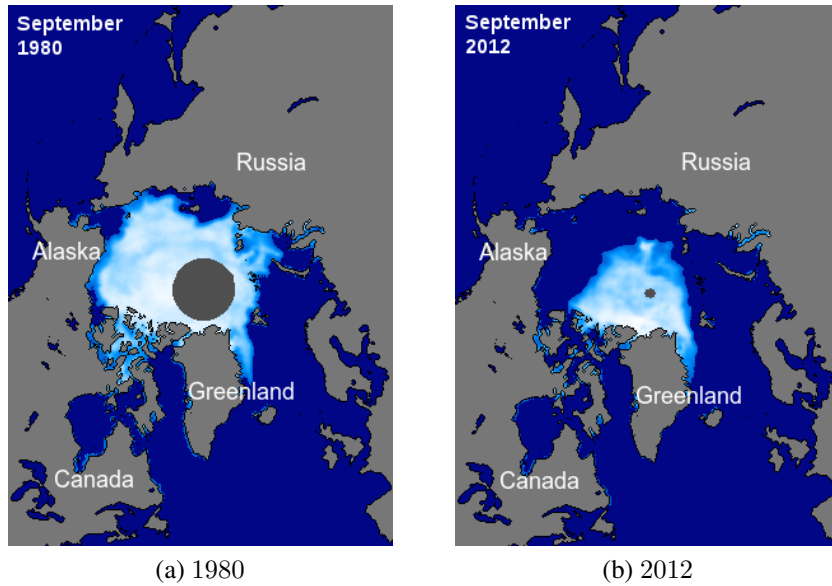


Figure 1.1: September Arctic sea ice extent for 1980 and 2012 from passive microwave data (Fetterer et al., 2002, updated daily). Images show the minimal Arctic sea ice extent.

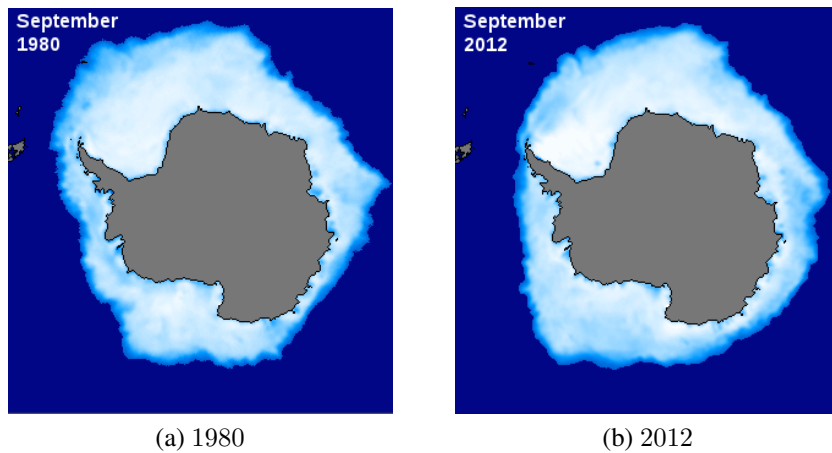


Figure 1.2: September Antarctic sea ice extent for 1980 and 2012 from passive microwave data (Fetterer et al., 2002, updated daily). Images show the maximal Antarctic sea ice extent. Here, the maximal extent rather than the minimal extent was shown to better illustrate regional variations from 1980 to 2012.

Microstructure

Sea ice is a complex medium composed of multiple phases (solid ice, liquid brine, gas, and solid precipitates), heterogeneous in both structure and chemistry, that varies over temporal, thermal, and spatial regimes. The importance of microstructure on the bulk

properties of sea ice (e.g., albedo, transmissivity, permeability, electrical conductivity) is becoming increasingly more relevant in a changing climate (e.g., Eicken, 2003; Petrich et al., 2006). When both freshwater and sea ice thicken, air bubbles become entrapped and cause scattering of light. This increases the albedo of the ice as more incoming shortwave radiation is reflected. Sea ice differs both macroscopically and microscopically from freshwater ice through the presence of salt and liquid brine inclusions. For example, sea ice is generally brighter than an equivalent thickness of freshwater ice, leading to a higher albedo. For both ice types, the majority of longwave radiation is absorbed (Grenfell, 1983; Grenfell and Perovich, 1984, 2004).

The presence of salt also leads to differences in how the ocean responds to atmospheric cooling relative to freshwater. A warm freshwater lake exposed to cold temperatures will be well-mixed due to convective overturning. However, since the maximum density of freshwater occurs at 3.98 °C (Weast, 1969), once the surface waters drop below this temperature, a stable stratification of the lake water column will be created. Conduction becomes the primary source of heat transport, and there is a rapid decrease in the heat flux to the surface. This allows the surface to freeze while the underlying water layers remain warm. The presence of salt both lowers the freezing point (T_f) and the temperature of maximum density (T_m) of water as shown in Fig. 1.3 (Maykut, 1985). As can be seen, the density of water with salinity greater than 24.7 psu always decreases with temperature since T_m decreases faster than T_f . Therefore, for the ocean with a salinity of approximately 34 psu, there is an unstable stratification even as the surface waters cool towards freezing. These differences are exaggerated at high latitudes since relative to other oceans, polar oceans have small thermal but large salinity variations largely due to the influence of the sea ice (Emery et al., 1991). As a result, continual convection in the upper ocean impacts the growth mechanisms of sea ice, and relative to freshwater ice, occurs under more dynamic conditions.

To analyze the growth mechanism for sea ice it is helpful to have knowledge of the

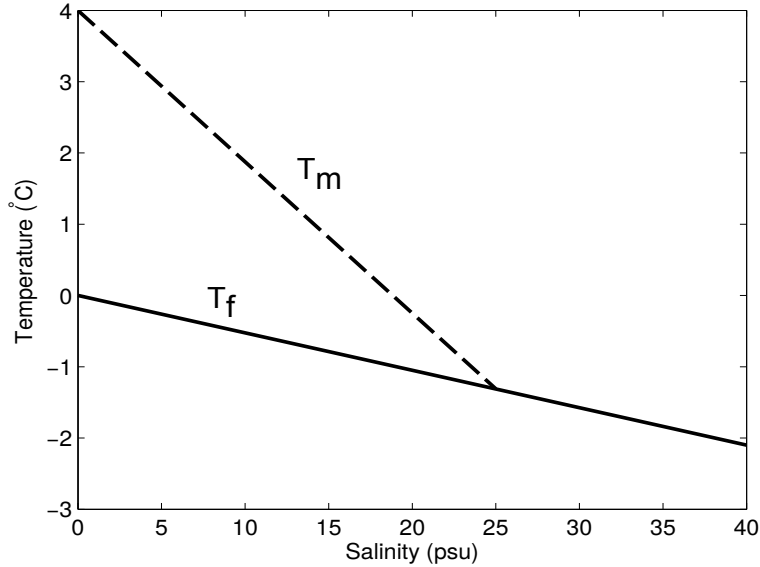


Figure 1.3: Freezing point T_f (solid line) and temperature of maximum density T_m (dashed line) for water as a function of salinity (Maykut, 1985).

crystal lattice structure. The vast majority of ice, and in fact all natural snow and ice on Earth's surface, is in the hexagonal 1h phase, one of the 15 crystalline phases (Hobbs, 1974; Schulson, 1999). Ice crystal structure is defined by the principal sixfold rotational c-axis perpendicular to the basal plane, as is shown in Fig. 1.4 (Weeks and Ackley, 1982). The basal plane is then defined by three equal-length a-axes with 120° angles between them. Ice 1h has a low packing efficiency of approximately 0.34, and thus, ice is less dense than water (Hobbs, 1974; Schulson, 1999). Each H_2O molecule is hydrogen bonded to four nearest neighbor molecules located at vertices of a regular tetrahedron (Bragg, 1921). Near its melting point, the lattice parameters are $a = 0.4523 \text{ nm}$ and $c = 0.7367 \text{ nm}$, resulting in a ratio $\frac{c}{a} = 1.628$ (Lonsdale, 1958; Owston, 1958). The ice lattice is arranged in such a manner that only two bonds are broken for fracture along the basal plane, which helps explain the increased growth rate in this plane. Conversely, fracture along any plane normal to the basal plane requires four or more bonds to be broken (Weeks and Ackley, 1982).

The basal plane of the ice crystal is smooth at the molecular level, while the perpendicular crystal phases often have a rougher surface (Hobbs, 1974; Thomas and

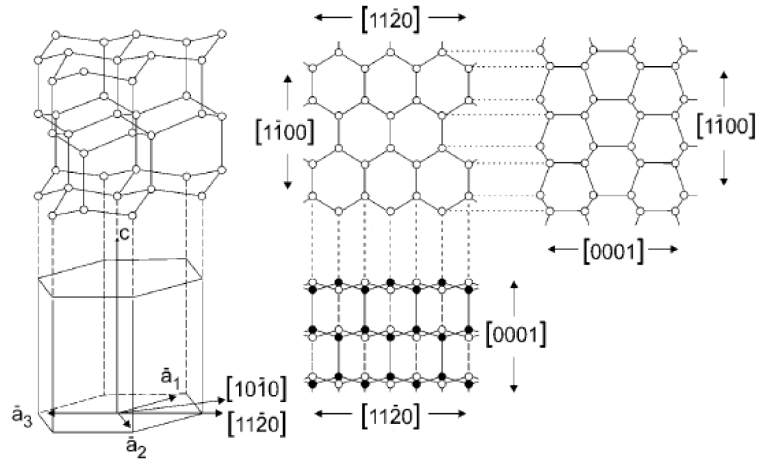


Figure 1.4: Crystal structure of ice 1h as given by Weeks and Ackley (1982). The left side shows a three-dimensional view, while the other images show three different two-dimensional views.

Dieckmann, 2009). Without the existence of a step-producing defect for a new plane of atoms, growth along the c -axis requires a high activation energy (Weeks and Ackley, 1982). Consequently, faster growth rates occur on the basal plane itself due to differences in interface kinetics. Further, ice crystals with a pre-existing horizontal c -axis have a smaller distance to grow parallel to the axis of heat flow, which leads to growth rates that are two orders of magnitude faster than for other oriented crystals (Hallet, 1964). As these crystals quickly outpace the growth of other crystals, the sea ice is soon dominated by crystals with horizontal c -axes (Weeks and Ackley, 1982). Although initially there is a random distribution in the direction of the horizontal c -axis, eventually a preferred azimuthal orientation dominates growth. Ice crystals with their c -axis aligned with the primary ocean current direction have been shown to have a slight growth advantage (Gow, 1978; Kovacs and Morey, 1978). As will be discussed in more detail later, the thickness of the stable boundary layer at the growing interface is decreased by the increase in turbulence.

Sea Ice Growth

As can be seen in Fig. 1.3, the freezing range of seawater is approximately $-1.8\text{ }^{\circ}\text{C}$ due to the presence of dissolved salts. Fallen snow and the solid impurities in ocean water provide ample sites for nucleation, and therefore little supercooling is needed or homogeneous nucleation is observed (Weeks and Ackley, 1982). Initially, ice crystals in the shape of needles or platelets form and are suspended in the upper layers of the ocean. These crystals are known as frazil ice, and range in size from few to tens of millimeters with a thickness less than 1 mm (Weeks and Ackley, 1982). As the frazil ice packs together, it yields ice with a granular texture. The formation of this ice requires the removal of both heat and salts away from the ice-ocean interface and into the air and water, respectively (Weeks and Ackley, 1982). Wind and wave turbulence continually mixes the frazil ice until a thickening slush called grease ice is formed. At this point, there is no longer a direct exchange between the atmosphere and the ocean. Once the solid fraction of the slush reaches 30 – 40%, strong waves cause the formation of ice disks known as pancake ice (Martin and Kauffman, 1981). Individual pancakes continually bump and grind each other, congealing into larger pancakes of up to 0.5 m thick, and forming a semi-consolidated ice cover with raised edges (Lange et al., 1989; Wadhams et al., 1987). Although the ice surface looks flat, it actually consists of individual pancakes stacked and tilted on top of each other. In calm conditions however, the absence of wind and wave turbulence allows for the frazil crystals to freeze together in a thin sheet known as nilas ice. This sheet thickens, reducing in transparency, and eventually congelation growth takes over as the dominant ice growth process (Wadhams et al., 1987).

With atmospheric temperatures below freezing, there is a heat flux upwards from the ice-ocean interface. If the flux is greater than the heat provided to the interface by the ocean, new ice growth continues downwards releasing latent heat. This is known as congelation ice and occurs in the vertical direction, maintaining the horizontally-oriented *c*-axes. This

ice is columnar in texture with grain size ranging from 1 – 10 cm (Lange et al., 1989; Weeks and Ackley, 1982). Congelation ice has a slower growth rate than frazil ice due to the required heat transfer through the ice above, and this rate steadily decreases with ice thickness (Weeks and Ackley, 1982). We note that between frazil ice and congelation ice there is a transition zone of both granular and columnar ice.

The underside of the growing sea ice has been observed to be parallel rows of long blades of ice with thin layers of brine, leading to a brine channel spacing of 0.5 – 1.0 mm (Harrison and Tiller, 1963). This zone of lamellae is generally 1 – 3 cm in length, has an ice fraction of 0 – 70%, and constitutes what is known as the “skeletal layer” of sea ice (Weeks and Ackley, 1982). This skeleton layer is important biologically as it is home to one of the greatest concentration of phytoplankton in the world’s oceans (Eicken, 2003). In this layer, as sea water freezes, salts are rejected from the ice, and thus, the salinity increases in front of the advancing ice-ocean interface. As this is diffusion-limited, there exists an exponentially decreasing salt concentration gradient away from the interface towards the ocean. This salt concentration gradient corresponds to a gradient in the equilibrium freezing point of a thin water layer ahead of the ice-ocean interface as shown in Fig. 1.5. The added salinity near the interface will also correspond to a liquid with a lower freezing temperature than that of the underlying water, establishing a temperature gradient in the water. These two conditions result in a downward salt flux and an upward heat flux.

Since heat transfer is faster than salt diffusion, there is a region of supercooled water and what is known as constitutional supercooling (Fig. 1.5). The criterion for this condition is given by (Weeks and Ackley, 1982):

$$\frac{G_L}{v} < \frac{mX_0}{D} \left(\frac{1-k}{k} \right) \quad (1.1)$$

where G_L is the temperature gradient of the liquid, v is velocity of the moving interface, m is the slope of the liquidus line, X_0 is the initial salt concentration (far from the interface),

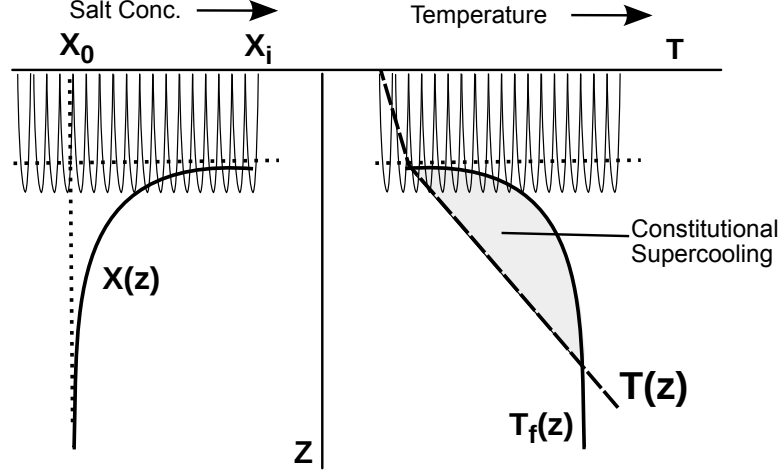


Figure 1.5: Schematic of the skeletal layer and constitutional supercooling adapted from Eicken (2003). The ice lamellae are shown along the top extending into the ocean below. The left side plots the salinity gradient, while the right side plots the thermal gradient. Shaded is the region of constitutional supercooling. $X(z)$ represents the salt concentration at depth z , $T(z)$ represents the temperature of the liquid at depth z , and $T_f(z)$ represents the freezing point of the liquid at depth z . X_0 and X_i are the salt concentrations far from and at the ice interface, respectively.

D is the diffusion coefficient, and k is equilibrium partition coefficient. Because the temperature gradient in the ocean is difficult to ascertain and is not the rate limiting factor, an alternate approach was proposed based upon the temperature gradient in the solid G_S (Tiller, 1962):

$$\frac{G_S}{v} < -\frac{mX_i(1-k)}{D} \quad (1.2)$$

where the composition of the liquid (X_i) at the interface is $\frac{X_0}{k}$, and the above is a more stringent condition since $G_S > G_L$. This can be analyzed using the equations (Weeks and Ackley, 1982):

$$t = \frac{\rho L h^2}{2\kappa \Delta T_0} \quad (1.3a)$$

$$v = \frac{dh}{dt} = \frac{\kappa \Delta T_0}{\rho L h} \quad (1.3b)$$

$$G_S = \frac{\Delta T_0}{h} \quad (1.3c)$$

and yields the criterion

$$\frac{\rho L}{\kappa} < \frac{-mX_0}{D} \left(\frac{1-k}{k} \right) \quad (1.4)$$

where t is time, ρ is density of the ice, L is the latent heat of fusion per unit mass, ΔT is the difference between the upper temperature of the ice and the freezing temperature of the seawater, h is the ice thickness, and κ is the thermal conductivity of the ice. In sea ice, this typically results in the following requirement for constitutional supercooling:

$$10^{-4} < \left(\frac{1-k}{k} \right) X_0 \quad (1.5)$$

and thus, non-planar interfaces are favored except for very small solute concentrations (Weeks and Ackley, 1982).

Constitutional supercooling leads to the growth of lamellar solid/liquid interface as small bumps on the bottom surface have a growth advantage. The supercooled water acts as a heat sink creating a positive feedback loop and more lamellae. The orientation of the lamellae is such that they are perpendicular to the primary current direction as this enhances the rate at which salt is removed from the interface (Weeks and Wettlaufer, 1996). It has been shown that a reduction in growth velocity corresponds to an increase in the brine layer spacing with maximum values reaching several millimeters (Nakawo and Sinha, 1984). The importance of the skeletal layer is that it provides a mechanism for entrapping brine. As the ice platelets begin to thicken, they become interconnected forming vertical pockets of brine that can trap 10 – 40% of the sea salt ions, whereby 99.9% of impurities are expelled during the formation of freshwater ice (Eicken, 2003). The faster the ice growth, the less time there is for brine expulsion and more brine is entrapped. Thus, as the ice depth thickens, the growth rate slows, initially brine volume decreases (prior to brine migration discussed later), and brine layer spacing increases. This trend, combined with the fact that the bottom of the ice is warmer with a greater brine volume fraction, results in a C-shape profile for sea ice salinity. The final result is a cellular structure of sea ice with layers

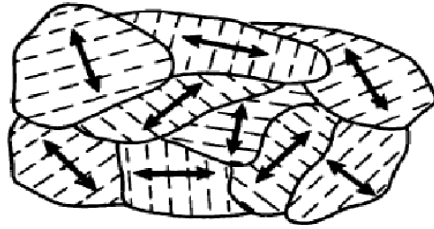


Figure 1.6: Schematic of the cellular structure of sea ice as seen from Maykut (1985). Solid curved lines represent grain boundaries, dashed lines represent brine layers/ice platelets, and arrows show the direction of the c -axis. Note that the c -axis direction is perpendicular to the ice platelets.

perpendicular to the horizontal c -axis (Fig. 1.6) that strongly influence the bulk thermal and mechanical properties of the ice (Maykut, 1985).

Around Antarctica the combination of greater wave turbulence, stronger winds, and more open leads and polynas favors the growth of frazil ice. In fact, frazil ice growth can represent up to 60 – 80% of the ice cover in the more dynamic Southern Ocean (Lange et al., 1989). Conversely, the relatively calm Arctic has a larger percentage of congelation ice. However, future reductions in Arctic ice extent might lead to an increased prevalence of frazil ice and initial data have already shown an increased proportion of granular ice in the Arctic (Perovich and Richter-Menge, 2009). Additionally, too great a weight from snow causes depression of the sea ice, and the potential for flooding. If this occurs, the snow then forms additional granular ice that is nearly indistinguishable from frazil ice. Due to its visual similarity, stable oxygen isotopes are used to help determine the relative amounts of each ice type. Generally, flooding can account for about 20% of ice growth, with upwards of 50% in the dynamic Antarctic (Jeffries et al., 1994).

To study the kinetics of ice growth, we start with an energy balance at the bottom of the

ice where the majority of growth occurs, especially in the Arctic. We start with

$$F_c - F_w = \rho_i L \frac{\partial H}{\partial t} \quad (1.6a)$$

where F_c is the conductive heat flux out of the ice-ocean interface into the ice, F_w the heat flux from the ocean into the interface, ρ_i the density of ice, and $\frac{\partial H}{\partial t}$ is the thickness change, with fluxes positive if upwards (Eicken, 2003). Since heat flow in the Antarctic ocean can reach several tens of W m^{-2} , ice cover reaches a maximum thickness even during the winter. This occurs once $F_c = F_w$. From this relation, it is apparent episodes having large oceanic heat fluxes can significantly thin the ice cover by melting from below. We now proceed following Eicken (2003), assuming F_w to be known. We first linearize the atmospheric heat flux

$$F_a = -k(T_a - T_s) \quad (1.6b)$$

where k is an effective heat transfer coefficient between the surface and the atmosphere, and $T_a - T_s$ is the temperature difference between them. Assuming a linear temperature profile in the ice and snow during the growth season, we note that we have for the snow and ice

$$F_c = -\lambda_s \frac{T_s - T_i}{h_s} \quad (1.6c)$$

$$F_c = -\lambda_i \frac{T_i - T_w}{H} \quad (1.6d)$$

where λ_s and λ_i are the thermal conductivity in snow and ice, respectively, T_i and T_w are the temperature at the snow-ice and ice-ocean interfaces, respectively, and h_s and H are the thicknesses of the snow and ice, respectively. Combining Eq. 1.6b, Eq. 1.6c, and Eq. 1.6d with the fact that $F_a = F_c$ yields

$$-\left(\frac{1}{k} + \frac{h_s}{\lambda_s} + \frac{H}{\lambda_i}\right) F_c = T_a - T_w \quad (1.6e)$$

Solving for F_c and plugging into Eq. 1.6a yields

$$\frac{\partial H}{\partial t} \rho_i L = -\frac{T_a - T_w}{\frac{1}{k} + \frac{h_s}{\lambda_s} + \frac{H}{\lambda_i}} - F_w \quad (1.6f)$$

For simplicity, we assume snow depth scales with ice depth such that $h_s = r_s H$ for some constant of proportionality. We also let $F_w = 0$ and integrate over time:

$$H^2 + \frac{2\lambda_i}{k} \left(1 + \frac{\lambda_i}{\lambda_s} r_s\right)^{-1} H = \frac{2\lambda_s}{\rho_i L} \left(1 + \frac{\lambda_i}{\lambda_s} r_s\right)^{-1} \int -(T_a - T_w) dt \quad (1.7)$$

Although the above equation is daunting, a few simplifications yields information under special circumstances. We assume a known and constant surface temperature ($k \rightarrow \infty$), constant T_a , and no snow ($r_s = 0$). This results in Stefan's growth law:

$$H^2 = \frac{2\lambda_i(T_w - T_a)}{\rho_i L} t \quad (1.8)$$

and we see that the thickness of the sea ice increases with the square root of time.

The above kinetics can be combined with empirical data to create relatively accurate models for sea ice growth. In the Arctic, ice growth occurs almost entirely from the bottom of the sea ice downwards, with an average winter rate of about 0.5 cm per day (Eicken, 2003). As the sea ice thickens, this growth rate slows as it becomes increasingly more difficult to transfer heat from the ocean to the atmosphere. In the Antarctic, growth rates are slower due to the presence of snow, which acts as a good insulator. Combined with a greater oceanic heat flux around $F_w = 20 \text{ W m}^{-2}$, congelation ice growth from below is limited to a thickness of about 0.5 m (Eicken, 2003).

Salts

Until presently herein, discussion of the presence of salts in sea ice has mostly been ignored. Despite its low packing efficiency, most salt ions cannot be incorporated into

the ice crystal lattice, with notable exceptions being F^- and NH_4^+ (Weeks and Ackley, 1982). Thus, salt ions such as Na^+ , K^+ , Ca^{2+} , SO_4^{2-} , CO_3^{2-} , Cl^- , and Mg^{2+} are rejected from the ice crystal structure during the freezing process. This results in both increased salt concentrations in the liquid brine surrounding the ice and expulsion of salts into the seawater below. However, due to the non-planar lamellar solid/liquid interface, some salt becomes entrapped in brine inclusions during growth. Therefore, the sea ice system is best described as a two-phase, two-component, reactive porous medium, consisting of a pure solid ice matrix and interstitial liquid saline brine (Feltham et al., 2006). Temperature, pressure, and other seasonal weather fluctuations lead to brine movement in the ice (described in more detail below), and as a result, the brine inclusions form an interconnected, vertically-oriented brine channel network providing pathways for heat, gas, and salt transport.

With its brine channel network, sea ice is filled with phase boundaries that are considered to always be in local equilibrium. That is, the liquid temperature is equal to the liquidus temperature for the given local salinity. Changes in temperature correspond to changes in the salinity of the interstitial brine, and thus, change the equilibrium freezing point. Following the convention of Notz (2005), it is helpful here to differentiate between bulk salinity, S_{bu} , and brine salinity, S_{br} , defined as:

$$S_{bu} = \frac{m_{\text{salt}}}{m_L + m_S} \cdot 10^3 \text{ppt} \quad (1.9a)$$

$$S_{br} = \frac{m_{\text{salt}}}{m_L} \cdot 10^3 \text{ppt} \quad (1.9b)$$

If we define the solid (ϕ_m^S) and liquid (ϕ_m^L) mass fractions to be:

$$\phi_m^S = \frac{m_S}{m_L + m_S} \quad (1.9c)$$

$$\phi_m^L = (1 - \phi_m^S) = \frac{m_L}{m_L + m_S} \quad (1.9d)$$

we note that

$$\phi_m^L = (1 - \phi_m^S) = \frac{S_{bu}}{S_{br}} \quad (1.9e)$$

From the mass fractions, we can multiply by molar volumes to obtain molar fractions X_S and X_L that are used from here on. Since the ratio of the solid to liquid fraction determines many of the thermodynamic, electrical, mechanic, and optical properties in sea ice, it is important to have an understanding of the bulk salinity and its temporal evolution (Notz, 2005).

Sea ice can be considered what is known as a ‘‘mushy layer,’’ and the corresponding theory yields relationships for a given region to describe the conservation of heat and composition (Feltham et al., 2006). For sea ice, the local energy balance can be written:

$$c_m \frac{\partial T}{\partial t} + c_b \mathbf{v} \cdot \nabla T = \nabla \cdot (k_m \nabla T) + L_v \frac{\partial \phi^S}{\partial t} + A_R \quad (1.10a)$$

where T is temperature in Kelvin, ϕ^S is the solid volume fraction, c_m is the effective heat capacity of sea ice, c_b is the heat capacity of the brine, t is time, \mathbf{v} is the Darcy velocity (volume flux of brine per unit cross-sectional area), L_v is the latent heat of fusion per unit volume, and A_R represents the absorption of shortwave radiation that has passed through the upper sea-ice surface (Feltham et al., 2006). The local salt conservation can be written as

$$(1 - \phi^S) \frac{\partial X_L}{\partial t} + \mathbf{v} \cdot \nabla X_L = \nabla \cdot (D_m \nabla X_L) + \frac{\rho_S}{\rho_L} (X_L - X_S) \frac{\partial \phi^S}{\partial t} \quad (1.10b)$$

where X_L and X_S is the concentration of salt in the liquid brine and within the ice crystal (nearly zero), respectively, ρ_L and ρ_S the brine and ice density, respectively, and $D_m = (1 - \phi^S) D_L$ where D_m and D_L are the mushy layer and brine diffusion coefficients of salt (Feltham et al., 2006). Local equilibrium is maintained if the interstitial salt transport is short relative to the timescale of thermal variations, which scales with t . Thus, we have the requirement $t > \frac{\delta^2}{D_L}$, where δ is the solid-element spacing. In sea ice, $\delta \approx 10^{-4} - 10^{-3}$ m and $D_L \approx 10^{-9} \text{ m}^2\text{s}^{-1}$, and thus, $t > 10 - 10^3$ s. Since temperature variations are on

the timescale of a day, the assumption of local equilibrium is valid. Therefore, the linear relationship of the liquidus curve (used implicitly for the derivation of the critical gradient for constitutional supercooling) $T_e = mX_L + T_0$ eliminates X_L and we have:

$$(1 - \phi^S) \frac{\partial T}{\partial t} + \mathbf{v} \cdot \nabla T = \nabla \cdot (D_m \nabla T) + \frac{\rho_S}{\rho_L} [T - T_e(X_S)] \frac{\partial \phi^S}{\partial t} \quad (1.10c)$$

The pioneer in creating a phase diagram for sea ice/water was Assur, whose original diagram is given in Fig. 1.7 (Assur, 1958). For simplicity, he assumed sea water consisted of water and the ions Na^+ , K^+ , Ca^{2+} , SO_4^{2-} , Cl^- , and Mg^{2+} . Since Na^+ and Cl^- account for 85% of all ions, while the others bring that total to 99%, this is a good approximation. As mentioned before, during the solidification of ice, sea salts are rejected into the liquid brine. In addition, a thermal gradient exists as cold atmospheric conditions cool the top of the sea ice while the bottom remains near -1.8°C . This thermal gradient encompasses the eutectic temperature of some of the primary components of sea salt, and thus, can greatly affect the distribution and concentration of these salts. As the temperature continues to decrease, ϕ^S and consequently S_{br} increase. Once the temperature decreases to -8.2°C , the brine is supersaturated with respect to sodium sulphate and mirabilite ($\text{Na}_2\text{SO}_4 \cdot 10\text{H}_2\text{O}$) precipitates out. Similarly, other precipitates such as ikaite ($\text{CaCO}_3 \cdot 6\text{H}_2\text{O}$) at -2.2°C , hydrohalite ($\text{NaCl} \cdot 2\text{H}_2\text{O}$) at -22.9°C , sylvite (KCl) at -36.8°C , and Antarcticite ($\text{CaCl}_2 \cdot 6\text{H}_2\text{O}$) at -55°C form as the temperature decreases (Weeks and Ackley, 1982). However, even at the coldest temperatures when $\phi^S > 92\%$, there is a liquid layer that is important for organisms who spend the winter within the sea ice (Eicken, 2003).

A full understanding of the salinity profile in sea ice requires an analysis of the desalination process governed by four different mechanisms: brine pocket diffusion, brine expulsion, gravitational drainage, and flushing (Notz, 2005). Theory dictates that during the winter, the brine pockets are colder at the top leading to a salinity gradient. To establish equilibrium, there would be a downward diffusion of salt through the brine pockets.

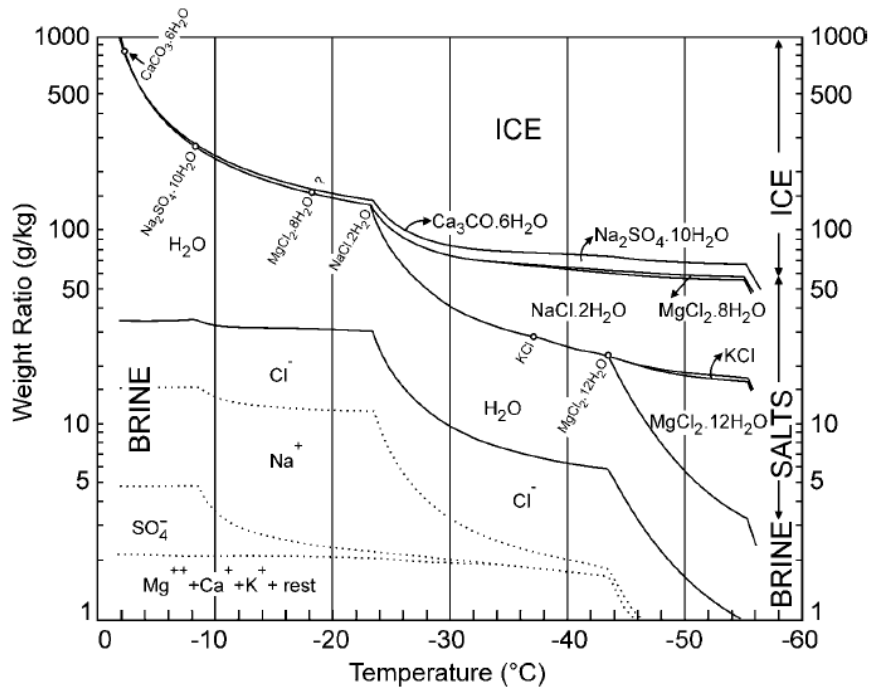


Figure 1.7: Phase diagram for brine, sea ice, and its salts as presented by Assur (1958)

However, further theoretical and experimental work has shown that the velocity of this process is too small to have any meaningful effect (Notz, 2005). As described above, during initial stages of sea ice growth, brine expulsion is an important mechanism. This leads to a movement of solute due to density differences between the ice and brine, whose effect can be seen by the last term in Eq. 1.10b (Feltham et al., 2006). Although brine expulsion continues to move brine downwards, it is typically at a velocity less than the rate of ice growth. Thus, brine expulsion does not have a large effect on the bulk salinity profile (Notz, 2005).

Since natural cooling of sea ice occurs from above, brine salinity is greatest at the top of the ice. This corresponds to a higher density and an unstable brine-salinity profile develops. The gravitational overturning to reestablish equilibrium is known as gravitational drainage, and is responsible for the large majority of the desalination (Wettlaufer et al., 1997). Finally, summer melting of the sea ice cover causes an influx of freshwater that

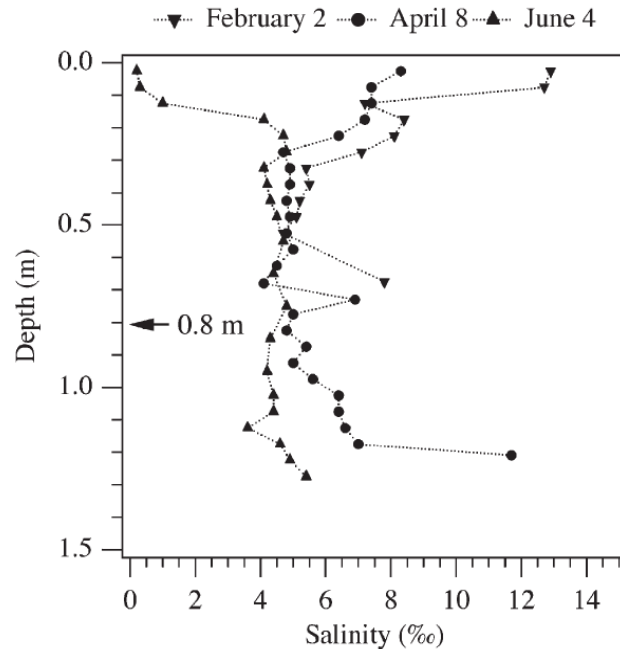


Figure 1.8: Salinity profiles for three ice cores from Barrow, AK. Note how a flushing episode is clearly evident from the core taken on June 4. Data from Backstrom and Eicken (2006)

percolates through the ice matrix in a process known as flushing. Since the brine volume fraction of sea ice is highly dependent upon both salinity and temperature, understanding the seasonal microstructural evolution is critical for accurate interpretation and modeling of sea ice properties. Collectively, these processes help create salinity profiles such as the ones shown in Fig. 1.8 (Backstrom and Eicken, 2006).

Brine Channels and Transport

The highly sensitive temperature dependence of the morphology of brine networks is not well-understood, presenting challenges in the interpretation and prediction of sea ice in global climate models. To describe transport processes through sea ice, it is important to have a quantitative understanding of the connectivity of brine channels. Golden et al. (1998) developed a general rule of thumb known as “The Rule of Fives,” which states that a connected brine network develops for a brine volume fraction of 5%, occurring at

about -5 °C and with a salinity of about 5‰ in first-year sea ice. Percolation theory helps to mathematically characterize the temporal evolution of pore space by theoretically predicting permeability, and consequentially when transitions to connectedness may occur (Grimmett, 1999; Stauffer and Aharony, 1994). Thus, following the convention of Golden et al. (1998), we apply percolation theory to sea ice to better understand the Rule of Fives.

We start with the simple integer lattice in \mathbb{Z}^d with bonds joining nearest neighboring sites that can either be open with probability $0 \leq p \leq 1$ or closed with probability $1 - p$. Groups of connected open bonds are termed open clusters and the average cluster size increases with p . There exists a critical threshold p_c , called the percolation threshold, such that for $p \geq p_c$ there is an infinite cluster. For $d = 2$, it turns out that $p_c = 0.5$ (see Fig. 1.9), while for $d = 3$, $p_c \approx 0.25$ (Stauffer and Aharony, 1994). Although for sea ice $d = 3$, experimental results have shown that $p_c \neq 0.25$, but rather $p_c = 0.05$ (e.g., Weeks and Ackley, 1982). This incongruity was solved by comparing the cellular microstructure of sea ice to compressed powders (Golden et al., 1998). For compressed powders, a key geometrical parameter is the ratio $\xi = R_p/R_m$, where R_p is the radius of the large polymer particles and R_m is the radius of the smaller metal compounds (Malliaris and Turner, 1971). Increasing ξ leads to smaller values for p_c , although as ξ reaches larger values, p_c becomes relatively invariant. Golden et al. (1998) found that for ξ ranging from 44 – 17, p_c ranges from 3 – 7%, respectively. When applied to columnar sea ice, this results in $p_c = 0.05$, consistent with experimental results. For granular ice, ξ will be smaller and consequently, p_c is greater for granular ice than columnar ice (Golden et al., 1998).

Knowledge of the brine channel connectivity leads to an understanding of the permeability of sea ice. For simplicity, we will consider the permeability tensor to consist of two equal horizontal components κ_{h_1} and κ_{h_2} , and a vertical component κ_v . Previous work has found that sea ice anisotropy leads to κ_v being larger than κ_h by at least a factor of seven (Freitag and Eicken, 2003; Petrich et al., 2006). Since fluid flow is closely tied to the porosity of the medium, much work has been devoted to finding a relationship between

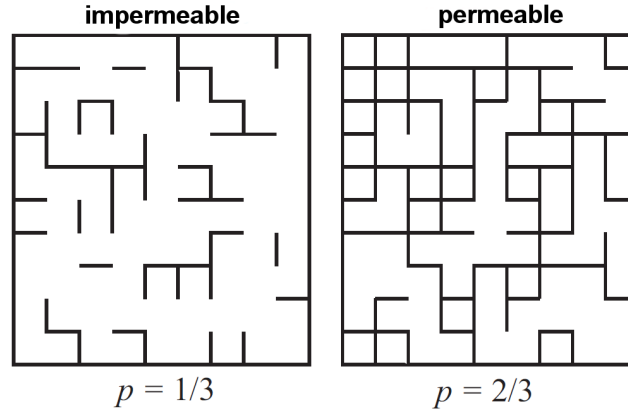


Figure 1.9: Schematic illustrating percolation threshold in two dimensions. For $p < 0.5$ the system is impermeable (e.g., left panel), but for $p > 0.5$ there exists an infinite connected cluster and the system is considered permeable (e.g., right panel).

permeability and porosity. However, since brine only moves through the open porosity, it is helpful to differentiate between the total porosity ϕ_t and the effective porosity ϕ_e . Using a percolation model, Petrich et al. (2006) developed the relationship:

$$\phi_e = \begin{cases} 0 & \text{for } \phi_t \leq 0.054 \\ 0.34(\phi_t - 0.054)^{0.41} & \text{for } 0.054 < \phi_t \leq 0.09 \\ \phi_t & \text{for } 0.09 < \phi_t \end{cases} \quad (1.11)$$

This empirical relationship led to the vertical component of the permeability tensor for young first-year sea ice to be estimated as (Petrich et al., 2006):

$$\kappa_v = 3 \times 10^{-8} \text{ m}^2 \phi_e^{3.9} \quad \text{for } 0.05 \leq \phi_e \leq 0.2 \quad (1.12)$$

Using X-Ray μ -computed tomography to analyze the sea ice pore space, Golden et al. (2007) further developed percolation theory to create a numerical model that matched field measurements of permeability as is shown in Fig. 1.10. It is interesting to note that air temperature alone can lead to the sudden permeability transition when the brine channel network becomes disconnected for $\phi_e < 0.05$ (Golden et al., 1998). Although the

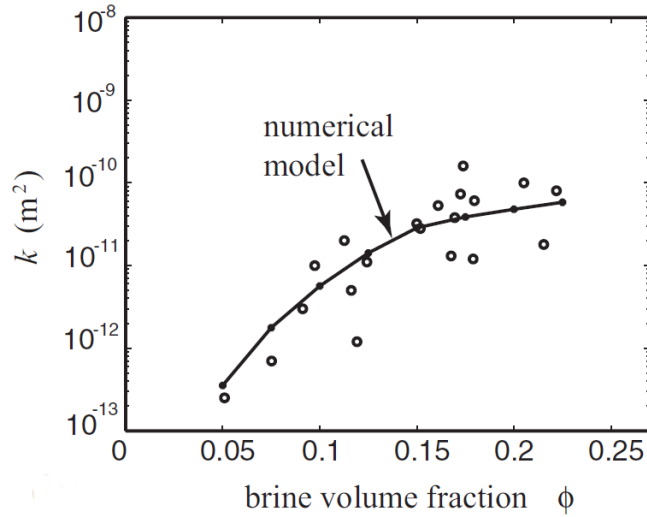


Figure 1.10: Numerical model of sea ice permeability as a function of brine volume fraction. The open circles are field data collected from Barrow, Alaska, while the solid line is the numerical model (Golden et al., 2007)

basic phenomenon of permeability can be described and modeled by current percolation theory, more work is needed to fully capture the spatial and temporal variability, degree of permeability, and the details of the pore network.

Atmospheric Interactions

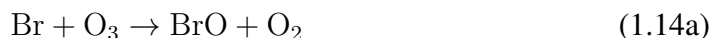
As suggested earlier, a primary importance of sea ice permeability and the brine channel network is that it provides a mechanism for transporting salts to the surface snow and atmosphere interface. Snow lying above the sea ice has been found with enriched salinities (> 2 psu) up to heights of 0.1–0.2 m above the snow/ice interface due to upwards migration of brine by capillary action (e.g., Domine et al., 2004; Massom et al., 2001). Wind pumping through the snowpack aids in the transport of these halides to the air interface (Colbeck, 1997). Fractionation due to salt precipitation of the brine in sea ice results in the snow above having a different chemical signature than sea spray, usually with sulfate depletion and bromide enrichment (Abbatt et al., 2012). In addition, the heavier halides are drawn to the air-water interface due to increased polarizability (Gladich et al., 2011; Jungwirth

et al., 2006). With iodide playing a smaller role due to its decreased abundance, there is an increased importance of bromide relative to chloride at the surface. In total, the net result of salt transport to the air interface is that it provides a source of readily activated halides that play an important role in tropospheric chemistry.

In the 1970s, it was recognized that halogens, specifically chlorofluorocarbons (CFCs), were leading to the destruction of the stratospheric ozone layer (Molina and Rowland, 1974). Chlorine was identified as the catalyst through the following chain reaction:

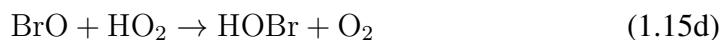
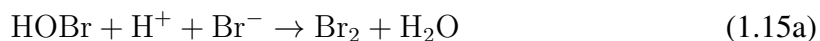


Further research in the 1980s led to the discovery of the springtime Antarctic ozone hole in the lower stratosphere (Farman et al., 1985). As research on halogen chemistry and ozone depletion continued, it was hypothesized that stratospheric ozone depletion via a mechanism similar to Reaction 1.13 may also occur with bromine as the halogen (Wofsy et al., 1975):



Although it was found that bromine does not play a significant role in stratospheric ozone depletion, it is the main catalyst for ozone depletion events (ODEs) in the lower troposphere (Barrie et al., 1988). By measuring ozone and filterable bromine in Alert, Canada, Barrie et al. (1988) observed an inverse relationship between the two suggesting the importance of Reaction 1.14. The full mechanism below was later worked out by Fan and Jacob (1992), although work remained in determining the location for initial bromine activation and is

discussed in more detail in Chapter 3 (Abbatt et al., 2012).



Current research though has identified several characteristics and conditions that optimize the above “bromine explosion” mechanism. It is well established that the critical steps are heterogeneous reactions and require a suitable surface to bring the different phases in contact (e.g., Adams et al., 2002; Huff and Abbatt, 2002). Satellite observations from the Global Ozone Monitoring Experiment (GOME) enable global observations of both ozone and BrO atmospheric concentrations (Burrows et al., 1999), and recently have been able to isolate tropospheric concentrations (Theys et al., 2011). These satellite observations helped identify the correlation of bromine release with first-year sea ice (Lindberg et al., 2002; Wagner et al., 2001), which was later verified with ground-based observations (Simpson et al., 2007a). Because Reaction 1.15 is photochemically driven, sunlight is also required and thus, the polar springtime has the highest occurrence of the bromine explosion (Simpson et al., 2007b). It is well documented that the key step for the uptake of additional bromide, Reaction 1.15a, is pH dependent, and thus, more bromine release is associated with more acidic snow (Pratt et al., 2013; Simpson et al., 2007b). However, others have found the freezing process to eliminate the pH dependency (Adams et al., 2002; Huff and Abbatt, 2002).

Although accounting for only 2% of tropospheric ozone depletion, chlorine does play an important role in tropospheric chemistry (Simpson et al., 2007b). Similar to

Reaction 1.15a, HOBr can help oxidize Cl^- and form BrCl through the reaction:

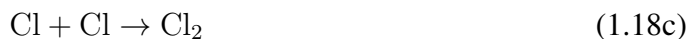


Photolysis of BrCl yields both chlorine radicals and later HOCl, which in return can oxidize more Cl^- , and leads to the formation of reactive Cl_2 gas (Wren et al., 2013). Once formed, chlorine plays an active role in the oxidation of many volatile organic compounds (VOCs), especially CH_4 , through the pathway (Simpson et al., 2007b; von Glasow and Crutzen, 2007):



It should be noted that due to the greater electron affinity of chlorine, it is less likely to be oxidized than bromine and plays a more substantial role as an oxidant. Although initial formation of Cl_2 occurs subsequent to Br_2 and later BrCl formation, the processes can occur simultaneously, and do not require complete depletion of Br^- first (Wren et al., 2013). While the importance of chlorine to tropospheric chemistry is recognized, many of the details of its production and recycling remain not well understood (Abbatt et al., 2012; von Glasow and Crutzen, 2007).

The hydroxyl anion OH^- and hydroxyl radical OH are participants in many of the atmospheric reactions occurring in the boundary layer, playing a large role in determining the oxidizing potential of the troposphere. One such pathway leads to the release of chlorine gas through the aqueous-phase surface reactions (Oum et al., 1998):



The formation of the hydroxyl radical is closely coupled to nitrogen fluxes, as several

mechanisms exist that depend upon the photolysis of the nitrate anion (Dominé and Shepson, 2002; Grannas et al., 2007; Simpson et al., 2007b). Direct photolysis of nitrate leads to radical O^- , which can then combine with protons H^+ to form OH (Dominé and Shepson, 2002). The other byproduct, NO_2 , is also rapidly protonated to form HONO, and later photolysis releases more hydroxyl radicals (Zhou et al., 2001). In addition, the photolysis of ozone in the presence of water vapor is another mechanism for OH production (Mauldin et al., 2001). It should be noted that hydroxyl chemistry is closely coupled to the formation of HO_2 , and many similar mechanisms, such as the photolysis of H_2O_2 , lead to formation of HO_2 . Furthermore, OH can combine with organic materials in the snowpack to form HCHO and subsequent HO_2 upon photolysis (Grannas et al., 2007). These processes occur ubiquitously throughout the snowpack, and are some of the driving forces in the bromine explosion (Dominé and Shepson, 2002).

The implications of halogen tropospheric chemistry are still being studied. The cycling of other chemical species, such as mercury, has been known to be coupled to halogen chemistry. For example, atmospheric mercury depletion events (AMDEs) have been observed to occur episodically at the same time as bromine explosion events and ODEs (e.g., Steffen et al., 2008). Once BrO and Br have formed via Reaction 1.15, mercury can be oxidized via (Lindberg et al., 2001; Lu et al., 2001):



The oxidized Hg^{2+} is then deposited onto the snow surface and into the ocean, where it can become incorporated into the food chain. As the climate continues to change, it is imperative that we have a full understanding of all of the global impacts of halogens in the atmosphere. Since many of the reactions are favored by lower pH, the increasing acidity of snow suggests a growing increase in the release of halogens into the near-future atmosphere

(von Glasow and Crutzen, 2007). This is coupled with an increasingly more first-year ice cover in the Arctic, which is inherently more saline with greater salt mobility.

Purpose of this Work

In this thesis, the polar transport of salts from the ocean, through the sea ice, and into the troposphere will be examined. We will start with a discussion of the analytical methods used in this work to study snow and sea ice in Chapter 2. In Chapter 3, measurements of the chemical composition of surface and blowing snow will be presented. This will provide insight into the chemical processes that occur once salts reach the boundary layer, and specifically on which surfaces they can occur. Since the primary source of salts in snow lying on sea ice is upward migration of salt from the ice itself, we will next study the sea ice itself. In particular, Chapter 4 will investigate the microstructural location of bromide and other salts within the sea ice. Knowledge of where the salts are located will be compared to microstructural analysis of the sea ice completed using x-ray micro-computed tomography. Chapter 5 will present the measured sea ice microstructure, while a mathematical network model of the brine channels will be given in Chapter 6.

METHODS

Sample Collection and Preparation

In October - November 2012, we collected 9-cm diameter sea ice cores, surface snow, and blowing snow over first-year sea ice in the Ross Sea, Antarctica. Two primary field sites were chosen, based upon prevailing wind direction, to maximize contact of the blowing snow with first-year sea ice. Their locations are shown in Fig. 2.1. Butter Point Site was located 6.5 km from the open ocean and 35 km north of the Ross Ice Shelf. Iceberg Site was located 55 km northwest of Butter Point, and since the ice edge located to the east follows the shore, the distance to open water here was also 5 km. Iceberg Site was chosen based upon the presence of a 740 m long and 35 m high iceberg located 250 m to the west that would block winds sourced over land, maximizing blowing snow collection from over sea ice. At each of these two sites, we collected blowing snow, surface snow, and a single ice core. For each site, a 5.5 m blowing snow collection tower was erected for the time period of 11 October– 8 November 2012. Collection baskets made out of 150 μm nylon monofilament mesh and 7" diameter by 14" long (Midwest Filter Corporation, Lake Forest, IL) were placed at four different heights: 0.3, 2.0, 3.0, and 5.5 m above the snow surface. The sites were visited approximately every other day, and collection baskets were switched even if no snow was collected. Baskets were triple rinsed with deionized (DI) water between uses. Surface snow samples were collected each of the 12 days the sites were visited. The ice cores extracted from Butter Point and Iceberg sites were 1.78 and 1.89 m in length, respectively.

The snow surface was quite different between the Butter Point Site and the Iceberg Site. Snow depth maps showing the spatial distribution of snow over a 24×24 m grid are presented in Fig. 2.2. Butter Point site had very little snow (less than 10 cm) with low

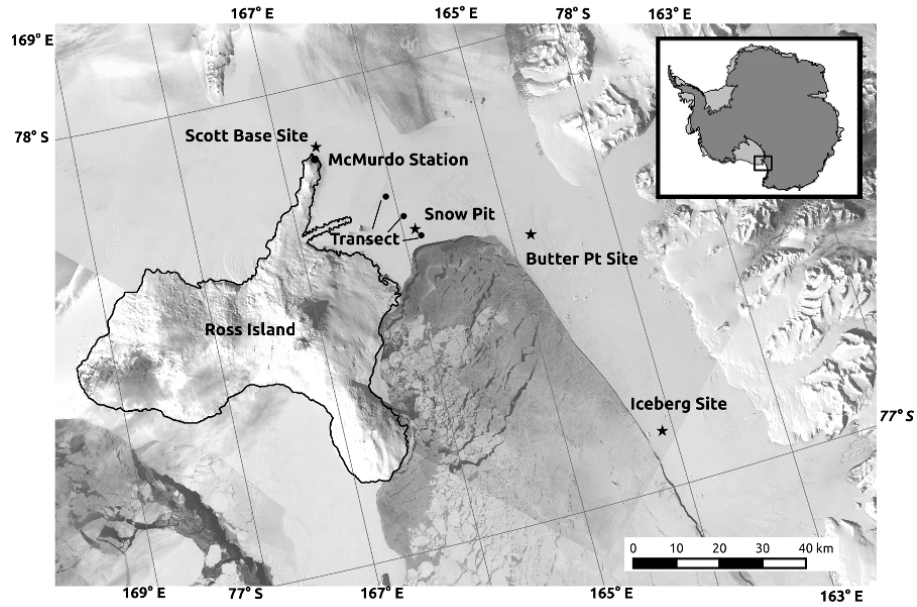


Figure 2.1: Map of the Ross Sea region showing all field sites. Ice cores were extracted from Butter Point Site, Iceberg Site, Scott Base Site, and along the Transect. The basemap is from Landsat imagery.

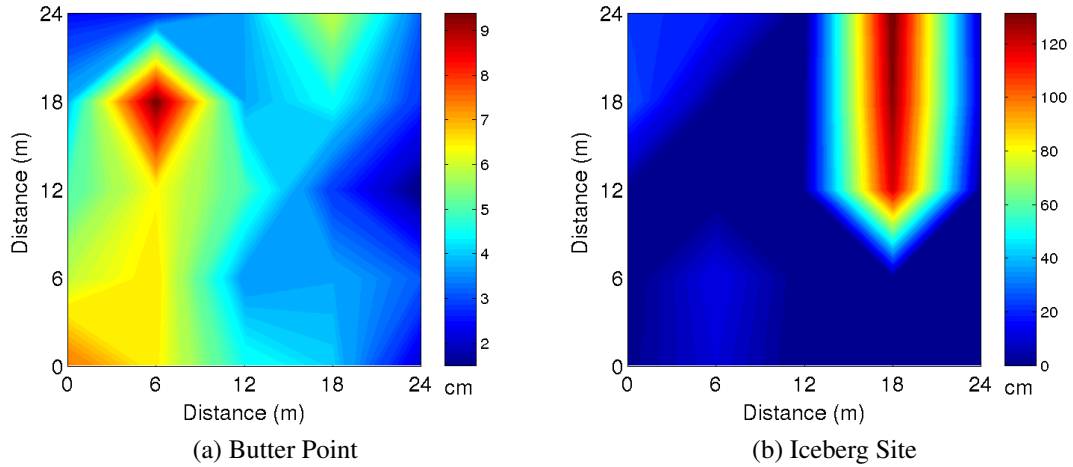


Figure 2.2: Snow depth maps for Butter Point Site and Iceberg Site

spatial variability. Conversely, at the Iceberg Site there was a strong prevalence of rafted ice and sastrugi that led to significant snow drifts. The large difference in surface roughness has a significant impact upon the ability to loft blowing snow.

In addition, we selected three sites located on a transect that were 6, 12, and 18 km,

respectively, southeast of the ice edge. At each of these three sites, we extracted an ice core, which had lengths of 1.70, 1.80, and 1.82 m, respectively, and two surface snow samples (shallow and deep depths). To compare all of our first-year sea ice samples to multi-year ice, we selected one final site located over multi-year ice 700 m off-shore from Scott Base, Ross Island. The sea ice core extracted from this site was 1.96 m. Snow samples and sea ice cores were transported at a constant temperature of $-20\text{ }^{\circ}\text{C}$ using Blue ice packs back to Thayer School of Engineering's Ice Research Laboratory at Dartmouth College and stored in a $-33\text{ }^{\circ}\text{C}$ cold room prior to analysis.

The chemical composition and microstructure of the sea ice cores were analyzed using a combination of ion chromatography (IC), synchrotron X-ray micro-fluorescence (XRF), and X-ray micro-computed tomography (μCT) as will be described in detail below. In preparation, each sea ice core was first cut in half vertically, with half of the core to be sampled for analysis, while the other half was stored for optical thin-sections and safekeeping. At 10-cm intervals for the length of each core, a 2-cm subsample was extracted, while the remaining 8 cm of ice was stored for preservation. From these 2-cm slices, a portion was melted for IC, cubic samples were cut for μCT , and rectangular slices were cut for XRF. Surface and blowing snow samples were melted and only analyzed by IC for chemical composition as the microstructure of the snow was not preserved.

Vertical thin sections for each sea ice core were prepared and are shown in Fig. 2.3. Horizontal thin sections at 10-cm intervals for each core are given in Chapter 4. All six ice cores show the expected small-grain granular ice near the top of the core, and large-grain columnar ice deeper in the core. This transition zone is around 18 cm, 28 cm, and 80 cm for the Butter Point, Iceberg Site, and Scott Base cores, respectively. The three cores along the transect from the sea ice edge inwards have transitions around 14 cm, 48 cm, and 38 cm, respectively. The multi-year Scott Base core likely has a much higher percentage of granular ice due to the formation of snow ice when sea water floods over the top of the ice pack. Although the bulk of the columnar ice has vertically oriented grains, there are some

regions of small grains, horizontal grains, and occasional cracking. This is especially true in the Butter Point ice core. Some of these regions may be the result of partial rafting of the ice floes. The Iceberg Site core exhibits the largest and most vertically aligned grains, likely as a result of calmer ocean conditions as a result of the nearby iceberg.

Ion Chromatography

Ion-exchange chromatography, or ion chromatography (IC), was developed in 1975 to separate analytes in a solution based upon their affinity for a particular substrate (Small et al., 1975). A mobile liquid phase containing the sample is passed through a stationary phase to which ions and polar molecules are retained by coulombic interactions. The retention time of each analyte is primarily dependent upon its polarizability. By selecting the appropriate stationary phase for the separation column and then choosing a corresponding strength eluent, it is possible to separate the desired analytes in a sample by their retention times. For this work, the anions Cl^- , Br^- , SO_4^{2-} , and NO_3^- were of primary interest, and thus the AS15-9 μm bead diameter, 4 mm \times 250 mm analytical anion column was selected in conjunction with the AG15 4 mm \times 50 mm guard column. This separation column uses positively-charged quaternary ammonium compounds ($\text{R}_4\text{-N}^+$) as the ion exchange groups attached to the packing material. The AS15 anion exchange column is a high capacity (225 μeq) column, meaning there are a large number of ion exchange groups per unit volume of the column. The column was also chosen for increased selectivity of the desired analytes to ensure adequate separation, as well its high efficiency to ensure narrow peaks.

Samples were injected into the Dionex-600 system using an autosampler and eluted by a 38 mM NaOH solution at a flow rate of 1.2 mL/min. Initially, hydroxyl anions (OH^-) from the eluent occupy the binding sites of the ion exchange groups. However, once the sample reaches the separation column, the analytes exchange with OH^- based upon their affinity for the column. Several competing factors determine the nucleophilicity of the

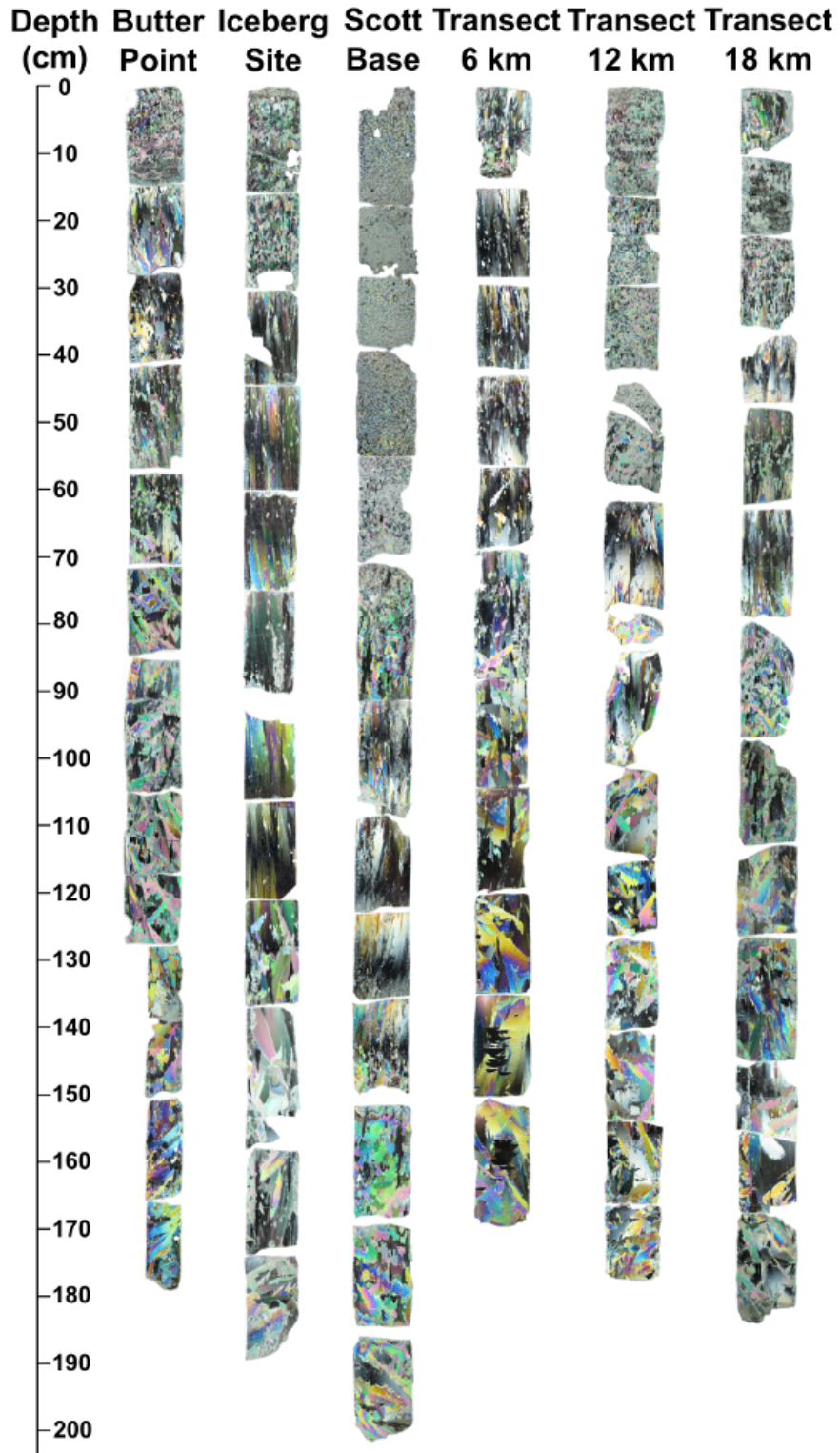


Figure 2.3: Vertical thin sections of the six sea ice cores in this study. Thin sections were prepared by thinning each section of sea ice to a thickness of approximately 0.5 mm using a microtome. Thin sections were then imaged using cross-polarizing filters to visualize the different grains.

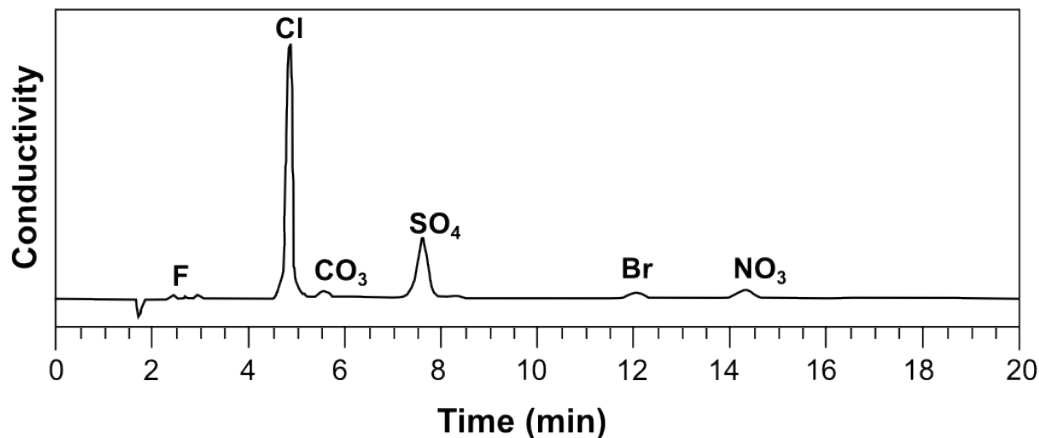


Figure 2.4: Representative IC chromatogram. The total run time per sample was 20 min with the water drop occurring around 1.8 min. Although the Cl peak dominates the chromatogram, peaks for the other analytes of interest were still above baseline noise and were able to be integrated. We do note the occurrence of a small peak for carbonate shortly after the Cl peak.

analyte including the charge, electronegativity, hydrogen bonding to the solvent, steric hindrance, and polarizability. In general, as the size of a halide increases, it becomes more polarizable and a better nucleophile, thereby being retained longer on the exchange column. In addition, in protic solvents such as NaOH, strong hydrogen bonding results in bulkier complexes with reduced nucleophilicity. The smaller halides form stronger hydrogen bonds, and thus remain in the mobile phase and elute through the column faster. With all of the above effects considered for the AS15 quaternary ammonium compound stationary phase and a NaOH eluent, the elution order for the analytes of interest was $\text{Cl}^- > \text{SO}_4^{2-} > \text{Br}^- > \text{NO}_3^-$. This resulted in chromatograms such as the one shown in Fig.2.4. Temperature control is very critical for IC, and therefore a LC 25 chromatogram oven set was used and set at 30 °C for all elutions.

To measure the concentration of each analyte after passing through the anion exchange column, the eluate was first passed through a Thermo Scientific Dionex ERS 5000 Electrolytically Regenerated Suppressor (ERS) set at a current of 100 μA . The ERS suppresses the signal from the eluent and increases the signal to noise ratio, by converting all anions to their corresponding acids. The conductivity response of the eluate was then

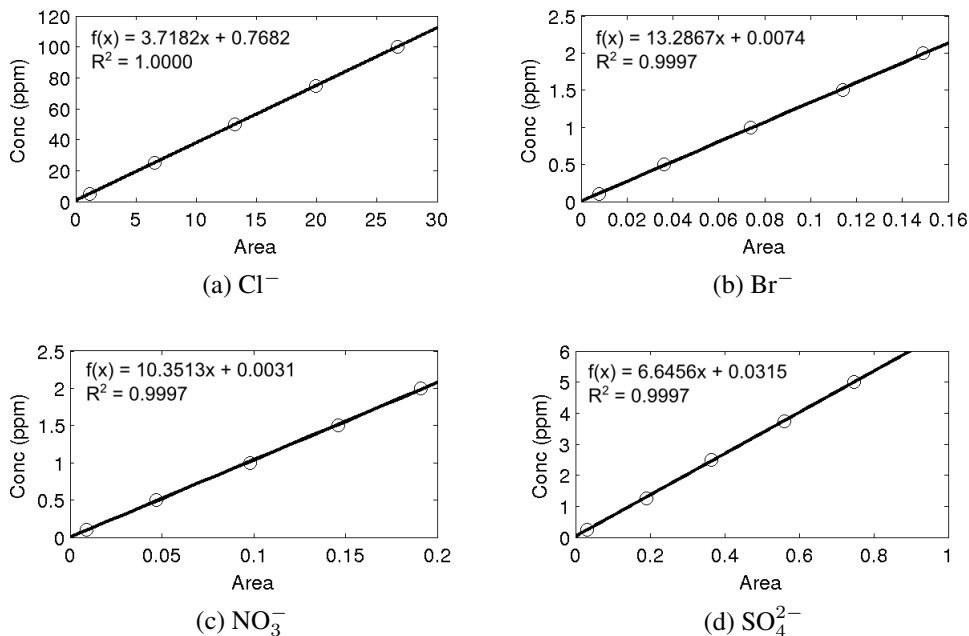


Figure 2.5: IC standard calibration curves. Open circles represent the five standard solutions and the solid line is the line of best fit. For all analytes, linear regression on each standard curve yielded a fit with $r^2 > 0.9997$.

measured using a CD 25 conductivity detector. Noise of the conductivity signal was measured at approximately $0.003 \mu\text{S}$. To determine the detection limits and quantification limits of our analysis, we used the RMSE method as described by Corley (2003). This yielded IC detection limits of 0.6, 0.1, 0.04, and 0.03 g/m^3 and limits of quantification of 2, 0.3, 0.1, and 0.1 g/m^3 for chloride, sulfate, bromide, and nitrate, respectively. Blank water samples and a set of five standards were run before and after each IC run. An example set of standard calibration curves are shown in Fig.2.5. For each analyte, linear regression on each standard curve yield a fit with $r^2 > 0.9997$.

All surface snow and blowing snow samples were melted into acid-rinsed HDPE vials, and diluted by a factor of five with DI water. Those samples falling outside of the calibration standard concentrations were further diluted to fall within the desired range. Each ice core was sub-sampled every 10 cm, melted, and diluted by a factor of 50, except for the bottom-most sample that was diluted by a factor of 100. A 0.5 mL aliquot of each diluted snow and ice sample was then analyzed for anion concentrations as described above.

X-Ray Micro-Fluorescence Spectroscopy

To identify the precise microstructural and stratigraphic location of the constituent salts in sea ice, samples were analyzed at Argonne National Laboratory's Advanced Photon Source (APS) using synchrotron x-ray micro-fluorescence spectroscopy (XRF). APS provides the brightest x-rays in the western hemisphere by circulating electrons around a 1.1 km circular ring 270,000 times per second. To achieve this, first electrons are emitted from a cathode and accelerated to 450 MeV in a linear accelerator. Using a booster synchrotron, electrons are then further accelerated from 450 MeV to 7 GeV. Electromagnets focus the electrons into a narrow beam that is approximately $300 \mu\text{m} \times 60 \mu\text{m}$ as they finally orbit around the full aluminum-alloy vacuum chamber ring at a current of 100 mA. Bending magnets and undulators are then used to generate x-rays for a wide variety of uses at 40 sectors located tangentially to the ring. For this project, we worked at beamline 13-ID-E at Sector 13, operated by the GeoSoilEnviro Center for Advanced Radiation Sources (GSECARS) of the University of Chicago.

The aim of this work was to quantitatively map the location of impurities in sea ice, determining if they are located at grain boundaries, in brine channels, and/or throughout the crystal lattice of ice. X-rays can penetrate deeper into a sample than electrons and thus, can be used to identify impurities located both on surfaces and at interfaces within samples several millimeters in thickness. The undulator at beamline 13-ID-E provides a highly tunable (2.4 – 28 keV with a spectral resolution of 1 eV), high flux of spatially coherent photons that can detect concentrations as low as one ppm for many of the impurities in sea ice. Previously, synchrotron x-ray radiation has been used to study the atomic structure (e.g. Baker et al., 2000; Varshney et al., 2009) and chemistry (Angelis et al., 2005; Cibirin et al., 2008) of ice. Cibirin et al. (2008) melted ice cores from multiple Antarctic and alpine sites and used XRF to study the chemical signature of filtered dust particles collected. By utilizing a cell wrapped with an Ultralene[®] film, Angelis et al. (2005) were able to

maintain accreted ice from Lake Vostok at $-140\text{ }^{\circ}\text{C}$ and map the location of impurities found at grain boundaries and brine micro-droplets. The study described in this thesis is the first to examine natural sea ice using synchrotron x-ray radiation and XRF.

As x-rays pass through a specimen, some of the energy is scattered and absorbed by the atoms in the sample. The intensity I of the signal after passing through the sample can be given by the Beer-Lambert law:

$$I = I_0 e^{-\mu x} \quad (2.1)$$

where I_0 is the initial beam intensity, μ is the linear attenuation coefficient, and x is the distance traveled. Absorption of the x-ray signal can be attributed to three dominant processes: the photo-electric effect, Compton scattering, and elastic scattering. Here we will focus primarily on the photo-electric effect as it is the key attenuation mechanism with both XRF and μCT (Ketcham and Carlson, 2001; Newville, 2004). The photoelectric effect results when the incoming x-ray photon energy is transferred to an inner shell electron, thereby ejecting it and giving off a photo-electron. We note that absorption of the incident x-ray only occurs if the x-ray energy is greater than the binding energy of the electron. The inner shell hole that is created is subsequently filled by an outer shell electron dropping in energy, and simultaneously emitting a photon to offset the reduction in energy, an effect known as fluorescence. We also note that:

$$\mu \approx \frac{\rho Z^4}{AE^3} \quad (2.2)$$

where ρ is the sample density, Z is the atomic number, A is the atomic mass, and E is the x-ray energy (Newville, 2004). This states that heavy elements are significantly more absorbing than lighter elements, an effect that will be important for μCT below (Ketcham and Carlson, 2001).

The K absorption edges for chlorine and bromine occur at 2.822 keV and 13.474 keV, respectively (Elam et al., 2002). Thus by tuning to an incident 18 keV x-ray beam, we

are able to use XRF to map the location of the primary anions of interest (Cl and Br), as well as K, Ca, Sr, Fe, Zn, and Cu. The incoming beam was first passed through a Si(111) monochromator with an incoming flux of between 2×10^{10} and 1.5×10^{11} photons per second and focused to a $2 \mu\text{m} \times 4 \mu\text{m}$ beamsize. The beam then passes through a series of slits and bent focusing mirrors prior to striking the sample, and then ejects inner shell electrons from the incident area as described above. The fluorescence signal is then detected by a SII Vortex ME-4 four-element silicon drift diode array detector. The signal over a 0.1 s period was recorded as a $2 \text{ mm} \times 2 \text{ mm}$ region of each sample with step sizes of $10 \mu\text{m}$ was scanned.

The energy of the emitted photon is characteristic of the element from which it fluoresced. For Br, the fluoresced K_α peak, corresponding to a drop from an L3 electron, occurs at 11.924 keV while the K_β peak, corresponding to a drop from an M3 electron, occurs at 13.292 keV (Elam et al., 2002). The strongest peak for Cl is for a K_α peak occurring at 2.622 keV, while the K_β peak occurs at 2.812 keV (Elam et al., 2002). Samples were cut small enough in thickness such that the incident beam would probe the entire thickness of the sample. The penetration depth is defined as the distance at which the x-ray strength has been reduced to $1/e \approx 37\%$ of its original strength, which for an 18 keV x-ray beam is approximately 9.6 mm (Elam et al., 2002). The emitted photon then must travel out of the ice sample and a linear path of air before striking the detector. Since the emitted photon is at a lower energy level than the incoming beam, the penetration depth is smaller for the fluorescence signal. For Br K_α and K_β , these distances are 3.1 and 4.3 mm, respectively. Thus, although the incoming beam reaches the entire sample thickness, detected Br signal is only from the top 3 – 4 mm. Due to the lower energy emitted photons for Cl, the penetration depth for K_α is $35 \mu\text{m}$, and therefore XRF only detects surface features for Cl. Although x-ray attenuation also occurs in the linear path of air between the sample and the detector, this can be reduced by enclosing the entire experimental setup in a helium-filled zippered polyethylene bag. This was particularly important for low energy Cl

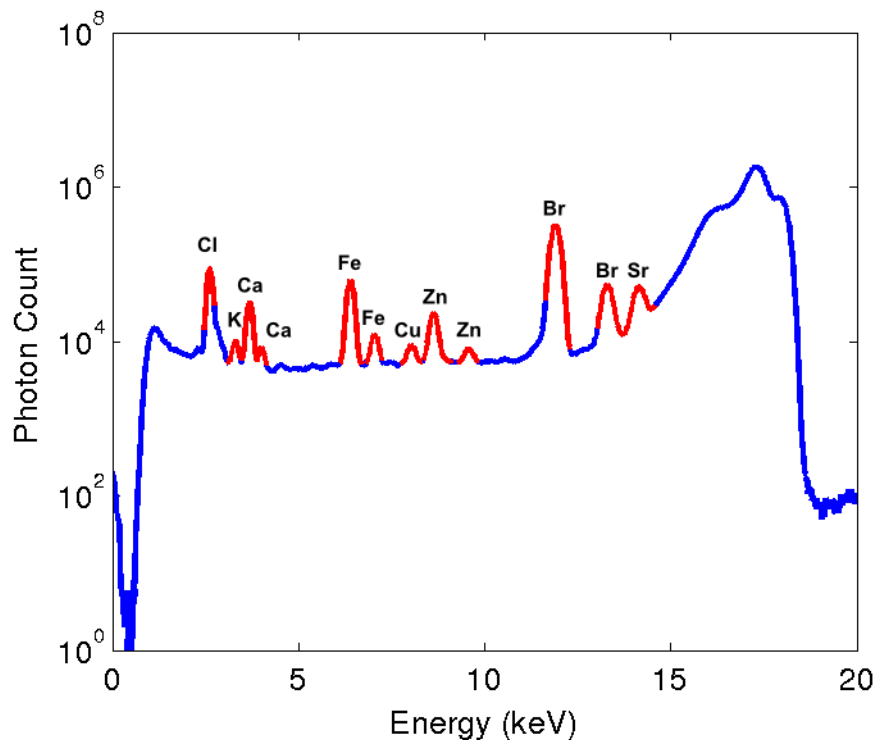


Figure 2.6: Example XRF spectrum for a typical sample. The incoming x-ray beam energy was 18 keV and the photon count was summed over all four detectors. Lines are smooth in this example as it is a summation over the entire $2 \text{ mm} \times 2 \text{ mm}$ region scanned. The energy intervals corresponding to elements of interest are highlighted in red.

detection and helped increase the photon count at the detector for all elements. Estimated detection limits were roughly single digit ppm for the elements of interest. Under these conditions, we were able to obtain x-ray spectra such as the one shown in Fig. 2.6.

The experiments were conducted over three separate visits to APS in March 2013, March 2014, and August 2014. Prior to visiting APS, ice cores were sub-sampled every 10 cm as described above. Each sample was cut into approximately $10 \text{ mm} \times 20 \text{ mm} \times 5 \text{ mm}$ slices and then shaved smooth with cleaned razor blades. To reduce the possibility of sampling multiple grains and to ensure grain boundaries could adequately be detected, we attempted to select samples with grain boundaries oriented perpendicular to the sample surface. Samples were transported to APS while being maintained at $-25 \text{ }^\circ\text{C}$ in a polystyrene foam cooler with dry ice and blue ice packs. Each sample was then press

fit into a small acrylic sample holder and frozen in place with a few drops of water. During analysis, samples were kept between $-18\text{ }^{\circ}\text{C}$ and $-21\text{ }^{\circ}\text{C}$ using a Peltier thermoelectric module cooling stage built by GSECARS. A thin film of Kapton encased the sample and holder to prevent the formation of frost on the sample surface. Samples were analyzed as described above, yielding $2\text{ mm} \times 2\text{ mm}$ elemental maps with $10\text{ }\mu\text{m}$ spatial resolution.

X-Ray Micro-Computed Tomography

The use of X-ray micro-computed tomography (μCT) has exploded over the past decade due to rapid advances in instrumentation technology and accessibility (Ketcham and Carlson, 2001; Stock, 2008). In fact, there are currently over 15 manufacturers producing commercial laboratory sized μCT systems in addition to the specialized synchrotron radiation source μCT systems available (e.g. APS, Swiss Light Source [SLS], European Synchrotron Radiation Facility [ESRF]) (Stock, 2008). The primary advantage of μCT is that it provides a non-destructive three-dimensional visualization and characterization of the internal features of a material with spatial resolution down to several microns, or even submicron with x-ray magnification optics available on certain commercial instruments and at some synchrotron beamlines. Once the phases of a given material have been segmented, the analysis of the μCT data then produces quantitative measurements on the topology, connectivity, and structure of the material. This has natural applications for analyzing the microstructure of different porous media in fields varying from sea ice (Golden et al., 2007; Obbard et al., 2009b) in the geosciences to bone analysis in biology (Campbell et al., 2007) to cement in material engineering (Naik et al., 2006).

In essence, the components of a μCT system are an x-ray source, absorption of the x-rays in the specimen, a scintillator, and a photo detector. For this work, we used a Skyscan 1172 μCT scanner that uses a sealed microfocus x-ray tube with a spot size of $5\text{ }\mu\text{m}$ to produce a fixed conical, polychromatic x-ray source. In order to choose the accelerating voltage for the x-ray source, it is helpful to have an approximation for the expected

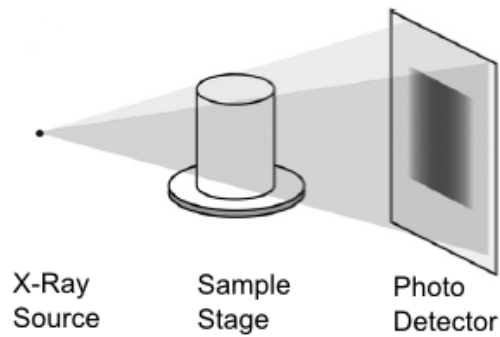


Figure 2.7: Schematic of cone-beam μ CT (Landis and Keane, 2010). Samples were rotated 180° about their vertical axis at 0.7° steps.

absorption of the specimen. As discussed above in Eq. 2.1 and Eq. 2.2, x-ray attenuation is given by the Beer-Lambert law and attenuation decreases with increasing x-ray energy. Unlike XRF, for μ CT one is interested in x-ray transmission rather than absorption, where different phases of the sea ice samples have different compositions and densities, and will thus transmit varying amounts of radiation. It was determined that setting the x-ray source at an accelerating voltage of 40 kV and a current of $250 \mu\text{A}$ provided the best contrast for imaging sea ice.

From the sub-samples described above (collected every 10 cm along the length of each core), specimens were cut into cubes measuring approximately 10 mm on a side. The samples were frozen onto a cooling stage that could maintain the sample at a desired set point. Each sample was then rotated 180° about its vertical axis at 0.7° steps, and the attenuated x-rays are imaged at each step. To ensure best results, it is preferable that the x-ray beam passes through a roughly equal amount of specimen at each rotational step. The geometry and spot size of the x-ray source determines the acquisition time required and the spatial resolution of the scan (Landis and Keane, 2010). Cone beam systems rapidly reduced scan time by allowing a complete projection to be imaged in a single step as is shown in Fig. 2.7. For the setup used for this work, scan time was approximately 20 min and the pixel size was $15 \mu\text{m}$.

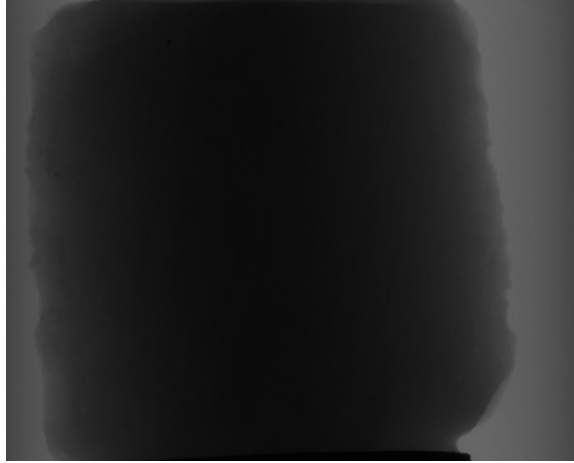


Figure 2.8: An example μ CT projection radiograph. Regions of darker shade are more strongly absorbing of x-rays. As the sample was rotated 180° , 258 radiographs were collected and then combined to produce a three-dimensional reconstruction.

The final step of the scanning process is detecting the x-rays that pass through the specimen after each rotational step. The x-rays strike a scintillator screen that converts the x-rays into visible light photons that are then detected by a camera (Landis and Keane, 2010). Our Skyscan 1172 scanner utilizes a 1.3 Mp (1280×1024) cooled Hamamatsu CCD camera fiber-optically coupled to the scintillator. For each rotation step, a single projection radiograph is produced with 4096 (12-bit) brightness graduations. An example projection radiograph is shown in Fig. 2.8

The next step of the μ CT process is tomographic reconstruction of the projection radiographs into stacked two-dimensional gray-scale slices in the z-direction (vertical direction). First, the dark-field image acquired with no x-rays present is subtracted from each projection radiograph. Then, each radiograph is divided by the white-field or “flat-field” image, which is acquired with the x-rays on but no specimen present. For a given rotation angle, the radiographs represent a line integral of the x-ray photons not attenuated. The mathematics for this problem was worked out in 1917 by Johann Radon. It involves taking what is known as the Radon transform

$$p(r, \theta) = \int f(x, y) \delta(x \cos \theta + y \sin \theta - r) dx dy \quad (2.3)$$

where $p(r, \theta)$ is the recorded signal, δ is the delta function, and $f(x, y)$ is the desired quantity. Thus, the Radon Transform must be inverted, which is done either through an algebraic approach or Fourier Transform back projection algorithms (Landis and Keane, 2010). We used Skyscan’s NRECON reconstruction software to perform the reconstruction, which transforms the x-ray projections from each step using a modified Feldkamp cone-beam algorithm to a stack of gray-scale cross-section images.

The output from the reconstruction step is that each voxel is assigned a value on an arbitrary scale known as CT values or Hounsfield Units (HU). A correspondence to linear attenuation coefficients can be made by assigning water 0 HU and air -1000 HU. Thus, a substance x has a value in HU calculated by (Ketcham and Carlson, 2001)

$$HU = 1000 \times \frac{\mu_x - \mu_{water}}{\mu_{water}} \quad (2.4)$$

With a properly calibrated scale, the density of an unknown phase can thus be measured. However, this is rarely done in the geosciences due to not using a monochromatic beam, chemical variability of materials, wide range of scanning conditions, and density changes within a given phase (Ketcham and Carlson, 2001). In this study, linear attenuation coefficient endpoints of 0 to 0.07 were chosen to encompass the range of HU/CT values encountered in all samples, thereby enabling the conversion of each voxel into a standard 0 – 255 gray-scale.

The primary limitation of μ CT is anything that reduces the ability to set proper thresholds during segmentation. Thermal drift of the x-ray source during imaging was corrected by taking a few extra projection radiographs spaced at 45° rotational steps. These post-analysis images are then compared to the original radiographs to determine the degree of thermal drift. Ring artifacts arise in the gray-scale image as a result of shifts in the output of individual detectors (Ketcham and Carlson, 2001). These shifts are often due to factors such as changes in temperature or beam strength, and result in anomalous values

occurring in a ring centered on the rotational axis as the artifact affects each projection image. Ring artifacts were removed in the image post-processing by subtracting out the anomalous values for the compromised detector prior to reconstruction. Beam hardening is the most common artifact in images, and is the result of low energy x-rays preferentially being attenuated as they pass through the specimen (Ketcham and Carlson, 2001). Thus, the mean x-ray energy observed at the center of the specimen is greater than that observed near the edges. This results in the middle appearing darker than expected and edges appearing brighter. Since the degree of beam hardening was relatively small for this work, post-processing correction was sufficient and the use of filters during imaging was not necessary. Voxels that represent partial volumes of different phases present challenges during thresholding as a voxel is generally assigned to a single phase. The observed gray-scale value represents an average of the phases present. Regardless of the resolution of the μ CT, partial volume effects will result in some degree to a blurring of boundaries (Ketcham and Carlson, 2001). To reduce some of the noise in an image and help with boundary effects, pixels were smoothed based upon neighboring pixels using a Gaussian kernel.

Once image post-processing was completed, an interior cubic region of interest (ROI) measuring 7.5 mm on each edge was selected and used for morphometric analysis using Skyscan's CTAn software package. The ROI comprises the inner region of the total sample volume, removing any distortion of the microstructure due to sample preparation. The critical step in the entire μ CT process is thresholding the gray-scale images to set the boundaries of individual phases, since this dictates all subsequent qualitative and quantitative measurements. Generally, images are segmented into a binary image by selecting a single cutoff value on the gray-scale. Multiple thresholds can be used to create trinary images (or even images with more classes). However, trinary images are often best segmented through the use of multiple binary images as is shown in Fig. 2.9. Segmentation for trinary images can be improved by doping a phase with an ion containing a strong absorption edge, as has been done using KI in soil systems (Costanza-Robinson

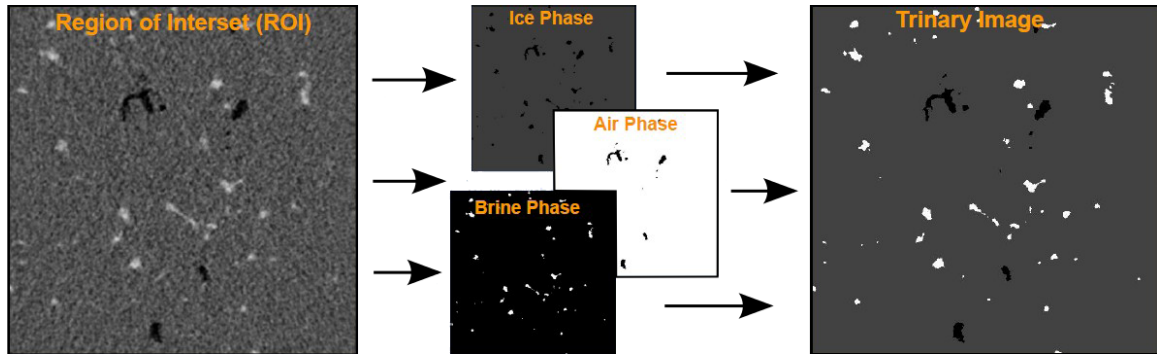


Figure 2.9: Thresholding a trinary image of sea ice, where black represents air, white represents brine, and gray represents ice. First, a region of interest (shown on the left) is selected. A high threshold is set to pull out a binary image of only the brine phase. Next, a low threshold is set to pull out only the air phase. The in-between gray-scale values are used to pull out a binarized ice phase. The three binary images are then combined to create the trinary image shown on the right

et al., 2008). Duplicate scans are then completed with X-ray energies above and below the absorption edge, however this technique is best used with a synchrotron radiation source where monochromatic radiation and highly tunable x-ray energies are available.

Slight adjustments to the cutoff values for a given phase can lead to significant differences in measured microstructural quantities. For example, Tarquis et al. (2009) used four different threshold values on a binary image to analyze the fractal dimension of soils, and noticed that although general trends did not change, measured values for porosity and fractal dimension varied significantly with the threshold level set (Tarquis et al., 2009). Thresholding can either be done manually by the user or through automated algorithms. Manual thresholding requires that the user compare binarized and gray-scale images thoroughly until a proper threshold value is set. Naturally, this method is subject to user bias and variability between different studies.

There are a variety of automated thresholding algorithms to remove the human element, which can be categorized into several classes (Baveye et al., 2010). First, histogram shape-based methods set thresholds by examining the histogram of gray-scales and look for a certain feature such as the minimum value between two peaks. This is the method utilized for this work, and is shown in Fig. 2.10. Since the same thresholds were to be used for

all samples analyzed, the histograms of several representative samples were first examined and average optimized values for each of the three phases were selected. Clustering-based methods examine where peaks are located (i.e. clustering of gray-scale values) and set a threshold such as the midpoint between the peaks. The popular Otsu method that minimizes the weighted sum of within-class variance for each phase in a binary image falls in this class (Otsu, 1979). Entropy-based methods examine the image for “fuzzy” regions of mixed phases and attempt to set a threshold based on these values. Attribute-based methods take a final metric, such as porosity or object volume, that might be known for a given specimen. Then, the threshold is adjusted until the desired quantity matches the “known” value. Others have used images obtained using scanning electron microscopy (SEM) to help determine appropriate thresholds for the binarized μ CT images (Chen and Baker, 2010; Lomonaco et al., 2008). Spatial methods look at the dependency of neighboring voxels and set the phase of a voxel based partially upon this information. Finally, local methods such as adaptive thresholding allow for a variety of thresholding values to be set, which depends in part upon the local statistics and contrast of the voxel in question (Baveye et al., 2010). Batenburg and Sijbers (2009) proposed setting various thresholds and then analyzing the projected image that would have been produced. This method then chooses the threshold that minimizes the difference between the original projected image and the various reproduced images. Creating clear thresholds continues to challenge μ CT users and new techniques are still being developed.

The data output from μ CT is both qualitative and quantitative, with each providing complementary information useful in characterizing the internal structure of the porous media. Qualitatively, software programs allow the user to visualize the full three-dimensional features of both the object and the pore structure. Quantitatively, the user is provided with both two- and three-dimensional data that provide information regarding phase definition, shape, and connectivity for each phase. For a three-phase media such as warm sea ice, each phase is isolated and then analyzed separately to provide a full

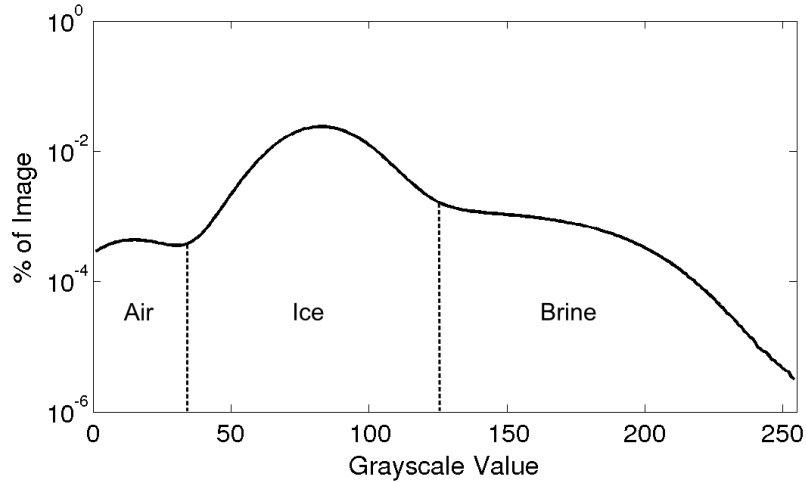


Figure 2.10: Representative histogram for thresholding μ CT images. The middle peak represents the gray-scale values corresponding to the ice phase. Values on the left correspond to the air phase (black) and values to the right correspond to the brine phase (white). The inflection points for the middle peak were used to set precise thresholding values. Since these values were relatively constant from sample to sample, the same values could be used for all images.

quantitative description of the microstructure. Once thresholds have been set to segment each phase, simple voxel summations can provide volume, porosity, and surface area measurements. A frequently used descriptor is the specific surface area, which is the ratio of the surface area to volume for a given phase.

A variety of parameters exists to describe the shape of each phase. First, the structure model index (SMI) provides a measure of surface convexity and the plate-like/rod-like architecture of a given phase. The surface of each object is dilated by one pixel, and the resulting surface area is calculated. SMI is defined as $SMI = 6 \left(\frac{S' \times V}{S^2} \right)$, where S' is the derivative of the change in surface area (units of length), V is the initial volume, and S^2 is the surface area prior to dilation. For benchmarks, SMI values of 4, 3, and 0, represent spheres, cylinders, and plates, respectively. For each voxel in a given phase, the structure thickness is calculated by determining the largest sphere that encompasses the voxel, yet is entirely inscribed within the object. The structure thickness is then given as the mean over all voxels. To calculate the structure separation, the same calculation is completed,

but for the non-object (i.e. pore) phase. To calculate the fractal dimension of an object, the box counting algorithm is implemented. A variety of box sizes is chosen, and for each size the number of boxes required to cover the phase is counted. Then, the number of boxes is plotted versus the size of the particular box on a log-log scale. The slope of this line yields the fractal dimension.

One final metric regarding the phase shape is the degree of anisotropy. First, the mean intercept length is calculated by sending a line through the three-dimensional image, and dividing the length of the line by the number of intersections with the solid phase. This process is repeated for a large number of three-dimensional angles. A polar plot of the mean intercept lengths is created by making an ellipsoid with boundaries defined by the mean intercept length for each angle. Any given ellipsoid can be characterized by a matrix, and the eigenvalues for this matrix are calculated, which correspond to the lengths of the semi-major and semi-minor axes. The ratio of the largest to smallest eigenvalues provides a metric for the degree of anisotropy, with 1 representing a perfectly isotropic object.

To have a full understanding of the internal structure, it is helpful to have an understanding of the topology and connectivity of a given phase. The Euler number $\chi(x)$ in topology provides such a metric, where $\chi(x) = \beta_0 + \beta_1 + \beta_2$ and β_0 , β_1 , and β_2 are the three Betti numbers. These define the number of objects, the connectivity, and the number of voids, respectively, and $\chi(x)$ represents the number of connections that need to be severed before an object becomes multiply connected (i.e. separated into two objects). The fragmentation index is an inverse metric of the connectivity, and is defined as, $\left(\frac{S_1 - S_2}{V_1 - V_2}\right)$ where S_1 and S_2 represent the surface area before and after dilation and V_1 and V_2 represent the volume of a phase before and after dilation. Smaller (and even negative) values for the fragmentation index correspond to a prevalence of concave surfaces. Large number of concave surface is associated with multiply connected objects and thus well-connected networks. By combining all of the metrics for all three phases, it is possible to have a full quantitative description of the internal microstructure of sea ice using μ CT.

THE ROLE OF BLOWING SNOW IN THE ACTIVATION OF BROMINE OVER FIRST-YEAR ANTARCTIC SEA ICE

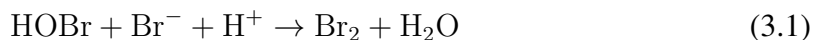
Lieb-Lappen, R. M. and Obbard, R. W.: The role of blowing snow in the activation of bromine over first-year Antarctic sea ice, *Atmos. Chem. Phys.*, 15, 7537-7545, doi:10.5194/acp-15-7537-2015, 2015.

Abstract

It is well known that during polar springtime halide sea salt ions, in particular Br^- , are photochemically activated into reactive halogen species (e.g., Br and BrO), where they break down tropospheric ozone. This research investigated the role of blowing snow in transporting salts from the sea ice/snow surface into reactive bromine species in the air. At two different locations over first-year ice in the Ross Sea, Antarctica, collection baskets captured blowing snow at different heights. In addition, sea ice cores and surface snow samples were collected throughout the month-long campaign. Over this time, sea ice and surface snow $\text{Br}^- / \text{Cl}^-$ mass ratios remained constant and equivalent to seawater, and only in lofted snow did bromide become depleted relative to chloride. This suggests that replenishment of bromide in the snowpack occurs faster than bromine activation in mid-strength wind conditions (approximately 10 m/s) or that blowing snow represents only a small portion of the surface snowpack. Additionally, lofted snow was found to be depleted in sulfate and enriched in nitrate relative to surface snow.

Introduction

The polar springtime is a season of change, most notably in temperature, sea ice coverage, return of the sun, and weather, but it also signals the onset of many photochemically driven atmospheric chemical reactions, such as tropospheric ozone depletion events (ODEs) (e.g., Barrie et al., 1988). Boundary layer ozone in polar regions has been observed to fall dramatically periodically in the spring in both the Arctic (Barrie et al., 1988) and Antarctic (Kreher et al., 1997; Wessel et al., 1998). These tropospheric ODEs are initiated by increased concentrations of reactive bromine gases (BrO and Br) resulting in a catalytic removal of ozone (Fan and Jacob, 1992; Frieß et al., 2004; McConnell et al., 1992); however the mechanism by which Br enters the atmosphere is not well understood (Abbatt et al., 2012). The heterogeneous reaction producing bromine gas and hypothesized to explain the “bromine explosion” is given by Fan and Jacob (1992):



Proposed surfaces on which this reaction may occur have included sea spray (Sander et al., 2003), frost flowers (Kaleschke et al., 2004; Rankin et al., 2000), surface snow (Simpson et al., 2005), aerosols (Frieß et al., 2004; Vogt et al., 1996), and blowing snow (Yang et al., 2008).

Although some bromide may arrive via sea spray produced aerosol (Sander et al., 2003), this mechanism is relatively less efficient and does not produce aerosol with the observed sulfate depletion (Wagenbach et al., 1998). As seawater freezes, salt rejection leads to an increasingly saline brine (Thomas and Dieckmann, 2009). Specific salts precipitate out of solution when solubility limits are reached below $-2\text{ }^\circ\text{C}$ (Light et al., 2003), producing brine with different ion ratios than those found in seawater. The brine is expelled to the ice/snow or ice/atmosphere surface, where it forms a fractionated surface skim and slush (Rankin et al., 2002). This reservoir of bromide and other sea salts can be incorporated into

frost flowers by wicking, or into the snow lying on sea ice by upward migration through capillary forces (Perovich and Richter-Menge, 1994). It may be transported by the lofting of snow from sea ice with subsequent sublimation and return of the aerosol to the snowpack (Jones et al., 2009; Yang et al., 2008). However, the physical surface at which bromide activation occurs remains a subject of some debate.

It has been shown that brine is wicked upward by frost flowers that form on fresh sea ice, yielding a highly saline surface with the aforementioned sulfate depletion, and that the dendritic nature of frost flowers magnifies the surface area available for atmospheric interactions (Rankin et al., 2002). However, studies have shown that frost flowers do not significantly increase the surface area available for heterogeneous reactions (Domine et al., 2005; Obbard et al., 2009a) and that frost flowers are not easily broken and lofted (Obbard et al., 2009a). Instead, they accumulate snow on their windward side in strong winds and when broken, fall where they are (Obbard et al., 2009a). Laboratory studies of frost flowers have also shown that frost flowers are quite stable in winds up to 12 m/s, and aerosol production is not observed under these conditions (Roscoe et al., 2011). Further, Simpson et al. (2005) and Obbard et al. (2009a) found that frost flowers are not depleted in bromide relative to sodium and chloride, indicating they are not the immediate source of bromine-depleted snow nor the location of the heterogeneous reactions activating bromine. It has also been shown that first-year sea ice contact better correlates to increased BrO concentrations than does contact with potential frost flower regions (Simpson et al., 2007a).

In Simpson et al. (2005) however, the snowpack did have Br^-/Na^+ ratio fluctuations by 2 orders of magnitude with bromide depletions of up to 90%, suggesting bromine was released in the aerosol phase or in the snowpack itself. Sea salts can migrate upwards through the snowpack as high as 17 cm, even in cold conditions where slush is not present (Domine et al., 2004; Massom et al., 2001). Surface snow is readily acidified by interactions with trace atmospheric acids, which provides a suitable environment for halogen activation as bromine activation is more efficient in acidic conditions and in environments with a

higher Br^-/Cl^- ratio (Pratt et al., 2013). Pratt et al. (2013) further hypothesized that the snowpack interstitial air is the primary location for the heterogeneous reactions, with wind pumping providing a vehicle to release the bromine into the boundary layer.

Yang et al. (2008) proposed a fourth mechanism for bromine activation that involves the lofting of snow from sea ice with subsequent sublimation and either direct bromine release or return of the aerosol to the snowpack. In the model, lofted snow particles were allowed to sublimate to a particle size of $< 10 \mu\text{m}$, whereby the particles instantaneously released bromine or were potentially scoured by more blowing snow particles. Snow salinity was found to have a nonlinear relationship with bromine production, and the reaction rate varied with dry aerosol particle size. It was shown that $1.3 \mu\text{m}$ particles yielded the most efficient release of bromine since the smaller aerosol could be lofted further and longer (Yang et al., 2008). Further work showed that snow in the sea ice zone may contain enough salt when lofted by wind to produce the necessary aerosol to explain the observed Antarctic ODEs (Yang et al., 2010). While it may be difficult for saturated snow lying on surface skim to become lofted, snow in the upper layers could wick up salts yet remain mobile, providing enormous capacity for transporting bromide into the boundary layer. Yang et al. (2008) provides the theoretical framework and model-based data for the physical measurements observed and presented in this manuscript.

ODEs have been found to occur at a range of wind speeds, something that has made agreement upon a mechanism difficult. Some have observed that ODEs require low winds, a stable boundary layer, and a relatively clear sky, or the movement of air masses from such regions (Simpson et al., 2007b). Using measurements and modeling, Albert et al. (2002) found rapid ozone depletion in the top 10 cm of the snowpack due to diffusion and ventilation in moderate winds. More recently, ODEs have been recorded during high winds ($> 12 \text{ m/s}$), which increase the snow surface area exposed via blowing snow, and thus, the probability of contact between the gaseous and condensed phases required to initiate bromine release (Jones et al., 2009). During the 2009 OASIS campaign in Barrow, AK, high

winds were observed to correspond with increased BrO concentrations (Frießet al., 2011). This was accompanied by decreased HOBr, suggesting that blowing snow likely provided additional surfaces for heterogeneous HOBr loss (Liao et al., 2012). These high wind halogen activation events may have a more widespread role when considering the impact of ODEs on regional tropospheric chemistry (Jones et al., 2010). Additionally, higher winds may enhance the availability of radical bromine precursors in the snowpack, accelerating bromine activation (Toyota et al., 2011). On the contrary, others (e.g., Halfacre et al., 2014; Helmig et al., 2012) have found no correlation between ODEs and wind speed. However, the lack of low ozone observations at high wind speed may be a result of enhanced mixing (Helmig et al., 2012). Although the chemistry of snow has been well studied (Domine et al., 2004; Grannas et al., 2007; Massom et al., 2001), there has been no attempt until now at segregating snow capable of wind transport or snow actually blown by wind.

It is noted that both Cl₂ and BrCl play a role in halide boundary layer chemistry and ODEs (Abbatt et al., 2012), but the focus of this work is on bromine because it is a far more efficient catalyst of ozone loss. As the main constituents of seawater, both chloride and sodium have been used as sea salt tracers, and thus chloride was used here to both determine snow and ice salinity and relative activity of other anions. Previous work has shown that sulfate is influenced both by mirabilite precipitation and atmospheric interactions, while nitrate is uncorrelated with sea salt and is deposited as a byproduct of other reactions (Krnavek et al., 2012).

Methods

Two field sites on first-year sea ice in the Ross Sea, Antarctica, were chosen, based upon prevailing wind direction, to maximize contact of the blowing snow with the first-year sea ice. Their locations were shown in Fig. 2.1. Butter Point Site was located 6.5 km from the open ocean and 35 km north of the Ross Ice Shelf. Iceberg Site was located 55 km northwest of Butter Point, and since the ice edge located to the east follows the shore,

the distance to open water here was also 5 km. Iceberg Site was chosen based upon the presence of a 740 m long and 35 m high iceberg located 250 m to the west that would block winds sourced over land, maximizing blowing snow collection from over sea ice. At each site, a 5.5 m blowing snow collection tower was erected for the time period of 11 October - 08 November 2012. Collection baskets made out of 150 μm nylon monofilament mesh and 7" diameter by 14" long (Midwest Filter Corporation, Lake Forest, IL) were placed at four different heights: 0.3, 2.0, 3.0, and 5.5 m above the snow surface.

The sites were visited approximately every other day, and collection baskets were switched even if no snow was collected. Baskets were triple rinsed with DI water between uses. Surface snow samples were collected each of the 12 days the sites were visited. In addition, 1.78 m and 1.89 m ice cores were extracted from Butter Point and Iceberg sites, respectively. Snow samples and sea ice cores were transported at a constant temperature of $-20\text{ }^{\circ}\text{C}$ back to Thayer School of Engineering's Ice Research Laboratory at Dartmouth College and stored in a $-33\text{ }^{\circ}\text{C}$ cold room.

Winds during the field campaign were generally mild, only surpassing 10 m/s on a few occasions. Site visits were not feasible during stormy weather, and much of the blowing snow captured during those periods sublimated in the baskets prior to collection as observed by a webcam. Thus, only on 25 October were blowing snow samples collected at both sites and all four heights. The collected snow was the result of approximately 10 m/s southerly winds on 24 October. Visibility at McMurdo station during this blowing snow event dropped below 0.5 miles for about 4 h. Temperatures ranged from $-20.5\text{ }^{\circ}\text{C}$ to $-11.5\text{ }^{\circ}\text{C}$ with an average relative humidity of 69% on 24 October and -17.5 to $-13.5\text{ }^{\circ}\text{C}$ with an average relative humidity of 61% on 25 October. These temperatures were a couple of degrees warmer than the average for the rest of the field campaign.

All surface snow and blowing snow samples were melted into acid-rinsed HDPE vials, and diluted by a factor of 5 with DI water. Those samples falling outside of the calibration standard concentrations were further diluted to fall within the desired range. Each ice core

was sub-sampled every 10 cm, melted, and diluted by a factor of 50, except for the bottom-most sample that was diluted by a factor of 100. A 0.5 mL aliquot of each diluted snow and ice sample was then analyzed for anion concentrations.

Anion chromatography was completed using a Dionex-600 IC system, equipped with a LC 25 chromatogram oven set at 30 °C, GD 50 gradient pump, CD 25 conductivity detector, AS15 anion column with a AG15 guard column, and an auto-sampler. A 38 mM NaOH eluent was used at a flow rate of 1.2 mL/min and the SRS current was set to 100 μ A. Pressure in the column was 1,600 psi and the signal noise was approximately 0.003 μ S. Peak analysis was performed using Chromeleon 6.8 software with a 5 point standard calibration curve. IC detection limits were 0.6, 0.1, 0.04, and 0.03 g/m³, yielding limits of quantification of 2, 0.3, 0.1, and 0.1 g/m³ for chloride, sulfate, bromide, and nitrate, respectively.

Cation concentrations in the ice cores were measured by Xiahong Feng and Josh Landis (Dartmouth Earth Science Department) using inductively coupled plasma - optical emission spectrometry (ICP-OES). Results from these measurements as well as cation and anion concentrations from a nearby multi-year ice core are given in Appendix A. As discussed previously, both sodium and chloride are commonly used as tracer ions to determine relative activity of other ions (Krnavek et al., 2012). Since sodium is affected by mirabilite precipitation and anions are the focus of this study, chloride is used as the primary sea salt tracer here. In Appendix A, correlation plots for all anions and cations relative to both chloride and sodium are also presented.

Results

Raw anion concentrations for sea ice, surface snow, and blowing snow samples are provided in the Supplement to this Chapter. Sea ice anion concentrations had nearly identical profiles for Butter Point and Iceberg cores, with both showing the expected C-shape profile (see Fig. 3.1) (Eicken, 1992). Note that the deepest sample for Iceberg

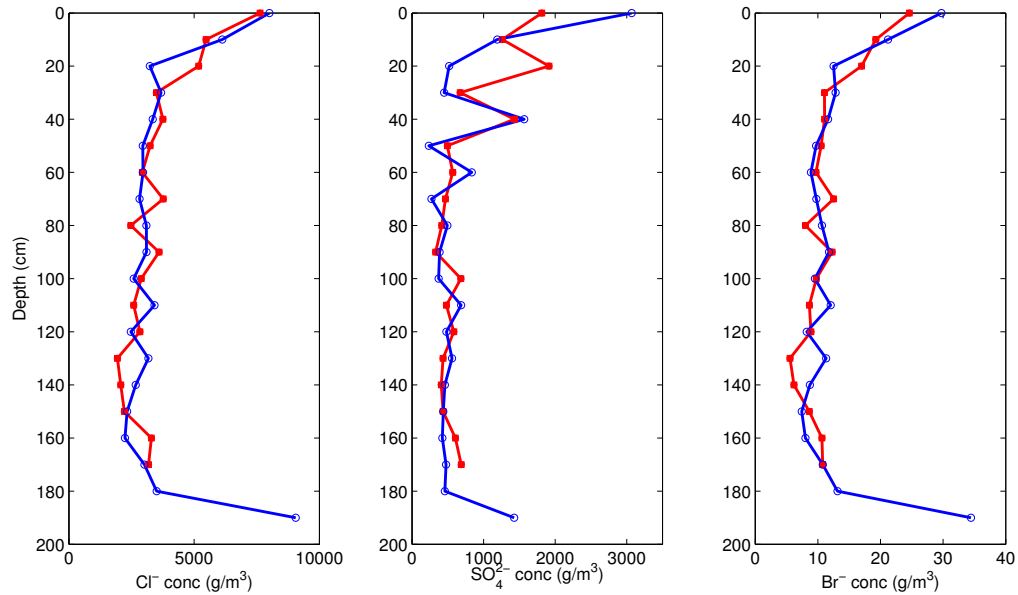


Figure 3.1: Anion concentrations for sea ice cores. Butter Point Site samples are shown in red filled-in squares and red lines, while Iceberg Site samples are shown in blue open circles and blue lines.

Site was directly at the base of the core, while the deepest sample for Butter Point was 8 cm above the base, due to a mushy, poorly defined basal layer, and thus missed the saltiest portion. Chloride concentrations ranged from 2,000 – 8,000 g/m^3 , while bromide concentrations ranged from 5–35 g/m^3 . Sulfate concentrations ranged from 2–3,000 g/m^3 , with increased variation observed over the top 40 cm of both cores. Nitrate concentrations were below detection limits for all sea ice core samples.

Surface snow anion concentrations varied greatly, but were of similar magnitude at the two sites and showed no noticeable trend with time over the field campaign. Concentrations ranged from 200–5,000 g/m^3 chloride, 1.0–16 g/m^3 bromide, 20–2,300 g/m^3 sulfate, and 0 – 1.2 g/m^3 nitrate, though the majority of samples was below detection limits in nitrate. If we assume Cl concentrations to be a good proxy to estimate salinity using sea water ion ratios, this corresponds to a mean surface snow salinity of 3 PSU, with a range of 0.4 – 9 PSU. There was little snow cover at Butter Point with the surface varying from completely wind scoured to several cm of snow. Iceberg Site had a more variable snowpack, with prevalent rafted ice and sastrugi, resulting in snow depths varying from tens of cm to over

1 m. A 21 cm snow pit was dug 15 km from Butter Point Site to study a more consistent snowpack that is representative of the greater first-year sea ice of the region. In this snow pit, both chloride and bromide concentrations increased steadily from the snow surface to the snow/ice interface, with concentrations ranging from 500 – 1,600 g/m³ chloride and 1.5 – 6 g/m³ bromide. Sulfate concentrations ranged from 30 – 50 g/m³, but showed a C-shaped profile with highest concentrations found near the top and bottom of the snow pit. A second snow pit located slightly closer to the open ocean showed similar trends.

Anion concentrations from the blowing snow samples collected on 25 October in both towers varied greatly, including separate samples from the same collection baskets, indicating that blown snow can be quite varied in its salt concentration. Concentrations ranged from 50 – 6,800 g/m³ chloride, 0.2 – 18.5 g/m³ bromide, 3 – 240 g/m³ sulfate, and 0.4 – 23 g/m³ nitrate. Using chloride concentrations to derive an estimate of salinity, blowing snow samples ranged from 0.1 to 12 PSU. Comparing the 0.3 m and 5.5 m baskets at both sites suggests a 10-fold increase in salinity from 0.6 to 6 PSU. However, when all blowing snow samples are considered, there is not a statistically significant trend of increasing salt concentration with basket height, except for nitrate where concentrations increased with height above the snow surface.

Anion concentrations can provide a general understanding of the overall salinity of the snow and ice, but in order to understand chemical reaction behavior, it is instructive to calculate anion concentration ratios. The Br⁻/Cl⁻ mass ratio has long been used as a metric for analyzing both frozen and liquid saline water samples, and comparing measured values to the well established 1 : 290 ratio observed in seawater (Morris and Riley, 1966). This ratio is plotted in Fig. 3.2 for all samples at both sites. Br⁻/Cl⁻ mass ratios were relatively constant for all sea ice samples (1 : 281 ± 24) and all surface snow samples (1 : 296 ± 22). However, there was a linear correlation between Br⁻/Cl⁻ mass ratios for blowing snow relative to height at both Butter Point ($r^2 = 0.89$) and Iceberg Site ($r^2 = 0.93$). Sulfate mass ratios in sea ice, surface snow, and blowing snow did not show as clear a trend

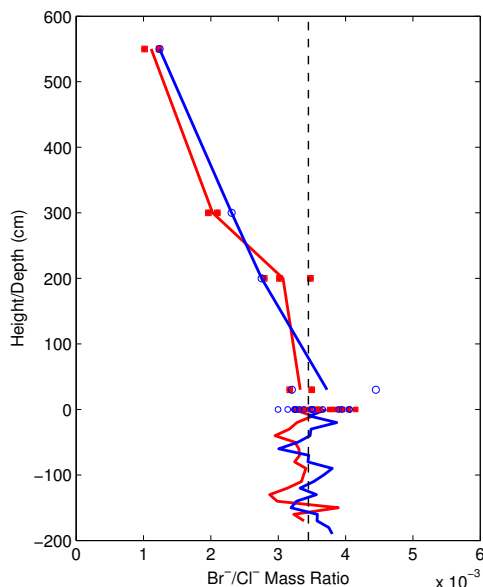


Figure 3.2: Br^-/Cl^- mass ratios for sea ice (negative heights), surface snow (height of 0), and blowing snow (height above snow surface). Blowing snow lines connect averages for each basket height. Butter Point Site samples are shown in red filled-in squares and red lines, while Iceberg Site samples are shown in blue open circles and blue lines. The standard ocean Br^-/Cl^- mass ratio is shown as a black dashed line (Morris and Riley, 1966).

(Fig. 3.3). In sea ice, the $\text{SO}_4^{2-}/\text{Cl}^-$ mass ratio was roughly 1 : 7 in the bottom half of the cores, consistent with what is generally observed in seawater (Morris and Riley, 1966), but varied from approximately 1 : 2 to 1 : 12 in the upper halves of the cores. Surface snow mass ratios also were quite variable ranging from 1 : 1 to 1 : 19 with no clear correlations. Collected lofted snow was quite depleted in sulfate with mass ratios reaching 1 : 20 to 1 : 40, but did not show the linear trend with height observed with bromide.

Discussion

Observation of bromide depletion relative to other salts is an indication of heterogeneous atmospheric chemical reactions and bromine activation (Adams et al., 2002; Huff and Abbatt, 2002; Simpson et al., 2005). Although there was some variability in Br^-/Cl^- mass ratios for sea ice and surface snow, these ratios were remarkably constant, just over 1 : 300. As shown in Fig. 3.2, signs of bromide depletion occur above the snowpack, with greater

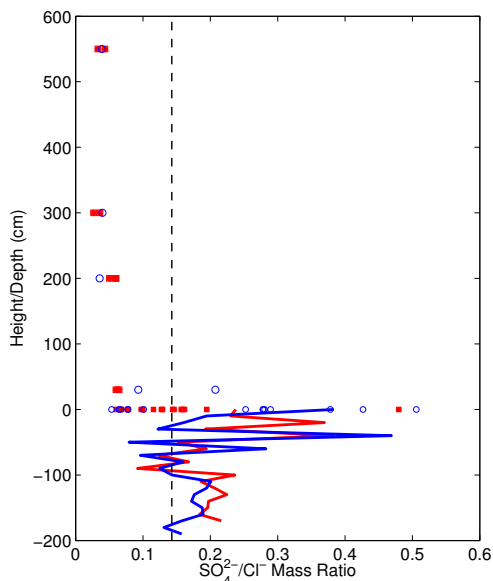


Figure 3.3: $\text{SO}_4^{2-}/\text{Cl}^-$ mass ratios for sea ice (negative heights), surface snow (height of 0), and blowing snow (height above snow surface). Butter Point Site samples are shown in red filled-in squares (snow samples) and a red line (sea ice), while Iceberg Site samples are shown in blue open circles (snow samples) and a blue line (sea ice). The standard ocean $\text{SO}_4^{2-}/\text{Cl}^-$ mass ratio is shown as a black dashed line (Morris and Riley, 1966).

depletion occurring at greater heights, reaching mass ratios of nearly 1 : 1000 at heights of 5.5 m. This is consistent with aerosol observations by Duce and Woodcock (1971) that measured increased bromide depletion with height, albeit at tropical latitudes. They noted a strong particle size dependence with increased bromide depletion corresponding to mid-sized aerosol particles. Further studies have shown that particle size influences the mode of transport and it may not be realistic to differentiate snow saltation and suspension based solely on wind speed and height (Nemoto and Nishimura, 2004). Nevertheless, both processes greatly increase the snow surface area exposed for gas-phase reactions by as much as 3,000 times that of surface snow (Pomeroy and Brun, 2001). It is noted that snow blowing at the windspeed will have no relative motion compared to the gases and gas-phase diffusion becomes an important consideration, especially for large grain particles. Local turbulence however, will help to overcome some of these diffusion limitations (Nemoto and Nishimura, 2004). We also note that sublimation of blowing snow particles likely has a strong effect on anion concentrations. Consistent with the mechanism suggested by Yang

et al. (2008), lighter particles would remain airborne for longer periods of time, leading to suspension at greater heights and more time for photochemical reactions. However, since particle sizes were not measured in this study, we solely mention the potential sublimation may have on increasing bromine release through this pathway.

A depletion factor (DF) was defined such that $DF = 0$ signifies no bromine depletion in particles, and $DF = 1$ signifies complete depletion (Yang et al., 2005). We note that a negative value for DF indicates bromine enrichment. Averaging the Br^-/Cl^- mass ratios at each height for Butter Point yields $DF = 0.04, 0.11, 0.41,$ and 0.68 for heights of $0.3, 2.0, 3.0,$ and 5.5 m, respectively. At Iceberg Site, $DF = -0.08, 0.20, 0.33,$ and 0.64 for the four heights, respectively. Depletion factors were relatively small for both surface snow and ice core samples, with values ranging from -0.20 to 0.13 and -0.13 to 0.17 , respectively. These values are consistent with previously reported values and currently used in some models (Sander et al., 2003; Yang et al., 2005). Previously, Simpson et al. (2005) observed up to 90% bromide depletion in surface snow, while Jacobi et al. (2012) observed up to 70% depletion in snow mobilized 5 cm above the surface. The latter study also noted that during a blowing snow event, there was first bromide enrichment in the snow during the initial part of the storm followed by later bromide depletion (Jacobi et al., 2012). An increased depletion factor can either signify bromide depletion due to bromine release or chloride enrichment from, for example, gaseous HCL uptake. If the latter hypothesis were true, one would expect to observe increased chloride concentrations in higher baskets. The lack of an observed chloride trend with height leads to our interpretation that the decreased mass ratio is a clear indicator of bromine activation. Interestingly, lower Br^-/Cl^- ratios have also been found to correspond with a decrease in chlorine release (Wren et al., 2013). This is due to the fact that BrCl plays a critical role in chlorine production. BrCl is initially formed from the reaction between HOBr and Cl^- , and then upon later photolysis, can lead to chlorine release (Wren et al., 2013).

Previously, bromine activation and ODEs were observed in both low (< 5 m/s) and

high (> 12 m/s) winds (Jones et al., 2009). Here, the blowing snow event occurred during moderate winds of approximately 10 m/s. Since the wind was from the south and there was no new precipitation, it is safe to assume that the snow originated from the surface of first-year sea ice. It is noted that the blowing snow event lasted approximately 4 – 6 h, and that snow samples from the baskets were not collected until 10 – 12 h later. During this time, wind speeds dropped to less than 5 m/s, and it is possible that the collected snow was exposed to further wind scouring. However, all baskets would have experienced a similar degree of scouring in these minimal winds and the effect would be minor over the short time period prior to collection. Further, the collected snow was mostly windpacked, suggesting it was unlikely the wind penetrated both the $150\ \mu\text{m}$ nylon monofilament mesh of the basket and the interior bulk of the snow. Future studies, however, may attempt to better seal off collected blown snow.

The surface snow Br^-/Cl^- mass ratios at both sites showed little variation and no observed trend with date or meteorology over the month-long campaign. If there was a significant amount of lofted snow being depleted in bromide and then falling back to the snow surface, one might expect to detect a signal in the surface snow chemistry. The lack of recorded bromide depletion in the surface snow may indicate that either surface snow bromide concentration is quickly replenished or that blowing snow represents only a small portion of the surface snowpack. Surface snow will be replenished in bromide through interaction with saline brine (Oldridge and Abbatt, 2011), deposition of HOBr as a byproduct of the reaction between BrO and HO₂, deposition of HBr, and deposition of aerosol-phase bromine. In cold ambient environments, frost flowers, surface snow, and the sea ice surface have been shown to be bromide enriched sources, likely due to the precipitation of NaCl (Kalnajs and Avallone, 2006; Morin et al., 2008). Additionally, recycling of deposited bromine plays a critical role with as much as 75% of deposited bromine being re-emitted into the gas phase as Br₂ or BrCl (Piot and von Glasow, 2008). In future work, it would be informative to collect both surface and blowing snow during

stronger wind events.

The sulfate depletion observed in lofted snow is consistent with the observations of others, most likely a product of mirabilite precipitation occurring at temperatures below $-8\text{ }^{\circ}\text{C}$ (Rankin et al., 2000). The range of $\text{SO}_4^{2-}/\text{Cl}^-$ mass ratios measured in surface snow and the upper halves of the ice cores is also likely due to similar interactions. Sulfate depletion can result from a wide variety of processes involving brine and mirabilite formation as brine constantly moves through sea ice and is also wicked up by surface snow (Krnavek et al., 2012). In addition, non-sea salt sourced sulfate may provide additional sulfate to the surface snowpack (Krnavek et al., 2012; Rankin and Wolff, 2003).

Nitrate concentration in seawater is highly dependent upon phytoplankton blooms, and therefore varies greatly from single digit g/m^3 to less than one g/m^3 (e.g., Arrigo et al., 1997; Gordon et al., 2000). Thus, it was not surprising that sea ice samples were below the quantification limit for nitrate. Surface snow samples also were generally below nitrate detection limits, and those with quantifiable concentrations showed no noticeable trend. Nitrate snow photochemistry is quite complex, with many processes both adding and subtracting nitrate from the snowpack (Grannas et al., 2007; Krnavek et al., 2012). Nitrate sources include biomass burning, lightning production, soil exhalation, and anthropogenic pollutants that can be carried long distances through atmospheric transport (Galloway et al., 2004; Krnavek et al., 2012). The increase in nitrate concentration observed with basket height may be attributed to increased atmospheric interactions higher above the snowpack. Additionally, basket nitrate concentration may also be influenced by interactions occurring while the snow was sitting in the basket but prior to collection, as cycling of different nitrogen-containing compounds is relatively fast and can vary greatly during a day (Grannas et al., 2007). Considering the number of competing reactions, more data points would be needed to make conclusive statements regarding the cycling of nitrate in the polar boundary layer.

Conclusion

In summary, this work examined the mass ratio of Br^-/Cl^- in blowing snow during mid-strength winds to better understand mechanisms leading to bromine activation. It was found that while Br^-/Cl^- mass ratios remained relatively constant for sea ice and surface snow, bromide becomes strongly depleted relative to chloride in lofted snow. Thus, we conclude the blowing snow particles provide a very viable surface for the initial heterogeneous reactions initializing ODEs to occur. The findings of this study are consistent with previous modeling results (Yang et al., 2010), suggesting that blowing snow has the capacity to explain the occurrence of ODEs in the polar springtime.

This research was supported by a National Science Foundation (NSF) Grant #1043145. The authors would like to thank Anthony Faiia, Josh Landis, Dave Ferris, Howard Roscoe, and the two referees for guidance with IC and insightful suggestions in preparing this manuscript.

All data is available online at <http://engineering.dartmouth.edu/materials/bromide/data.html>

Supplement

Table 3.1: Raw anion concentrations for blowing snow samples collected on 25 October, 2012, and measured using a Dionex-600 IC system.

Site	Height (m)	Cl ⁻ (g/m ³)	Br ⁻ (g/m ³)	SO ₄ ²⁻ (g/m ³)	NO ₃ ⁻ (g/m ³)
Butter Pt	0.3	400	1.3	26	0.4
Butter Pt	0.3	460	1.6	28	0.4
Butter Pt	2.0	23	0.1	1	0.3
Butter Pt	2.0	62	0.2	4	0.4
Butter Pt	2.0	63	0.2	4	0.5
Butter Pt	3.0	4,500	9.5	160	20
Butter Pt	3.0	670	1.3	18	4.3
Butter Pt	5.5	1,400	1.4	47	9.9
Butter Pt	5.5	4,900	6.0	210	30
Iceberg	0.3	150	0.5	14	0.2
Iceberg	0.3	280	1.3	59	0.4
Iceberg	2.0	6,700	18.5	240	13
Iceberg	3.0	2,600	6.0	100	8.3
Iceberg	5.5	3,900	4.9	150	23

Table 3.2: Raw anion concentrations of surface snow samples collected in October – November, 2012, and measured using a Dionex-600 IC system. All nitrate samples marked BQL were below the quantification limit of 0.1 g/m³.

Site	Date	Cl ⁻ (g/m ³)	Br ⁻ (g/m ³)	SO ₄ ²⁻ (g/m ³)	NO ₃ ⁻ (g/m ³)
Butter Pt	10/15	3,400	13	1,600	0.3
Butter Pt	10/15	2,400	8.0	350	0.3
Butter Pt	10/15	950	3.7	150	BQL
Butter Pt	10/17	940	3.0	120	0.5
Butter Pt	10/25	780	2.8	78	BQL
Butter Pt	10/25	1,800	6.9	210	BQL
Butter Pt	10/25	2,700	9.5	210	BQL
Butter Pt	10/25	420	1.5	29	BQL
Butter Pt	10/25	920	3.7	120	BQL
Butter Pt	10/25	1,300	4.9	250	BQL
Butter Pt	10/26	330	1.2	20	0.5
Butter Pt	10/29	350	1.2	50	BQL
Butter Pt	10/31	470	2.0	77	BQL
Butter Pt	11/02	2,200	7.8	210	BQL
Butter Pt	11/06	3,700	13	590	1.2
Iceberg	10/11	1,400	4.4	87	0.3
Iceberg	10/15	4,600	15	1,200	0.9
Iceberg	10/15	550	2.1	160	0.1
Iceberg	10/15	440	1.7	34	BQL
Iceberg	10/17	3,700	13	1,100	0.5
Iceberg	10/19	1,100	4.7	1,600	BQL
Iceberg	10/25	2,100	7.3	140	BQL
Iceberg	10/25	1,100	4.4	58	BQL
Iceberg	10/25	3,700	13	1,600	BQL
Iceberg	10/25	2,300	8.2	2,300	BQL
Iceberg	10/26	370	1.2	100	0.5
Iceberg	10/29	1700	5.1	480	BQL
Iceberg	10/31	150	0.5	74	0.2
Iceberg	11/02	2,000	6.5	160	BQL
Iceberg	11/06	1,400	5.2	540	BQL
Iceberg	11/08	2,300	7.8	240	BQL

Table 3.3: Raw anion concentrations of sub-samples taken every 10-cm for the length of two ice cores collected at Butter Point Site and Iceberg Site, respectively, and measured using a Dionex-600 IC system. All nitrate measurements in the two ice cores were below the quantification limit of 0.1 g/m³.

Site	Depth (m)	Cl ⁻ (g/m ³)	Br ⁻ (g/m ³)	SO ₄ ²⁻ (g/m ³)
Butter Pt	0	7,600	25	1,800
Butter Pt	10	5,500	19	1,300
Butter Pt	20	5,200	17	1,900
Butter Pt	30	3,500	11	670
Butter Pt	40	3,800	11	1,400
Butter Pt	50	3,200	11	490
Butter Pt	60	2,900	9.7	570
Butter Pt	70	3,800	13	470
Butter Pt	80	2,500	8.0	420
Butter Pt	90	3,600	12	330
Butter Pt	100	2,900	9.8	680
Butter Pt	110	2,600	8.7	480
Butter Pt	120	2,800	8.9	590
Butter Pt	130	1,900	5.6	440
Butter Pt	140	2,100	6.2	410
Butter Pt	150	2,200	8.6	440
Butter Pt	160	3,300	11	610
Butter Pt	170	3,200	11	690
Iceberg	0	8,000	30	3,100
Iceberg	10	6,000	21	1,200
Iceberg	20	3,200	13	520
Iceberg	30	3,700	13	450
Iceberg	40	3,300	12	1,600
Iceberg	50	2,900	9.7	230
Iceberg	60	3,000	8.9	840
Iceberg	70	2,800	9.8	270
Iceberg	80	3,100	11	490
Iceberg	90	3,100	12	390
Iceberg	100	2,600	9.5	370
Iceberg	110	3,400	12	690
Iceberg	120	2,500	8.2	480
Iceberg	130	3,200	11	560
Iceberg	140	2,700	8.7	460
Iceberg	150	2,300	7.4	440
Iceberg	160	2,200	8.0	420
Iceberg	170	3,000	11	480
Iceberg	180	3,500	13	460
Iceberg	190	9,100	34	1,400

CHARACTERIZING THE MICROSTRUCTURAL LOCATION OF SALTS USING X-RAY MICRO-FLUORESCENCE SPECTROSCOPY

Introduction

The aim of this work was to quantitatively map the location of impurities in sea ice, determining if they are located at grain boundaries, in brine channels, and/or throughout the crystal lattice of ice. Although it is well known that salts are expelled from the ice matrix during the freezing process and the bulk of impurities lies in brine inclusions and channels, providing quantitative and visual evidence with high resolution remains an ongoing process. By increasing our knowledge of the brine network microstructure, we yield a better understanding of the transport of heat, gases, and chemical species through sea ice. Here we used synchrotron x-ray micro-fluorescence spectroscopy (XRF) to detect and identify the precise microstructural and stratigraphic location of the constituent salts in sea ice.

X-rays can penetrate deeper into a sample than electrons and thus, can be used to identify impurities located both on surfaces and at interfaces within samples several millimeters in thickness. Argonne National Laboratory's Advanced Photon Source (APS) provides the brightest x-rays in the western hemisphere, and generates highly tunable x-ray beams at one of 40 sectors. Due to the wide range of emitted wavelengths, APS advances research in materials science, physical and chemical sciences, metrology, geosciences, environmental sciences, biosciences, medical sciences, and pharmaceutical sciences. Some of the common techniques include spectroscopy for characterizing chemical bonding and electron motion, scattering analysis for understanding the structure of crystals and large

molecules, and imaging in a variety of fields (e.g., cell biology, lithography, infrared microscopy, radiology, and x-ray tomography).

Previously, synchrotron x-ray radiation has been used to study the atomic structure (e.g. Baker et al., 2000; Varshney et al., 2009) and chemistry (Angelis et al., 2005; Cibirin et al., 2008) of ice. Cibirin et al. (2008) melted ice cores from multiple Antarctic and alpine sites and used XRF to study the chemical signature of filtered dust particles collected. By utilizing a cell wrapped with an Ultralene[®] film, Angelis et al. (2005) were able to maintain accreted ice from Lake Vostok at -140 °C and map the location of impurities found at grain boundaries and brine micro-droplets. Furthermore, synchrotron radiation has been used with tomography to study the three-dimensional structure and characteristics of laboratory grown sea ice and frost flowers (Hutterli et al., 2008; Peterson et al., 2015). Initial results studying vapor-deposited ice have shown that there are distinctive regions of brine and ice, however, the distribution of brine is heterogeneous, with thickness varying from tens of microns to less than one micron (Peterson et al., 2015). Preliminary results also suggest that Br may behave differently than Cl at temperatures less than -25 °C, whereby Br may be found preferentially on ice surfaces and increasing its availability for heterogeneous reactions (Hutterli et al., 2008). The current study is the first to examine natural sea ice using synchrotron x-ray radiation and XRF.

Methods

XRF analysis was completed at APS Sector 13, which is operated by the GeoSoilEnviro Center for Advanced Radiation Sources (GSECARS) of the University of Chicago. We used beamline 13-ID-E that provides a highly tunable, high flux of spatially coherent photons that can detect concentrations as low as one ppm for many of the impurities in sea ice. We tuned the incident x-ray beam to 18 keV, allowing us to map the location of the primary anions of interest (Cl and Br), as well as K, Ca, Sr, Fe, Zn, and Cu. The beam was monochromatized with a Si(111) double-crystal monochromator, producing a flux of

between 2×10^{10} and 1.5×10^{11} photons per second, and focused using Kirkpatrick-Baez mirror pair to a $2 \mu\text{m} \times 4 \mu\text{m}$ beamsize. The fluorescence signal is then detected by a SII Vortex ME-4 four-element silicon drift diode array detector. The signal over a 0.1 s period was recorded as a $2 \text{ mm} \times 2 \text{ mm}$ region of each sample was scanned by the beam with step sizes of $10 \mu\text{m}$.

The energy of the emitted photon is characteristic of the element from which it fluoresced. The primary peaks used in this study were for the K_α line, which corresponds to a drop in energy of a L3 electron to the K shell. For Cl, K, Ca, Br, and Sr, these peaks are centered at 2.622, 3.313, 3.692, 11.924, and 14.165 keV, respectively (Elam et al., 2002). Samples were cut small enough in thickness such that the incident beam would probe the entire sample. The penetration depth is defined as the distance at which the x-ray strength has been reduced to $1/e \approx 37\%$ of its original strength, which for an 18 keV x-ray beam is approximately 9.6 mm (Elam et al., 2002). The emitted photon then must travel out of the sample through the ice and a linear path of air before striking the detector. Since the emitted photon is at a lower energy level than the incoming beam, the penetration depth is smaller for the fluorescence signal. For the given elements Cl, K, Ca, Br, and Sr, penetration depths were $35 \mu\text{m}$, $69 \mu\text{m}$, $95 \mu\text{m}$, 3.1 mm, and 5.1 mm, respectively (Elam et al., 2002). Thus, although the incoming beam reaches the entire sample thickness, detected Br and Sr signal is only from the top 3 – 5 mm. Due to the lower energy emitted photons for Cl, K, and Ca, XRF only detects near-surface features for these elements.

Although x-ray attenuation also occurs in the linear path of air between the sample and the detector, this can be reduced by enclosing the entire experimental setup in a helium-filled zippered polyethylene bag. This was particularly important for the lighter elements, but helped increase the photon count at the detector for all elements. The experiments were conducted over two separate visits to APS in March 2013 and August 2014, but the helium environment was only used during the second set of experiments. Thus, only Br measurements are presented from the first trip, while measurements from all five elements

of interest are presented from the second trip. Prior to visiting APS, ice cores were subsampled every 10 cm and a selection of these subsamples was chosen for analysis. Each sample was cut into approximately 10 mm \times 20 mm \times 5 mm slices, and each of these was shaved smooth with cleaned razor blades. To reduce the possibility of sampling multiple grains and to ensure grain boundaries could adequately be detected, we attempted to select samples with grain boundaries oriented perpendicular to the sample surface. Brine drainage was not observed during sample preparation. It should be noted that all samples were prepared such that images are in the xy-plane, looking down the vertical z-axis. Samples were transported to APS while being maintained at $-25\text{ }^{\circ}\text{C}$ in a polystyrene foam cooler with dry ice and blue ice packs. Each sample was then press fit into a small acrylic sample holder and frozen in place with a few drops of water. During analysis, samples were kept between $-18\text{ }^{\circ}\text{C}$ and $-21\text{ }^{\circ}\text{C}$ using a Peltier thermoelectric module cooling stage built by GSECARS. A thin film of Kapton[®] encased the sample and holder to prevent the formation of frost on the sample surface. Samples were analyzed as described above, yielding 2 mm \times 2 mm elemental maps with 10 μm spatial resolution.

During the 2014 visit, we also analyzed a blank Milli-Q water sample and two liquid standards to find a calibration curve enabling the estimation of concentration from elemental XRF maps. Although replicating the sample setup with frozen samples would be ideal, it was not possible to create such a standard as the freezing process rejects impurities leaving a non-homogeneous product. The measured photon count of the region scanned would then not be representative of the desired standard concentration. However, the difference in x-ray penetration depth between water and ice is negligible for the x-ray energies encountered in this study (Elam et al., 2002). Other than the phase difference, the rest of the experimental setup was kept constant, including the thickness of the sample. The two standards contained 0.5 g/m^3 (Standard #2) and 2.0 g/m^3 Br (Standard #5) and 25 g/m^3 (Standard #2) and 100 g/m^3 Cl (Standard #5), and were analyzed over 120 s. The peaks in the standards corresponding to Cl fluorescence were too close to the baseline

signal for accurate standard calibration. Thus, concentration estimation was only possible for Br elemental maps.

Results and Discussion

As the chosen $2\text{ mm} \times 2\text{ mm}$ region of interest for each sample was scanned in the x-ray beam, an XRF spectrum was collected for each pixel. The photon count at each energy level was summed over all four detectors yielding spectra such as shown in Fig. 4.1. In Fig. 4.1, the black line is the spectrum for the blank MilliQ water sample, the orange and purple lines are the spectra for Standards #2 and #5, respectively, and the blue line is an example spectrum for one of the samples. Some of the major peaks are labeled above. Noticeable in all spectra is the sharp drop-off in photon count at 18 keV since this was the energy level of the incoming x-ray beam. Measurable in most sample spectra were peaks corresponding to Cl K_α , K K_α , Ca K_α , Ca K_β , Fe K_α , Fe K_β , Ni K_α , Cu K_α , Zn K_α , Zn K_β , Br K_α , Br K_β , and Sr K_α . By integrating the area under each peak, we could arrive at an estimation of the relative intensity of each element in each sample. Since the sample apparatus was not enclosed in a helium environment during the 2013 visit to APS, these samples did not exhibit peaks for the lighter elements such as Cl, K, and Ca. During this visit, fluorescing x-rays from the lighter elements were mostly absorbed by air in the path from the sample to the detector. Note that although samples contain much higher concentrations of Cl than Br, the spectra peaks are much stronger for heavier elements such as Br, since their fluoresced x-rays can escape from a far greater depth.

Elemental Maps

To make an elemental map for each sample, the photon counts are summed over the desired energy levels for each pixel. For bromine, this corresponded to energy limits of 11.63–12.27 keV. Raw photon counts were all scaled by the incoming beam flux to account for fluctuations in the source beam strength. For visual display of relative intensities, all values were then scaled to 0 – 255. Bromine maps for Butter Point (first-year ice), Iceberg

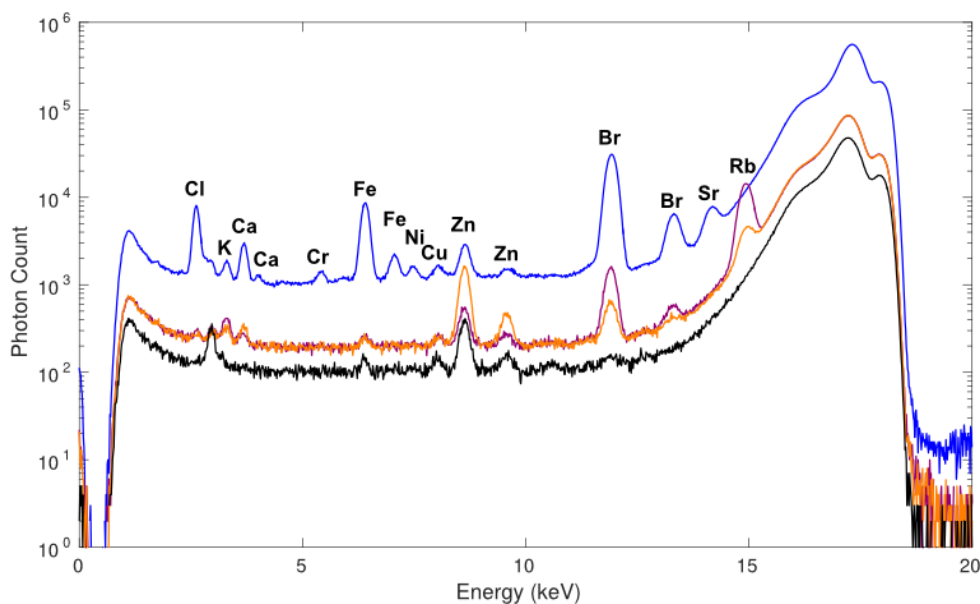


Figure 4.1: XRF spectra for a typical sample (blue), standard #2 (orange), standard #5 (purple), and MillQ water (black). Incoming x-ray energy was 18 keV. Spectra represent the sum of the photon counts over all four detectors. Note however that the collection time differed between the sample spectrum and the standard spectra, and thus, there is an offset between the different baselines. Peaks common in many of the samples are labeled for the sample spectrum.

Site (first-year ice), and Scott Base (multi-year ice) are presented in Figs. 4.2, 4.3, and 4.4, respectively. These figures illustrate that bromine is not evenly distributed throughout the ice core, with large variability both in depth and in horizontal heterogeneity. Further, maps for a given depth differ greatly between the three ice cores. This is likely due to the small scale of brine features. These elemental maps are highly dependent upon the precise region analyzed. However, despite this variability, there are still many features present that allow us to begin analyzing the microstructural location of salts in sea ice.

Beginning at the snow-ice interface, the 0-cm sample for both of the first-year ice cores (Fig. 4.2 and Fig. 4.3) show rounded features about 400 μm in diameter in the Br maps. These rounded features are also somewhat visible in the samples from 10 cm and 20 cm for both cores. This feature is not as noticeable in the multi-year ice core collected near Scott Base (Fig. 4.4). All three cores also exhibit very small circular features in the deepest

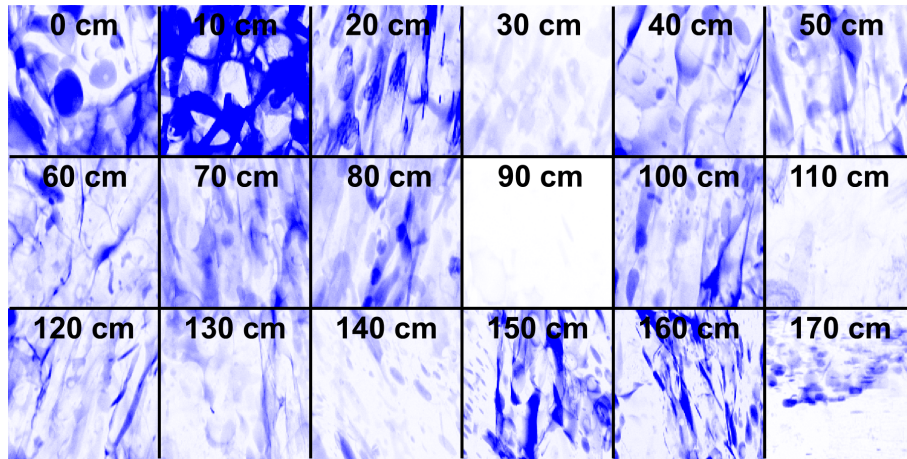


Figure 4.2: 2 mm × 2 mm Br maps of the Butter Point ice core for sub-samples taken at 10 cm intervals.

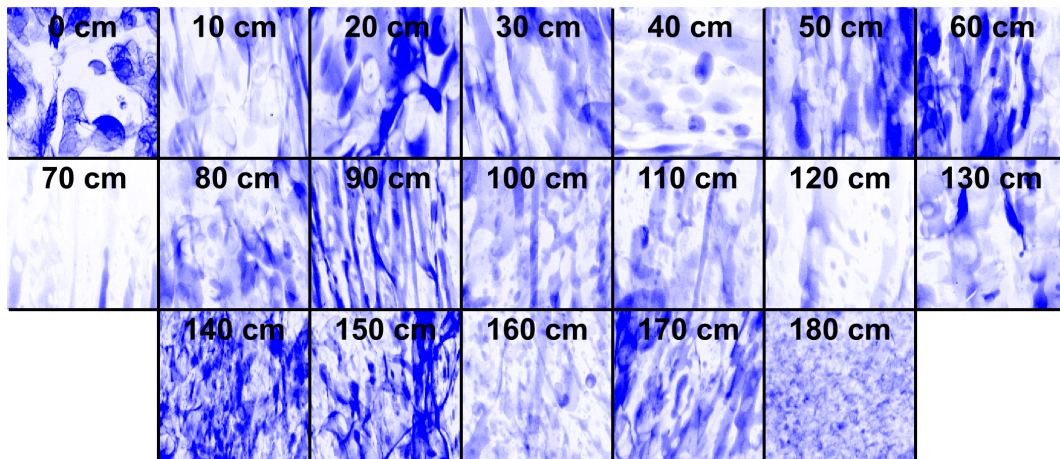


Figure 4.3: 2 mm × 2 mm Br maps of the Iceberg Site ice core for sub-samples taken at 10 cm intervals.

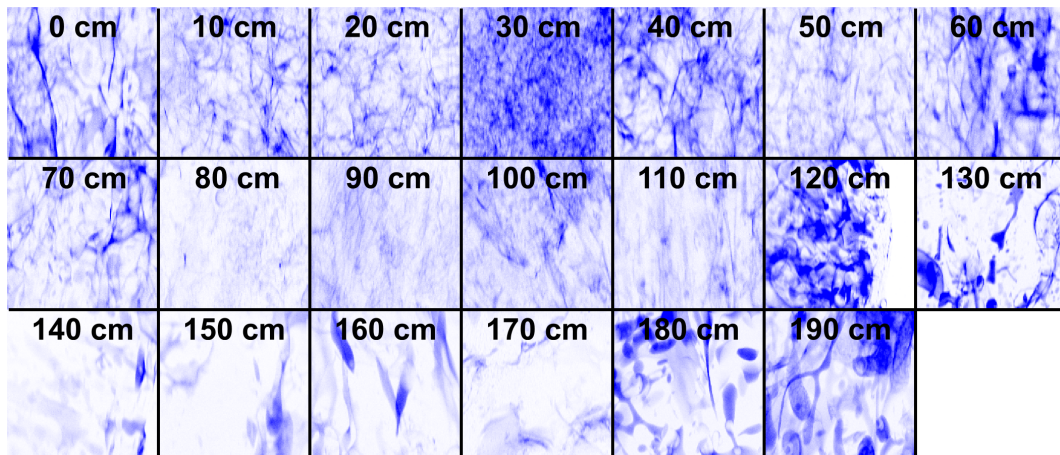


Figure 4.4: 2 mm × 2 mm Br maps of the Scott Base ice core for sub-samples taken at 10 cm intervals.

sample collected near the ice-ocean interface, but again, this feature is more prevalent in the first-year ice cores. By far, the most dominant feature throughout the bulk of all three ice cores is sets of parallel lines. The spacing of these lines is often on the order of magnitude of 0.5 mm. This line spacing is consistent with the spacing between lamellae during ice growth that later become the brine layers of sea ice (Harrison and Tiller, 1963). Exceptions to this general trend include the sample from 40 cm in the Iceberg Site core and samples from 30 cm and 120 cm in the Scott Base core. We also note that some samples have very low abundance of Br, such as samples at 30 cm and 90 cm in the Butter Point core and 70 cm in the Iceberg Site core.

The vertical thin sections in Fig. 2.3 exhibited a frazil/columnar ice transition roughly around 18 cm and 28 cm for the Butter Point and Iceberg Site core, respectively. Thus, the transition from rounded features to sets of parallel lines below 20 cm for the first-year ice cores is consistent with this observation. As noted in Chapter 2, the granular ice in the Scott Base ice core extended down to 80 cm, however it was likely a mix of frazil and snow-ice. The Br elemental maps for the Scott Base core in Fig. 4.4 did not have the same rounded features in the upper part of the core as did the first-year ice cores. However, there was indeed a transition occurring around 80 – 100 cm, but due to low concentrations of Br in these samples, it was difficult to pinpoint the precise depth of the transition point.

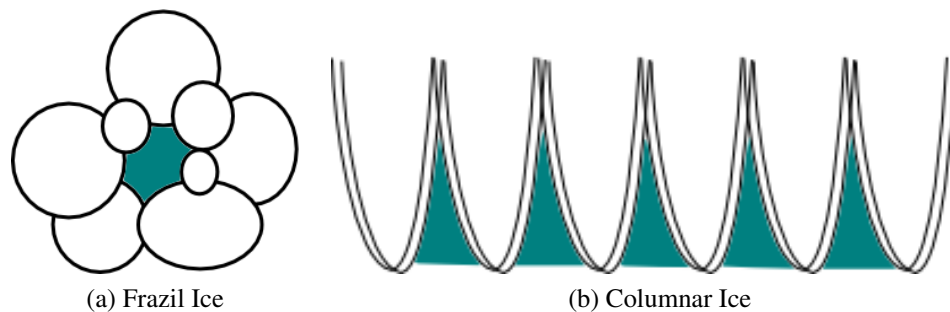


Figure 4.5: Sketches illustrating the difference in pore structure between frazil ice and columnar ice. In both images, the brine-filled pores are shown in teal. For frazil ice (left panel), the pores are best described as blobs. For columnar ice (right panel), the pores are best described as parallel sheets/layers.

In Fig. 4.5, the expected pore structures in frazil ice and in columnar ice are sketched.

For frazil ice the pore structure is composed of primarily rounded features, while for columnar ice the pores are found in sets of parallel sheets/layers. As will be further shown in Chapter 5, this pore structure was also observed in the μ CT images. Representative images of the brine phase in frazil ice and columnar ice are shown in Fig. 4.6. These three-dimensional visualizations match the expected shapes sketched in Fig. 4.5, and help explain the XRF Br images.

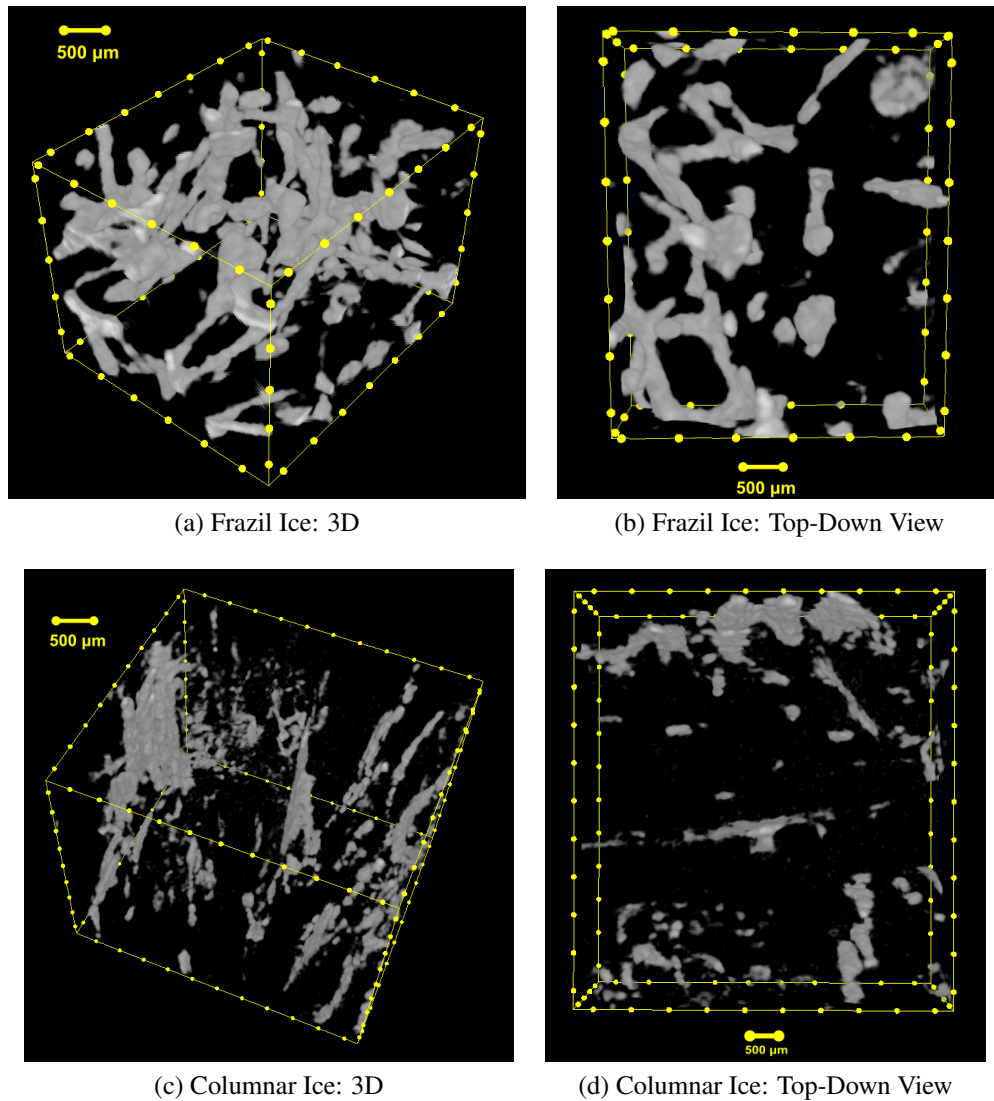


Figure 4.6: Representative μ CT images of the brine phase in frazil ice (top) and columnar ice (bottom). The left panels are three-dimensional images of the brine in samples from a depth of 0 cm and 130 cm in the Butter Point core, respectively. The right panels are the same samples viewed top-down to illustrate the structure in the horizontal plane.

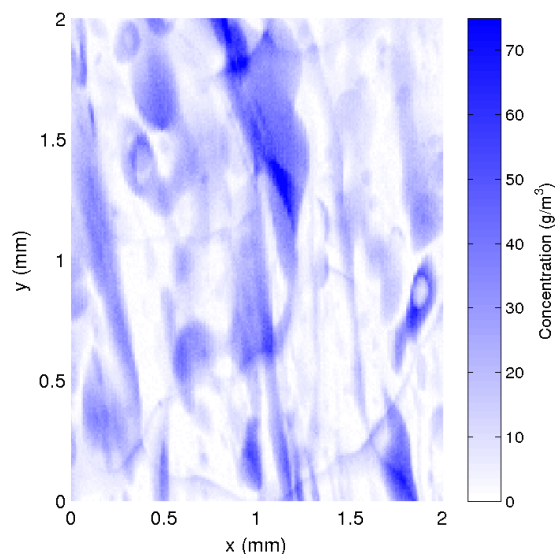


Figure 4.7: Representative Br XRF map scaled for concentration. Scale bar is a conversion from the 0 – 255 scale used in Figs. 4.2, 4.3, and 4.4 to one of concentration in g/m^3 . This particular sample is from a depth of 50 cm in the Butter Point ice core

The elemental maps in Figs. 4.2, 4.3, and 4.4 show the relative intensity of the Br signal. However, since photon counts are directly correlated with concentration, it is possible to get an estimate of concentration from these maps as well. To calibrate the signal, we analyzed two liquid standards and one blank Milli-Q water sample as describe above and shown in Fig. 4.1. On all spectra for all detectors, the baseline signal was first subtracted mathematically by estimating its signal within multiple shifted windows and then regressing the varying baseline to the window points using a spline approximation. Then, as described above for the sample maps, the photon counts were integrated over the Br K_α energy range 11.63 – 12.27 keV. Since standard spectra were collected over a longer time period, this count was scaled by 120/0.1 for comparison with sample spectra. Finally, the resulting numbers were scaled by the average incoming beam flux and normalized to the same 0 – 255 scale as the sample maps. This allowed us to calculate a scaling ratio of 2/7 to convert to concentration in g/m^3 as is shown in Fig. 4.7. This same approximate colorbar can be applied to the Br maps of Figs. 4.2, 4.3, and 4.4.

With this scaling ratio, the largest concentrations are roughly 70 g/m^3 and generally

occur in the linear brine layers described above. This is consistent with previous observations of 10 – 100 times greater brine salinity than bulk salinity (e.g., Notz, 2005; Weeks and Ackley, 1982). Although not a perfect proxy considering both the three-dimensional character of the measurement and the great spatial variability, it is encouraging to note that the averaged value over all samples and all pixels is roughly 5 g/m^3 . This value is relatively close to the bulk concentrations observed in Chapter 3.

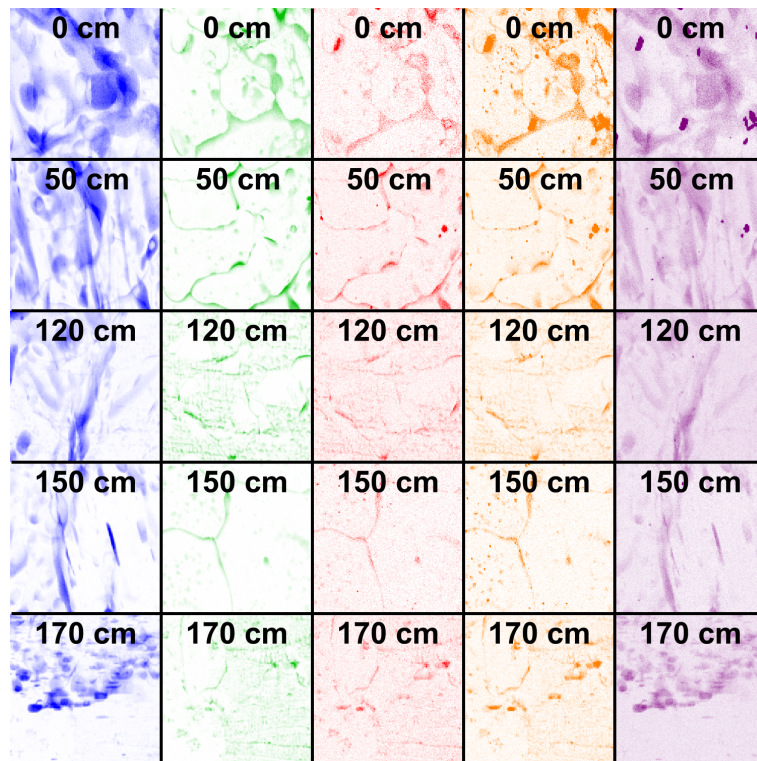


Figure 4.8: XRF elemental maps for Br (blue), Cl (green), K (red), Ca (yellow), and Sr (purple) for sub-samples taken at 10 cm intervals along the Butter Point ice core. For a given depth, all five images are from the same scan over a $2 \text{ mm} \times 2 \text{ mm}$ region.

By enclosing the experimental setup in a helium environment, we were able to map the location of Cl, K, Ca, and Sr, in addition to Br, during the 2014 visit to APS. Cl, K, Ca, and Sr peaks on the XRF spectra were integrated between the energy limits $2.47 - 2.72 \text{ keV}$, $3.11 - 3.42 \text{ keV}$, $3.49 - 3.87 \text{ keV}$, and $13.67 - 14.57 \text{ keV}$, respectively. This yielded elemental maps for each element similar to those shown above for Br. For this analysis, only a selection of subsamples from the Butter Point and Iceberg Site cores

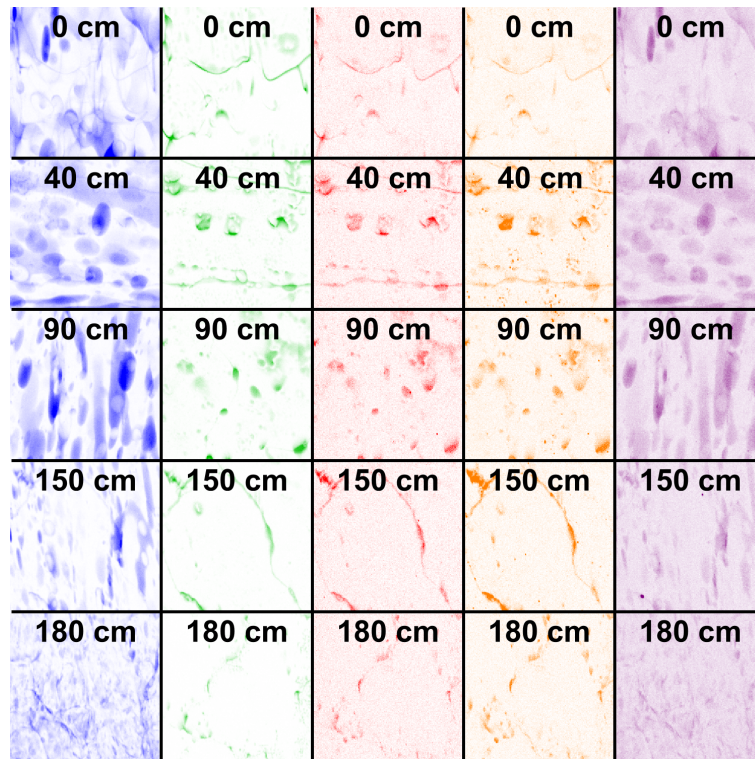


Figure 4.9: XRF elemental maps for Br (blue), Cl (green), K (red), Ca (yellow), and Sr (purple) for sub-samples taken at 10 cm intervals along the Iceberg Site ice core. For a given depth, all five images are from the same scan over a $2\text{ mm} \times 2\text{ mm}$ region.

was used. Representative samples from each depth are shown in Fig. 4.8 (Butter Point) and Fig. 4.9 (Iceberg Site). Most noticeable in Figs. 4.8 and 4.9 is the similarity of the Br and Sr maps and of the Cl, K, and Ca maps. Additionally, from each chosen depth a triplicate of subsamples were cut and analyzed to provide insight into reproducibility of the analysis. Triplicate elemental maps for top, middle, and bottom depths of the Butter Point and Iceberg Site cores are shown in Fig. 4.10. Qualitatively, although there is significant variability amongst the replicates, many of the same features can be seen across samples of a given depth. For example, the 0-cm depth samples particularly from the Butter Point ice core show complex and fine-scale heterogeneity for all salts. The ice at this depth is entirely frazil ice and consequently has small grain size. At mid-depths, the salts are primarily located at grain boundaries and in brine layers and channels across all replicates. The bottom depth samples for each core do not show a prevalence of grain

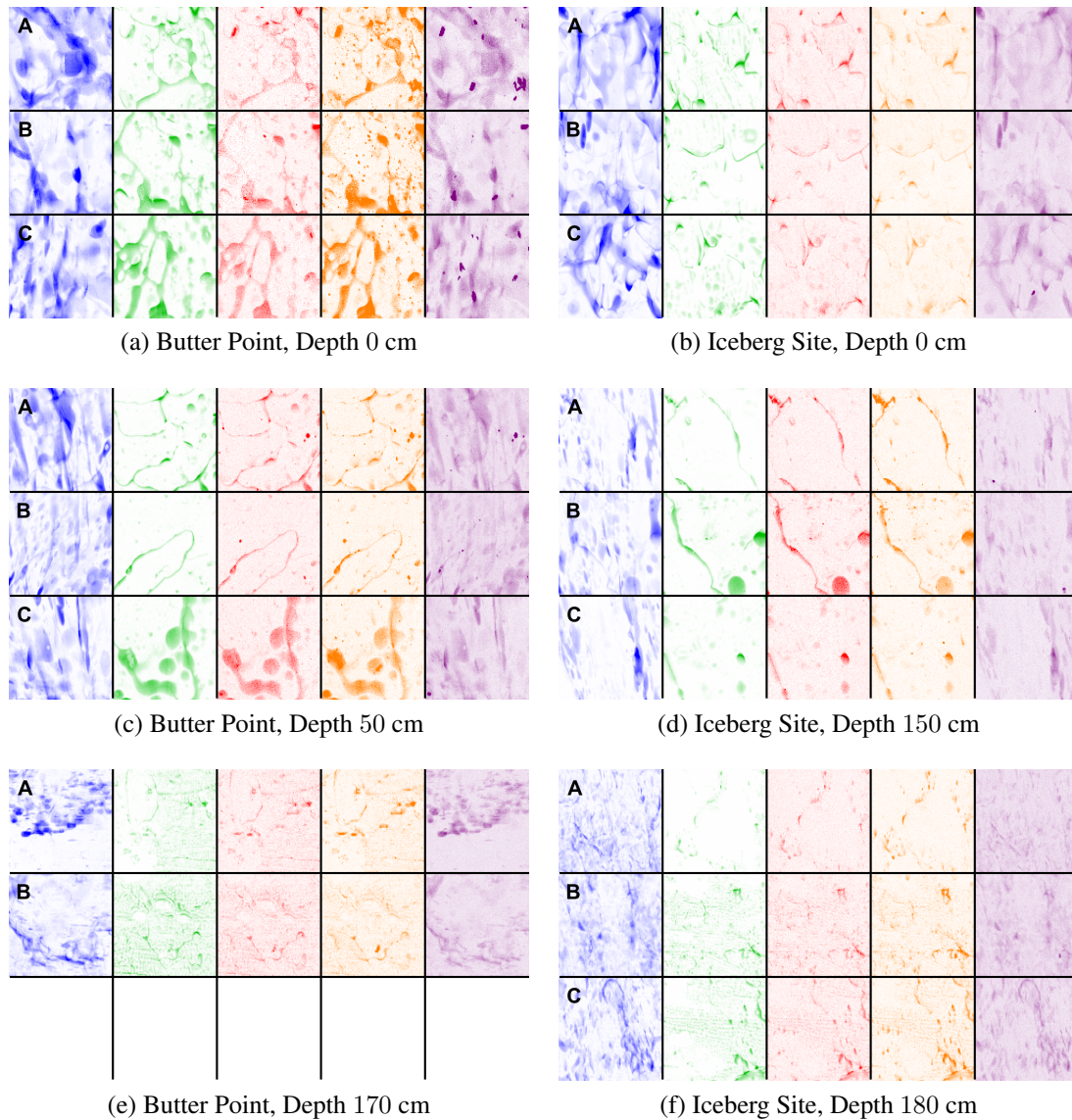


Figure 4.10: XRF replicate elemental maps for Br (blue), Cl (green), K (red), Ca (yellow), and Sr (purple) for select sub-samples of the Butter Point and Iceberg Site ice cores. For a given depth and a given row, all five images are from the same scan over a $2 \text{ mm} \times 2 \text{ mm}$ region. Each row represents a different sample for the given depth.

boundaries. Although the salt concentration is relatively large at this depth, the salts are located throughout the scanned region.

Correlation Between Different Salts

To better visualize the different correlations amongst elements, three-element overlay maps were created for select few samples. Overlay Br, Cl, and Sr maps for samples from

Butter Point and Iceberg Site cores are shown in Fig. 4.11. The blue and purple from Br and Sr maps generally coincide to form a violet regions, and with shapes consistent with observations above for Br only maps. There are regions, however, that appear brighter blue or lighter purple, indicative of primarily Br or Sr, respectively. This is especially noticeable at a depth of 0 cm for Butter Point where there are several purple circles about 100 μm in size. The green in these figures suggest that Cl maps are detecting different features than Br/Cl maps. In general, the green regions are restricted to lines measuring tens of microns in width, suggesting Cl is mapping surface grain boundaries. We note the appearance of some green approximately 100 μm circles, such as in the maps 50 cm for Butter Point and 90 cm for Iceberg site. In Fig. 4.12, we replace Sr with K to yield slightly different three-element overlap maps. Here it becomes apparent that some of the features detected with Sr, but not Br, also contain K. In addition, the green Cl regions take on a lighter/increased yellow shade, indicating the co-location of Cl and K. We note that Ca maps have a similar trend and effect as K maps.

To quantify the co-location of the elemental maps, Pearson's linear correlation coefficients were calculated for each pair of elements for each sample. The matrix of average correlation coefficients is presented in Table 4.1. The correlation coefficient of 0.81 between Br and Sr indicates a clear co-location between the two elements. Further, the high pair-wise correlations between Cl, K, and Ca suggest they are mapping similar features. The individual correlation matrices for each sample of Butter Point and Iceberg Site cores are depicted in Fig. 4.13, with the colors blue, green, red, black, and magenta signifying Br, Cl, K, Ca, and Sr, respectively. The mean over all samples for each element is shown as a thick dotted line, and matches the data in Table 4.1. Each line peaks at 1 for its respective element as each is correlated with itself by definition. Although there is some variability amongst the samples, the mean values well represent the overall trends.

To gain further insight into the microstructural location of the different salts, a principal component analysis was run on the collection of elemental maps for each sample. The five

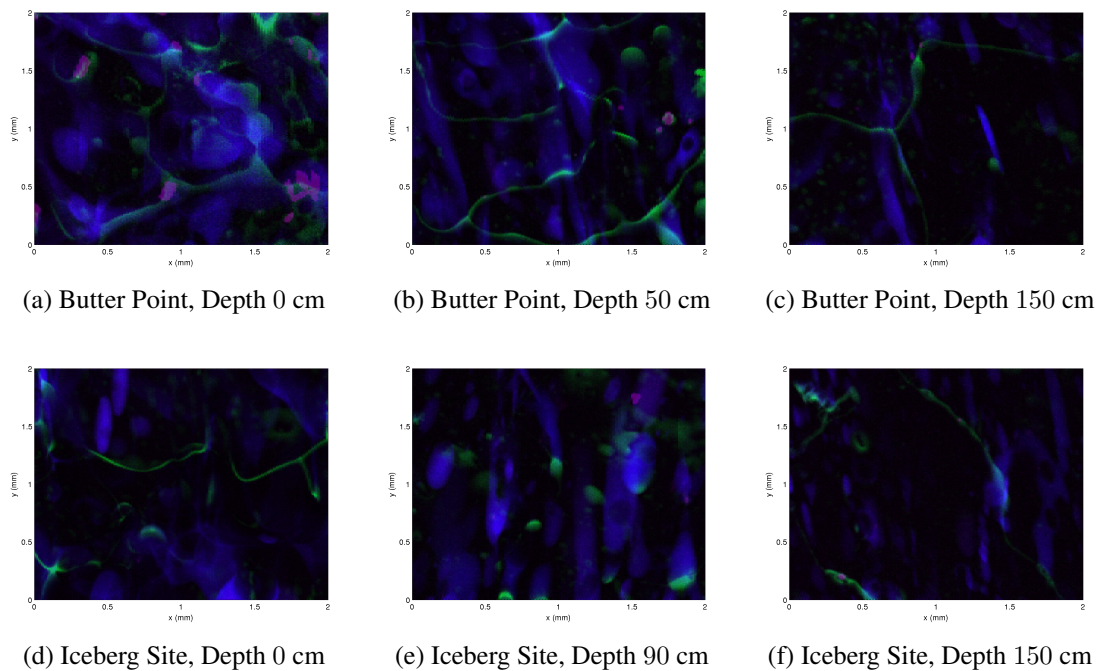


Figure 4.11: XRF elemental overlay maps showing Br, Cl, and Sr for selected subsamples. For these images, blue represents Br, green represents Cl, and purple represents Sr. As before, each image shows the $2\text{ mm} \times 2\text{ mm}$ region scanned.

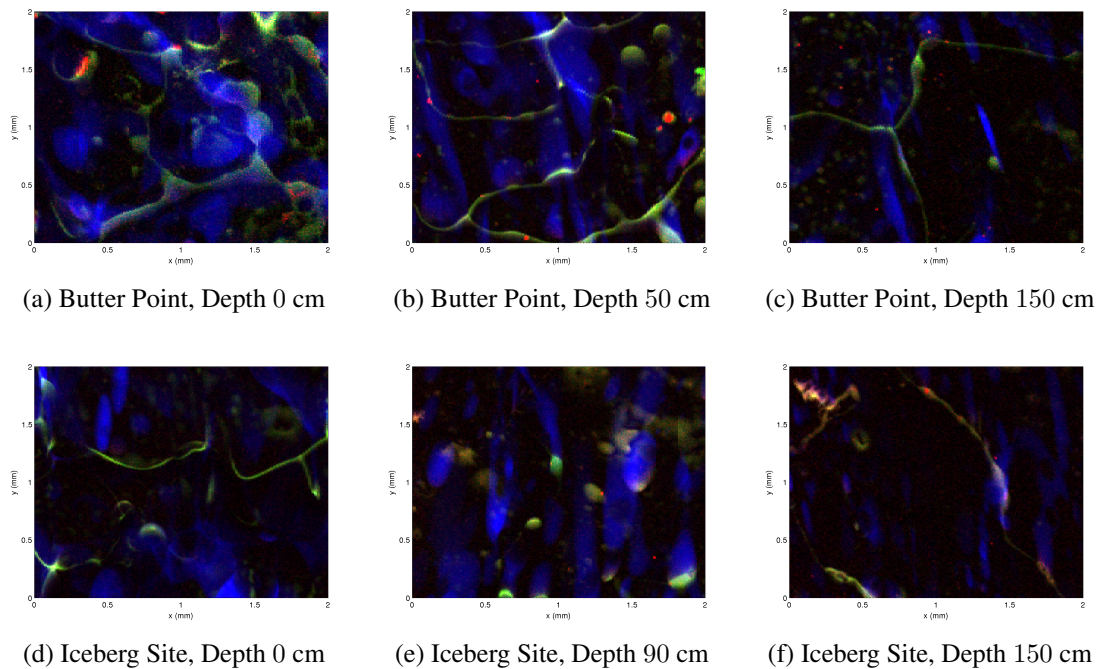


Figure 4.12: XRF elemental overlay maps showing Br, Cl, and K for selected subsamples. For these images, blue represents Br, green represents Cl, and red represents K. As before, each image shows the $2\text{ mm} \times 2\text{ mm}$ region scanned.

Table 4.1: Matrix of mean correlation values for relative amounts of Br, Cl, K, Ca, and Sr. For each XRF map, the correlation between each pair-wise set of elements was calculated. The mean value over all samples is given below

	Br	Cl	K	Ca	Sr
Br	1				
Cl	0.23	1			
K	0.25	0.73	1		
Ca	0.30	0.74	0.65	1	
Sr	0.81	0.20	0.24	0.29	1

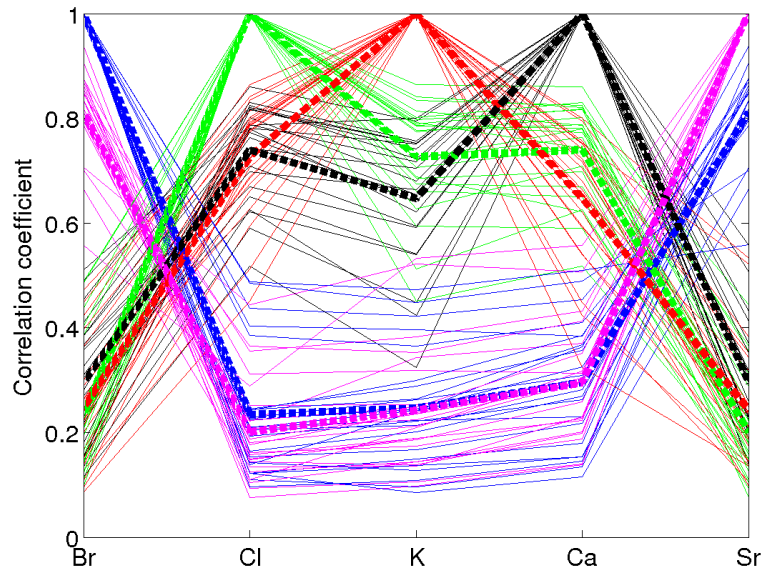


Figure 4.13: Pair-wise correlation values of different elements for all samples, with each color corresponding to a particular element. The colors blue, green, red, black, and magenta signify Br, Cl, K, Ca, and Sr, respectively, and each line represents a different XRF map. The thicker dashed lines represent the mean values across all XRF maps. Each element is by definition correlated to itself, and thus has a value of 1. High values for other elements signify correlation between the two elements (e.g., Br and Sr).

resulting components and the relative input from each element are shown in Fig. 4.14, where the lines for a particular component are different samples. The final panel of Fig. 4.14 displays the normalized eigenvalues of the covariance matrix, which yield an indication of the relative importance each component plays to the total variance in the image. For this panel, the red lines are for Butter Point and the blue lines are for Iceberg site cores. As can be seen in the figure, the first principal component tends to account for

50 – 75 % of the total variance. Meanwhile the second component accounts for 15 – 30 %, while the final three components have very minor effects. The first component has influences from all five elements, with not large fluctuations amongst the different salts. This is likely picking up the signal that all elements are found in brine regions but not throughout the bulk ice. The second component appears to split the samples into two groups, likely based on penetration depth. Many of the samples show a large influence from the Br/Sr signal, while a few show stronger influences from the Cl, K, and Ca signal. This second component suggests that generally, most of the variance within an image is due to the Br/Sr signal, except for a select samples. The third, fourth, and fifth components appear to pick out differences amongst K, Cl, and Ca, with Sr occasionally being related.

Trends with Depth

As observed previously, although there is significant variability amongst replicate samples from a given depth, there are still noticeable trends that show variation with depth. For this and subsequent analysis, we consider only samples scanned in 2014 in the helium environment, which reduced absorption by air between the sample and detector, and provided better Br calibration with the standards. Fig. 4.15 plots depth versus the maximum Br concentration measured for a single location (a) and the averaged Br concentration over the region scanned (b). Both figures show an overall decrease in Br concentration with depth. This differs from the expected c-shaped profile for salt concentrations in sea ice, and may be a result of either the significant spatial heterogeneity or a loss of brine during transportation. Although thermocouples recorded ambient container temperatures of roughly $-20\text{ }^{\circ}\text{C}$ during transport both from Antarctica to Dartmouth and from Dartmouth to APS, local sample environments might have differed slightly. Further, samples were transferred between cold rooms, containers, and analysis instruments where the potential for unnoticed brine drainage could have occurred. However, it should be noted that when the ice cores were analyzed for anion concentrations with IC, only the 190-cm depth of the Iceberg Site core showed an increase in salt concentration, completing the c-shape profile

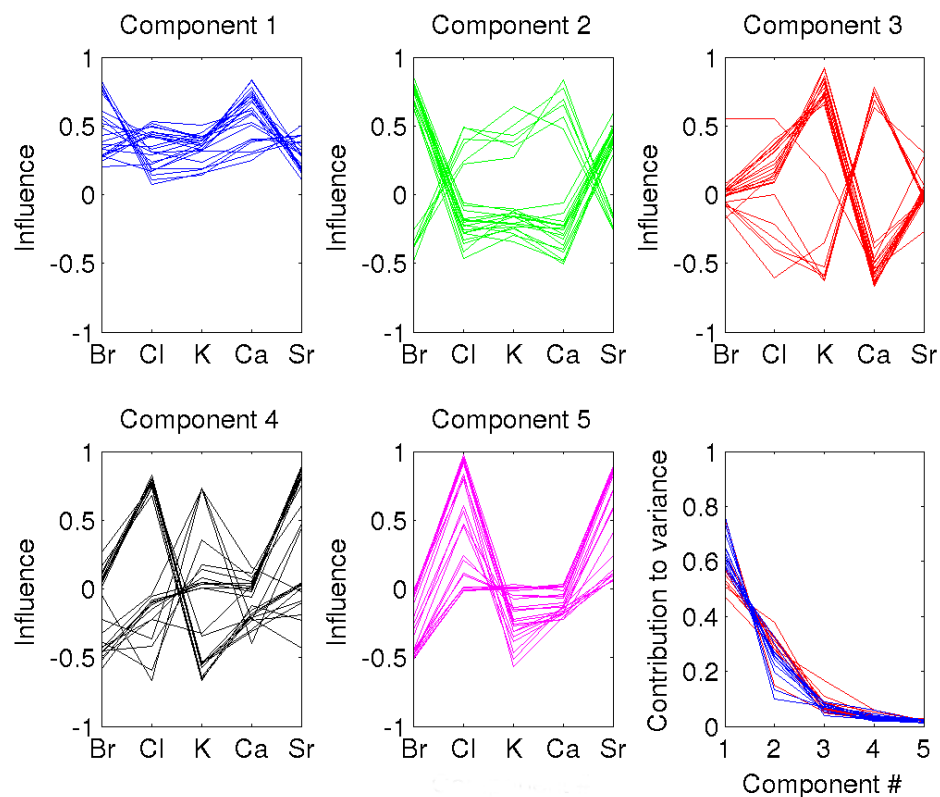


Figure 4.14: Principal component analysis of all sub-sample XRF maps. The first five panels show the relative contribution of each element to the respective principal components, where each color is representing a different component and each line represents a different sub-sample. The final panel shows the normalized eigenvalues of the covariance matrix, which yield an indication of the relative importance each component plays to the total variance in the image. Here the blue and red lines represent Butter Point and Iceberg Site ice core samples, respectively.

(Fig. 3.1). Since the ice at 190 cm was fairly soft and mushy, a thin section for XRF analysis was not obtained from this depth. The averaged concentrations do show a slight increase for the lowest sample of each core, suggesting that there is indeed increased salts in the ice at lower depths. Interestingly, the average value across all samples in Fig. 4.15(b) is 8.6 g/m^3 , which compares favorably with concentrations measured with IC in Fig. 3.1.

The Br XRF maps were then binarized to isolate regions containing significant concentrations of Br, and the shape of these regions were analyzed. Quantitative metrics for describing the spatial distribution of these regions are shown versus depth in Fig. 4.16. The top-left plot indicates that Br-concentrated regions become more elongated in shape

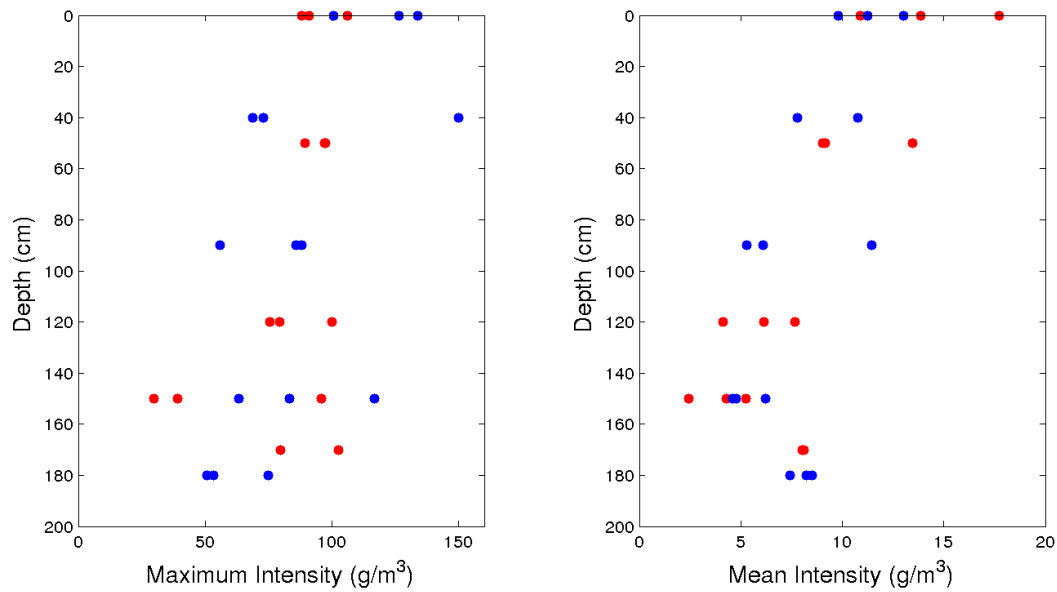


Figure 4.15: Maximum (a) and mean (b) intensities for XRF elemental Br maps from the 2014 APS visit. Samples from the Butter Point ice core are shown in red, while samples from the Iceberg Site ice core are shown in blue. For each depth chosen, a triplicate of samples were scanned.

deeper in the core. This is likely explained by the greater prevalence of columnar ice, which restricts the brine, and consequently the salts, to vertically oriented sheets/layers. The connectivity of the Br-concentrated regions was observed to decrease with depth. In the frazil-growth zone in the upper part of the core, brine and salts occupy complex regions that are multiply connected, while this connectivity decreases in the columnar-growth zone. Consistent with the observations above from Fig. 4.15, the overall coverage of the Br-concentrated regions decreased with depth. Finally, the mean size of the Br-concentrated regions also decreased with depth as is shown in the bottom-right plot of Fig. 4.16.

Comparison to Thin Sections

To better identify the features detected with XRF, horizontal thin sections roughly 0.5 mm in thickness of each sample were prepared and analyzed under cross-polarizing filters. Thin sections for Butter Point, Iceberg Site, and Scott Base ice cores are presented in Figs. 4.17, 4.18, and 4.19. Together with the vertical thin sections presented in Fig. 2.3,

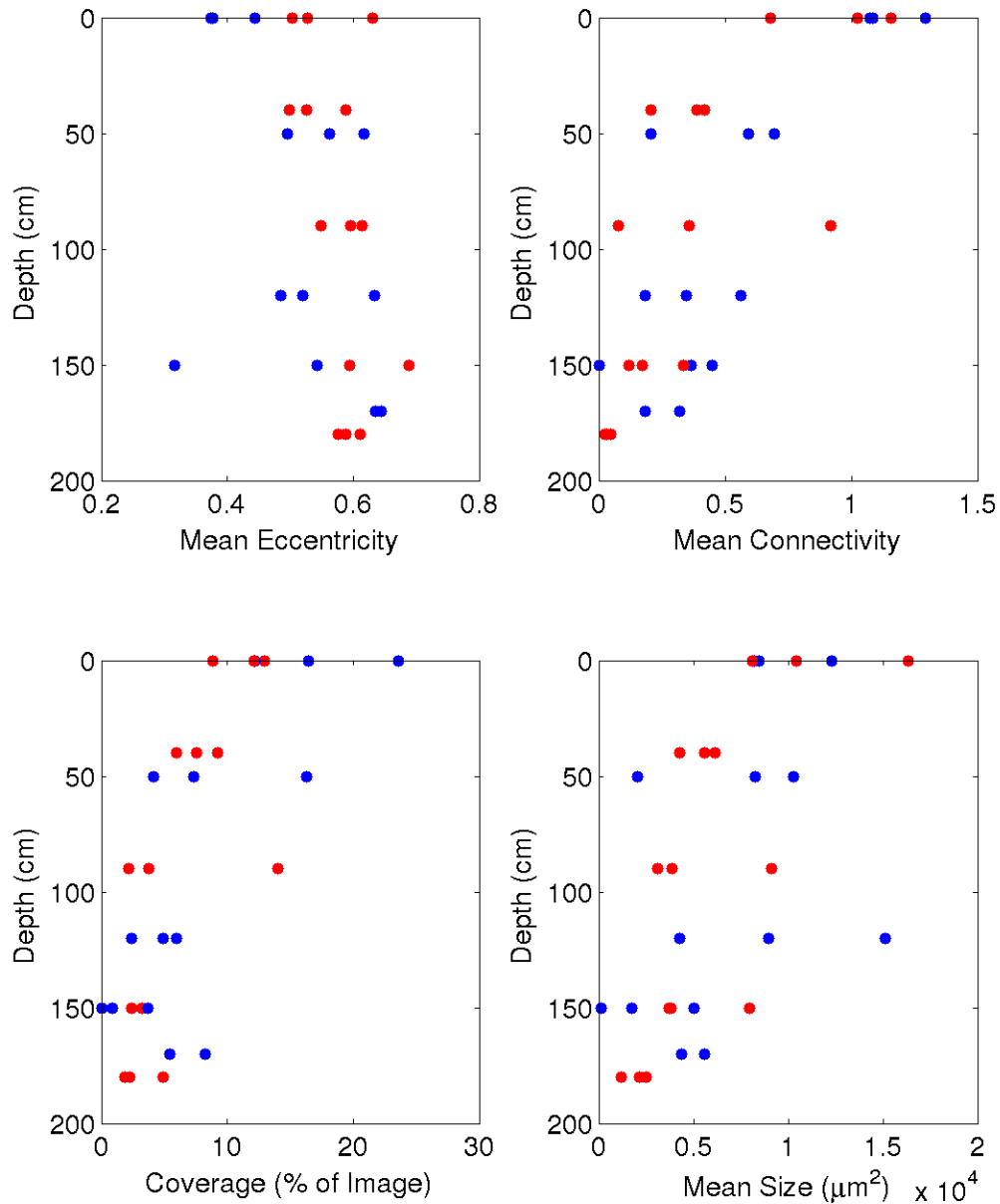


Figure 4.16: Metrics for quantifying the shape of the Br-concentrated regions of XRF maps from the 2014 APS visit. Samples from the Butter Point ice core are shown in red, while samples from the Iceberg Site ice core are shown in blue. For each depth chosen, a triplicate of samples were scanned.

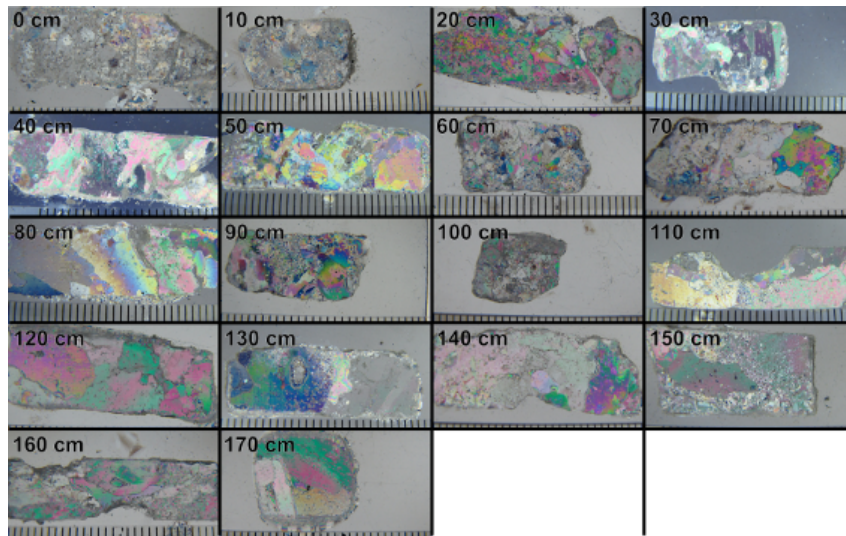


Figure 4.17: Horizontal thin sections of sub-samples from the Butter Point ice core. Tick marks are spaced at 1 mm intervals. Thin sections were prepared by thinning each sub-sample to a thickness of approximately 0.5 mm using a microtome. Thin sections were then imaged using cross-polarizing filters to visualize the different grains.

these thin sections provide a good visualization of the microstructure and grain boundaries of each core. The granular/columnar transitions observed here are in good agreement with what was observed earlier from the vertical thin sections. Additionally, the horizontal thin sections can provide insight to the width of each grain, subgrain feature, brine inclusion, and air bubbles and spatial variability. Because the samples analyzed by XRF are of horizontal slices, the same horizontal thin sections can help identify the features observed. Although the $2 \text{ mm} \times 2 \text{ mm}$ regions scanned with XRF correspond to the horizontal thin sections presented, the kapton window prevented direct observation of the region scanned. Thus, for most of the analysis we rely on feature size to indirectly correlate our observations.

Fig. 4.20 presents the best direct matching found of XRF images to a location on horizontal thin sections. Two regions were located on a thin section from the 150-cm sample of the Iceberg Site core that were likely the regions scanned. As can be seen on the different elemental overlays, the grain boundaries visible in the thin section are well detected by the Cl, K, and Ca maps. Both XRF and thin section images also show small

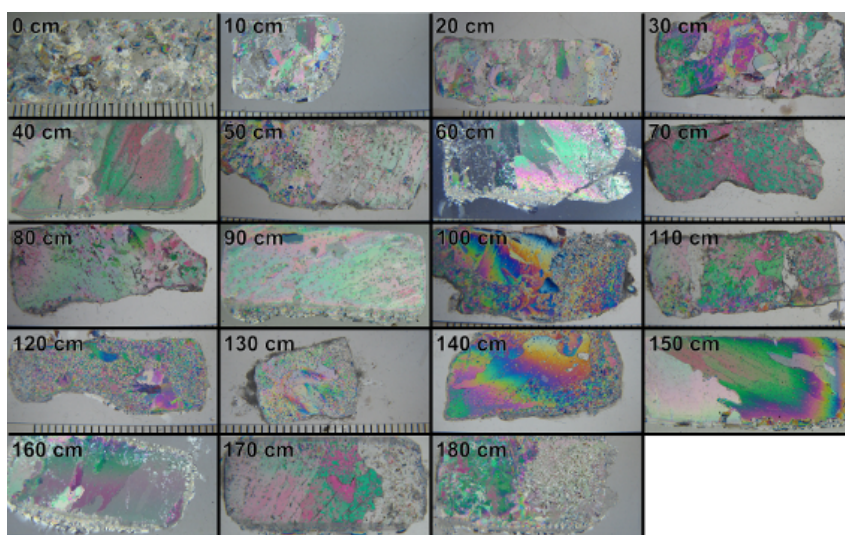


Figure 4.18: Horizontal thin sections of sub-samples from the Iceberg Site ice core. Tick marks are spaced at 1 mm intervals. Thin sections were prepared by thinning each sub-sample to a thickness of approximately 0.5 mm using a microtome. Thin sections were then imaged using cross-polarizing filters to visualize the different grains.

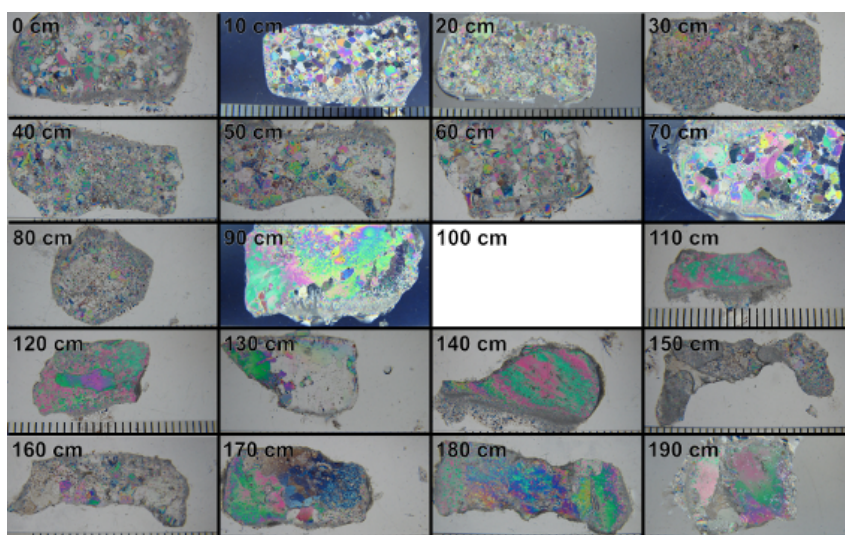


Figure 4.19: Horizontal thin sections of sub-samples from the Scott Base ice core. Tick marks are spaced at 1 mm intervals. Thin sections were prepared by thinning each sub-sample to a thickness of approximately 0.5 mm using a microtome. Thin sections were then imaged using cross-polarizing filters to visualize the different grains. Note that the sample from 100 cm was damaged during cutting, and thus could not be imaged.

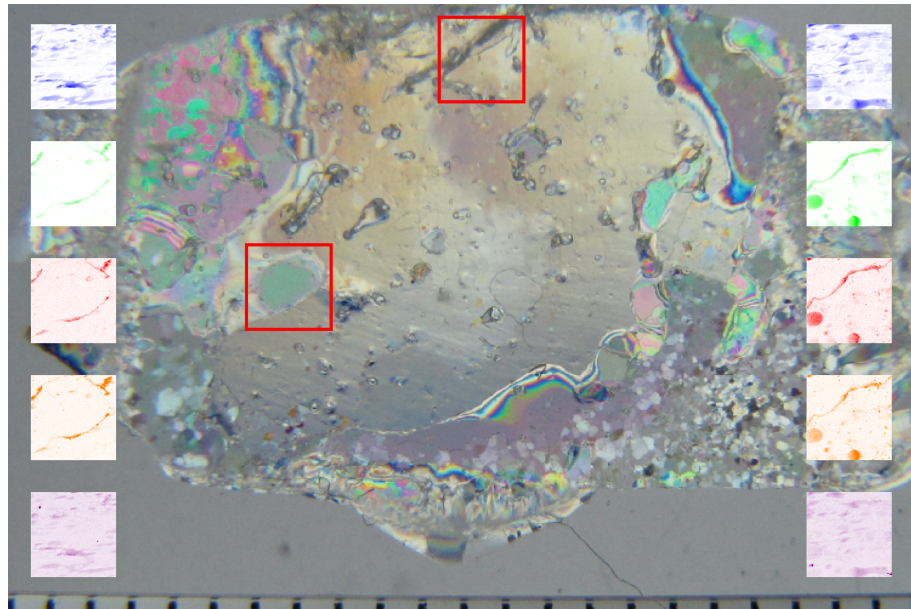
circular features of the same size that are likely brine channels. The Br and Sr maps show additional features that are not visible in the thin sections. Due to their greater penetration depth, these elemental maps are likely detecting features from deeper within the sample, such as brine inclusions not visible in the thin section that was imaged.

The lower region identified in Fig. 4.20 was further examined to investigate particular features within the image. Two unique features of the Cl elemental map were isolated and are shown in Fig. 4.21. The first was a small circular shape located in the middle of the image, while the second encompassed a portion of the grain boundary. The XRF x-ray spectrum for these isolated features were compared to the x-ray spectrum for the whole region in Fig. 4.22. Both features had strong peaks corresponding to Cl (2.622 keV), as would be expected. The small circular feature however, had large peaks corresponding to elevated Cr (5.415 keV), Fe (6.405 keV for $K\alpha$ and 7.059 keV for $K\beta$), and Ni (7.480 keV), which was not observed in the grain boundary spectrum. Further, this feature was not visible in the thin section of Fig. 4.20. This suggests that the feature may be a dust particle that was removed during preparation of the thin section. Although both feature spectra had peaks for K, Ca, Br, and Sr (3.313, 3.692, 11.924, and 14.165 keV, respectively), the relative magnitude of the grain boundary spectrum peaks was greatly enhanced.

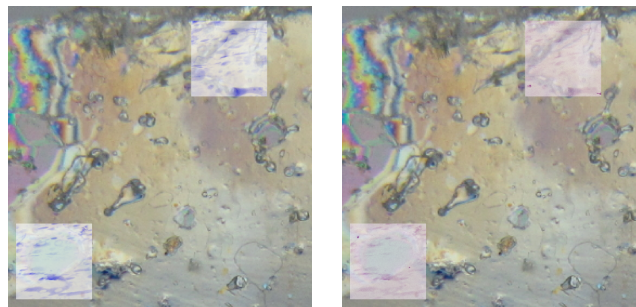
Trace metals have been found in Antarctic sea ice sourced from dust, upwelling, re-suspension of shelf sediments and re-mineralization, and the importance of biogeochemical cycling of these metals has only recently been studied (Lannuzel et al., 2011). The XRF spectra from both visits to APS contained peaks at 6.405 keV, 8.046 keV, and 8.637 keV, corresponding to Fe, Cu, and Zn, respectively. XRF elemental maps for these three metals are given in Appendix B.

Conclusion

We have successfully utilized XRF to map the microstructural location of various impurities in sea ice, quantified the distribution of Br, and noted specific features of the

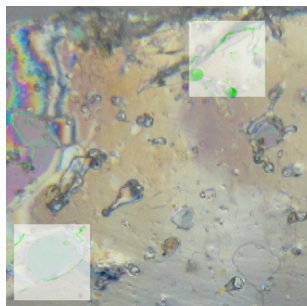


(a) Scanned regions

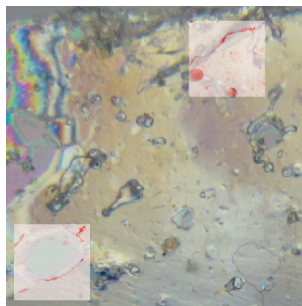


(b) Br

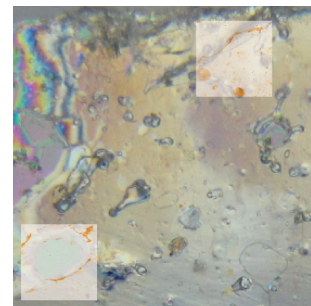
(c) Sr



(d) Cl



(e) K



(f) Ca

Figure 4.20: Comparison of XRF elemental maps to a horizontal thin section (tick marks are spaced at 1 mm intervals). Two regions that were likely scanned from the 150-cm sample of the Iceberg Site core were located and are highlighted in the first panel. The following five panels are blowups of those two regions with the Br, Cl, K, Ca, and Sr XRF maps overlaid on top. The grain boundaries detected in the Cl, K, and Ca maps seem to match well with the grain boundaries visible from the horizontal thin section. Br and Sr maps appear to be detecting features from deeper within the sample.

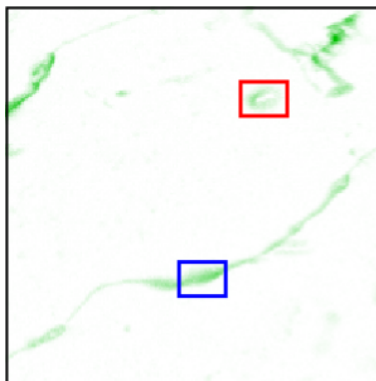


Figure 4.21: Two features of interest from the Cl XRF map. The sample is from a depth of 150 cm in the Iceberg Site ice core. The small circular shape in the middle is highlighted in red, while the second encompassing a portion of the grain boundary is shown in blue.

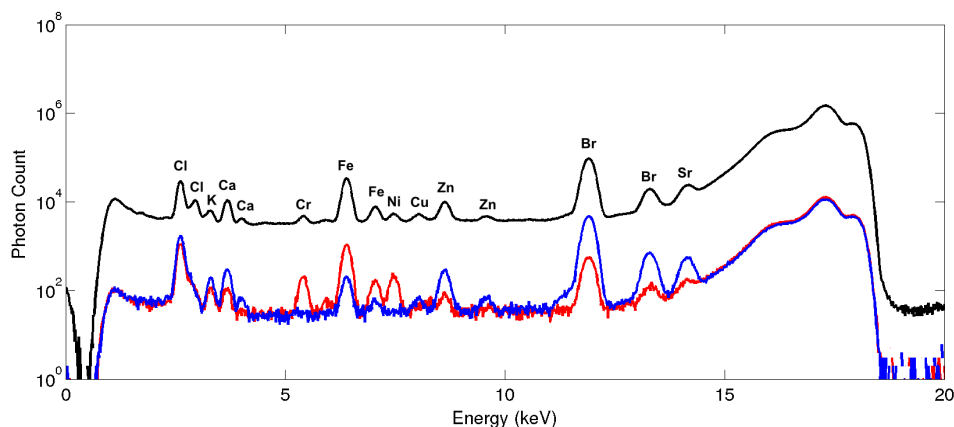


Figure 4.22: XRF x-ray spectra for the 150-cm sample of the Iceberg Site core (black) and two features of interest. The circular shape identified in Fig. 4.21 is shown in red and the grain boundary selection is shown in blue. Note that because the blue and red regions are integrating over a smaller region than the full $2 \text{ mm} \times 2 \text{ mm}$ region shown in Fig. 4.21, they have a lower baseline than the full spectrum shown in black.

sea ice structure that different elements can elucidate. Throughout the bulk of all ice cores, salts tended to be concentrated in sets of parallel lines spaced roughly 0.5 mm apart, which corresponds to the spacing of lamellae in the skeletal region during initial ice growth. Variations from this structure were found primarily near the top of each core where frazil ice is present, and at the very bottom of each core. Thus, results from this study demonstrate that the initial spatial distribution of salts remains mostly intact. Calibration of the Br elemental maps showed bulk concentrations to be $5 - 10 \text{ g/m}^3$, with concentrations

ten times larger found in the brine layers.

By enclosing the experimental setup in a helium environment, it was possible to also map the location of lighter elements. XRF elemental maps showed co-location of Br and Sr, as well as co-location of Cl, K, and Ca. This is most likely due to differences in the penetration depth for each element, where the Br and Sr fluorescence signal is from the top 3 – 5 mm, while the signal from Cl, K, and Ca is only from the top 100 μm . This enables the simultaneous identification of different features in the sea ice microstructure. Through comparison with horizontal thin sections, we could verify surface linear features in the Cl, K, and Ca maps were indeed grain boundaries. Br and Sr elemental maps identified deeper features, such as brine layers. Finally, by examining the fluorescence signal for particular trace metals, it is possible to isolate particular features that are likely dust and sediment particles entrapped in the sea ice.

ANALYZING BRINE CHANNEL MORPHOLOGY USING X-RAY MICRO-COMPUTED TOMOGRAPHY

Lieb-Lappen, R. M. , Golden, E. J., and Obbard, R. W. Metrics for interpreting the microstructure of sea ice using x-ray micro-computed tomography, *Cold Reg. Sci. Technol.*, in review, 2015.

Abstract

As the character and dynamics of sea ice change in a rapidly changing climate, it is critical to have a detailed understanding of the fine microstructure of sea ice. Advances in x-ray micro-computed tomography (μ CT) technology have enabled non-destructive three dimensional analysis of the brine channel morphology with resolution down to several microns. In this study, we examine six ice cores collected from the Ross Sea, Antarctica. Metrics were developed to describe the shape, size, and topology of the brine channels and air pockets in sea ice. A cubic sub-sample measuring 3.75 mm on edge was found to be the representative elementary volume for sea ice μ CT analysis with these metrics. All samples were observed to have vertically oriented cylindrical brine channels, with increased branching and connectivity observed at lower depths. The highest degree of vertical anisotropy was detected through the bulk middle, with increased variability near the top and bottom of each core. Air pockets were found to be mostly spherical in shape, except vertically elongated in multi-year ice.

Introduction

The use of X-ray micro-computed tomography (μ CT) has exploded over the last decade due to rapid advances in instrumentation technology and accessibility (Ketcham and Carlson, 2001; Stock, 2008). In fact, there are currently over 15 manufacturers producing commercial laboratory sized μ CT systems in addition to the specialized synchrotron radiation source μ CT systems available (e.g. Advanced Photon Source [APS] at Argonne National Laboratory, Swiss Light Source [SLS], European Synchrotron Radiation Facility [ESRF]) (Stock, 2008). The primary advantage of μ CT is that it provides a non-destructive three-dimensional visualization and characterization of the internal features of multiphase and porous materials with spatial resolution down to several microns. Once the phases of a given material have been segmented, the analysis of the μ CT data then produces quantitative measurements on topology and structure of the material. This has natural applications for describing microstructure mathematically and modeling microstructure-dependent properties of different porous media in fields varying from sedimentary rock and sea ice (e.g., Golden et al., 2007; Obbard et al., 2009a) in the geosciences to bone analysis in biology (e.g., Campbell et al., 2007) to engineered composite materials (Naik et al., 2006).

μ CT utilizes the fact that phases of different composition and density have varying absorption and transmission of x-ray radiation. Through the photoelectric effect, heavier elements are significantly more absorbing of x-rays than lighter elements, allowing separate phases to be differentiated (Ketcham and Carlson, 2001). Since sea ice consists primarily of three phases (ice, brine, and air) with quite different compositions, it is well suited for μ CT structural analysis.

The use of cooling stages has permitted μ CT to be used to study the pore structure of cryospheric samples such as snow (e.g., Chen and Baker, 2010; Wang and Baker, 2013) and firn (e.g., Freitag et al., 2004; Gregory et al., 2014; Lomonaco et al., 2008; Schneebeli and

Sokratov, 2004). Pringle et al. (2009) analyzed CsCl-doped laboratory-grown sea ice and observed changes in brine channel connectivity at varying temperatures. Results supported percolation-theory predictions of critical anisotropic connectivity thresholds (Golden et al., 2007; Pringle et al., 2009). More recently, methods for and which involved analyzing field-collected sea ice have been developed (Maus et al., 2009, 2013; Obbard et al., 2009a). Maus et al. (2009) developed methods using synchrotron μ CT by first centrifuging samples and storing at sub-eutectic temperatures. Although this protocol could not distinguish between closed, brine-filled pores and ice, the open porosity was removed of liquid and thus, less-likely to be altered during storage and transport (Maus et al., 2009). Further work with this method provided insight into pore size distribution, permeability, and applications to modeling oil entrapment, although no critical percolation threshold was observed (Maus et al., 2013). The work in this study builds off of the methods developed by (Obbard et al., 2009a) further developing segmentation methods and then developing metrics for quantifying the microstructure of sea ice. Here we present considerations, protocols, and metrics that are critical for this analysis. To demonstrate the methodology, we use results from natural first-year and multi-year sea ice cores, and also examine issues of spatial variability and representative volumes.

Methods

Sample Preparation

Sea ice cores were collected in October - November 2012 from six different locations in the Ross Sea, Antarctica, as was shown in Fig. 2.1. The first two sites, named Butter Point and Iceberg Site, were located on first-year ice about 5 km from the open ocean at distances of 35 km and 55 km from the Ross Ice Shelf, respectively. The measured thickness of the ice at these two locations were 1.78 m and 1.89 m, respectively. The next three sites were also on first-year ice and located on a transect at distances of 6, 12, and 18 km southeast from the ice edge, with thicknesses of 1.70, 1.80, and 1.82 m, respectively. To compare

the microstructure of first-year sea ice to multi-year ice, an additional ice core measuring 1.96 m in length was extracted 700 m off-shore from Scott Base, Ross Island. All sea ice cores were transported at a constant temperature of $-20\text{ }^{\circ}\text{C}$ back to Thayer School of Engineering’s Ice Research Laboratory at Dartmouth College and stored in a $-33\text{ }^{\circ}\text{C}$ cold room. μCT analysis was then completed on cubic sub-samples measuring 1.5 cm on edge that were extracted every 10 cm along the length of each ice core.

Scanning

The components of a μCT system are an x-ray source, sample stage, a scintillator, and a photo detector. For this work, we used a Skyscan 1172 μCT scanner that uses a sealed microfocus x-ray tube with a spot size of $5\text{ }\mu\text{m}$ to produce a fixed conical, polychromatic x-ray source. In order to choose the accelerating voltage for the x-ray source, it is helpful to know the expected absorption of the specimen, and ensure minimum transmission does not drop below 20%. For 30 kV x-rays, the mass attenuation coefficient for water/ice is $0.3756\text{ cm}^2/\text{g}$, while for 40 kV x-rays it is $0.2683\text{ cm}^2/\text{g}$ (Hubbell and Seltzer, 1995). Since sea ice has an approximate density of $900\text{ kg}/\text{m}^3$ (Hutchings et al., 2015; Timco and Frederking, 1996), this leads to linear attenuation coefficients of $\mu = 33.804\text{ m}^{-1}$ and $\mu = 24.147\text{ m}^{-1}$ for 30 kV and 40 kV x-rays, respectively. The resulting x-ray transmission is expressed by the Beer-Lambert law:

$$I = I_0 e^{-\mu x} \quad (5.1)$$

where I_0 is the initial beam intensity, μ is the linear attenuation coefficient, and x is the distance traveled. Since $x \approx 0.015\text{ m}$ for all samples, roughly 40% of the x-ray signal is attenuated for 30 kV x-rays and 30% of the x-ray signal is attenuated for 40 kV x-rays. Ice cores collected from Butter Point, Iceberg Site, and Scott Base were scanned at an accelerating voltage of 40 kV and a current of $100\text{ }\mu\text{A}$. By increasing the accelerating voltage to 40 kV with a current of $250\text{ }\mu\text{A}$ for samples from the transect cores, we were able to reduce acquisition time, while maintaining adequate contrast. A test sample was

run at both settings, and by implementing appropriate segmentation as discussed below, we showed that differences between the two scans were negligible.

Each sample was frozen onto a Peltier thermoelectric cooling stage that could maintain it at $-20\text{ }^{\circ}\text{C}$. Each sample was then rotated 180° about its vertical axis in 0.7° steps, and the transmitted x-rays were imaged at each step. The geometry and spot size of the x-ray source determines the acquisition time required and the spatial resolution of the scan (Landis and Keane, 2010). For the setup used in this work, the resulting scan time was approximately 20 min and the voxel size was $15\text{ }\mu\text{m}$.

The final step of the scanning process is detecting the x-rays that pass through the specimen after each rotational step. The x-rays strike a scintillator screen that converts the x-rays into visible light photons that are then detected by a camera (Landis and Keane, 2010). Our Skyscan 1172 scanner utilizes a 1.3 Mp (1280×1024) cooled Hamamatsu CCD camera fiber-optically coupled to the scintillator. For each rotation step, a single projection radiograph is produced with 4096 (12-bit) brightness graduations. An example projection radiograph was shown in Fig. 2.8. Each day, prior to using the scanner, it is critical to normalize the detector by collecting a uniform dark and white signal. The exposure time is adjusted to ensure that the beam intensity is 50 – 70% without the flat field correction. When scanning at 30 kV the exposure time was 2662 ms, while at 40 kV the exposure time was reduced to 847 ms.

Reconstruction

The next step of the μCT process is tomographic reconstruction of the projection radiographs into two-dimensional gray-scale slices stacked in the z-direction. First, the dark-field image acquired with no x-rays present is subtracted from each projection radiograph. Then, each radiograph is divided by the white-field or “flat-field” image, which is acquired with the x-rays on but no specimen present. For a given rotation angle, the radiographs represent a line integral of the x-ray photons not attenuated. Skyscan’s NRECON reconstruction software was used to solve the inverted Radon transform, which

transforms the x-ray projections using a modified Feldkamp cone-beam algorithm to produce a stack of gray-scale cross-section images. During the reconstruction step, each voxel is assigned a value on an arbitrary scale known as CT values or Hounsfield Units (HU). A correspondence to linear attenuation coefficients and density can be made by using a calibrated scale with water equal to 0 HU and air equal to -1000 HU (Ketcham and Carlson, 2001). For all samples in this study, linear attenuation coefficient endpoints of 0 to 0.07 were chosen to encompass the range of HU/CT values encountered, thereby enabling the conversion of each voxel into a standard 0 – 255 gray-scale.

μ CT analysis is limited by anything that reduces the ability to set proper and consistent thresholds during segmentation. Thermal drift of the x-ray source during imaging, one such factor, was corrected by taking several extra projection radiographs spaced 45° apart. These post-analysis images are then compared to the original radiographs to determine the degree of thermal drift. Ring artifacts arise in the gray-scale image as a result of shifts in the output of individual detectors (Ketcham and Carlson, 2001). These shifts are often due to factors such as changes in temperature or beam strength, and result in anomalous values occurring in a ring centered on the rotational axis because the artifact effects each projection image. Ring artifacts were removed in the image post-processing by subtracting out the anomalous values for the compromised detector prior to reconstruction. Beam hardening is the most common artifact in images, and is the result of low energy x-rays preferentially being attenuated as they pass through the specimen (Ketcham and Carlson, 2001). Thus, the mean x-ray energy observed at the center of the specimen is greater than that observed near the edges. This results in the middle appearing darker than expected and edges appearing brighter. Since the degree of beam hardening was relatively small for this work, post-processing correction was sufficient and the use of filters during imaging was not necessary.

Voxels that represent partial volumes of different phases present challenges during thresholding as a voxel is generally assigned to a single phase. The observed gray-scale

value represents an average of the phases present. Regardless of the resolution of the μ CT, partial volume effects will lead to a blurring of boundaries to some degree (Ketcham and Carlson, 2001). To reduce some of the noise in an image and help with boundary effects, pixels were smoothed based upon neighboring pixels using a Gaussian kernel.

Once image post-processing was completed, a interior cubic volume of interest (VOI) measuring 7.5 mm on each edge was selected from the center of the scanned volume. Morphometric analysis on the VOI was completed using Skyscan's CTAn software package. By defining an interior VOI, we avoid microstructural damage due to sample preparation.

The critical step in the entire μ CT process is thresholding the gray-scale images to set the boundaries of individual phases, since this dictates all subsequent qualitative and quantitative measurements. Because sea ice is a three-phase media, the desired output is a trinary image with separate thresholds for ice, brine, and air. Trinary images are often best segmented through the use of multiple binary images as was shown in Fig. 2.9. If enhanced contrast is required for segmentation, trinary images can be improved by doping a phase with an ion containing a strong absorption edge, as has been done using KI in soil systems (Costanza-Robinson et al., 2008) and CsCl in laboratory-grown sea ice Golden et al. (2007); Pringle et al. (2009). In this technique, duplicate scans are done using X-ray energies above and below the absorption edge. This technique is best used with a synchrotron radiation source where monochromatic radiation and highly tunable x-ray energies are available. It was not required for proper segmentation of images here.

Slight adjustments to the critical threshold values for a given phase can lead to significant differences in measured microstructural quantities. For example, Tarquis et al. (2009) used four different threshold values on a binary image to analyze the fractal dimension of soils, and noticed that although general trends did not change, measured values for porosity and fractal dimension varied significantly with the threshold level set (Tarquis et al., 2009). Thresholding can either be done manually by the user or through

automated algorithms. Manual thresholding requires that the user compare binarized and gray-scale images thoroughly until a proper threshold value is set. Naturally, this method is subject to user bias and variability between different studies.

A variety of automated thresholding algorithms exist to remove the human element (e.g., clustering-based methods, the Otsu method, entropy-based methods, spatial methods examining neighboring voxels, inverse methods incorporating multiple thresholds) (Batenburg and Sijbers, 2009; Baveye et al., 2010). For this study, we successfully utilized a histogram shape-based approach that sets thresholds by examining the histogram of gray-scale values and identifies certain features, such as the minimum value between two peaks. The histograms in this study exhibited well-defined inflection point at phase transitions, as was shown in Fig. 2.10, enabling clear thresholding of phases. Since the same thresholds were to be used for all samples analyzed, the histograms of several representative samples were first examined, and average optimized values for each of the three phases were selected.

Metrics for Microstructural Analysis

The data output from μ CT is both qualitative and quantitative, with each providing complementary information useful in characterizing the internal structure of the porous media. Qualitatively, software programs allow the user to visualize the full three-dimensional features of both the object and the pore structure as is shown in Fig. 5.1. This software enables visualization of brine channel size via color-coding as shown in the right panel of Fig. 5.1. Quantitatively, the user is provided with both two- and three-dimensional data that provide information regarding definition, shape, and connectivity for each phase. For a three-phase media such as sea ice, each phase is isolated and then analyzed separately to provide a full quantitative description of the microstructure. Prior to analysis, objects measuring less than 25 voxels, or $8.4 \times 10^{-5} \text{ mm}^3$, are discarded as noise. Then, once thresholds have been set to segment each phase, simple voxel summations provide volume,

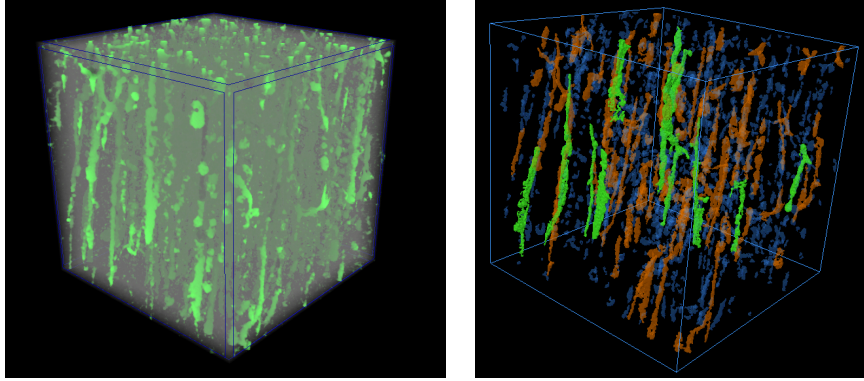


Figure 5.1: Three-dimensional visualization of sea ice with brine channels of a cubic VOI measuring 7.5 mm on each edge. Left panel shows all brine channels in green shown in green. The right panel color codes brine channels by size, where channels greater than 0.0337 mm^3 are colored green, channels between 0.0067 mm^3 are colored orange, and brine channels less than 0.0067 mm^3 are blue.

porosity, surface area, and specific surface area.

A variety of parameters exists to describe the shape of each phase. First, the structure model index (SMI) provides a measure of surface convexity and the plate-like/rod-like architecture of a given phase. The entire surface of each object is dilated by one pixel, and the resulting surface area is calculated. SMI is defined as $SMI = 6 \left(\frac{S' \times V}{S^2} \right)$, where S' is the space derivative of the change in surface area (units of length), V is the initial volume, and S^2 is the surface area prior to dilation. For benchmarks, SMI values of 4, 3, and 0, represent spheres, cylinders, and plates, respectively.

The structure thickness is an alternative metric for the size of an object that provides a measurement of the average object width. For each voxel in a given phase, the diameter of the largest sphere that encompasses the voxel, yet is entirely inscribed within the object is calculated. The structure thickness is then given as the mean diameter over all voxels. The structure separation is the inverse metric, providing a measurement on the spacing between individual objects. The same calculation as for structure thickness is completed, but for the non-object (i.e. pore) phase. The fractal dimension provides a measure of the dimensionality of an object, with non-integer values indicative of an object with fractal characteristics. It is calculated using the box counting algorithm, whereby boxes of a

variety of sizes are chosen, and for each size, the number of boxes required to cover the object is counted. When the number of boxes is plotted versus box size on a log-log scale, the slope of the line yields the fractal dimension.

One final metric regarding the phase shape is the degree of anisotropy. First, the mean intercept length is calculated by sending a line through the three-dimensional image, and dividing the length of the line by the number of intersections with the given phase. This process is repeated for a large number of line directions in three-dimensions. A polar plot encompassing all the mean intercept lengths is created by creating an ellipsoid with boundaries defined by the mean intercept length for each direction. Any given ellipsoid can be characterized by a matrix, and the eigenvalues for this matrix are calculated, which correspond to the lengths of the semi-major and semi-minor axes. The ratio of the smallest to the largest eigenvalues then provides a metric for the degree of anisotropy. A relative degree of anisotropy is then expressed on a 0 – 1 scale (0 is completely isotropic and 1 is completely anisotropic) through the equation:

$$DA = 1 - \frac{\lambda_3}{\lambda_1} \quad (5.2)$$

where λ_1 and λ_3 represent the largest and smallest eigenvalues, respectively.

To have a full understanding of the internal structure and of properties such as permeability, it is helpful to have an understanding of the topology and connectivity of a given phase. The Euler number $\chi(x)$ in topology provides such a metric, where $\chi(x) = \beta_0 + \beta_1 + \beta_2$ and β_0 , β_1 , and β_2 are the three Betti numbers. These define the number of objects, the connectivity, and the number of voids within objects, respectively, where the connectivity represents the number of connections that need to be severed before an object becomes disconnected (i.e. separated into two objects). The Euler number is useful in comparing connectivity of different objects as it is a topologically invariant metric. By utilizing all of these metrics for all three phases, it is possible to have a full quantitative

description of the internal microstructure of sea ice using μ CT.

Results

The brine, air, and ice phases for all sub-samples scanned were analyzed using the metrics described above. It should be noted that the phases are co-dependent, and therefore trends observed with a metric for a particular phase will be reflected in the other phases. For example, if there is a high brine volume fraction, the ice volume fraction by definition will be decreased. Thus, the following analysis focuses on a select number of metrics with a primary emphasis on the brine phase as it is the critical phase in determining sea ice microstructure. All samples were scanned at -20 °C, while actual in-situ temperatures varied from -2 °C at the ocean interface to between -14 °C and -18 °C at the top of the ice core. Although in-situ brine volume fractions would be greater than those measured here, the general shape and morphology of the brine network is still reflected at the colder temperature used for transport, storage, and scanning. Further work on analyzing the temperature sensitivity detected by μ CT is ongoing.

Brine

Figures presenting the definition and shape of the brine phase for all six cores are shown in Fig. 5.2. The brine volume fraction was generally less than 5%, with slightly higher fractions near the top of the core. The specific surface area increases from the top to the bottom of each core, with values relative consistent across all cores. The SMI for the brine phase was roughly 3 for all depths in all cores, indicative of a cylindrical shape, although there was more variability near the very top and bottom of each core. Structure thickness and separation were only calculated for the Butter Point, Iceberg Site, and Scott Base ice cores. For these cores, brine channels become slightly narrower deeper in the core as can be seen by a decreasing structure thickness and increasing separation with depth. The fractal dimension of the brine channels in all cores was roughly 2. The degree of anisotropy for the brine channels was greatest in the middle of each core, with values relatively similar

across the six cores as can be seen in the right panel of Fig. 5.3. The connectivity of the brine channels was quite varied, although exhibited a decreasing trend with depth as shown in Fig. 5.4. Several of the cores had a spike in connectivity at a single depth (e.g., depth of 90 cm for the Scott Base core, depth of 50 cm for the 12 km transect core), which often corresponded with a layer of small ice grains or at the transition from frazil to columnar growth, as observed under cross-polarizing lenses. However, when subtracted from the sum of the number of objects and cavities to yield the Euler number, the result was a relatively constant value of roughly 1000, except near the very top and bottom of the cores.

Air

For the first-year sea ice cores, the air phase represented less than 1% of the VOI and air pockets were generally spherical with an average SMI of slightly under 4 (Fig. 5.5). The multi-year ice core extracted near Scott Base had significantly more air bubbles, particularly near the top of the core, although many of these air bubbles were likely drained brine channels. The shapes of these air bubbles were also quite different, exhibiting more plate-like shapes with an average SMI of 0.8. The specific surface area of the air bubbles was similar to the brine channels, and also increased with depth in the core. The air bubble structure thickness and structure separation were relatively constant throughout the cores, with one notable exception of larger air bubbles at a depth of 50 – 60 cm in the Scott Base ice core. The fractal dimension of the air bubbles was also roughly two, but had more variability than did the brine channels. Like the brine channels, the air bubbles had increased degree of anisotropy in the vertical direction throughout the middle of each core, as is shown in the left panel of Fig. 5.3. The order of magnitude was similar to the brine channels as well, except for the Scott Base ice core, where the degree of anisotropy indicated nearly purely anisotropic air bubbles consistent with the hypothesis that these were drained brine channels.

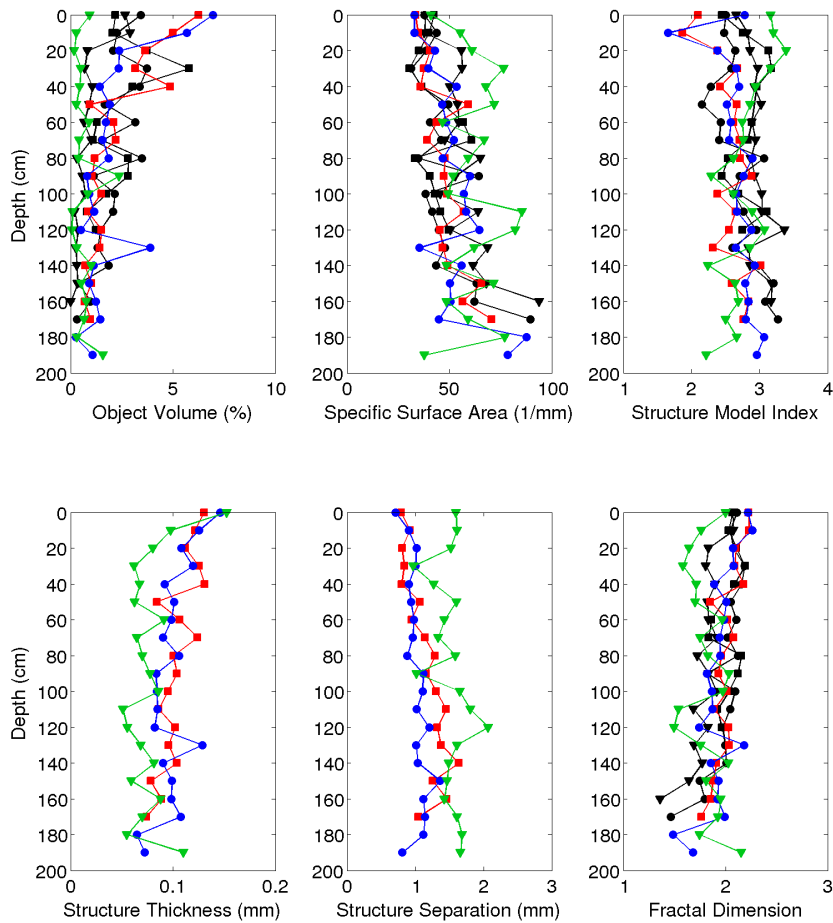


Figure 5.2: μ CT metrics for analyzing the definition and shape of brine channels. The red squares, blue circles, and green triangles represent the Butter Point, Iceberg Site, and Scott Base cores, respectively. The black squares, circles, and triangles show the data for the three cores along the transect at distances of 6, 12, and 18 km from the ice edge, respectively.

Ice

The ice phase fills nearly the entirety of each sample, with slightly smaller amounts at the top and bottom of each core. Figures illustrating the definition and shape of the ice phase are given in Fig. 5.6. The specific surface area was over an order of magnitude less than that of the air bubbles and brine channels. The precise values for SMI cannot be compared to the reference values for objects that occupy over half the VOI, because for

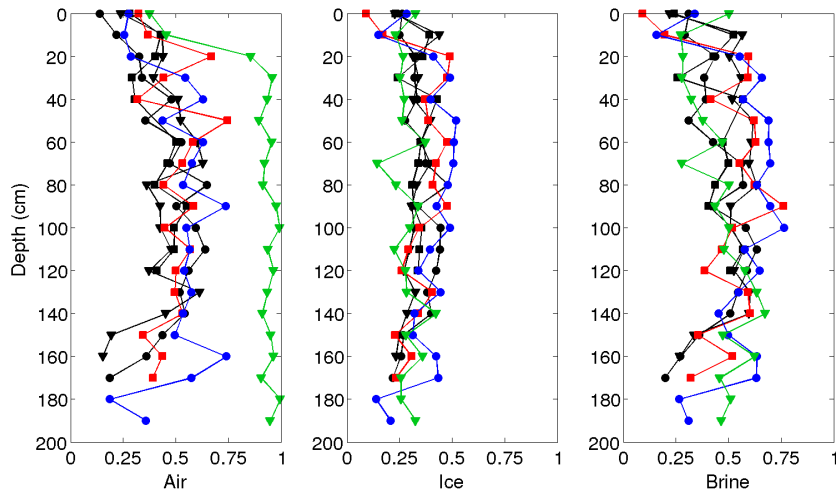


Figure 5.3: The degree of anisotropy for the air, ice, and brine phases. The red squares, blue circles, and green triangles represent the Butter Point, Iceberg Site, and Scott Base cores, respectively. The black squares, circles, and triangles show the data for the three cores along the transect at distances of 6, 12, and 18 km from the ice edge, respectively.

these large objects, the number of concavities force the SMI to become negative. However, the relative trend of decreasing SMI with depth illustrate the increased prevalence of these concavities at deeper depths. As expected, the structure thickness of the ice phase was an order of magnitude larger than for air bubbles and brine channels, with an average value of 1.0 mm. The fractal dimension of the ice phase at all depths matched the expected value of three for all cores.

Spatial Variability

To assess spatial variability, triplicate sub-samples were extracted from each depth and scanned for the Butter Point, Iceberg Site, and Scott Base cores. The percent object volume varied by less than 5% for all three phases for all sub-samples. Further, on average the specific surface area, SMI, structure thickness, structure separation, and degree of anisotropy varied by less than 5%. The fractal dimension values varied by less than 1% on all sub-samples. The only metrics with increased variability was Euler number and connectivity, which varied by approximately 15% for the brine channels. With such low measured variability, triplicate samples were not scanned for the three transect cores.

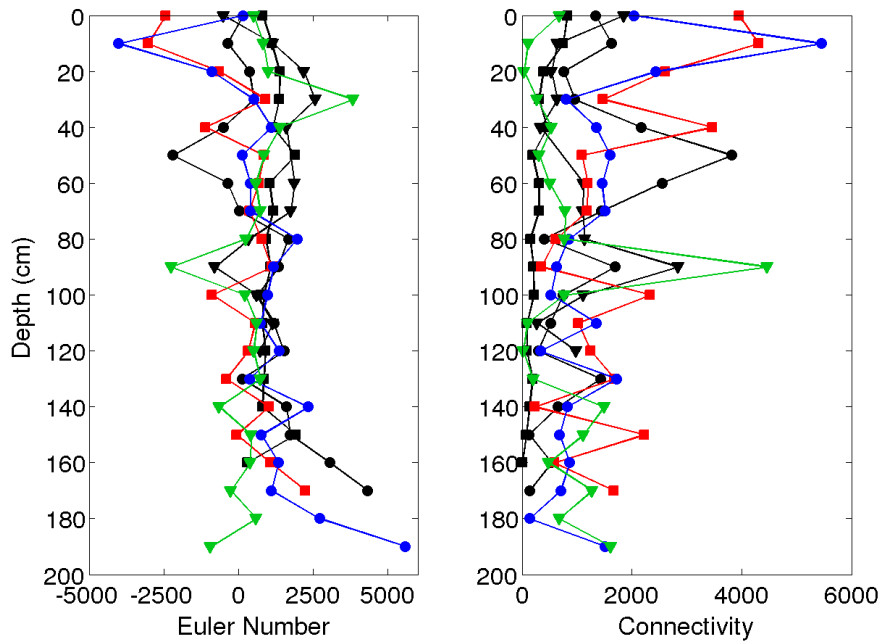


Figure 5.4: The Euler number and degree of connectivity of the brine channels. The red squares, blue circles, and green triangles represent the Butter Point, Iceberg Site, and Scott Base cores, respectively. The black squares, circles, and triangles show the data for the three cores along the transect at distances of 6, 12, and 18 km from the ice edge, respectively.

Prior to drawing conclusions from metrics obtained from μ CT, it is imperative to know the representative elementary volume (REV) for each metric. Following the methodology of Costanza-Robinson et al. (2011), we selected 13 different sized cubic VOIs, measuring 0.30, 0.60, 0.90, 1.20, 1.50, 1.88, 2.25, 2.63, 3.00, 3.75, 4.50, 6.00, and 7.50 mm on an edge. A given metric is expected to fluctuate for smaller VOIs, eventually converging upon a representative value as the VOI size reaches the REV. For each of the metrics presented above, the measured value for each phase was plotted as a function of VOI size. The resulting plots for specific surface area and structure thickness are shown in Fig. 5.7. As can be seen, this analysis yielded a REV for VOIs measuring 3.75 mm on an edge for all three phases on both metrics. This REV was consistent with that calculated for the other metrics, and thus, it was determined that the VOI measuring 7.5 mm on edge used in this study was sufficiently large.

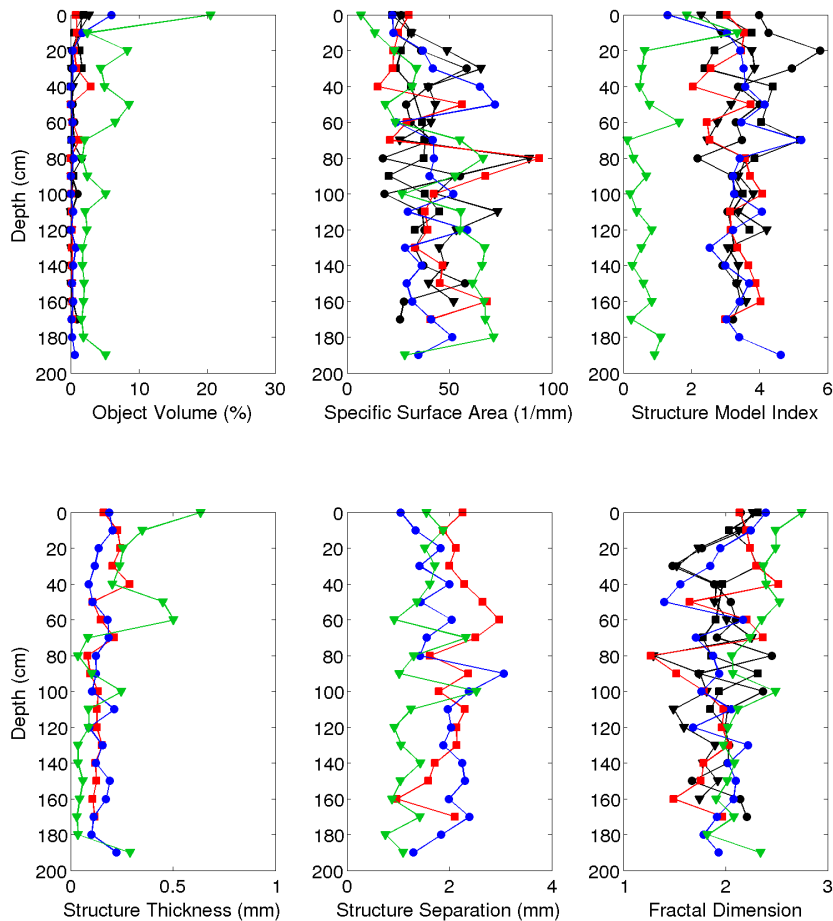


Figure 5.5: μ CT metrics for analyzing the definition and shape of air pockets. The red squares, blue circles, and green triangles represent the Butter Point, Iceberg Site, and Scott Base cores, respectively. The black squares, circles, and triangles show the data for the three cores along the transect at distances of 6, 12, and 18 km from the ice edge, respectively.

In addition, a single oversize scan was completed, albeit without the cooling stage due to height restrictions, for a larger rectangular prism sub-sample measuring 5 cm in height and 2 cm in width and length. Due to the larger size, the image resolution was reduced to 25 μ m. For comparison, 5 non-overlapping VOIs measuring the same 7.5 mm on edge were selected from within the larger sample, and the variability for each metric was analyzed. For the ice phase, the spread for most metrics was between 10% – 20%, with percent object

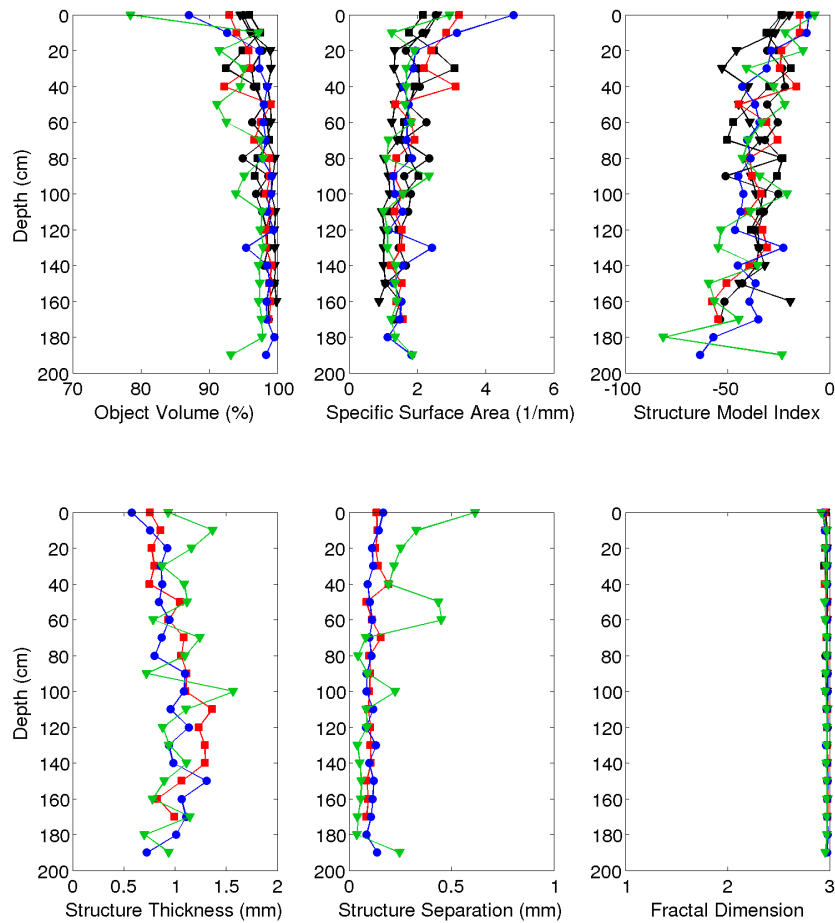


Figure 5.6: μ CT metrics for analyzing the definition and shape of the ice phase. The red squares, blue circles, and green triangles represent the Butter Point, Iceberg Site, and Scott Base cores, respectively. The black squares, circles, and triangles show the data for the three cores along the transect at distances of 6, 12, and 18 km from the ice edge, respectively.

volume and fractal dimension having variability of less than 1%. The brine phase varied 10% – 40%, except for fractal dimension which varied by 4%. The air phase varied the most, with most metrics varying between 30% – 60%. As the phase with the smallest objects, the air phase was likely most effected by the reduced resolution. The mean values were then compared to both the full scan measurements and the results from the nearest collected sample that was scanned at 15 μ m resolution. In general, the mean value differed

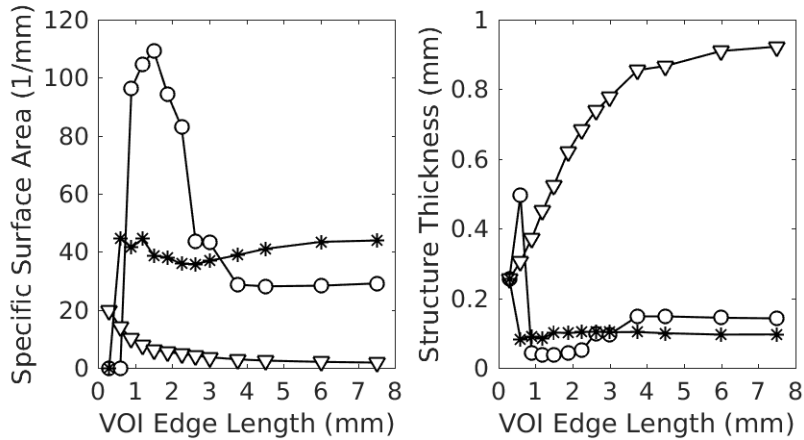


Figure 5.7: Analysis for calculating the representative elementary volume (REV) for specific surface area (left) and structure thickness (right). The open circles, open triangles, and stars represent the air pockets, ice, and brine channels, respectively.

by less than 5% from those calculated on the entire oversized scan, except for degree of anisotropy, which differed by 10% in the air phase. When the mean value for the samples scanned at 25 μm was compared to the sample scanned at 15 μm , the disparity between the two scans became evident. Differences were close to 50% disagreement for at least one phase on almost every metric, indicating that the poorer resolution had a significant effect on morphometric analysis.

Temperature Sensitivity

Although analysis of the temperature sensitivity of measured values remains ongoing, an initial sub-sample was studied to establish a lower-bound estimate. A single sub-sample from the top of the Butter Point ice core was scanned at its in-situ temperature of $-16\text{ }^{\circ}\text{C}$ and compared to the scan completed at $-20\text{ }^{\circ}\text{C}$. The brine volume fraction increased from 6.2% to 10.0% and the air volume fraction increased from 0.78% to 0.88%, and thus, the ice fraction decreased from 93.0% to 89.1%. This resulted in less than 5% change in the air phase for specific surface area, SMI, structure thickness, and connectivity. Structure separation and Euler number in the air phase changed by 24% and 36%, respectively. The brine phase specific surface area, structure thickness, and structure separation, and connectivity changed by 10% – 15%, while the SMI was only affected by 4.6%. The ice

phase changed by 20% – 30% for specific surface area, SMI, and structure thickness, while the structure separation and connectivity changed by 10% – 15%. The fractal dimensions for all phases was affected by less than 5%. The metric most affected by the change in temperature was the degree of anisotropy, which changed by 36%, 65%, and 75% for the air, ice, and brine phases, respectively.

Discussion

The metrics presented in this study provide a detailed microstructural description of the brine channels, air pockets, and ice of field-collected sea ice. Using an accelerating voltage of 40 kV with a current of 250 μ A provided an optimal balance of short acquisition time while maintaining sufficient image contrast for phase segmentation, and will be the preferred scanning parameters for future analysis. In comparison to prior μ CT analysis on laboratory-grown sea ice by Pringle et al. (2009), we have improved the voxel size to 15 μ m, increasing the ability to accurately define phase boundaries. Pringle et al. (2009) used targeted thresholding to matched expected values for porosity in determining phase boundaries, while the increased resolution presented here eliminates the need for prior knowledge or estimates. Additionally, the methodology developed by Obbard et al. (2009a) and used in this study does not require centrifuging samples, which eliminates the brine phase in open pores, while leaving it in closed pores.

The temperature sensitivity analysis indicated that, as expected, a four degree fluctuation did significantly alter the brine volume fraction and some of the metrics. However, many of the metrics, such as those describing the morphology of brine channels, saw a smaller degree of variation, suggesting that general shape is retained over some temperature fluctuation. Future work will include analyzing samples at in-situ temperatures to better quantify the importance of temperature.

The brine channels in all cores studied showed the expected cylindrical shape, with increasing surface area deeper in the core. This is likely due to a higher degree of branching

in the warmer ice deeper in the core. The increased branching was also detected by increased connectivity at lower depths. The high degree of anisotropy through the bulk middle of the core is likely a result of brine channels sandwiched between columnar ice growth. Increased variability near the top of each core, particularly in shape as exhibited by SMI, can be attributed to the frazil ice region.

Air pockets represented the smallest volume fraction phase and were mostly spherical in shape, except in the multi-year ice core collected at Scott Base where they were elongated in the vertical direction. This may be the result of diffusion driven by surface heating, or these features may be previous brine channels that had drained as the ice pack experienced seasonal temperature fluctuations and flushing events. Air pockets across all cores however, were relatively consistent in volumetric size. Since the ice phase represents nearly the entirety of the sample, the morphological metrics presented here are not as insightful as for the air and brine phases. However, it was observed that the prevalence of concavities increased with depth potentially due to the increased branching of brine channels observed.

Conclusions

This work further established the methodology for analyzing sea ice microstructure using μ CT, and presented results from six Antarctic sea ice cores stored isothermally. Metrics were developed to describe the shape, size, and topology of the different phases in sea ice. It was found that the REV for these microstructural metrics is a cube measuring 3.75 mm on each edge. Vertically oriented cylindrical brine channels were observed with increased branching at lower depths, while measurements of brine channel connectivity detected frazil/columnar transitions, as well as regions with decreased grain size. More work is needed, however, to fully understand the importance of maintaining in-situ temperature during analysis. By providing non-destructive qualitative and quantitative three-dimensional analysis, μ CT is a useful tool for understanding the fine microstructure of sea ice, with potential to add critical details for use in dynamical models of sea ice.

CHARACTERIZING BRINE CHANNELS

Introduction

The detailed microstructure of sea ice is critical in both governing the movement of brine between the ocean and the sea ice surface and controlling processes such as ice growth and decay (Petrich et al., 2006; Thomas and Dieckmann, 2009). As we noted in previous chapters, its complex pore structure influences many of the bulk thermal and electric properties of sea ice. The degree of permeability is of primary interest to a wide range of disciplines (e.g., biology and atmospheric chemistry) as it controls fluid flow through sea ice. In Chapter 1, we introduced the “Rule of Fives”, which provides a guideline for describing the percolation threshold in first-year columnar sea ice. Specifically, the ice becomes permeable to fluid transport at brine volume fractions greater than 5%, which is found in ice at about $-5\text{ }^{\circ}\text{C}$ with a salinity of about 5 parts per thousand (Golden et al., 1998). Although this rule of thumb is helpful in describing and modeling basic phenomenon, it does not fully capture the spatially and temporally evolving details of the sea ice microstructure. Here we provide a more topologically complete characterization of the morphology of the sea ice pore structure.

Previous research has recognized the importance of thermally activated percolation thresholds in sea ice research (e.g., Cox and Weeks, 1975; Golden et al., 1998; Thomas and Dieckmann, 2009; Weeks and Ackley, 1982). Pringle et al. (2009) studied single-crystal laboratory-grown ice using μCT to examine the thermal evolution of brine inclusions. They found that brine volume fraction and pore space structure depend upon temperature, with a percolation threshold observed at $4.6 \pm 0.7\%$. One expects natural polycrystalline ice to have a higher threshold as pathways are sensitive to grain boundaries, flaws, and a certain degree of horizontal transport (Pringle et al., 2009). Since different growth rates in natural

sea ice can produce different average spacing between brine layers, there is a potential for varying percolation thresholds and degree of connectivity (Nakawo and Sinha, 1984; Petrich et al., 2006; Pringle et al., 2009).

This chapter will describe in detail the morphology and variability of brine networks in first-year sea ice. We will develop a network model of the pore structure of sea ice and use topological techniques to characterize this brine network. This will yield a set of network statistics that we can later use as details and parameters in more sophisticated models of sea ice. Our framework enables models to statistically replicate the pore structure of sea ice as functions of depth and temperature. Future applications include investigating under what conditions the “Rule of Fives” applies, predicting bulk physical properties such as fluid permeability, and improving the ability to describe processes such as brine drainage and desalination. This approach provides advances in quantifying the brine connectivity in sea ice, which we can then incorporate into both global and regional sea ice models.

Methods

In Chapter 2, we presented six cores from different locations in the Ross Sea, Antarctica that we extracted during the October - November 2012 field campaign. Fig. 6.1 presents temperature profiles for these six cores. The five first-year ice cores had similar profiles, with coldest temperatures (located at the top of the core) dependent upon the day the core was collected, and ranging from $-13.8\text{ }^{\circ}\text{C}$ to $-17.7\text{ }^{\circ}\text{C}$. The multi-year ice core collected near Scott Base was insulated by 1.18 m of snow, and consequently had a smaller temperature gradient. To develop the mathematical brine channel network in this chapter, we will focus on the ice cores extracted from Butter Point and Iceberg site. These cores had temperature gradients of $-16.1\text{ }^{\circ}\text{C}$ to $-2.5\text{ }^{\circ}\text{C}$ and $-17.7\text{ }^{\circ}\text{C}$ to $-2.3\text{ }^{\circ}\text{C}$, respectively. To replicate these conditions, we rescanned each sub-sample from these two cores at its in-situ temperature using a Peltier cooling stage attached to the μCT scanner, and reanalyzed the data following the protocols developed in Chapter 5. However, as we will discuss in

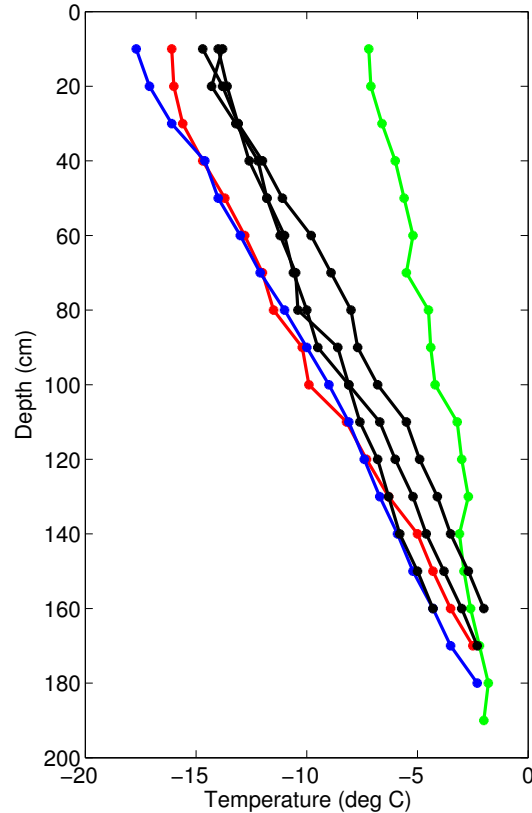


Figure 6.1: Temperature profiles of Antarctic sea ice cores collected during the October - November 2012 field campaign. The red, blue, and green lines represent the Butter Point, Iceberg Site, and Scott Base ice cores, respectively. The three black lines show the three ice cores extracted along the 18 km transect described in Chapter 2.

more detail later, it is likely that the cooling stage did not maintain the ice at the desired temperature for the warmer samples.

Once we imaged the samples by μ CT and processed the data as in Chapter 5, we converted the binarized images depicting the brine phase into a network model. By definition, a network is a collection of nodes and edges connecting the various nodes (Newman, 2011). Scientists and mathematicians use networks in a wide variety of fields to create simple representations of real world systems, from which they can capture critical features and model particular behavior of the system. For example, soil scientists and geologists used network models of pore space to study connectivity and permeability (e.g., Delerue et al., 2003; Pierret et al., 2002). Some of the common algorithms used in creating these networks include maximal ball, medial axis, and flow velocity methods

(Dong et al., 2008; Dwyer, 1993; Silin and Patzek, 2006). Here we use a version of maximal ball where we define the nodes of the network as a collection of points in three-dimensional space $\{p_i = (x_i^*, y_i^*, z_i^*) \in \mathbb{R}^3\}$, with each point assigned a radius/throat size $\{r_i\}$ (Dwyer, 1993; Silin and Patzek, 2006). By setting the network in the spatial setting of \mathbb{R}^3 with z representing the vertical direction, we are prepared to examine questions of brine movement upwards and downwards through the sea ice. We identify the nodes of the network $\{p_i\}$ by examining the binarized horizontal slices and locating the centroids of each two-dimensional connected component in each slice. The centroids are a reasonable approximation since viewed in two-dimensional slices, brine inclusions are primarily convex polygons with the centroid located inside the connected component (see Fig. 4.5) (Heijmans and Roerdink, 1998). We note that each node p_i located at (x_i^*, y_i^*, z_i^*) has a collection of points $\{x_i^j, y_i^j, z_i^j\}$ (where $z_i^j = z_i^*$ for all j) that collectively define the two-dimensional connected component of the brine channel at this z -value. We fit an ellipse to each connected component and we define the length of the semi-minor axis to be the throat size r_i assigned to the respective node p_i . This definition captures both the location and the size of the brine phase at any point in the sea ice. For two nodes p_{i1} and p_{i2} located in adjacent horizontal slices z_{i1}^* and z_{i2}^* (where $z_{i2}^* = z_{i1}^* + 1$), we place an edge between the two if $\{(x_{i1}^j, y_{i1}^j)\} \cap \{(x_{i2}^j, y_{i2}^j)\} \neq \emptyset$. Thus, we are able to depict the vertical connectivity of the brine phase through our definition of edges, while horizontal connectivity is captured within the definition of the node itself and we note that there are no horizontal edges. Since brine channels are primarily vertically oriented with branches splitting both upwards and downwards (Chapter 5), this network definition yields a good model for depicting brine movement. In Fig. 6.2, we illustrate the network definition by showing four two-dimensional slices from a representative sample. In all slices, black represents the air phase, white represents the brine phase, and gray represents the ice phase. Two example ellipses shown in red illustrate the definition of nodes with their corresponding radii. Black dashed lines depict the edge connecting nodes p_{i1} and p_{i2} and a few other representative edges

connecting adjacent nodes. As we will describe in more detail later, these edges represent branches of the brine channel. For each step downwards from a given node, the branch of the brine channel may grow or shrink, split into multiple branches, merge with other branches, remain constant, or stop, all with probabilities dependent upon the given node throat size, depth/temperature, and proximity to other nodes. This network is our basic analytic object and presents a model for the brine pore network, enabling the calculation of all percolation and permeability statistics.

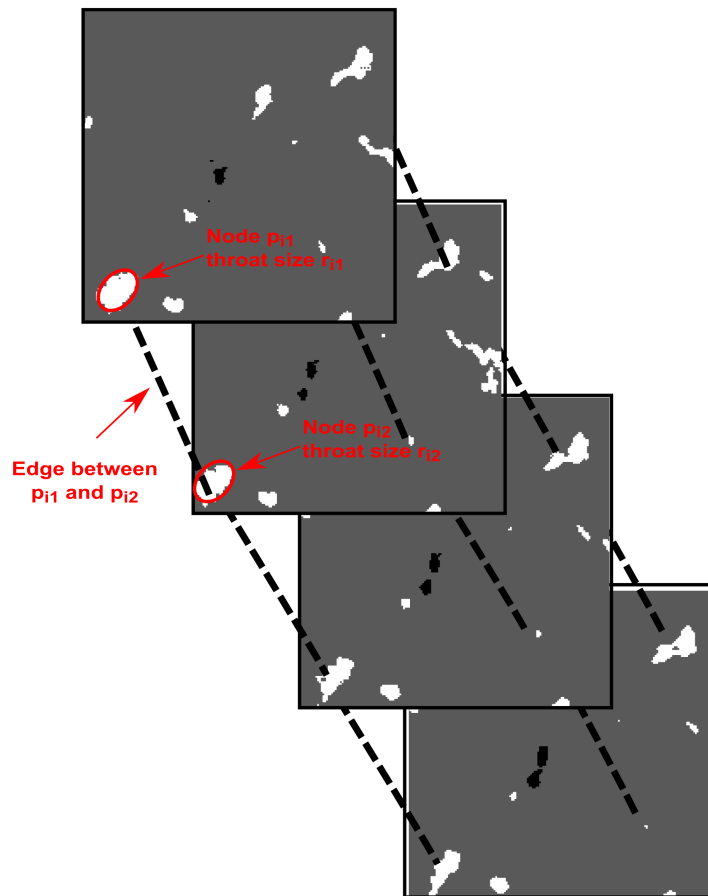


Figure 6.2: Sketch illustrating how the brine channel network is defined. Four horizontal two-dimensional slices are shown with lines connecting adjacent nodes (not all lines are drawn).

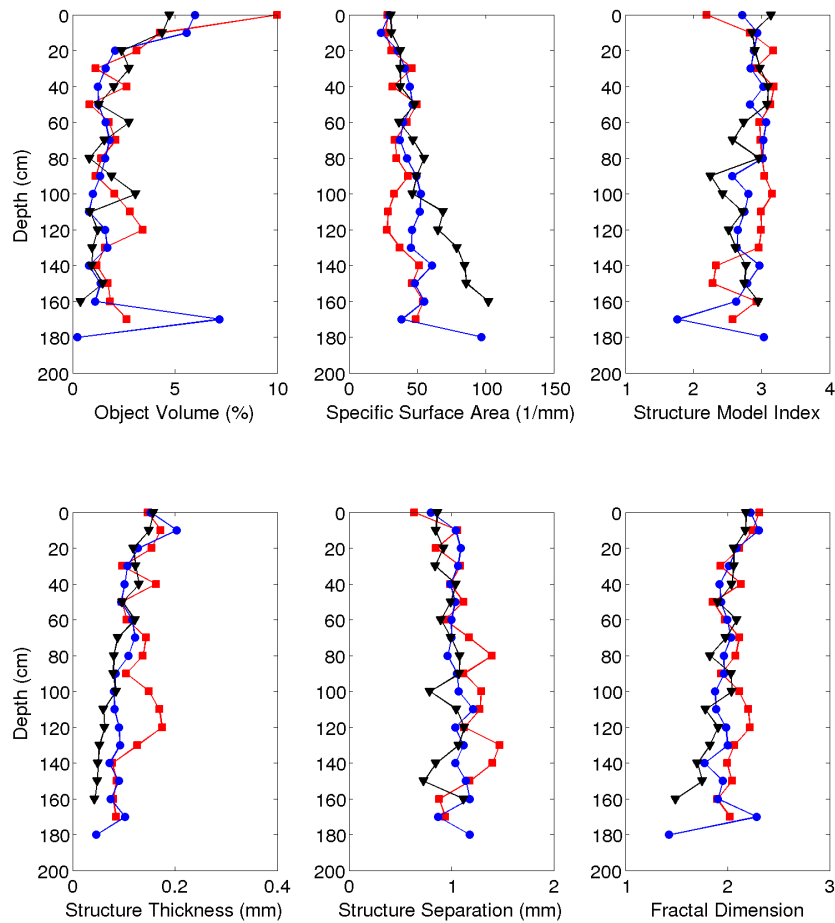


Figure 6.3: Definition and shape of brine channels scanned with a μ CT scanner and a Peltier cooling stage set at in-situ temperatures. The red squares, blue circles, and black triangles represent ice cores from Butter Point, Iceberg Site, and the first of the three cores extracted along the transect shown in Chapter 2, respectively.

Results from Scanning Sea Ice at In-Situ Temperatures

We repeated μ CT scans at in-situ temperatures for the Butter Point, Iceberg Site, and one of the transect cores. Fig. 6.3 shows plots similar to those in Chapter 5 presenting the definition and shape of the brine phase for these three cores rescanned at in-situ temperatures. The behavior in the top half of the core is similar to what we showed in Fig. 5.2, which we expect since the temperature in the top half of the core is relatively

cold and closer to -20 °C. Unlike the isothermal measurements in Chapter 5, however, at around 100 – 120 cm the brine volume fraction begins to increase and the expected c-shape profile begins to appear. Although this trend persists for a few samples, it does not continue as we would expect into the bottom of the core for the warmest temperature samples (see Fig. 6.1). This suggests that perhaps the Peltier cooling stage was not sufficiently warming the temperatures of samples beyond approximately -7 °C. Since the average temperature of the cold room housing the μ CT scanner was roughly -8 °C, either the cooling stage warming mode was not functional or that ambient cooling was faster than heating from the stage below. Thus, we will treat data points at depths below roughly 120 cm with caution, as we will discuss in more detail shortly. The histograms used for μ CT segmentation provide further evidence of insufficient warming of the bottom samples, such as the histogram shown in Fig. 6.4. Relative to the separation of peaks in the histograms for colder samples (see Fig. 2.10), the separation of peaks, particularly for the ice and brine phases, in Fig. 6.4 is less resolved, leading to a higher source of error in the binarized images. This may highlight that the cooling stage is not sufficiently melting the ice, leading to a slush that has x-ray attenuating properties between ice and brine. Segmenting all the slush with the brine phase (assuming it is possible to isolate only the slush from signal noise) leads to an overestimate of the brine phase and an inaccurate depiction of brine channel size and connectivity. Conversely, segmenting the slush with the ice phase leads to an underestimate of the brine phase and also an inaccurate depiction of the brine channels. Thus, we used segmentation thresholds that split the difference as best as possible, recognizing that there was indeed error in segmentation for these warmer samples. Unfortunately, this encompasses the region where the brine volume fraction crosses the 5% critical threshold, limiting the ability to test the “Rule of Fives.”

Since the cooling stage did not significantly warm samples beyond -7 °C, we were not surprised that general trends for all metrics did not differ significantly from those presented in Chapter 5 as the percolation threshold was not crossed. The main difference is that

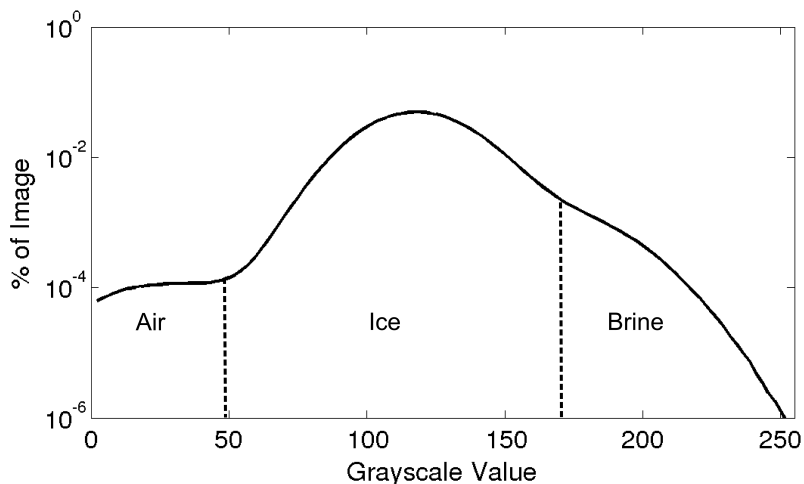


Figure 6.4: Representative histogram for thresholding μ CT images of warmer ice (sample from a depth of 160 cm in the Butter Point ice core). As in Fig. 2.10, the middle peak represents the gray-scale values corresponding to the ice phase. Values on the left correspond to the air phase (black) and values to the right correspond to the brine phase (white). Note that the inflection point segmenting brine from ice is less distinct than it is in Fig. 2.10.

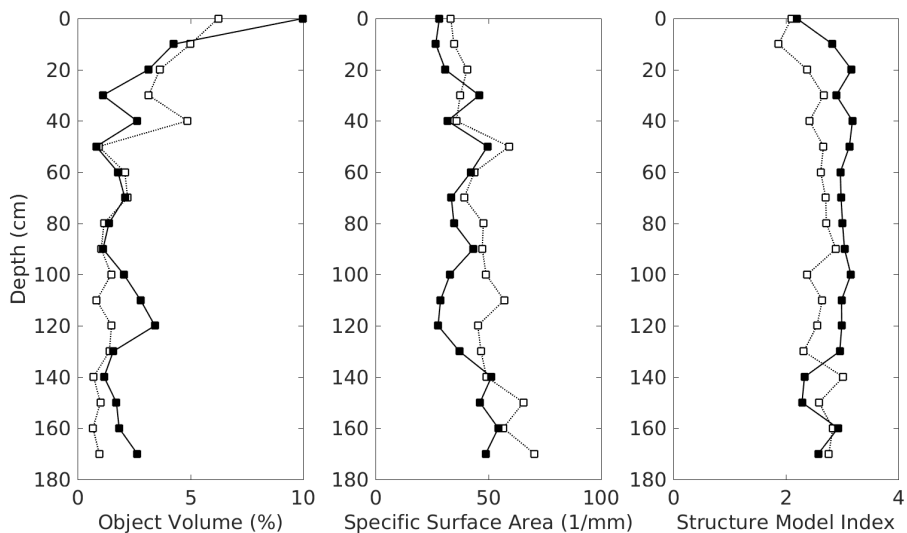


Figure 6.5: Comparison of the brine phase for the Butter Point ice core scanned at $-20\text{ }^{\circ}\text{C}$ (open squares and dashed line) and at in-situ temperatures (solid squares and solid line) using a Peltier cooling stage.

trends were generally smoother with some significant fluctuations near the bottom of the core, particularly for the 170-cm sample of the Iceberg Site core. As before, the brine phase specific surface area increased with depth, SMI was roughly 3, structure thickness

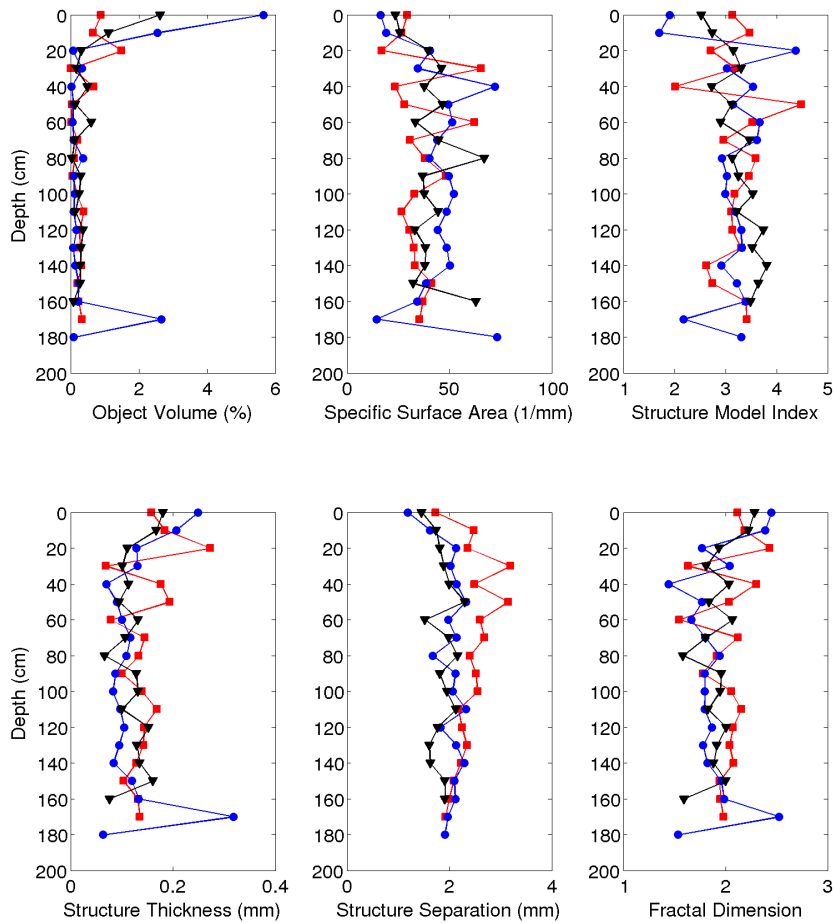


Figure 6.6: Definition and shape of air pockets scanned with a μ CT scanner and a Peltier cooling stage set at in-situ temperatures. The red squares, blue circles, and black triangles represent ice cores from Butter Point, Iceberg Site, and the first of the three cores extracted along the transect described in Chapter 2, respectively.

decreased, structure separation increased, and fractal dimension was roughly 2. Thus, consistent with Chapter 5 we still conclude that brine channels are primarily cylindrical in shape with more branches at lower depths. Fig. 6.5 presents a direct comparison of the brine volume fraction, specific surface area, and SMI for the Butter Point core scanned at $-20\text{ }^{\circ}\text{C}$ and at in-situ temperatures. Fig. 6.6 and Fig. 6.7 present metrics for defining the size and shape of the air and ice phases, respectively. Other than for the top few samples and the 170-cm sample, the air phase was less than 1% of the VOI. Air pockets were generally

spherical in shape (SMI close to 4) with a greater specific surface area at greater depths. Structure thickness, separation, and fractal dimension were mostly constant throughout all three ice cores indicating that air pocket shape is not dependent upon depth in the ice core. Metrics for the ice phase differed by an order of magnitude from the other two phases with comparable values to those in Fig. 5.6. SMI and structure separation decreased with depth, while structure thickness and fractal dimension were constant near expected values. Thus, we conclude that there are an increased number of concavities in the ice phase at lower depths, likely due to the increased branching of the brine channels, consistent with the conclusions in Chapter 5.

The degree of anisotropy for all three phases is presented in Fig. 6.8 and was nearly identical to the values given in Fig. 5.3. As expected, the brine phase had increased anisotropy throughout the middle of the core. The measure of connectivity and Euler number of the brine phase given in Fig. 6.9 fluctuated greatly, particularly for the sample at 170 cm in the Iceberg Site core. We present a more detailed analysis of the connectivity for the brine channels in the following section using the mathematical brine network.

We compared the μ CT-measured brine volume fraction to expected values derived from the Frankenstein and Garner relationship relating temperature, salinity, and brine volume fraction (Cox and Weeks, 1983; Frankenstein and Garner, 1967). For this analysis, we used the core temperatures presented in Fig. 6.1 and salinity values from Chapter 3. This yielded expected brine volume fractions for the two cores shown in the left panel of Fig. 6.10. From 0 cm to 120 cm, the measured brine volume fractions match the expected values remarkably well. However, below a depth of 120 cm in both cores, the expected brine volume fraction is much greater than what was measured using μ CT. For example, at a depth of 160 cm the expected brine volume fraction is 4.5 and 4.2 times greater than the values measured for samples from the Butter Point and Iceberg Site ice cores, respectively. This provides an estimate for the degree by which the cooling stage failed to heat the warmer samples.

To further test the effectiveness and limitations of the Peltier cooling stage, we scanned

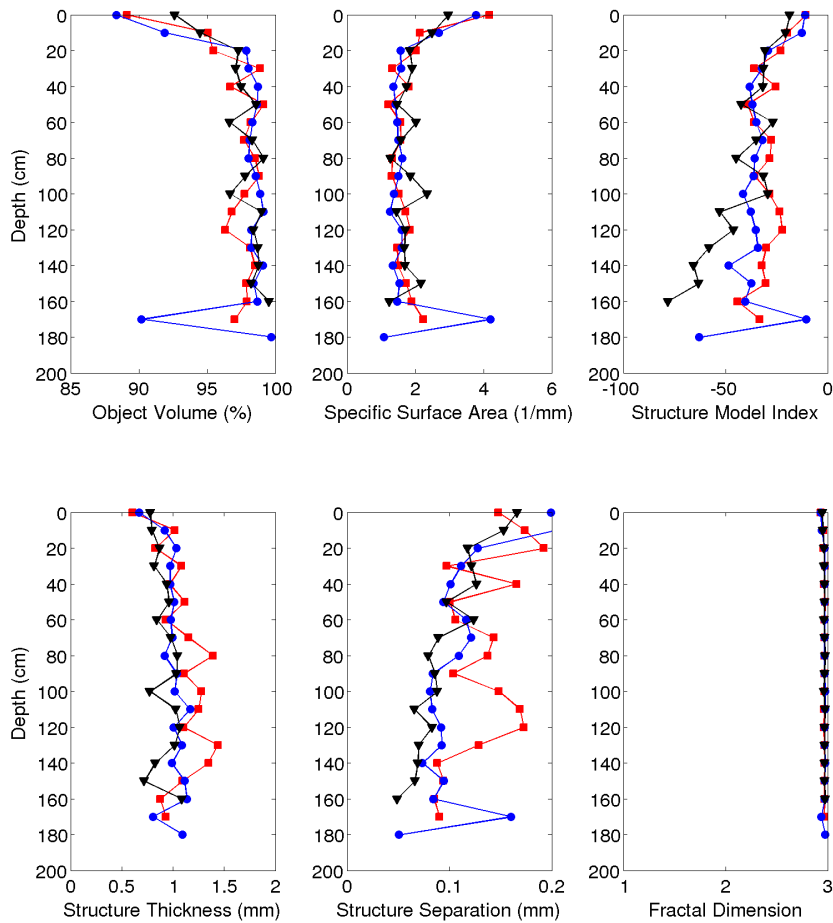


Figure 6.7: Definition and shape of the ice phase scanned with a μ CT scanner and a Peltier cooling stage set at in-situ temperatures. The red squares, blue circles, and black triangles represent ice cores from Butter Point, Iceberg Site, and the first of the three cores extracted along the transect described in Chapter 2, respectively.

a single sample from a depth of 120 cm in the Iceberg site at temperatures of $-20\text{ }^{\circ}\text{C}$ to $-2\text{ }^{\circ}\text{C}$ in $1\text{ }^{\circ}\text{C}$ increments. We expected the brine volume fraction to increase with warmer temperatures. However, the measured brine volume fractions for this sample were mostly constant across all temperatures. To quantify the difference from expected values, we compared the measured brine volume fractions to the expected values from the Frankenstein and Garner relationship in the right panel of Fig. 6.10. Despite the cooling stage reading temperatures spanning 18 degrees, the μ CT-measured brine volume fractions

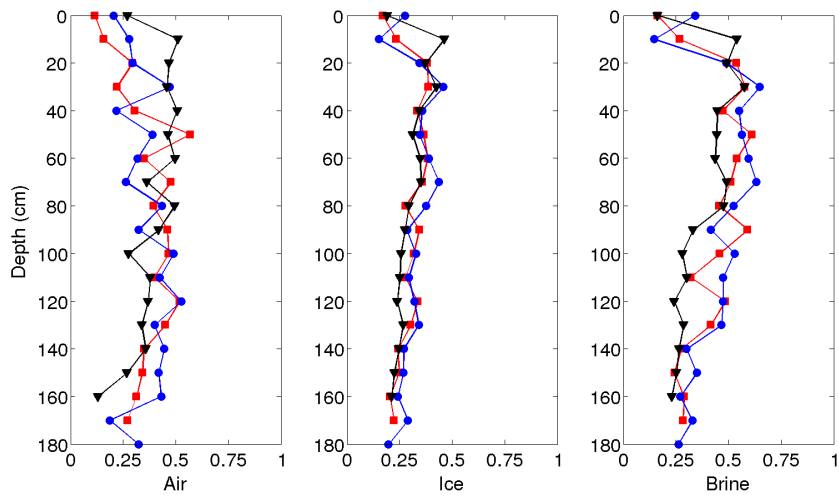


Figure 6.8: The degree of anisotropy for μ CT scans at in-situ temperatures. The red squares, blue circles, and black triangles represent ice cores from Butter Point, Iceberg Site, and the first of the three cores extracted along the transect in Chapter 2, respectively.

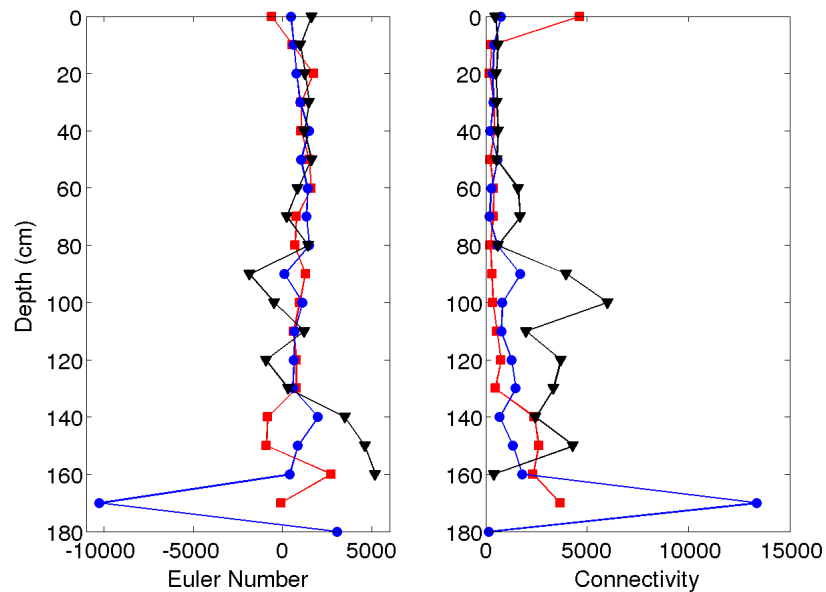


Figure 6.9: The Euler number and degree of connectivity of the brine channels for μ CT scans at in-situ temperatures. The red squares, blue circles, and black triangles represent ice cores from Butter Point, Iceberg Site, and the first of the three cores extracted along the transect in Chapter 2, respectively.

only varied from 1.2% – 2.0%. We note that the predicted brine volume fraction does not show a c-shape profile for this test because a single sample with set salinity was used for all scans. Thus, from the results of these comparisons we conclude that the cooling stage was not fully effective in thermally controlling the ice sample to the desired temperature, particularly for the warmer samples below 120 cm.

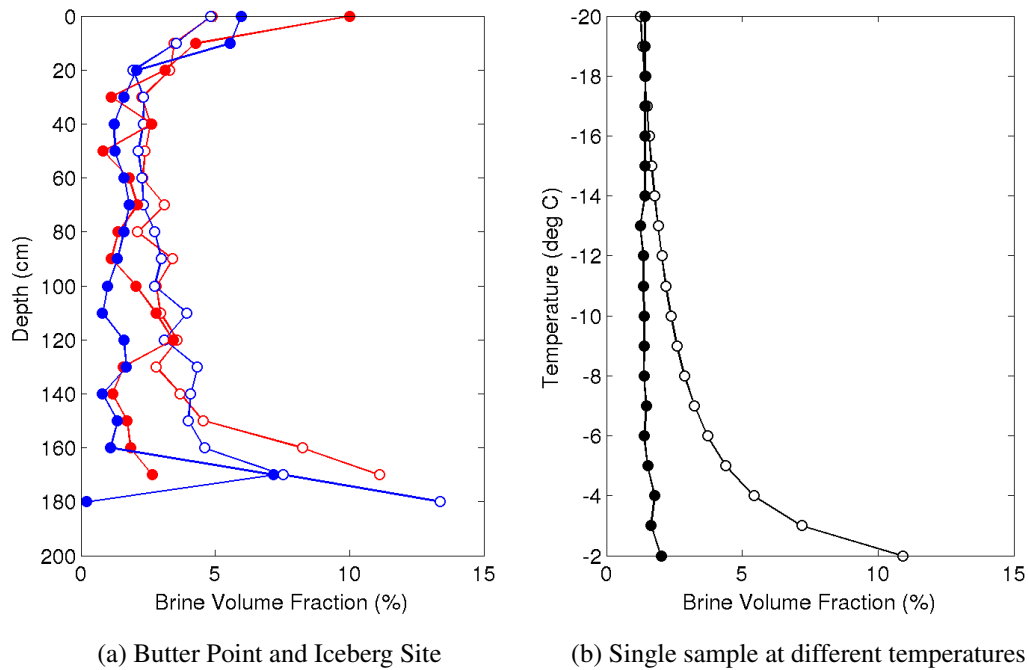


Figure 6.10: Comparing μ CT-measured brine volume fraction to the expected values derived from the Frankenstein and Garner relationship (Cox and Weeks, 1983; Frankenstein and Garner, 1967). The left panel shows results from the Butter Point (red) and Iceberg Site (blue) cores, where the μ CT-measured values are the filled circles and the expected values are the open circles. The right panel shows results from a single sample (120 cm from the Iceberg Site core) scanned at temperatures of $-20\text{ }^{\circ}\text{C}$ to $-2\text{ }^{\circ}\text{C}$, where the filled black circles are the μ CT-measured values and the open circles represent the expected values from the Frankenstein and Garner relationship.

Although the measured brine volume fractions were constant for the single-sample $-20\text{ }^{\circ}\text{C}$ to $-2\text{ }^{\circ}\text{C}$ temperature range experiment, we calculated the full set of μ CT analysis metrics to determine if there were any microstructural changes due to the cooling stage. If the cooling stage was fully functional, we would have expected an increase in brine volume fraction to be accompanied by brine channels growing in size (increase in

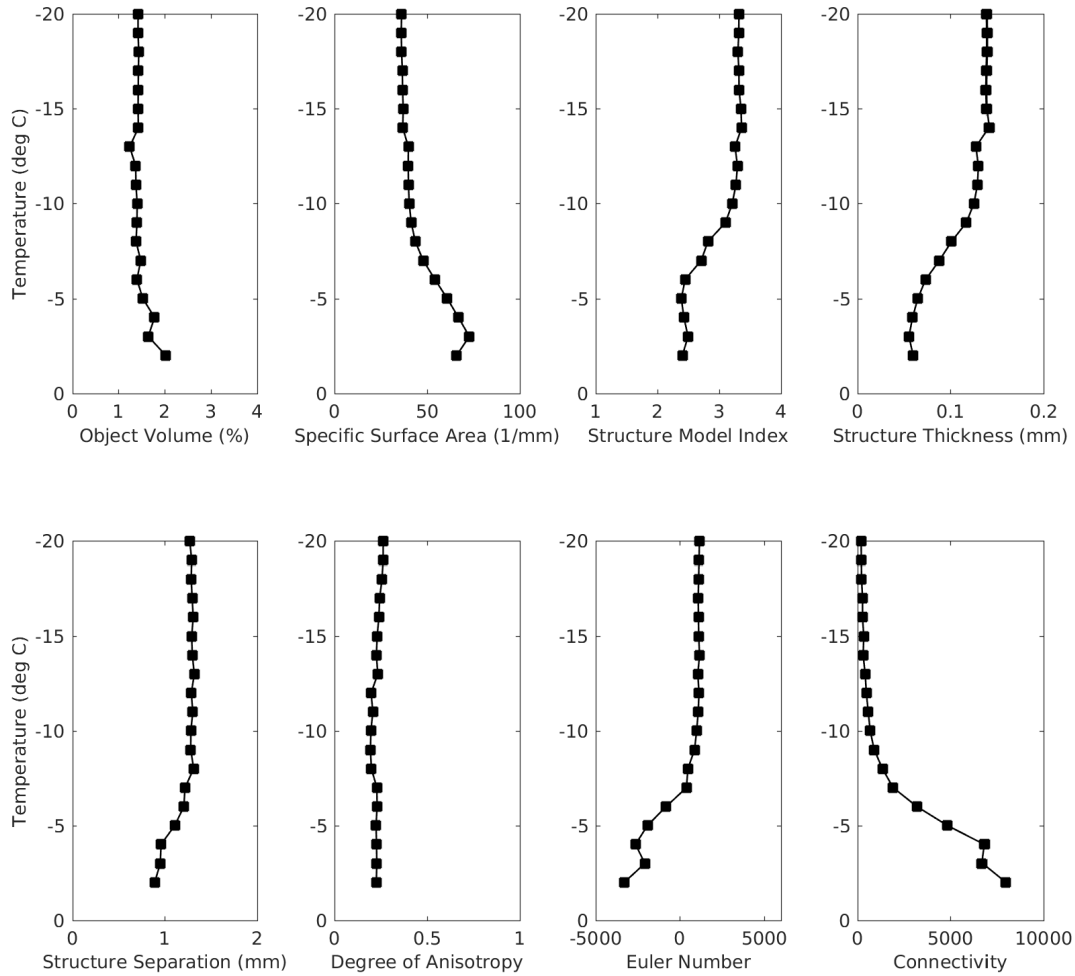


Figure 6.11: Metrics obtained from μ CT analysis of the brine phase for single sample scanned at varying temperatures from $-20\text{ }^{\circ}\text{C}$ to $-2\text{ }^{\circ}\text{C}$. The sample was from a depth of 120 cm in the Iceberg site ice core. Note that the direction of the y-axis is flipped to be consistent with the fact that warmer temperatures are found at lower depths in the sea ice.

structure thickness and decrease in specific surface area) and reaching a larger region of the sample space (increase in connectivity and increase in specific surface area). We expected the general shape (structure model index and degree of anisotropy) to remain constant. However, if the cooling stage only warmed the ice into a slush rather than a full phase change, we would expect larger increases in specific surface area and perhaps a decrease in SMI as the brine fills a more complex space. Fig. 6.11 shows the measured results illustrating the definition, shape, and connectivity of the brine phase for this experiment. We first note that most metrics are relatively constant for temperatures below $-8\text{ }^{\circ}\text{C}$. For

warmer temperatures, however, there were indeed noticeable changes in most metrics, indicating that the cooling stage did have some effect upon the sample. The brine channels of warmer samples had an increase in specific surface area, decrease in SMI, decrease in structure thickness and structure separation, decrease in Euler number, and increase in connectivity. Detecting microstructural changes at a constant brine volume fraction suggests that the cooling stage was beginning to melt some of the ice into a slush. However, due to the challenges in brine segmentation shown in Fig. 6.4, we are hesitant to make further physical interpretations from these results. The metrics for the air phase were remarkably constant across all temperatures, as would be expected since melting ice should turn into brine rather than air. Increases in temperature would not have a physical basis for significant changes to the air phase. The ice phase was mostly constant across all temperatures, but had some variation for warmer samples. For these samples, both the SMI and structure separation decreased in response to the changes in the brine phase.

Brine Network Model for Sea Ice

From the binarized images of the brine phase for the Butter Point and Iceberg Site ice cores, we created a mathematical network as we described above. We will use the term *network* to refer to the entire brine phase of a given sample and/or the entire brine phase of all samples in a given core. For a given sample, we define each brine *channel* to be a single connected component in the brine network. The number of brine channels per sample ranged from 830 to 4800, with maximum numbers occurring in samples from the top and bottom of the cores. In previous chapters we observed that these brine channels often appear in layers or sheets spaced approximately 0.5 – 1.0 mm apart due to the ice growth mechanism and original skeletal structure. A single brine channel is a complex web containing many different parts, which we will call the *branches* of the brine channel. We will define a *merge point* to be the node where two branches come together and a *split point* to be the node where a single branch splits into multiple branches. We note that flipping the

perspective of movement from downwards to upwards changes a *split point* into a *merge point* and vice versa. This is an important observation since we did not record the vertical orientation of the samples during cutting. Using this terminology, we use techniques from network theory to topologically characterize the brine network, gaining further insight into the complex connectivity and implications for permeability.

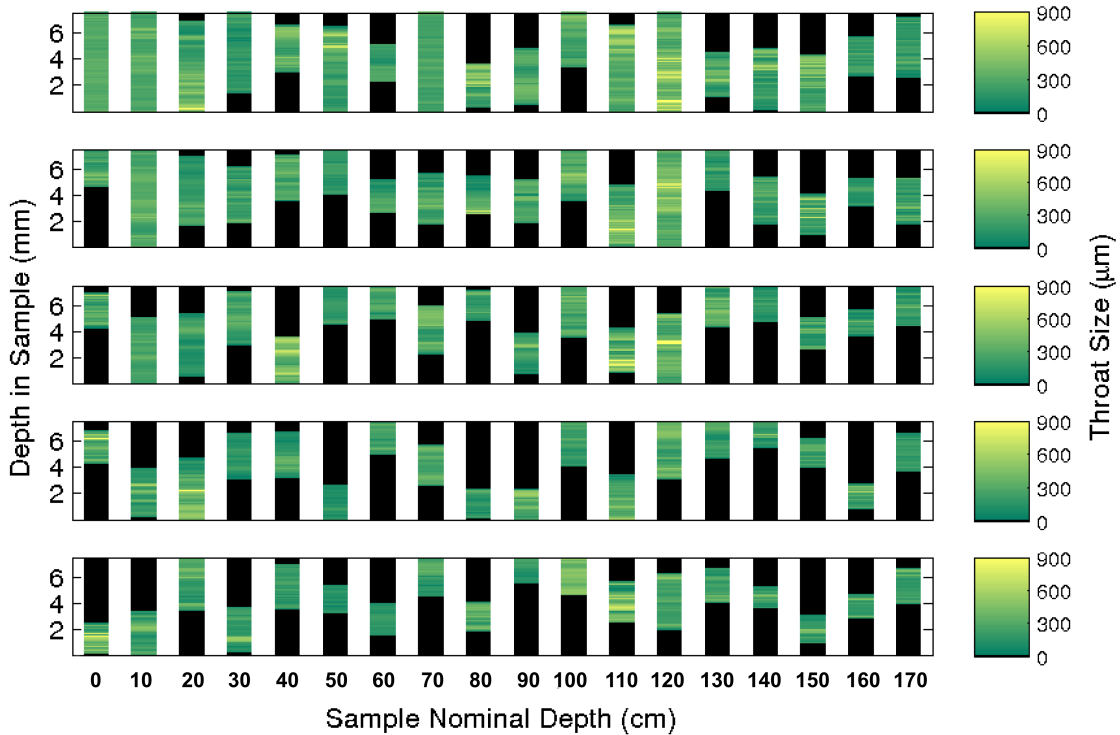


Figure 6.12: Average throat size $\{\bar{r}_{z_i}\}$ for the five largest brine channels of each sample for the Butter Point ice core. For each channel, at a given depth we calculated the average throat size of all nodes and color-coded accordingly. Note that there are only 6 channels that connect the top to the bottom of the sample.

In the analysis below, we will examine several metrics that describe the topology of the brine network and are important for fluid flow implications. For example, we will look at the throat sizes of the brine channels to gain an insight into the quantity of fluid that can move through different regions of a given brine channel. We will then look at specific branches, both in terms of the number of branches and the size of each branch to learn more about the specific pathway available for fluid movement. As part of this analysis, we will investigate whether the likelihood of a given branch to split into multiple branches

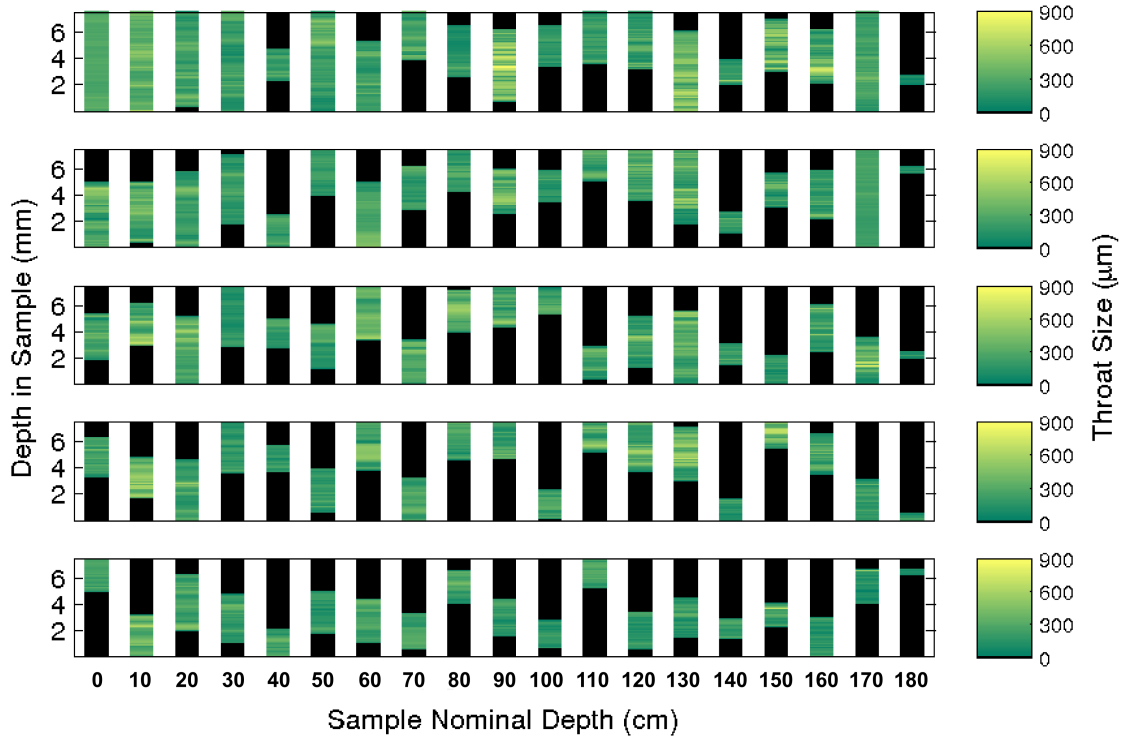


Figure 6.13: Average throat size $\{\bar{r}_{z_i}\}$ for the five largest brine channels of each sample for the Iceberg Site ice core. For each channel, at a given depth we calculated the average throat size of all nodes and color-coded accordingly. Note that there are only 6 channels that connect the top to the bottom of the sample.

is dependent upon the throat size of the parent branch. Finally, we will examine the size distribution of particular paths, looking for “pinch points” that may restrict flow and large regions that can provide maximize flow through the network. Together, these metrics will provide a detailed description of the micro-scale complexity of the brine network.

First, for each brine channel we calculated the average throat size $\{\bar{r}_{z_i}\}$ for all nodes $\{p_{z_i}\}$ at a given depth in the sample. Fig. 6.12 and Fig. 6.13 show the collection of these throat sizes for the five largest (by vertical extent) brine channels at each depth for the Butter Point and Iceberg Site cores, respectively. Fig. 6.14 and Fig. 6.15 provide a closer look at just the largest brine channel at each depth. There were 6 brine channels in each core that connected from the top to the bottom of the sample, with the majority of these channels found in samples from the top of each core. Generally speaking, the lengths of the vertical extent of the longest channel decreased with depth from the top of each core

to around 60 cm, increased from 60 cm to roughly 120 cm, and then decreased from 120 cm to the bottom of the core. The trend between the top of the core and roughly 120 cm is consistent with what we would expect due to brine volume fraction, temperature, and the expected c-shape profile. The channels from the lower depths, which had even warmer temperatures, did not reach in-situ temperatures during scanning as we described previously. We also note that both the lengths of the vertical extent and average throat size quickly diminished for channels beyond the few largest ones, as can be seen in the bottom panel of Fig. 6.12 and Fig. 6.13. Thus, we learn that fluid flow is most controlled by the behavior of the largest brine channel for a given section of sea ice.

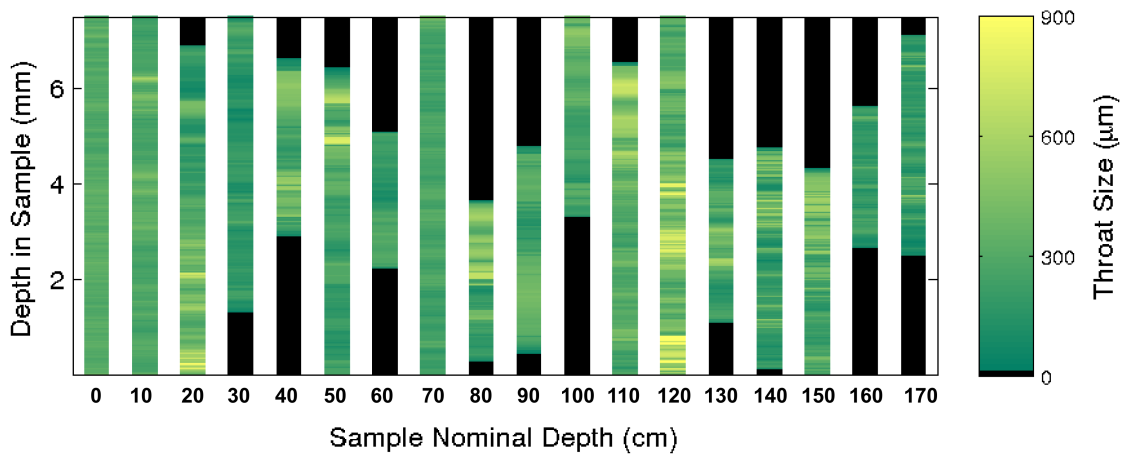


Figure 6.14: Average throat size $\{\bar{r}_{z_i}\}$ for the largest brine channels of each sample for the Butter Point ice core. For each channel, at a given depth we calculated the average throat size of all nodes and color-coded accordingly. Note that only channels at depths of 0, 10, 70, and 120 connect the top to the bottom of the sample.

The number of branches for a particular brine channel has potentially significant implications for fluid flow and permeability, such as influencing the rate at which chemical species may pass through the sea ice (Newman, 2011; Santiago et al., 2014; Yang et al., 1995). By increasing the number of branches, split points increase the number of potential paths through the sample. A higher number of paths increases the probability of finding a path connecting the top and bottom of a sample, thereby crossing the percolation threshold (Sahimi, 2011). Alternatively, split points can represent bottle-necks if the resulting child

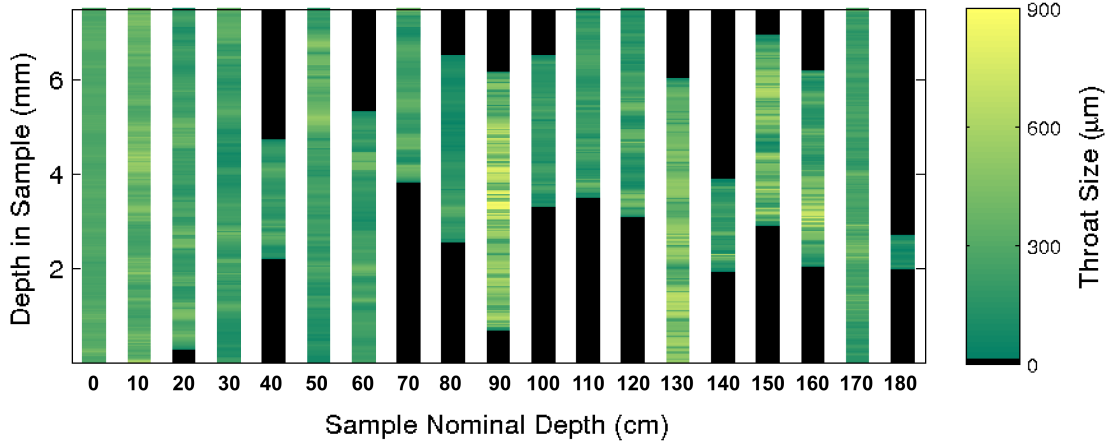


Figure 6.15: Average throat size $\{\bar{r}_{z_i}\}$ for the largest brine channels of each sample for the Iceberg Site ice core. For each channel, at a given depth we calculated the average throat size of all nodes and color-coded accordingly. Note that only channels at depths of 0, 10, 30, 50, and 170 connect the top to the bottom of the sample.

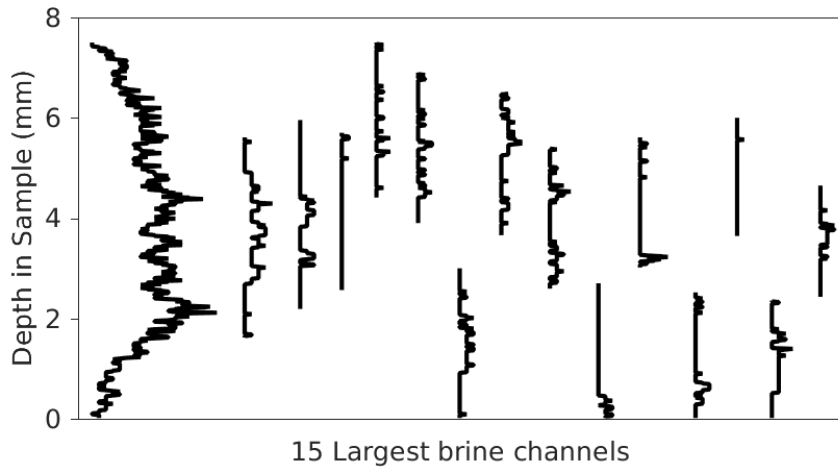


Figure 6.16: Number of branches at each depth for the 15 largest brine channels in the 70-cm sample of the Butter Point core. We measured the number of branches by the number of nodes at a given depth in the sample. Each line represents a separate channel, and the horizontal extent illustrates the number of branches.

branches have smaller throat sizes than the parent throat, measured either as a minimum or as an aggregate. In each two-dimensional horizontal slice, we defined a node for each two-dimensional connected component. Each two-dimensional connected component corresponds to a distinct branch of the brine channel, and thus, the number of branches at a given depth (i.e. particular horizontal slice) equals the number of nodes at this depth.

Fig. 6.16 shows the total number of nodes per depth for the 15 largest (by vertical extent) brine channels in the 70-cm sample of the Butter Point core. The largest channel had by far the largest number of branches, with a maximum of 20 branches at a depth of 2.1 mm from the bottom of the sample. Since this sample was from the columnar ice region, the maximum number of branches is relatively small. For comparison, the maximum number of branches for a sample in the frazil ice region at the top of the core was 124 nodes at a single depth. As expected, we find that brine channels in frazil ice have many more branches than brine channels in columnar ice, providing more distinct pathways for brine to move through the sample.

To visualize the number of branches and distribution of throat sizes, thereby gaining insight into the behavior of a channel, we recorded the throat size r_i of each node p_i for the largest brine channel. Fig. 6.17 and Fig. 6.18 plot the throat sizes as a function with depth in the sample for three different representative sample depths: top, middle, and bottom of the Butter Point and Iceberg Site cores, respectively. For each channel shown, there is a plot of $\{r_i\}$ at each depth unsorted and a second corresponding plot sorted by descending $\{r_i\}$ for a given depth in sample. The first plots illustrate the connectivity of given branches, while the second plots provide a visualization of the distribution of r_i . The sample extracted from 0 cm in each core is from a region of frazil ice, which we would expect to have brine channels that are not well connected and have a distribution of throat sizes independent of depth in the sample. In both Fig. 6.17 and Fig. 6.18, panel a shows that the brine network for this top-most sample was indeed not well connected, while panel b shows that there was an even distribution of throat sizes. The two plots for mid-depth networks are quite similar, illustrating less tortuosity and easier ability to track particular branches in the brine channel. The bottom sample of the Iceberg Site core had much larger throat sizes, although this sample was an anomaly in Fig. 6.3 and Fig. 6.9. We note that we did not observe a direct correlation between the number of branches and the throat size of those branches, as the distribution of throat sizes appeared to be more dependent upon the particular depth

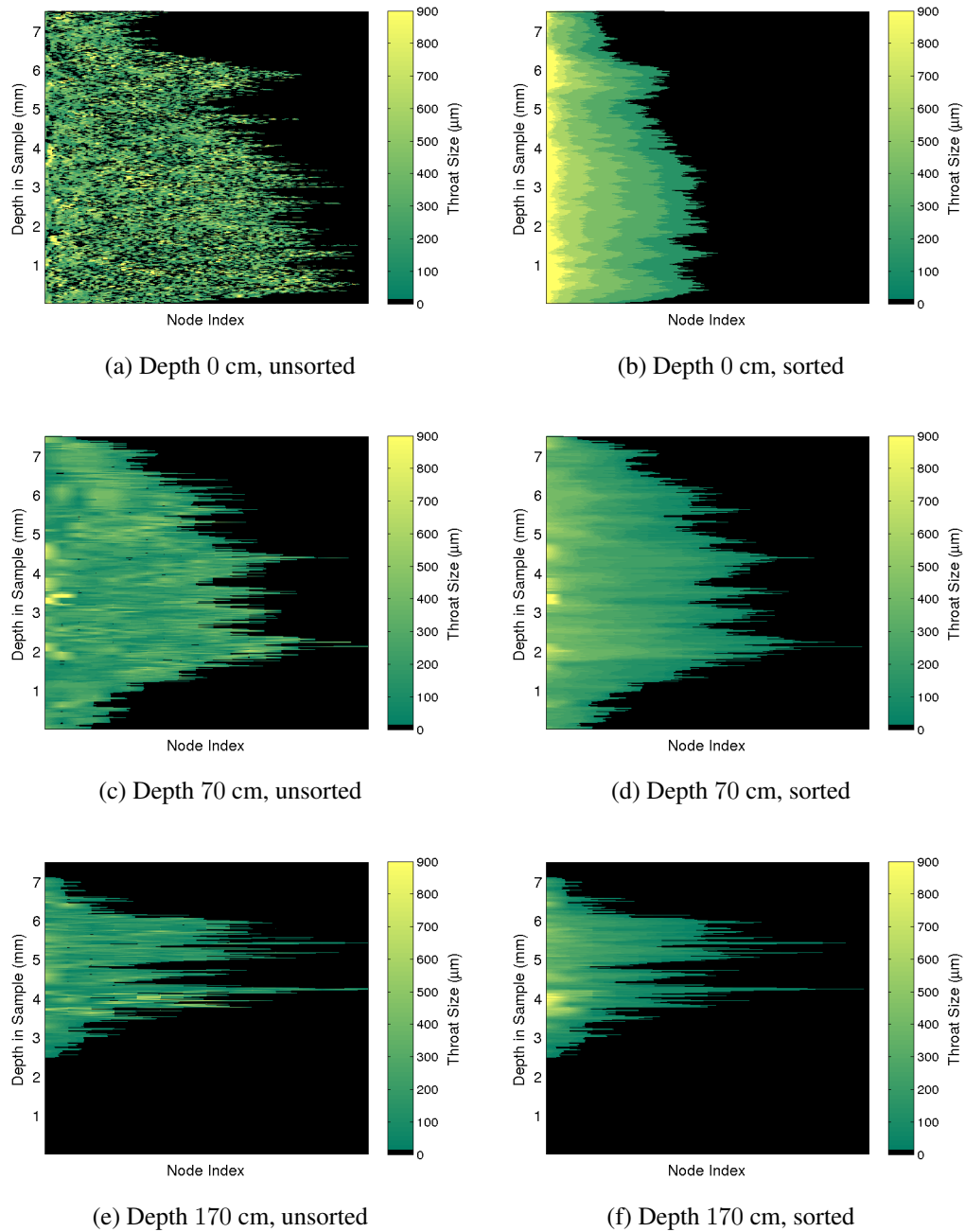


Figure 6.17: Throat size r_i of each node for the largest channel of representative samples in the Butter Point core. The top, middle, and bottom rows show the largest brine channel from the sample at 0, 70, and 170 cm, respectively. The left panels show the throat sizes at each depth in the sample unsorted, while the right panel sorts the throat sizes in descending order.

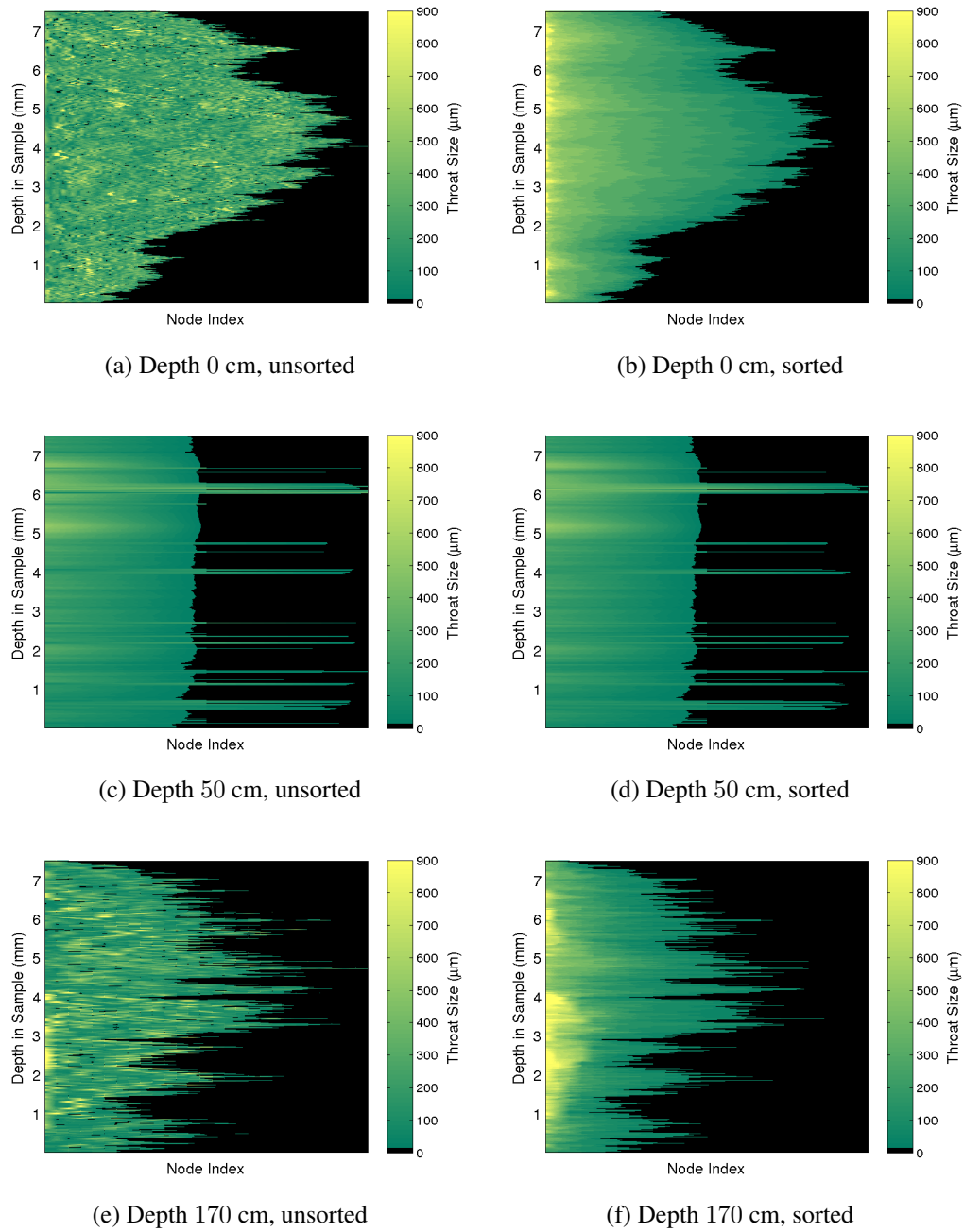


Figure 6.18: Throat size r_i of each node for the largest channel of representative samples in the Iceberg Site core. The top, middle, and bottom rows show the largest brine channel from the sample at 0, 50, and 170 cm, respectively. The left panels show the throat sizes at each depth in the sample unsorted, while the right panel sorts the throat sizes in descending order.

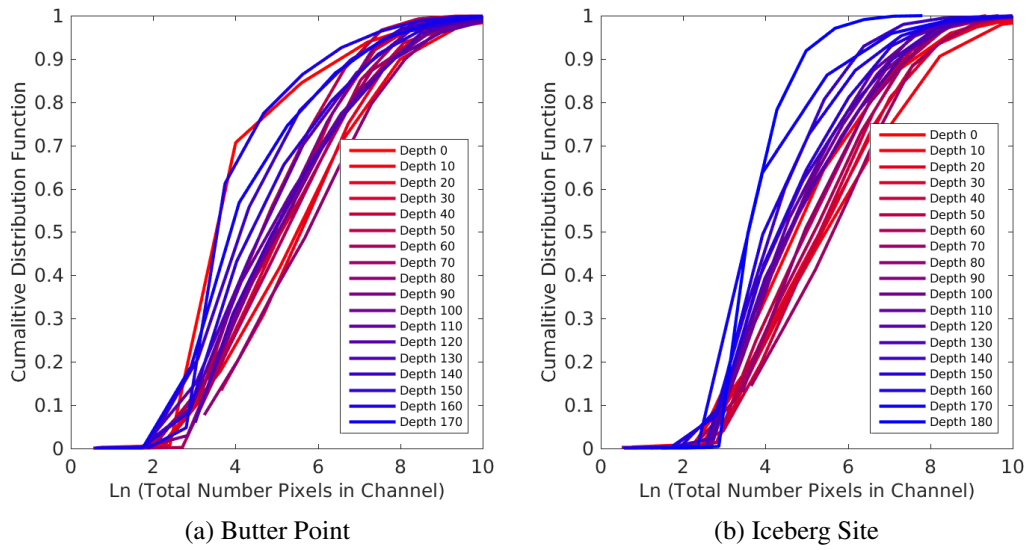


Figure 6.19: Cumulative distribution functions for number of brine channels as functions of the total number of pixels in the channel. The left and right panels are for the Butter Point and Iceberg Site ice cores, respectively. In both panels, each line represents a different sample depth where the lines are colored on a gradient from red representing the top of the core to blue for the bottom of the core. Note that pixels in the original μ CT images are $15 \mu\text{m}$ on each edge.

of the sample in the ice core, and consequently, the ice type of that sample. From this analysis, we learn that although there may be more branches for a given brine channel in frazil ice, the branches have better vertical connectivity in columnar ice. This means that fluid can more readily move upwards or downwards through the larger well-connected brine channels in columnar ice.

We next examined the fluid flow capacity of each channel by both summing the number of pixels associated with all nodes for each channel and summing the total throat sizes of all nodes in each channel. We note that this represents a region larger than the pathways used for current fluid flow since many branches do not connect the top of a sample to the bottom. However, when the ice begins to warm and the branches become more interconnected, the process will likely start from the existing regions containing brine. Thus, this metric offers a starting place for comparing the capacity for fluid flow across different samples. Fig. 6.19 shows cumulative distribution functions for the number of brine channels as functions of

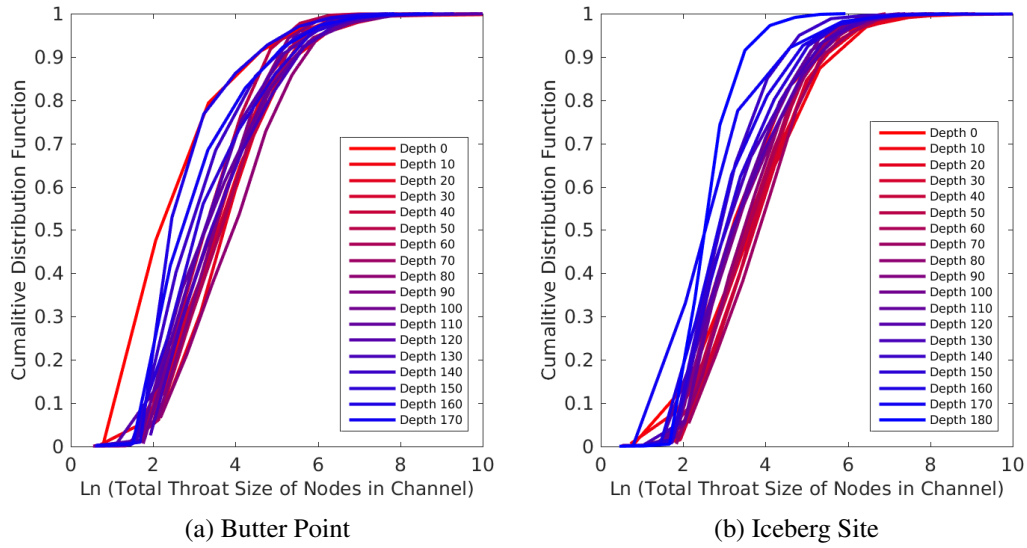


Figure 6.20: Cumulative distribution functions for number of brine channels as functions of the summed throat size of all nodes in the channel. The left and right panels are for the Butter Point and Iceberg Site ice cores, respectively. In both panels, each line represents a different sample depth where the lines are colored on a gradient from red representing the top of the core to blue for the bottom of the core. Note that throat sizes in the original μ CT images are $15 \mu\text{m}$ on each edge.

the total number of pixels in the channel, with each line represents a different sample depth. The lines are colored on a gradient from red representing the top of the core to blue for the bottom of the core. The distribution functions for all depths on both cores were remarkably similar, and pairwise Kolmogorov-Smirnov tests did not detect that any two curves were from different probability distributions ($p \geq 0.1$) (Graham and Hogg, 1978; Massey, 1951). Both cores did show a trend of increased probability of brine channels with more pixels occurring at shallower depths, with a more robust trend observed in the Iceberg Site core. This trend could be due to samples at lower depths having an increased number of isolated small channels that have yet to connect to larger channels. Since there is doubt as to whether the samples below 120 cm fully reached their in-situ temperatures, perhaps these small isolated channels would have connected to larger channels under warmer conditions. Fig. 6.20 presents similar cumulative distribution functions for the number of brine channels as functions of the summed throat size of all nodes in the channel.

The curves yield the same observations as before, with the Iceberg Site core again having a stronger correlation of increased probability of larger channels occurring at shallower depths. Likewise, Kolmogorov-Smirnov tests did not detect any two curves representing different probability distributions ($p \geq 0.1$). Any noticeable changes to the relative shape of the curves represent disproportionate changes in the shape of the brine channel with size of the channel, however, these variations were quite minor. In general, the shape of the curves in Fig. 6.20 are similar to those in Fig. 6.19. Thus, we conclude that brine channels in samples near the top of the core provide fluid multiple distinct pathways to move through the sample, while deeper in the core there is often only a few large channels with many small isolated paths that may connect under warmer ice conditions.

Next we examined the branching of particular nodes to understand the behavior of particular fluid flow paths. Following a branch of a channel downwards, at an individual node the branch may end, continue onwards, or split into multiple branches. Conversely, by looking upwards, a node can be considered to be the first in a new branch, the continuation of a branch, or the merging point of multiple branches. Thus, for each node in a brine channel, we can tally the number of edges above and below said node to determine the degree of splitting or merging of branches in the channel (Newman, 2011). Fig. 6.21 presents histograms for each core tallying the total number of nodes of each edge count for the five largest brine channels over all sample depths. All four histograms show similar decay for frequency with increasing quantity of splits/merges. The large majority of nodes do not display branching, and the number of two-way splits/merges was roughly the same as the number of times a branch started/ended. The Iceberg Site core had a larger number of higher order branching with a significant number of 7-way or 8-way splits/merges. As expected, a branch that splits is most likely to split into only two child branches, and thus for example, a contaminant introduced at a point source is likely restricted to a small horizontal region, following only a few separate paths through the ice.

With knowledge of the total number of split points and merge points, we then

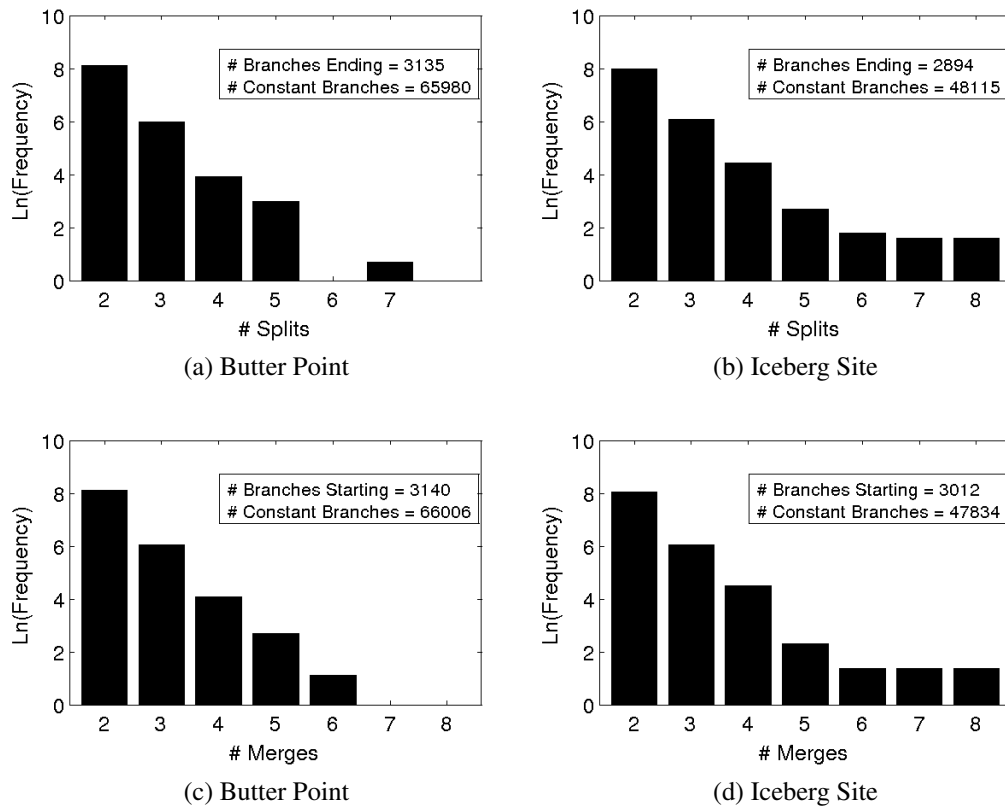


Figure 6.21: Histogram of nodes having different degree of edge counts. Looking downwards, splitting (panels a and b) represents an increase in the number of branches while merging (panels c and d) represents a decrease in the number of branches. Note that when a sample is flipped over, splits turn into merges and vice versa. Values of 0 represent that end or start of a branch and were tallied separately. Edge values of 1 for a node indicate that there has not been a split or merge and were also tallied separately. The left and right panels are histograms for the Butter Point and Iceberg site ice cores, respectively.

investigated the likelihood that branching was dependent upon the throat size. In Fig. 6.22 we plot the throat size distribution for nodes that died out, continued along a single branch, and split into multiple branches. As can be seen in the two left panels, when a branch died out, the final node throat sizes were relatively small, as we would expect. However, what is interesting is comparing the middle (constant branches) and right (splitting branches) panels. There is a noticeable increased likelihood for splitting of larger nodes than for smaller nodes, demonstrated by a shift to the right of the respective histograms. We observed similar trends for both the Butter Point and Iceberg Site ice cores. Statistically,

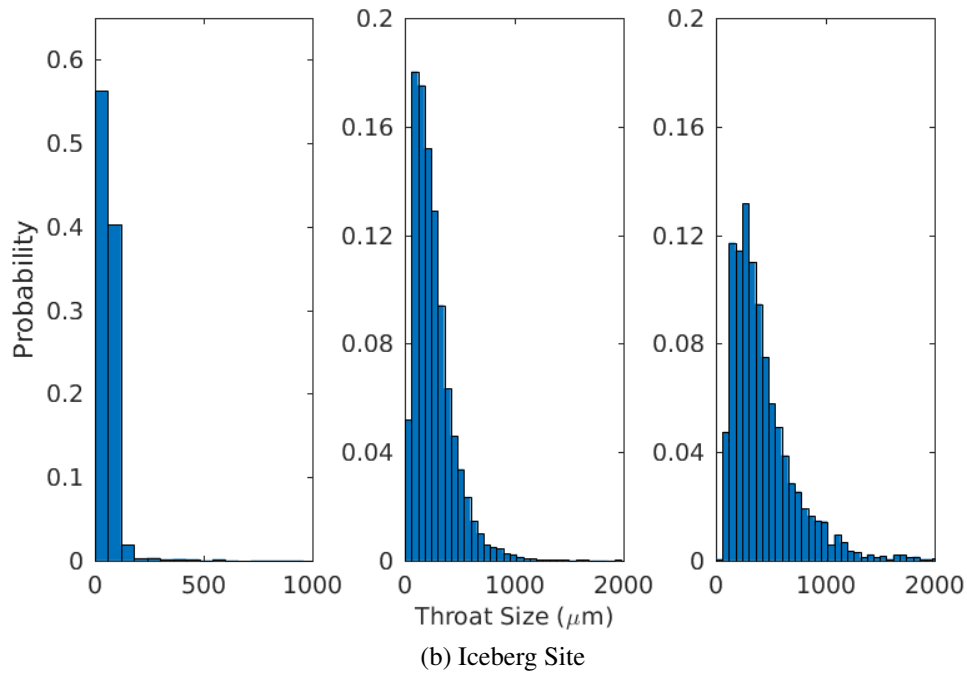
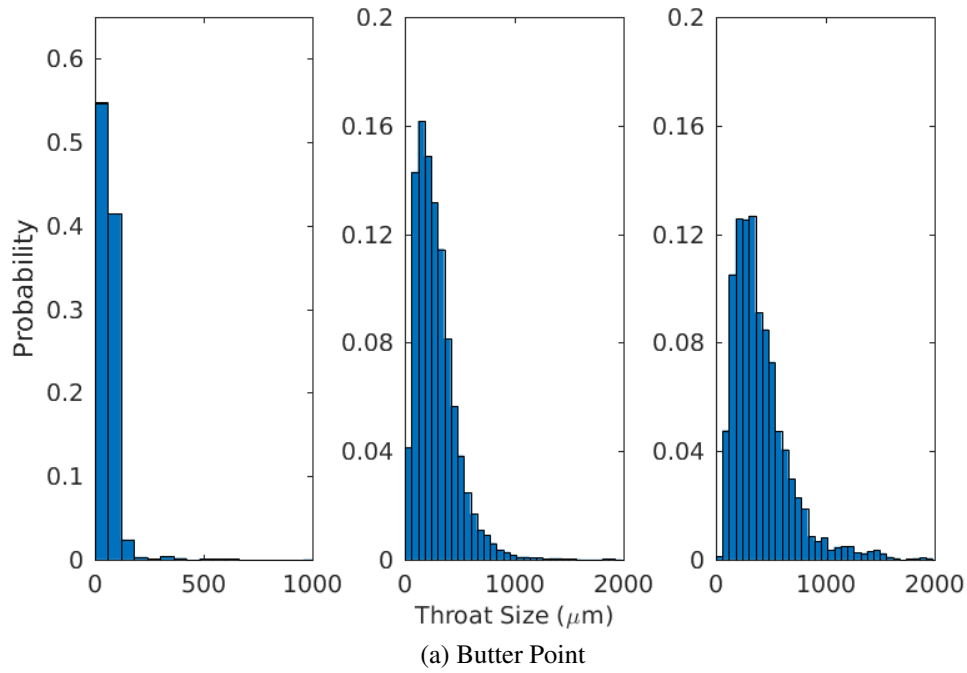


Figure 6.22: $\{r_i\}$ probability distribution for branching and non-branching nodes. Panel (a) shows $\{r_i\}$ for all nodes in the five largest brine channels for all depth samples in the Butter Point ice core, while panel (b) shows the corresponding nodes in the Iceberg Site ice core. For both panels, the left plot is for nodes with no outgoing edges (branch dies out), the middle plot is for nodes with one outgoing edge (continuing along same branch), and the right plot is for nodes with multiple outgoing edges (splitting of the channel).

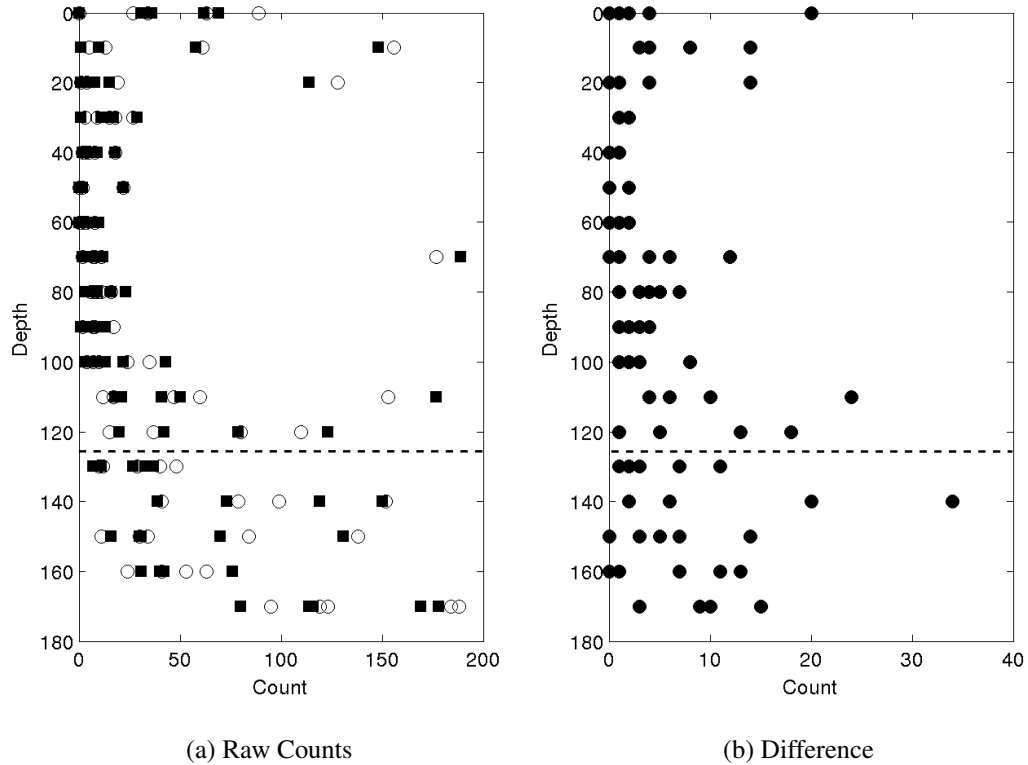


Figure 6.23: Topological complexity of the five largest brine channels in each sample for the Butter Point core. The left panel shows the total number of splits (open circles) and merges (black squares) over all nodes in a given channel. The right panel shows the absolute value of the difference between the number of splits and merges. The dashed line highlights the depth below which there is concern regarding the effectiveness of the cooling stage and whether samples were scanned at actual in-situ temperatures.

all three histogram distributions were pairwise significantly different from each other (Kolmogorov-Smirnov tests, $p \leq 0.1$) for both cores (Graham and Hogg, 1978; Massey, 1951). When a split occurred, we compared r_i for the parent node to the collection of r_i for the children nodes with similar behavior observed in both cores. 84% of the time for the Butter Point core and 86% of the time for the Iceberg Site, the sum of the throat sizes for the children node were greater than that of the parent node. However, the parent node was still larger than the largest child node 67% of the time for the Butter Point core and 68% of the time for the Iceberg site core. Thus, we learn that larger brine channels are more likely to split, and after the split, the fluid can access a larger region of the sea ice.

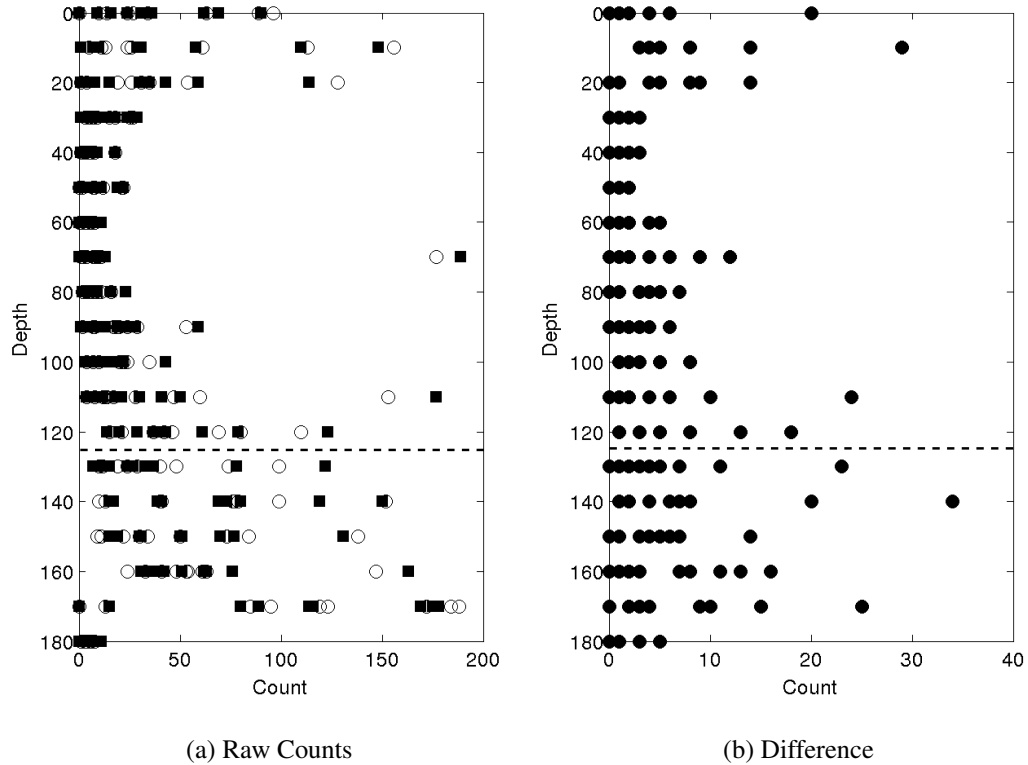


Figure 6.24: Topological complexity of the five largest brine channels in each sample for the Iceberg Site core. The left panel shows the total number of splits (open circles) and merges (black squares) over all nodes in a given channel. The right panel shows the absolute value of the difference between the number of splits and merges. The dashed line highlights the depth below which there is concern regarding the effectiveness of the cooling stage and whether samples were scanned at actual in-situ temperatures.

In addition, we summed the total number of edges leaving (splits) and entering (merges) each node over all nodes for the five largest brine channels of each sample. Plots showing these raw counts and the difference between the two are given for the the Butter Point and Iceberg Site cores in Fig. 6.23 and Fig. 6.24, respectively. When we consider split points and merge points separately, we are considering the network as a graph with directed edges. The difference between the number of splits and the number of merges (i.e. difference between number of incoming and outgoing edges) is a metric for the topological complexity of a network (Newman, 2011). The raw counts for number of splits and merges both had roughly a c-shape profiles for both cores, with largest values and variability observed

towards the bottom of the core. This is to be expected because the warmer part of the core allows for greater interconnectivity of branches in the brine network. For all brine channels, the number of splits was quite similar to the number of merges, and hence the differences between the two were quite small. However, there was still a general c-shape profile between 0 cm and 140 cm, indicating that topological complexity is greatest near the top and bottom of the core. This is consistent with frazil ice in the top of the core and increased branching in the warmer ice. Interestingly, both cores showed a decrease in topological complexity for the lowest samples below 140 cm. This could either be an artifact of not achieving actual in-situ temperatures with the cooling stage, or potentially an indication of a thought-provoking trend. If samples were not reaching in-situ temperatures, isolated channels may not have rejoined upon warming from storage temperatures, thereby reducing the number of split points and merge points. Alternatively, a possible explanation of a real trend could be that as brine channels widen for the warmest samples, branches join together, reducing the topological complexity. A consequence of reducing the number of branches is a reduction in the number of split points and merge points.

To assess fluid flow capabilities, we analyzed individual branches of brine channels to isolate particular paths through the network. By construction, moving from p_i to p_j along an edge must either increase or decrease the height in the sample by one step ($15 \mu\text{m}$). First, we treated the network as a directed graph and considered paths starting from the first node. Since the network does not allow lateral movement, each step along an edge corresponds to a $15 \mu\text{m}$ step downwards. Although previously 6 brine channels were found that connected the top to the bottom of a given sample, no such paths were found in the directed graphs. This is because all paths connecting the top to the bottom of a sample required movement upwards along a branch in order to reach the bottom. Fig. 6.25 shows an example of a brine channel where although the network is connected, any connecting path involves both upward and downward flow, such as the path highlighted in red. Thus, we selected the longest downward directed path from each brine channel, as well as any additional paths

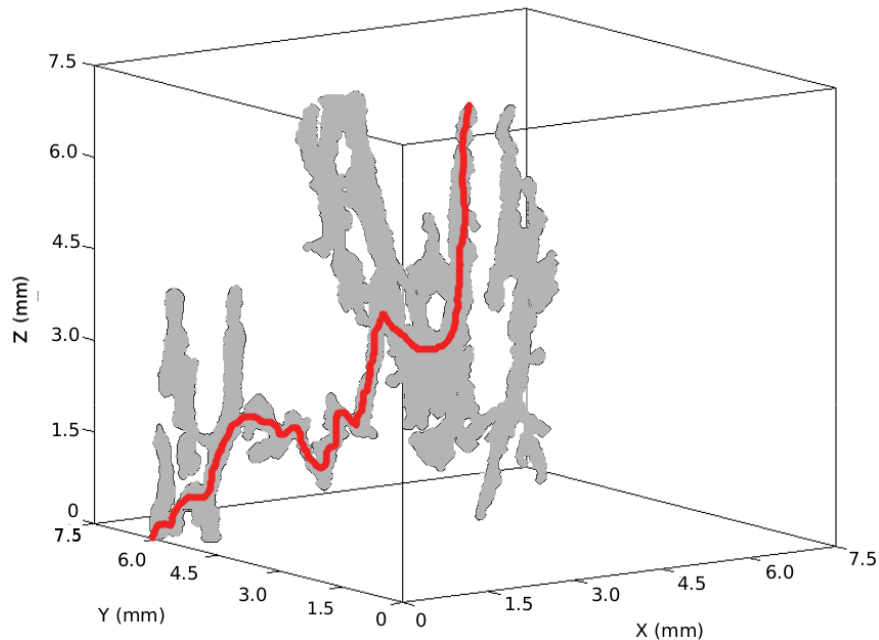
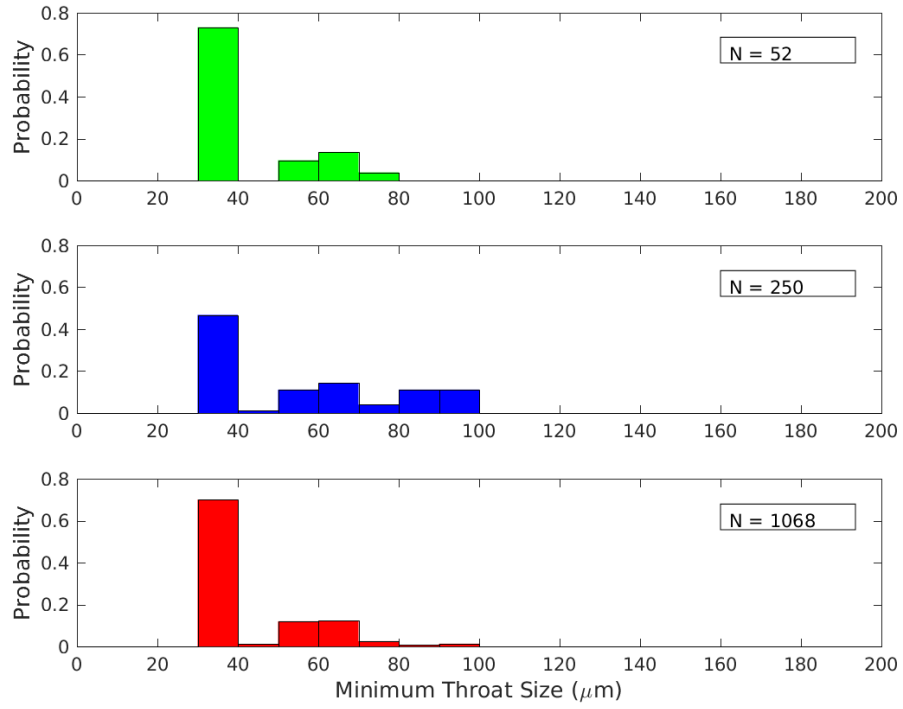


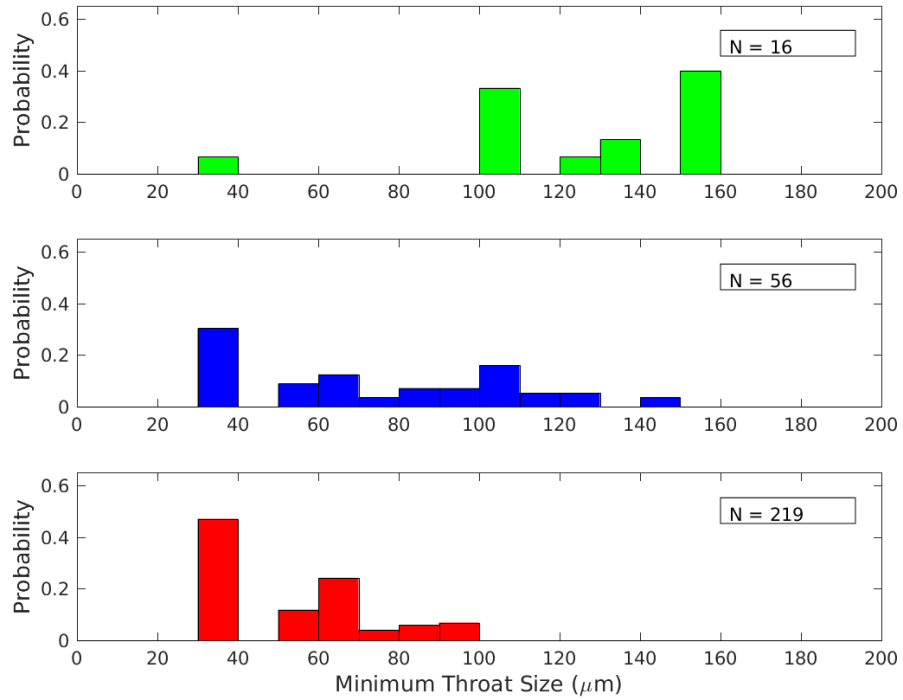
Figure 6.25: Largest brine channel at 70 cm in the Butter Point ice core. Although this brine channel connects from top to bottom, there is not a directed path that does so. Any connecting path involves movements both upwards and downwards. One such path is highlighted in red.

of the same length. This mimics a natural process such as gravity drainage, allowing us to study its influence on brine movement in the absence of pressure forces that aid upwards transport. Summing over all brine channels in the Butter Point core resulted in 63 763 directed paths. From this collection, we selected the 15 316 paths of length 50 steps (750 μm) for statistical analysis of minimum throat size (r^{min}), maximum throat size (r^{max}), and summed throat size. Appendix D provides histograms for these statistics partitioned by beginning (r_1) and ending (r_f) throat size.

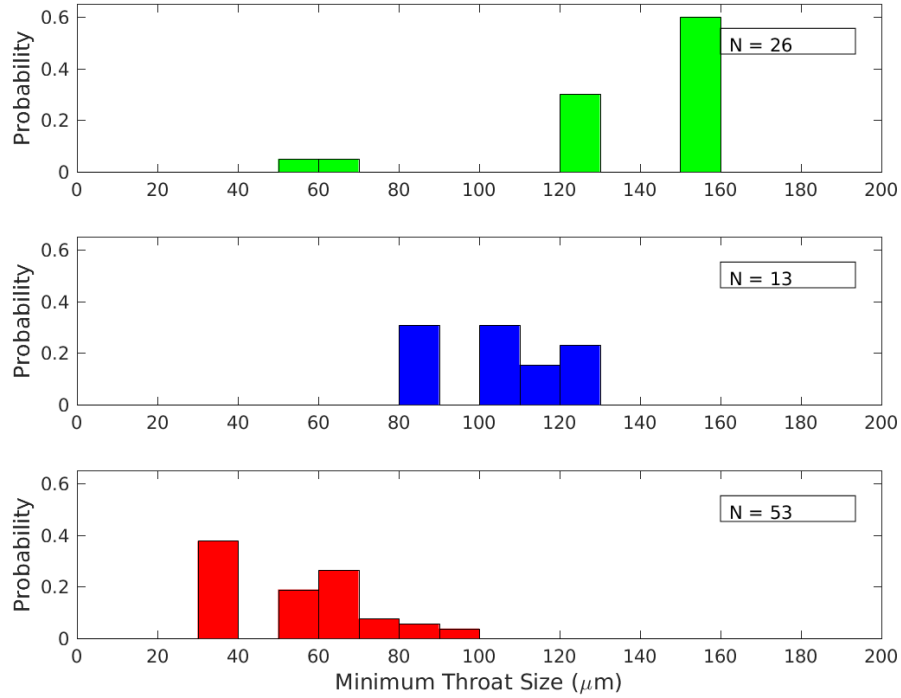
We completed a similar analysis on the brine channel network, however this time treating it as an undirected graph with bidirectional edges. To avoid complexities arising from cycles (repeating loops), we only considered different spanning trees (paths that reached every node but have no cycles). We used a depth-first search algorithm to find all paths reaching the maximum vertical extent of each channel (Newman, 2011; West,



(a) $r_f < 1500 \mu\text{m}$



(b) $1500 \leq r_f < 5250 \mu\text{m}$

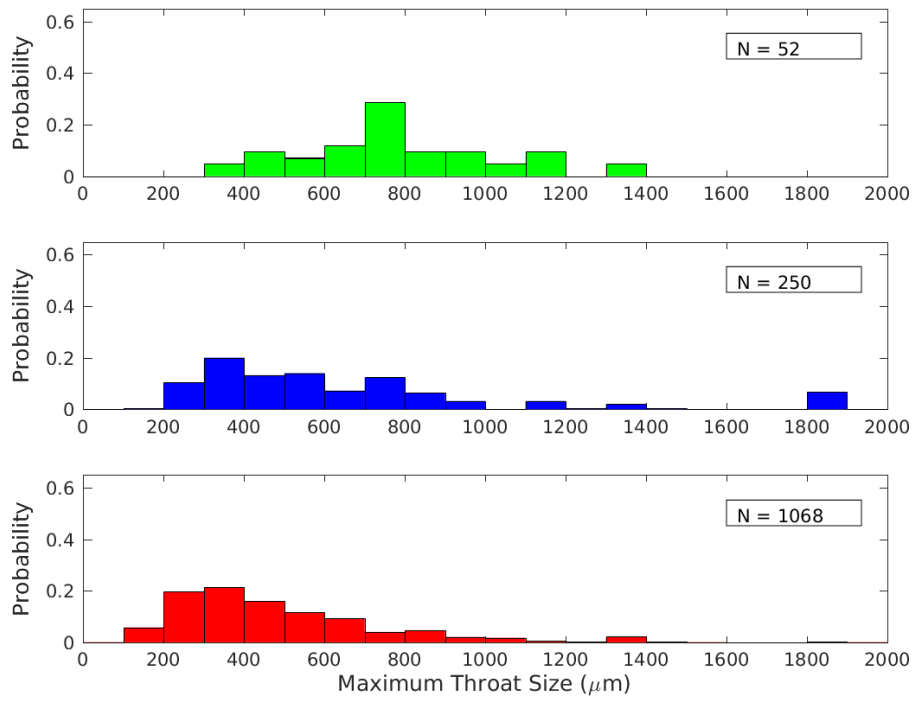


(c) $r_f \geq 52\,500 \mu\text{m}$

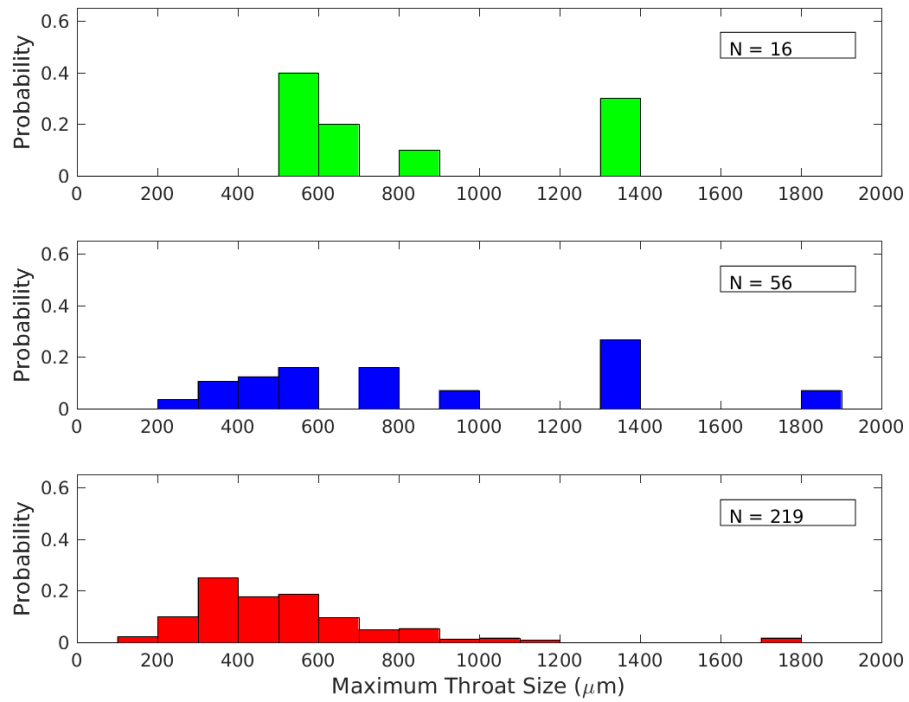
Figure 6.26: Probability distribution of r^{\min} of paths connecting the top to the bottom for all brine channels in the Butter Point ice core. Only paths greater than 50 steps, or $750 \mu\text{m}$ were considered. Panels a, b, and c represent channels where $r_f < 1500 \mu\text{m}$, $1500 \leq r_f < 5250 \mu\text{m}$, and $r_f \geq 52\,500 \mu\text{m}$, respectively. For all three panels, the colors red, blue, and green represent channels where $r_1 < 1500 \mu\text{m}$, $1500 \leq r_1 < 5250 \mu\text{m}$, and $r_1 \geq 52\,500 \mu\text{m}$, respectively.

2001). We checked results through comparison of the distance obtained using Dijkstra's algorithm for finding the shortest-path tree (Dijkstra, 1959; West, 2001). This resulted in 36 449 paths over all the brine channels in the Butter Point core, of which 1753 were of length 50 steps ($750 \mu\text{m}$). We note that we can use the adjacency matrix to calculate the number of different walks (paths including cycles) that connected the top and bottom of a sample (West, 2001). However, due to the size of the adjacency matrix, this became computationally too expensive for large brine channels.

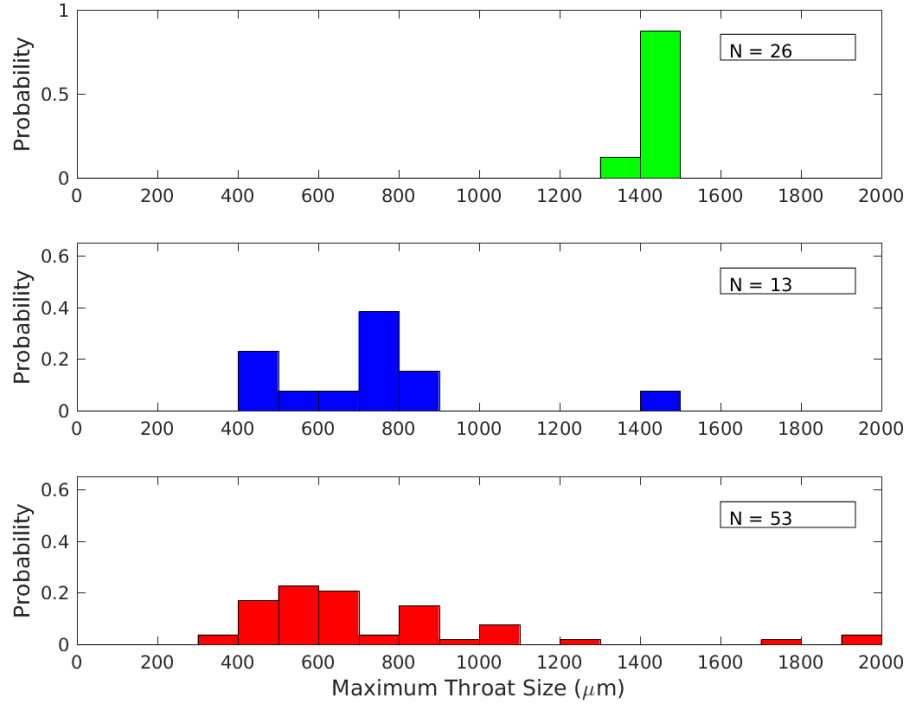
We used the 1753 paths of length > 50 steps to develop probability distributions for basic network statistics important for fluid flow such as r^{\min} , r^{\max} , and summed throat



(a) $r_f < 1500 \mu\text{m}$



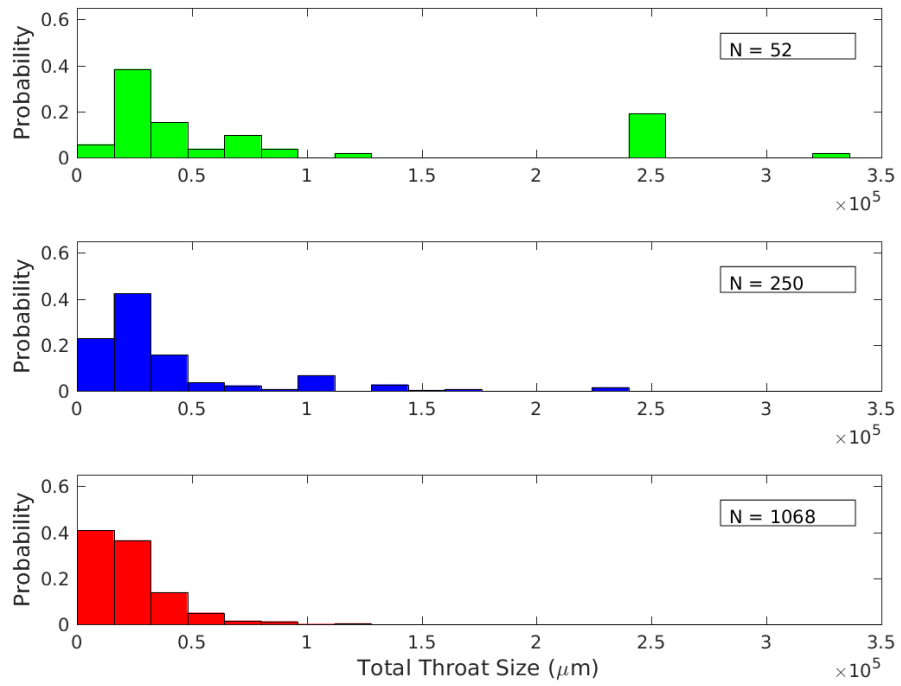
(b) $1500 \leq r_f < 5250 \mu\text{m}$



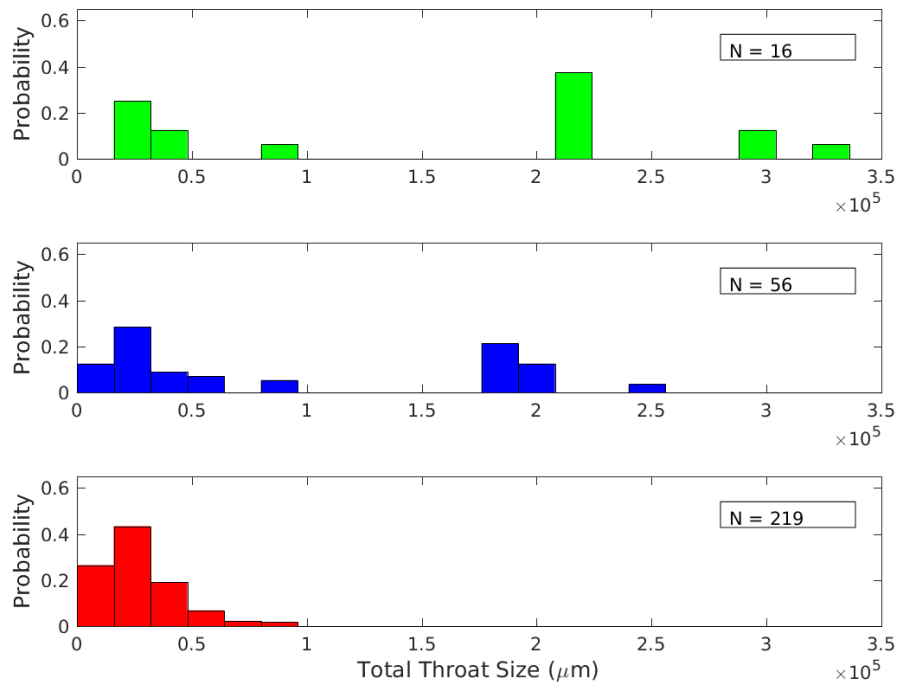
(c) $r_f \geq 52\,500 \mu\text{m}$

Figure 6.27: Probability distribution of r^{max} of paths connecting the top to the bottom for all brine channels in the Butter Point ice core. Only paths greater than 50 steps, or $750 \mu\text{m}$ were considered. Panels a, b, and c represent channels where $r_f < 1500 \mu\text{m}$, $1500 \leq r_f < 5250 \mu\text{m}$, and $r_f \geq 52\,500 \mu\text{m}$, respectively. For all three panels, the colors red, blue, and green represent channels where $r_1 < 1500 \mu\text{m}$, $1500 \leq r_1 < 5250 \mu\text{m}$, and $r_1 \geq 52\,500 \mu\text{m}$, respectively.

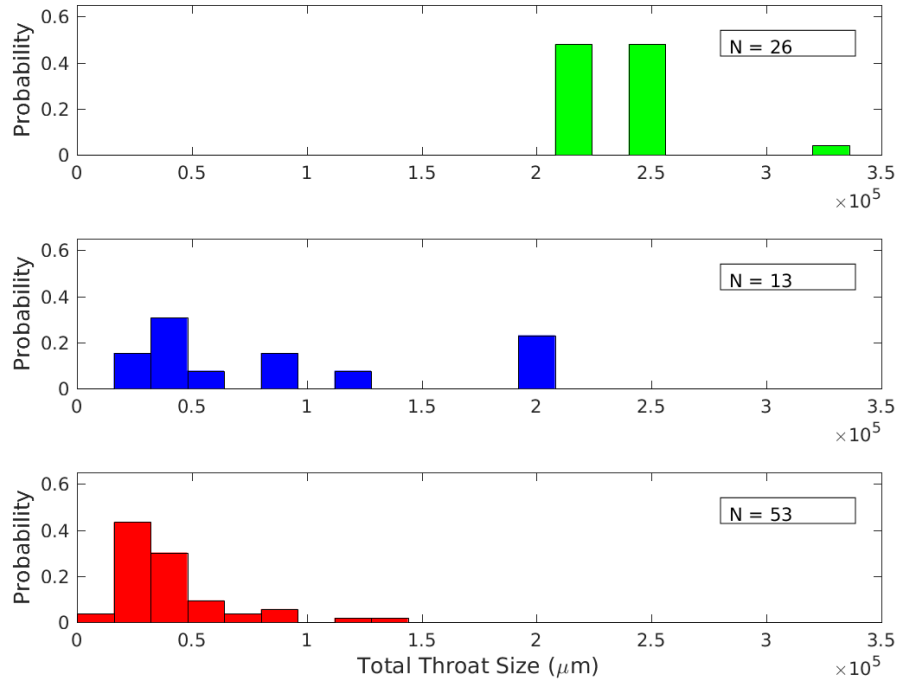
size of the path. These statistics can yield valuable information regarding the location and distribution of “pinch points,” large channels, and total fluid flow through a brine channel. First, the paths were split into 3 categories based upon the ending node (p_f) throat size: $r_f < 1500 \mu\text{m}$, $1500 \leq r_f < 5250 \mu\text{m}$, and $r_f \geq 52\,500 \mu\text{m}$. Then, we split each category into 3 sub-categories based upon the starting node (p_1) throat size, using bins of the same size ($r_1 < 1500 \mu\text{m}$, $1500 \leq r_1 < 5250 \mu\text{m}$, and $r_1 \geq 52\,500 \mu\text{m}$). This division resulted in splitting the paths into 9 separate sub-categories. For each sub-category, we calculated the probability distributions for r^{min} , r^{max} , and summed throat size of the path and we present these histograms in Figs. 6.26, 6.27, and 6.28, respectively. All figures are



(a) $r_f < 1500 \mu\text{m}$



(b) $1500 \leq r_f < 5250 \mu\text{m}$



(c) $r_f \geq 52\,500 \mu\text{m}$

Figure 6.28: Probability distribution of summed throat size of paths connecting the top to the bottom for all brine channels in the Butter Point ice core. Only paths greater than 50 steps, or $750 \mu\text{m}$ were considered. Panels a, b, and c represent channels where $r_f < 1500 \mu\text{m}$, $1500 \leq r_f < 5250 \mu\text{m}$, and $r_f \geq 52\,500 \mu\text{m}$, respectively. For all three panels, the colors red, blue, and green represent channels where $r_1 < 1500 \mu\text{m}$, $1500 \leq r_1 < 5250 \mu\text{m}$, and $r_1 \geq 52\,500 \mu\text{m}$, respectively.

color-coded by r_1 , with red, blue, and green histograms representing small, medium, and large throats, respectively. All histograms show the similar trend that both r_1 and r_f have a strong influence on resulting metrics, with larger r_1 and/or r_f having larger r^{\min} , r^{\max} , and total volumes. r_f had slightly more of an impact, particularly on r^{\min} . There were no clear general trends in regards to the shape of the distributions. However, we note that for the smallest r_f , all three histograms for r^{\min} had a large peak around $30 \mu\text{m}$ (Fig. 6.26). This peak corresponds to the smallest measurable branches, and we could potentially remove these paths from current fluid flow analysis. However, as the ice begins to warm, these “pinch points” are likely to have a significant impact on crossing percolation thresholds.

Conclusions

The primary objective of this chapter was to characterize the brine channel topology, morphology, and connectivity, thereby providing the statistical framework that could be used in creating a sea ice brine channel network model. Since there was roughly a linear correlation between sample temperature and depth in the ice core, trends observed with one variable could easily be converted to the other. Here we have presented quantitative metrics of the brine channel topological complexity, degree of connectivity, average and individual throat sizes, frequency of splitting and re-merging of branches, and minimum, maximum, spatial extent, and total size. The figures above represent a sampling of the different probability distributions that we can create for different subsets of the total collection of brine channels in a given core. When creating the full model, we would need to incorporate the probability distributions for all permutations of the parameter space.

The next step for this work would be to create the brine channel network model from the statistics presented here. For a sample at a given depth/temperature, first an initial set of nodes at the top height would be selected, where the nodes have throat sizes consistent with the probability distributions shown here. Branches could grow or shrink, split into multiple branches, merge with other branches, remain constant, or stop, all with probabilities dependent upon the given node throat size, depth/temperature, and proximity to other nodes. Although we showed many of these statistics in the figures of this chapter, we have as of yet not examined the influence of proximity of neighboring nodes. Further, there are parameter settings that need to be specified and may vary depending upon the question under investigation. For example, investigations of fluid flow through brine channels may use a different definition of connectivity than a study of electrical conductivity through sea ice. Here we have defined connectivity to be 26-connected pixels (face, edge, and corners) in three-dimensions and 8-connected pixels in two-dimensions (edge and corners), while 6-connected pixels (three-dimensions) and 4-connected pixels (two-dimensions) may be

more relevant to current fluid flow capacity. Conversely, the former definition may be more informative for certain applications such as studying electrical conductivity because corner adjacency is sufficient for transmitting electrical current. Likewise, it may be appropriate for analyzing the location of brine channels after a small degree of warming since corner-adjacent brine channels will become fully connected. However, once the appropriate parameters have been defined, the model described herein can help address questions such as how microstructural changes may be path dependent (e.g., whether to consider both upwards and downwards flow), how fluid flow may vary with depth, and what are the percolation implications of temperature fluctuations in an ice core. In summary, we successfully developed a method to incorporate μ CT data on the geometry of brine channels, whereby we can parameterize the pore networks using topological techniques that can be adjusted for depth and temperature, correlated with physical properties, and used in dynamical models of sea ice.

CONCLUSION AND FUTURE WORK

Climate change is having a drastic effect on polar sea ice and potentially on ocean-ice-atmospheric interactions. The porous structure of the ice provides a labyrinth of brine channels that transport heat, gases, salts, and other chemical species between the ocean and the boundary layer. Understanding the intricate details of the sea ice microstructure is critical for modeling and predicting changes in these transport processes. When the ocean freezes, salts are rejected into a saline network of brine channels that can transport salts upwards or downwards as a result of density differences and pressure and temperature fluctuations. Excluding the frazil ice near the surface, the bulk of the ice has a columnar structure due to the lamellae in the skeletal region during initial growth. The brine network fills the spaces between individual lamellae. After several months of sea ice growth, we found the salts to still be located with this inherent microstructure.

In this thesis, we started by examining evidence for the photochemically driven tropospheric reactions that occur once salts such as bromide reach the snowpack. By examining the mass ratio of Br^-/Cl^- in sea ice, surface snow, and blowing snow, we found that bromide becomes strongly depleted relative to chloride in lofted snow. This suggests that blowing snow particles provide a viable surface for heterogeneous reactions that produce reactive bromine, which can later be a catalyst for tropospheric ozone depletion events. This research, however, does not preclude other surfaces, such as the surface snowpack, from also providing an interface for these reactions. Thus, we conclude that lofted snow is one of the surfaces responsible for initiating the release of bromine into the troposphere.

Prior to reaching the snowpack, salts are found primarily in brine channels and layers, which have a structure that is inherited from the initial growth mechanism. We developed a technique using synchrotron x-ray micro-fluorescence to map the microstructural location

of various impurities in sea ice confirming our hypothesis. As part of this work, we quantified the distribution of Br and noted specific features of the sea ice structure that different elements can elucidate. Results showed Br concentrations in brine channels to be up to ten times larger than the $5 - 10 \text{ g/m}^3$ bulk sea ice concentrations. Elemental maps of Cl, K, and Ca detected salts almost entirely at grain boundaries near the surface, while Br and Sr maps enabled detection of deeper features, such as brine layers.

The spacing of the salts identified with XRF matched what we observed using μCT , thereby confirming that salts are indeed restricted to vertically oriented brine channels and layers. We then developed metrics to describe the shape, size, and topology of the different phases in sea ice. Brine channels showed increased branching at lower depths, while measurements of brine channel connectivity detected frazil/columnar transitions, as well as regions with decreased grain size. From these measurements, we then constructed a topological network model, allowing for a more detailed analysis of brine channel geometry, topological complexity, and degree of connectivity. This yielded a statistical framework with probability distributions of different brine channel metrics that can later be incorporated into a dynamical model of sea ice.

The brine network model that we created has far reaching applications for the sea ice community, as well as for the greater porous media community. The sea ice coverage in the Arctic is becoming increasingly thinner with a higher percentage of first-year ice, with its corresponding greater brine volume fraction (Perovich and Richter-Menge, 2009). Our model provides a method for both mapping out the current brine pathways and predicting how the pathways may change with temperature. Since the brine network transports salts to the snow surface, knowing the rate at which brine moves through the ice aids in predicting rates of chemical reactions in the snow surface requiring these salts. In Antarctica, there has been recent observations of large amounts of platelet ice underneath the sea ice due to the melting of the West Antarctic Ice Sheet (Langhorne et al., 2015). Our model can help predict the influence of increased amounts of platelet ice on the connectivity of the

brine channels. Further, the brine network strongly influences both the electric and thermal conductivity of the ice (Thomas and Dieckmann, 2009). Accurate three-dimensional models of the brine network in sea ice can improve predictions of these conductivities and help interpret corresponding sea ice observations. The sea ice biological community is interested in the many bacteria and sea ice algae living in the brine channels of the skeletal layer, and our model increases knowledge of their unique habitat (e.g., Lizotte, 2001; Thomas and Dieckmann, 2009). Beyond sea ice, researchers of other porous media such as soils, rocks, and bones are interested in understanding the connectivity and permeability of their respective media (e.g., Campbell et al., 2007; Costanza-Robinson et al., 2008; Santiago et al., 2014). We created the model in this thesis for any binarized phase of a three-dimensional media, and thus, we can apply it to research in a wide variety of fields.

The future direction of this work should be to create the full network model that can statistically produce an ensemble of brine channels given a depth and/or temperature. By altering either parameter, brine channels could grow or shrink accordingly, with consequences on whether they split into multiple branches, join with other branches, or die out. To complete this model, we need more work in obtaining measurements of sea ice samples at warmer temperatures, particularly for samples near 5% brine volume fraction. This would enable investigation of the physical basis behind the “Rule of Fives,” and to study under what conditions it may or may not hold. Further, we can address other permeability related questions, and how transport processes may change as the sea ice itself is changing.

ADDITIONAL SEA ICE ION CONCENTRATIONS AND CORRELATION PLOTS

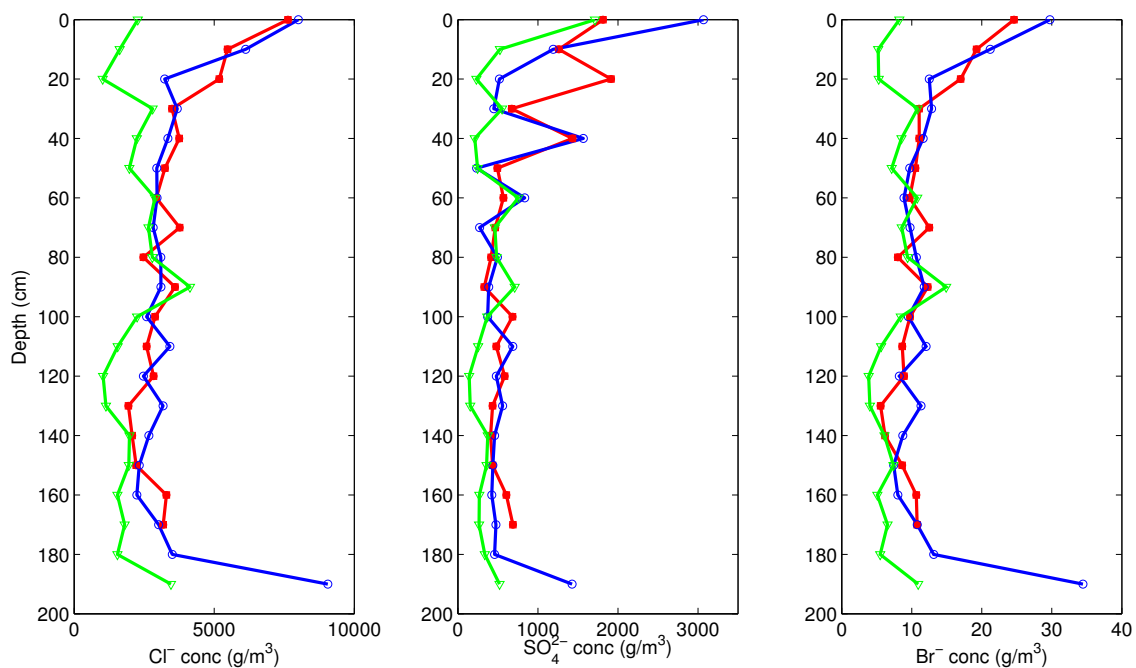


Figure A.1: Anion concentrations for the multi-year ice core collected near Scott Base is shown in green. For comparison, the anion concentrations for the Butter Point and Iceberg Site ice cores that were presented in Fig. 3.1 are shown in red and blue, respectively.

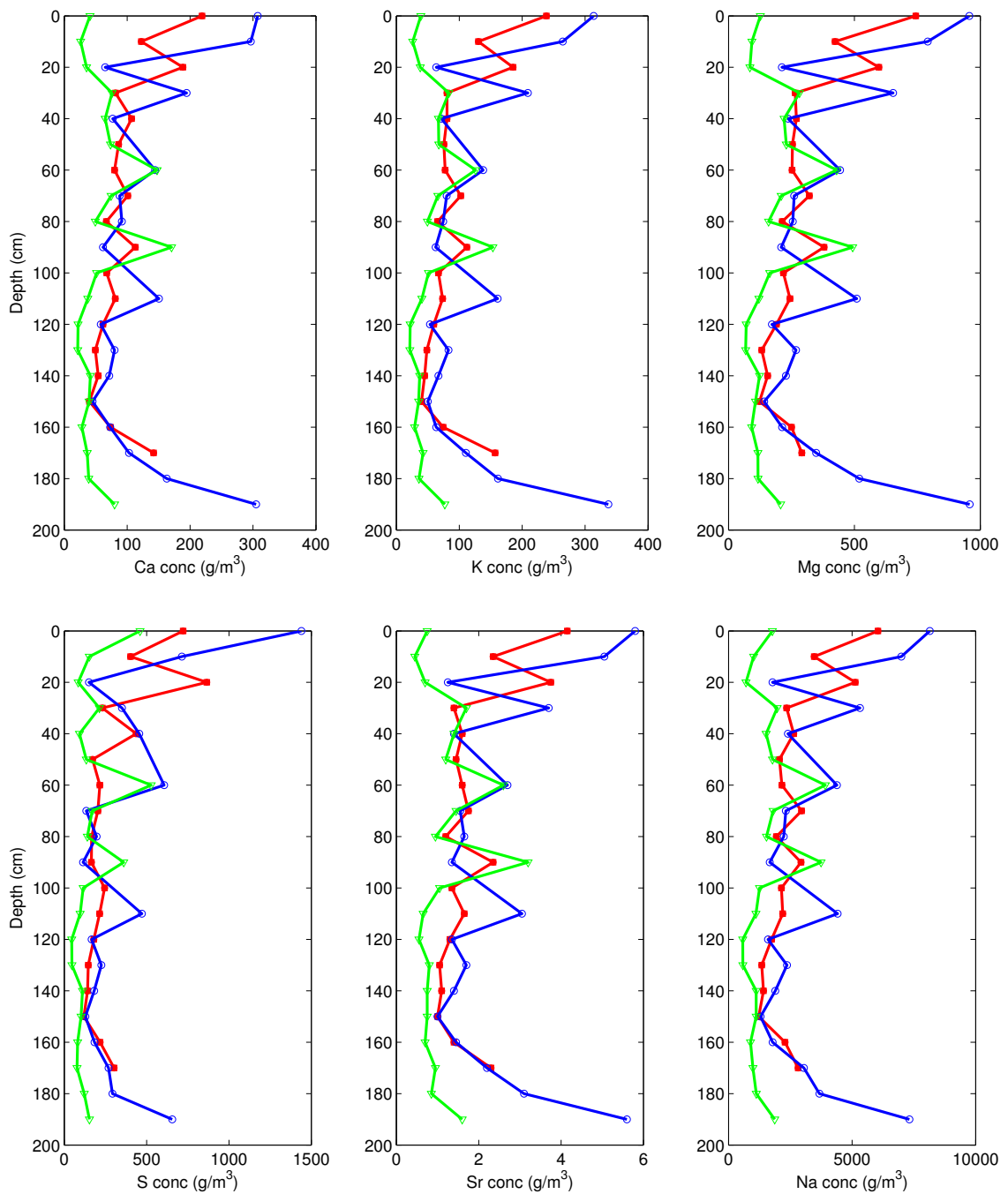
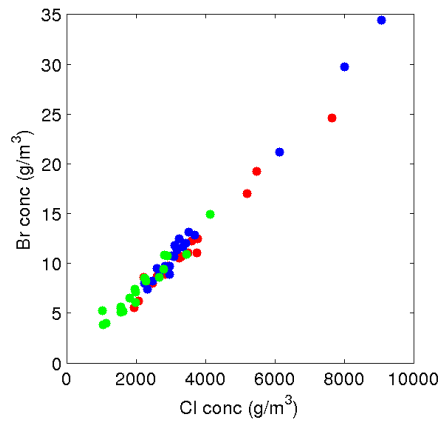
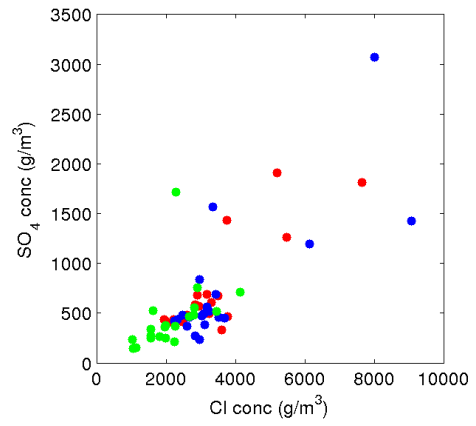


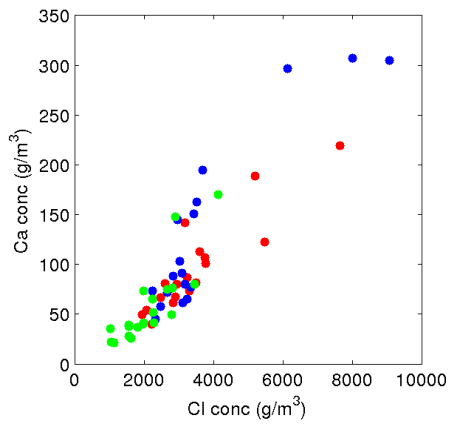
Figure A.2: Cations concentrations of Ca, K, Mg, S, Sr, and Na for sea ice cores. Profiles for the Butter Point, Iceberg Site, and Scott Base ice cores are shown in red, blue, and green, respectively.



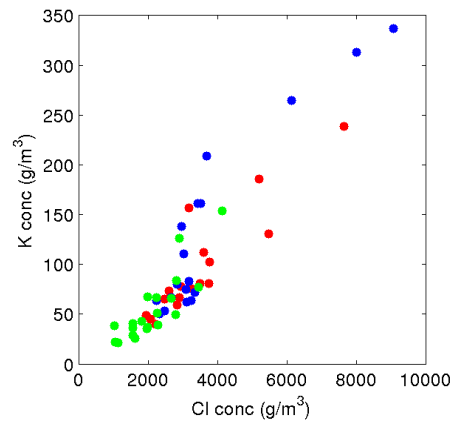
(a)



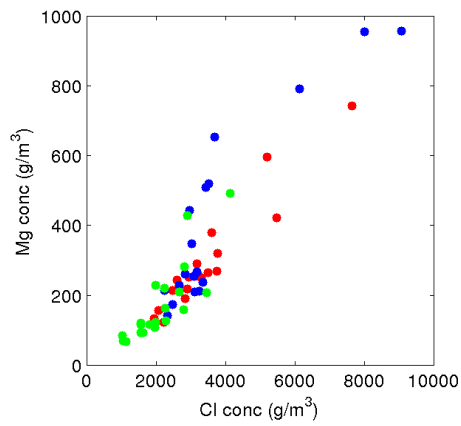
(b)



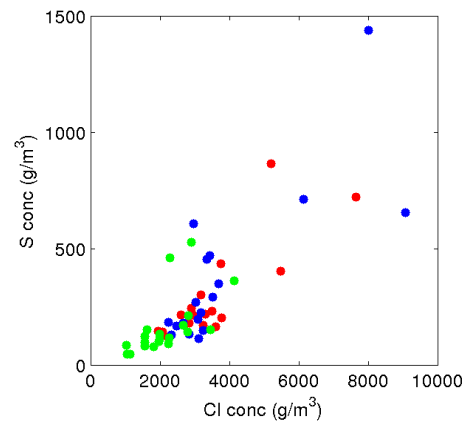
(c)



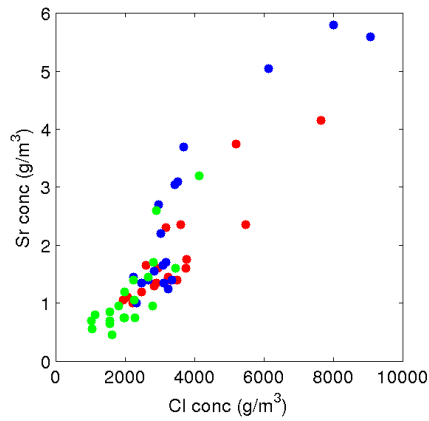
(d)



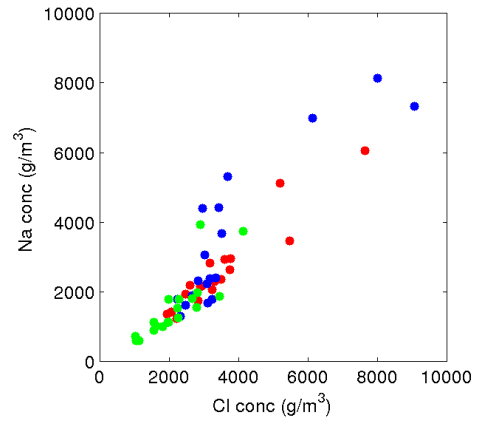
(e)



(f)

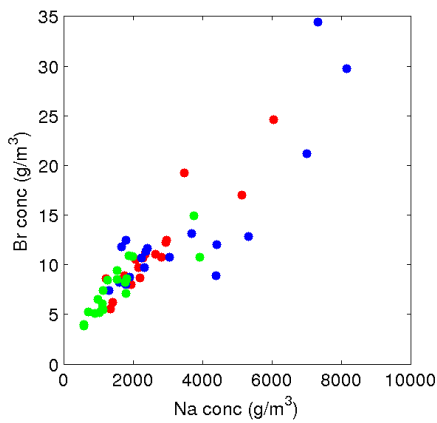


(g)

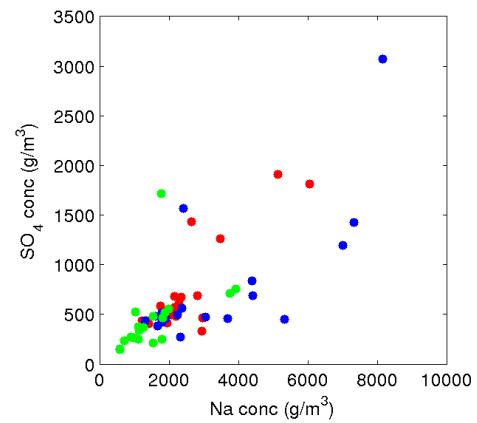


(h)

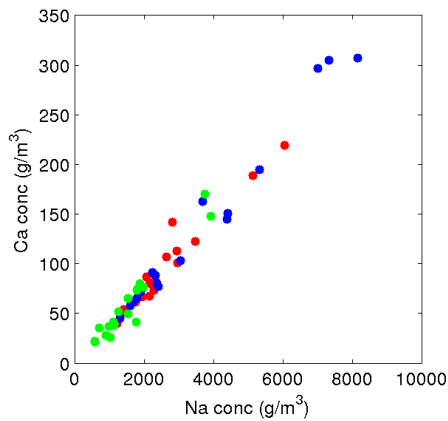
Figure A.3: Correlation plots of all measured ions versus Cl. Samples from the Butter Point, Iceberg Site, and Scott base ice cores are shown in red, blue, and green, respectively.



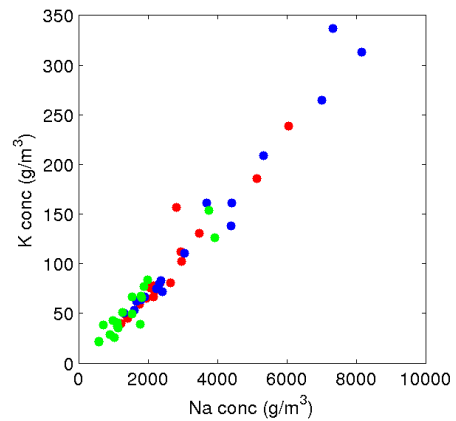
(a)



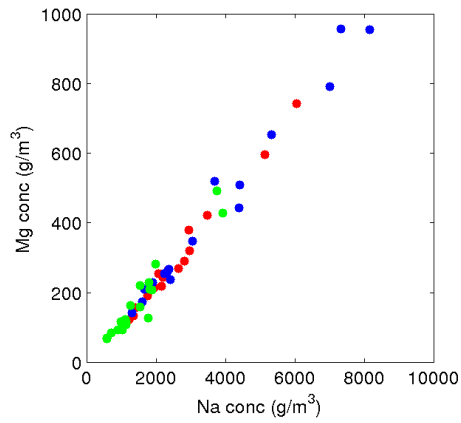
(b)



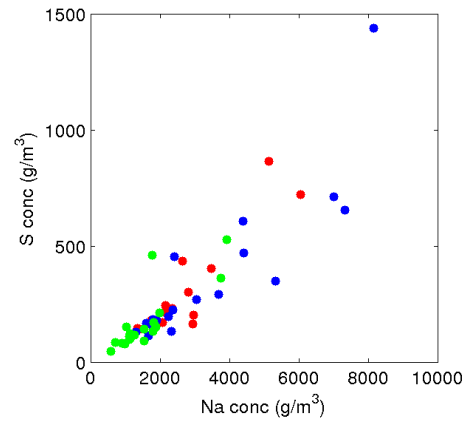
(c)



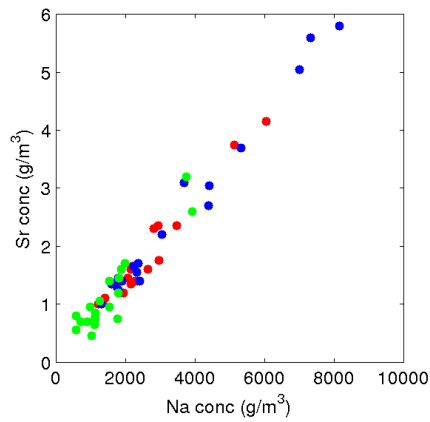
(d)



(e)



(f)



(g)

Figure A.4: Correlation plots of all measured ions versus Na. Samples from the Butter Point, Iceberg Site, and Scott base ice cores are shown in red, blue, and green, respectively.

XRF METAL ELEMENTAL MAPS

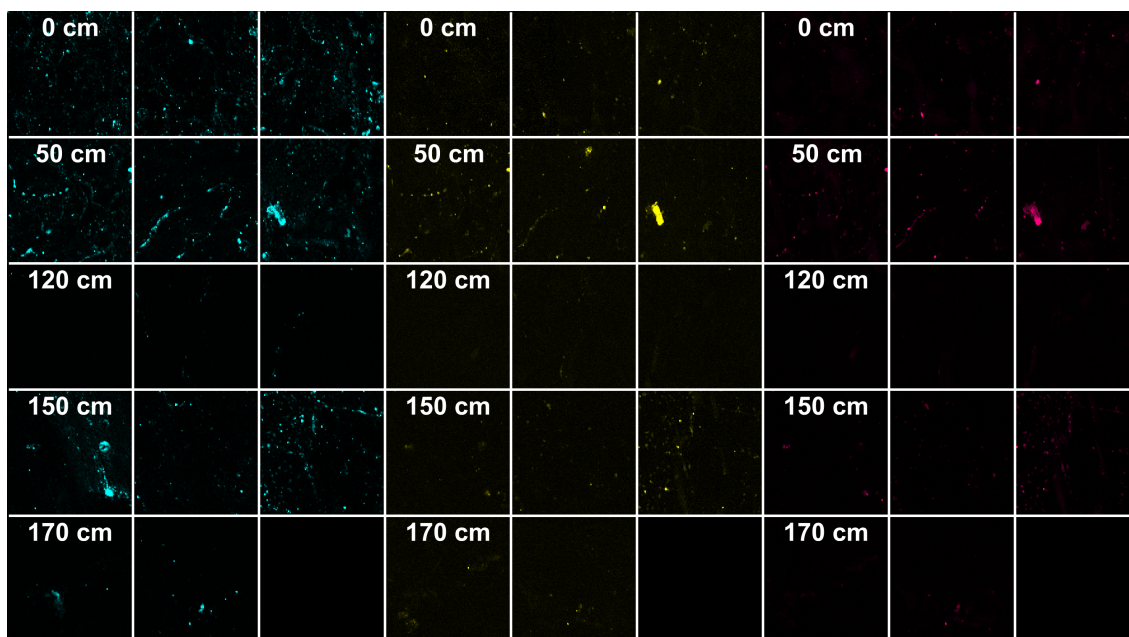


Figure B.1: XRF elemental maps for Fe (teal), Cu (yellow), and Zn (magenta) for subsamples taken at 10 cm intervals along the Butter Point ice core. For a given depth, there is a triplicate of sample scanned, each over a $2 \text{ mm} \times 2 \text{ mm}$ region.

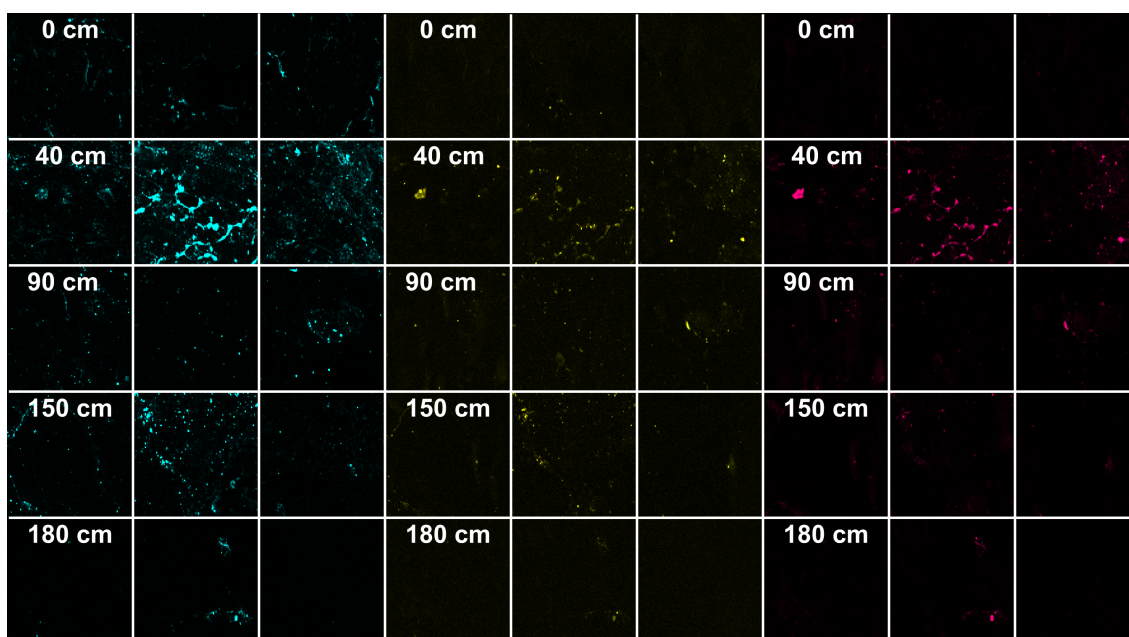
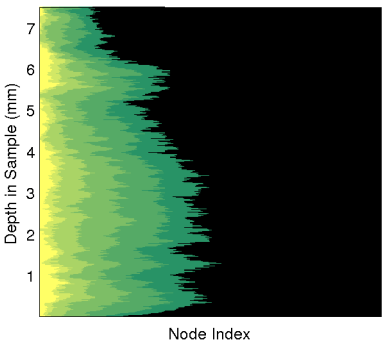
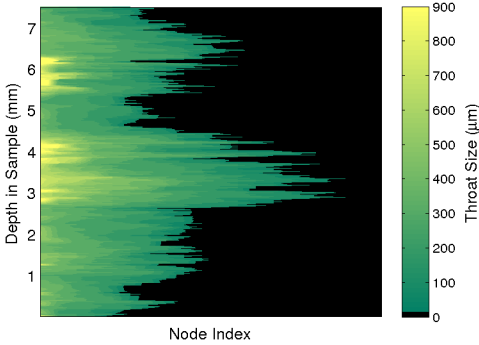


Figure B.2: XRF elemental maps for Fe (teal), Cu (yellow), and Zn (magenta) for subsamples taken at 10 cm intervals along the Iceberg Site ice core. For a given depth, there is a triplicate of sample scanned, each over a $2\text{ mm} \times 2\text{ mm}$ region.

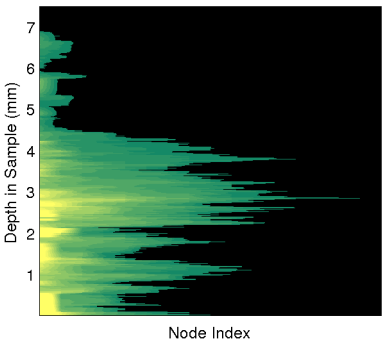
ADDITIONAL THROAT SIZE DISTRIBUTIONS



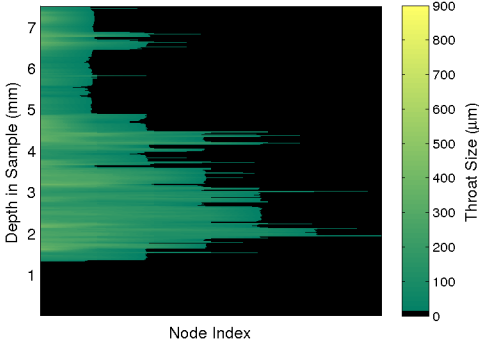
(a) Depth 0 cm, Butter Point



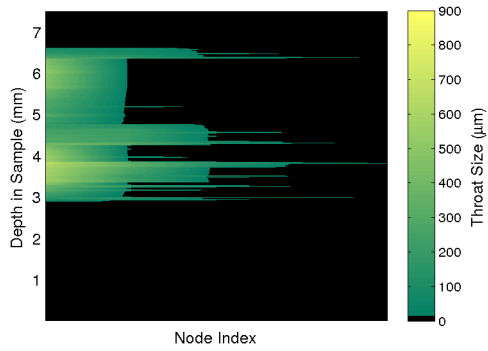
(b) Depth 10 cm, Butter Point



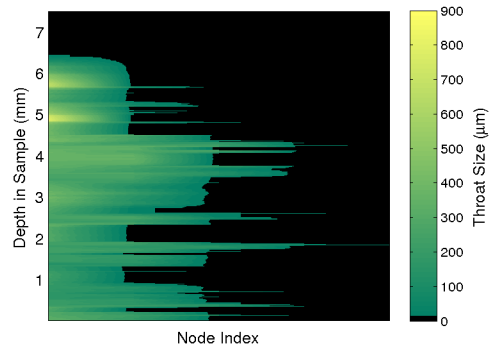
(c) Depth 20 cm, Butter Point



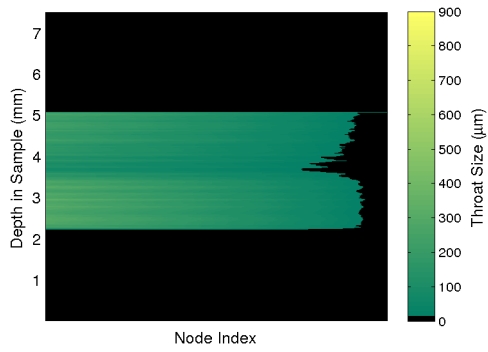
(d) Depth 30 cm, Butter Point



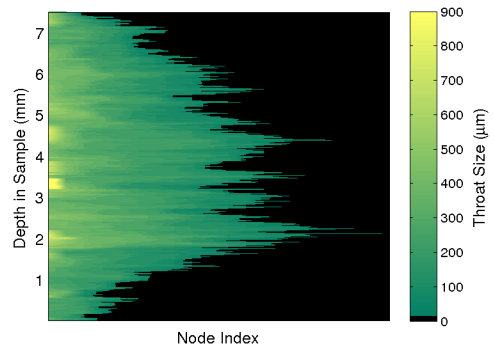
(e) Depth 40 cm, Butter Point



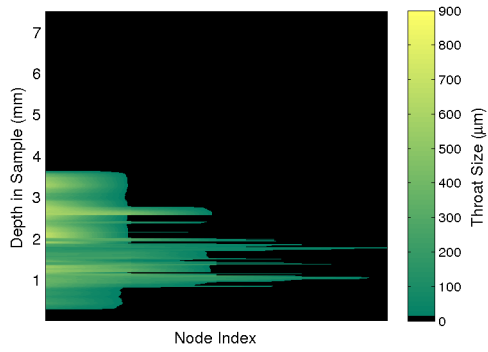
(f) Depth 50 cm, Butter Point



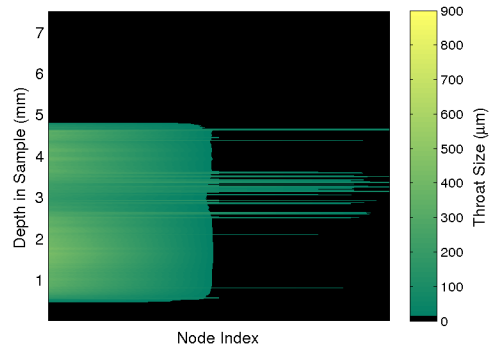
(g) Depth 60 cm, Butter Point



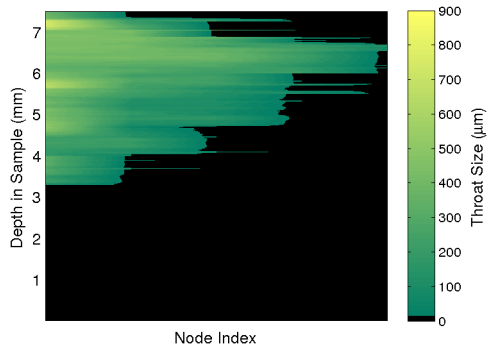
(h) Depth 70 cm, Butter Point



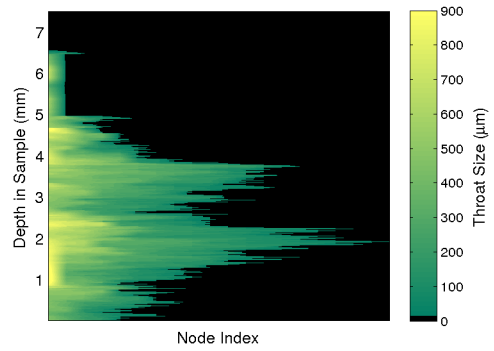
(i) Depth 80 cm, Butter Point



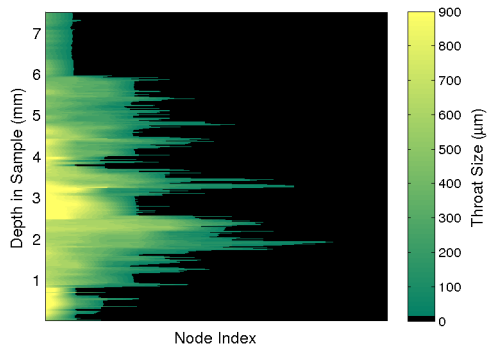
(j) Depth 90 cm, Butter Point



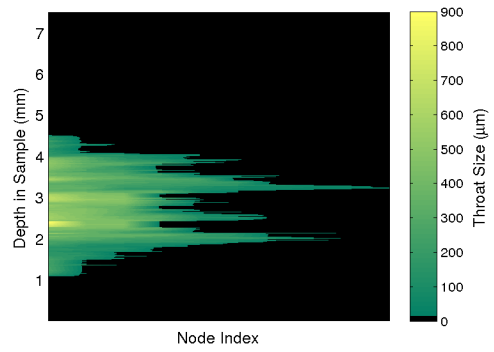
(k) Depth 100 cm, Butter Point



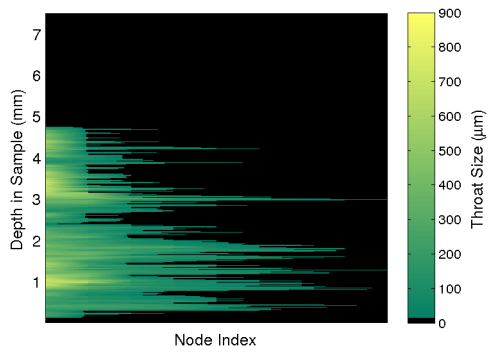
(l) Depth 110 cm, Butter Point



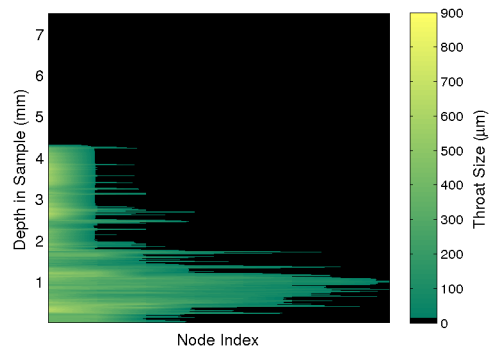
(m) Depth 120 cm, Butter Point



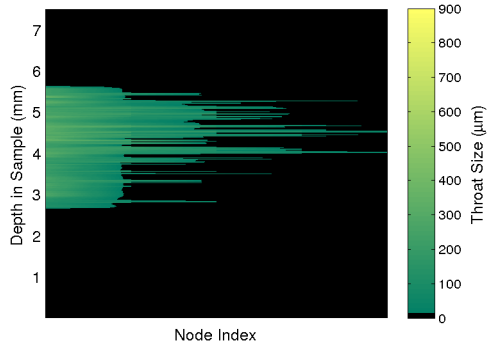
(n) Depth 130 cm, Butter Point



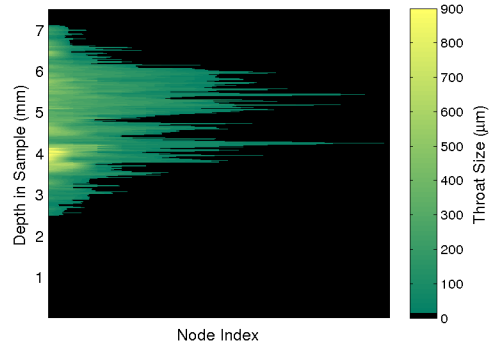
(o) Depth 140 cm, Butter Point



(p) Depth 150 cm, Butter Point

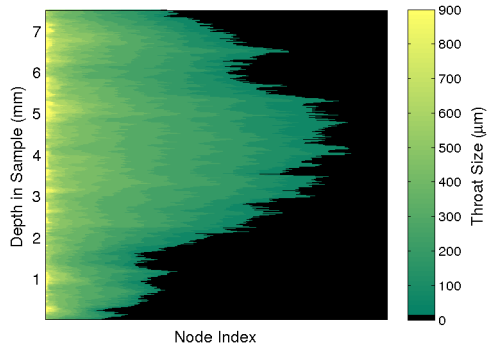


(q) Depth 160 cm, Butter Point

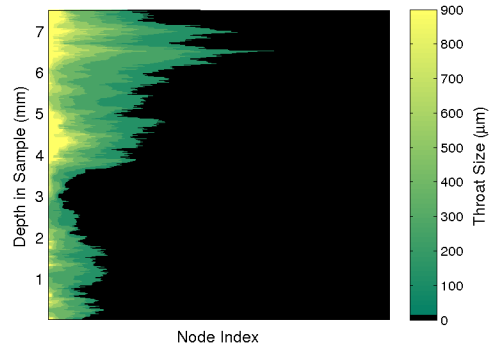


(r) Depth 170 cm, Butter Point

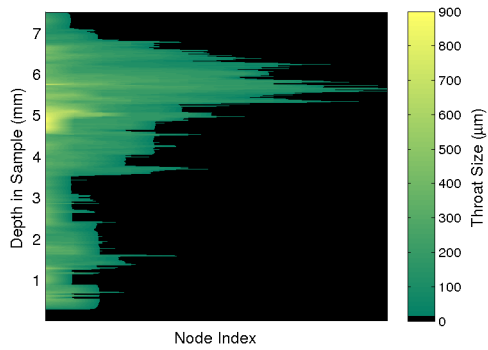
Figure C.3: r_i of each node for the largest channel of all samples in the Butter Point ice core.



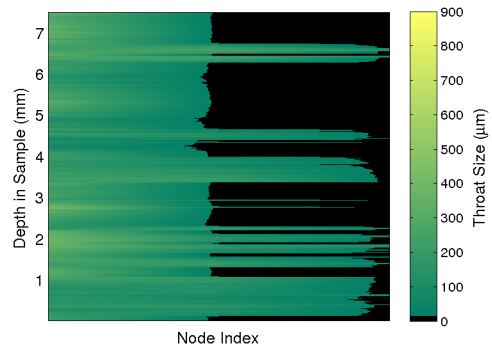
(a) Depth 0 cm, Iceberg Site



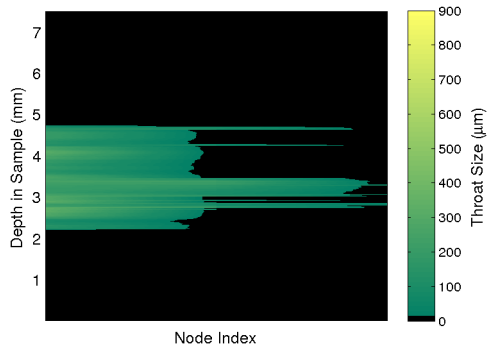
(b) Depth 10 cm, Iceberg Site



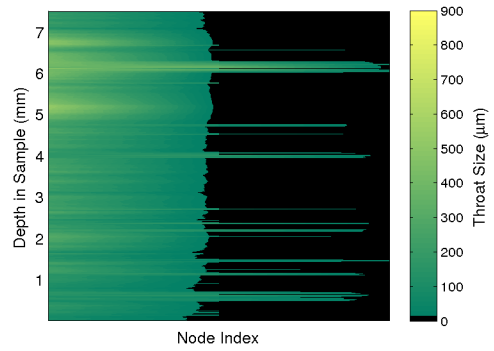
(c) Depth 20 cm, Iceberg Site



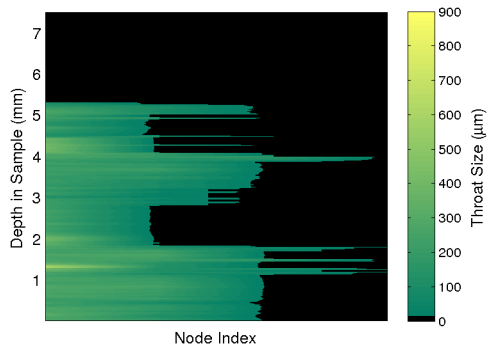
(d) Depth 30 cm, Iceberg Site



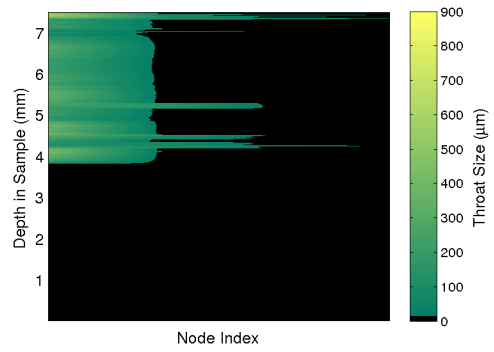
(e) Depth 40 cm, Iceberg Site



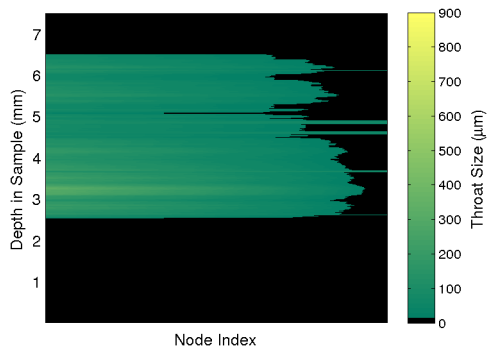
(f) Depth 50 cm, Iceberg Site



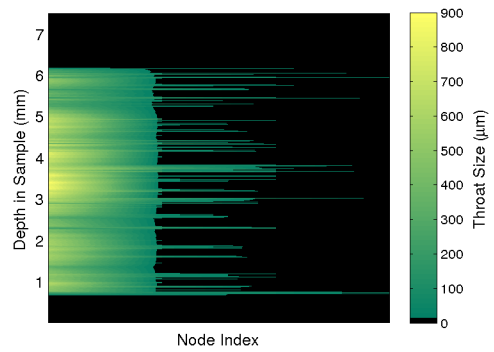
(g) Depth 60 cm, Iceberg Site



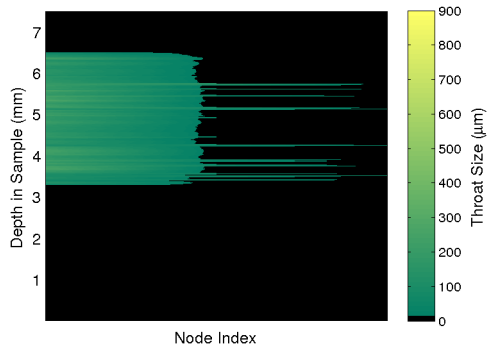
(h) Depth 70 cm, Iceberg Site



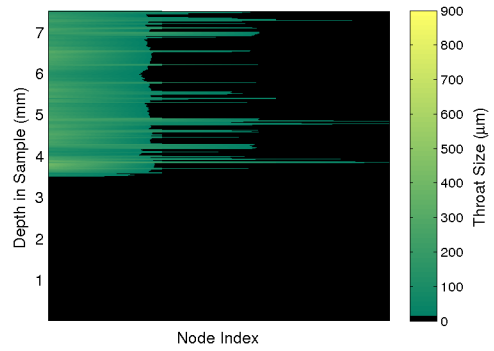
(i) Depth 80 cm, Iceberg Site



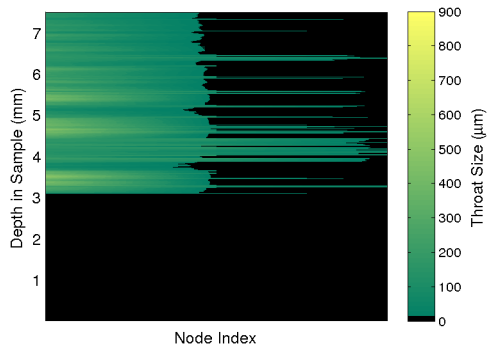
(j) Depth 90 cm, Iceberg Site



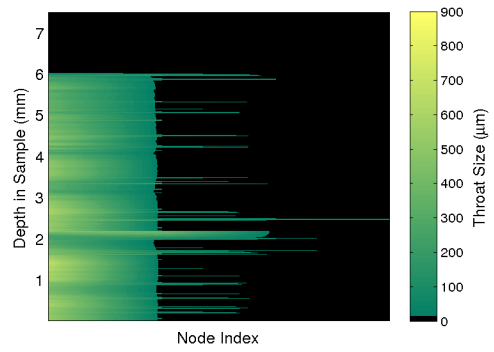
(k) Depth 100 cm, Iceberg Site



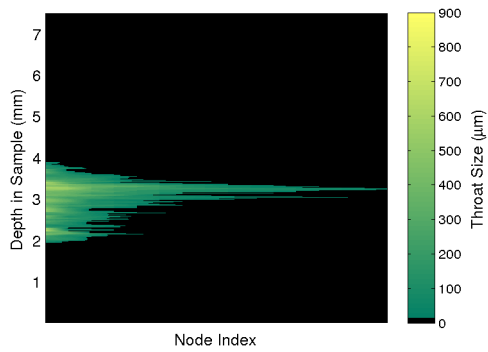
(l) Depth 110 cm, Iceberg Site



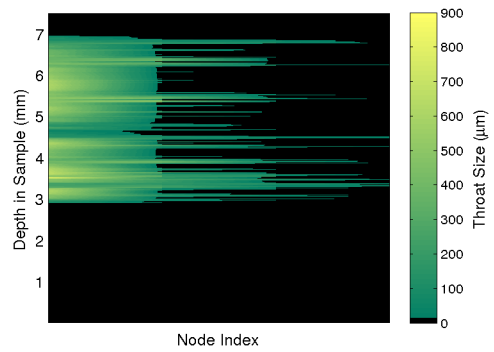
(m) Depth 120 cm, Iceberg Site



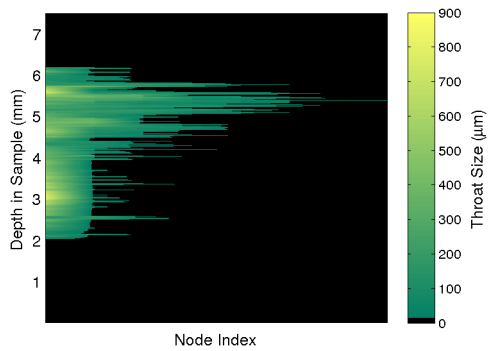
(n) Depth 130 cm, Iceberg Site



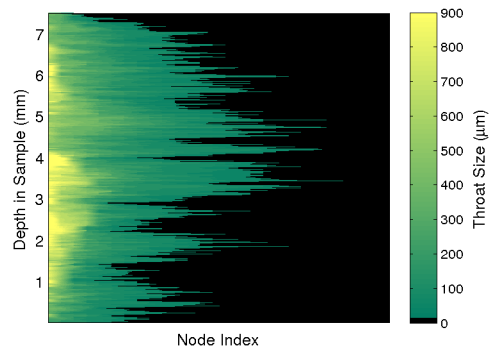
(o) Depth 140 cm, Iceberg Site



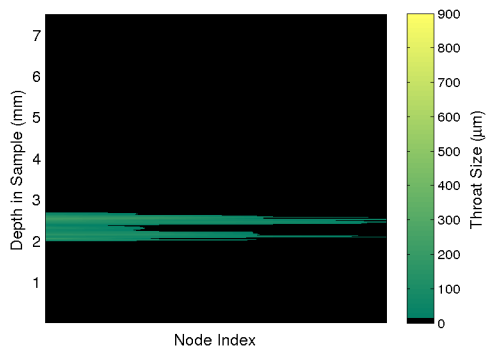
(p) Depth 150 cm, Iceberg Site



(q) Depth 160 cm, Iceberg Site



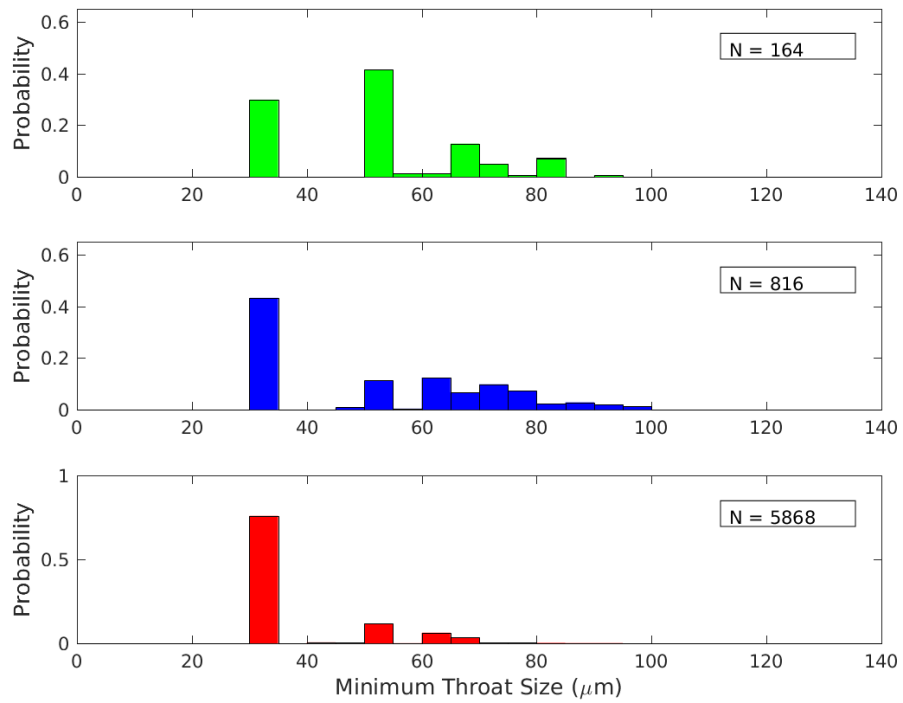
(r) Depth 170 cm, Iceberg Site



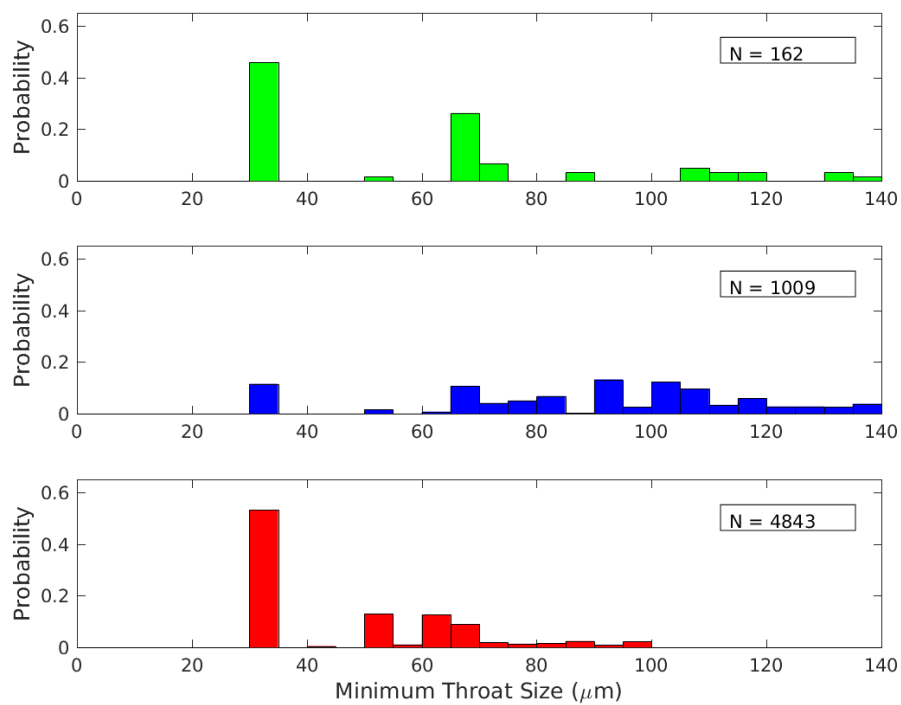
(s) Depth 180 cm, Iceberg Site

Figure C.6: r_i of each node for the largest channel of all samples in the Iceberg Site ice core.

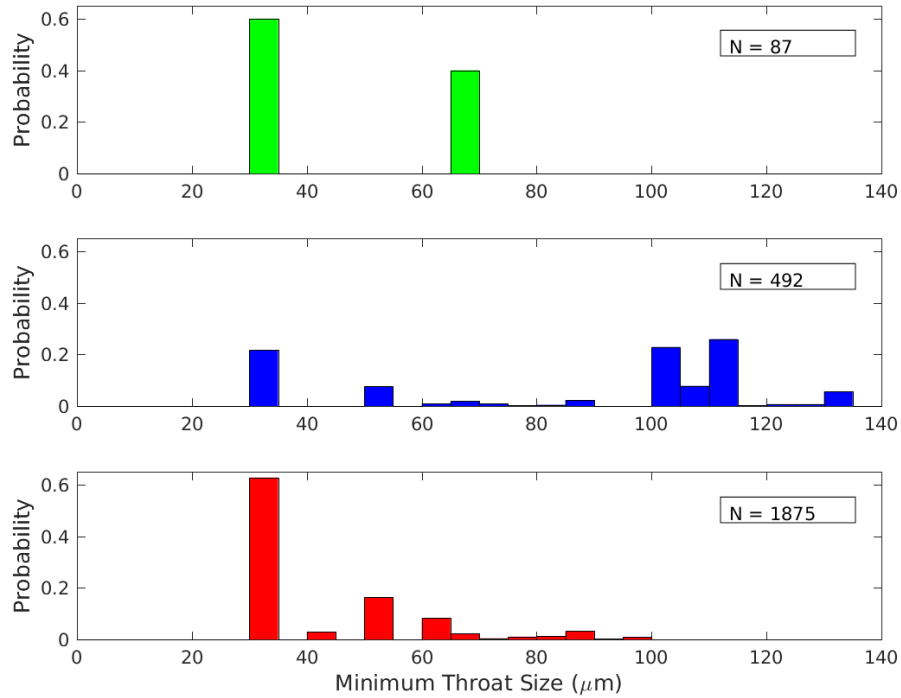
PROBABILITY DISTRIBUTIONS OF STATISTICS FOR DIRECTED PATHS



(a) $r_f < 1,500 \mu\text{m}$

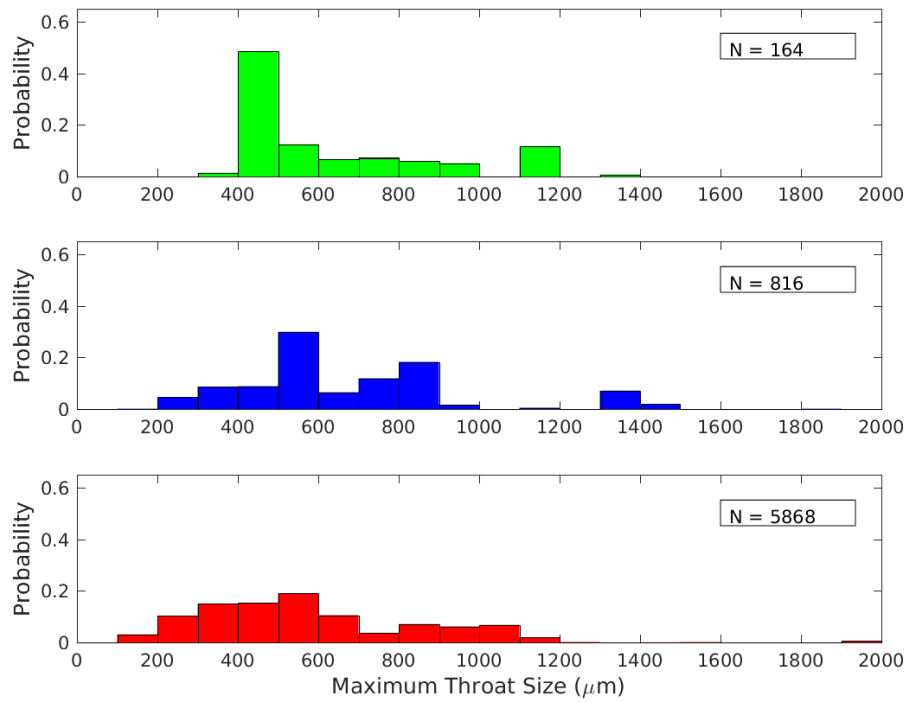


(b) $1,500 \leq r_f < 5,250 \mu\text{m}$

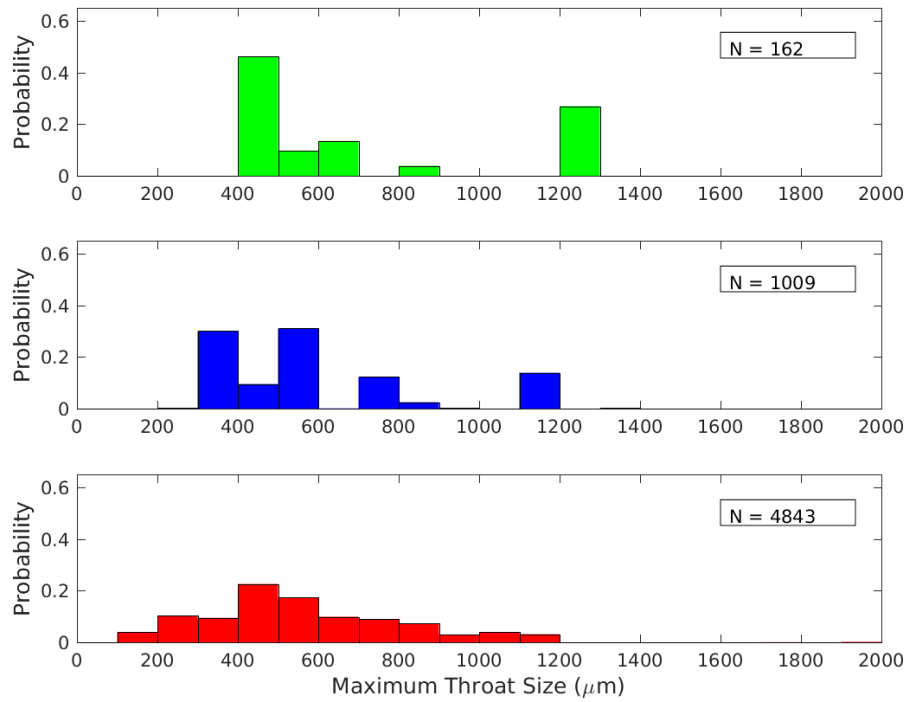


(c) $r_f \geq 52,500 \mu\text{m}$

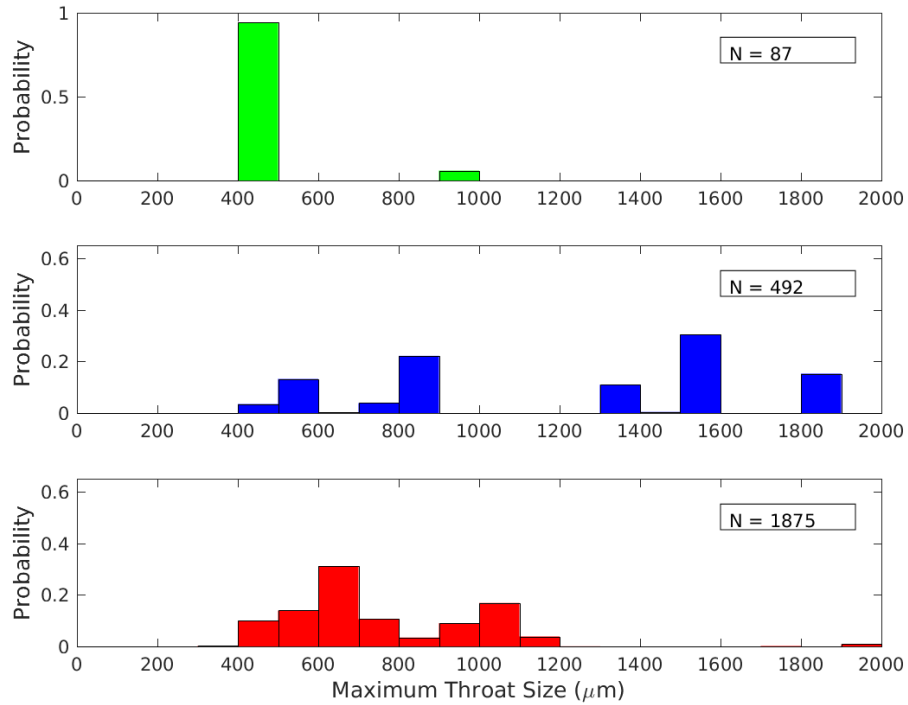
Figure D.2: Probability distribution of r^{\min} of longest directed paths from p_1 for all brine channels in the Butter Point ice core. Only paths greater than 50 steps, or $750 \mu\text{m}$ were considered. Panels a, b, and c represent channels where $r_f < 1,500 \mu\text{m}$, $1,500 \leq r_f < 5,250 \mu\text{m}$, and $r_f \geq 52,500 \mu\text{m}$, respectively. For all three panels, the colors red, blue, and green represent channels where $r_1 < 1,500 \mu\text{m}$, $1,500 \leq r_1 < 5,250 \mu\text{m}$, and $r_1 \geq 52,500 \mu\text{m}$, respectively.



(a) $r_f < 1,500 \mu\text{m}$

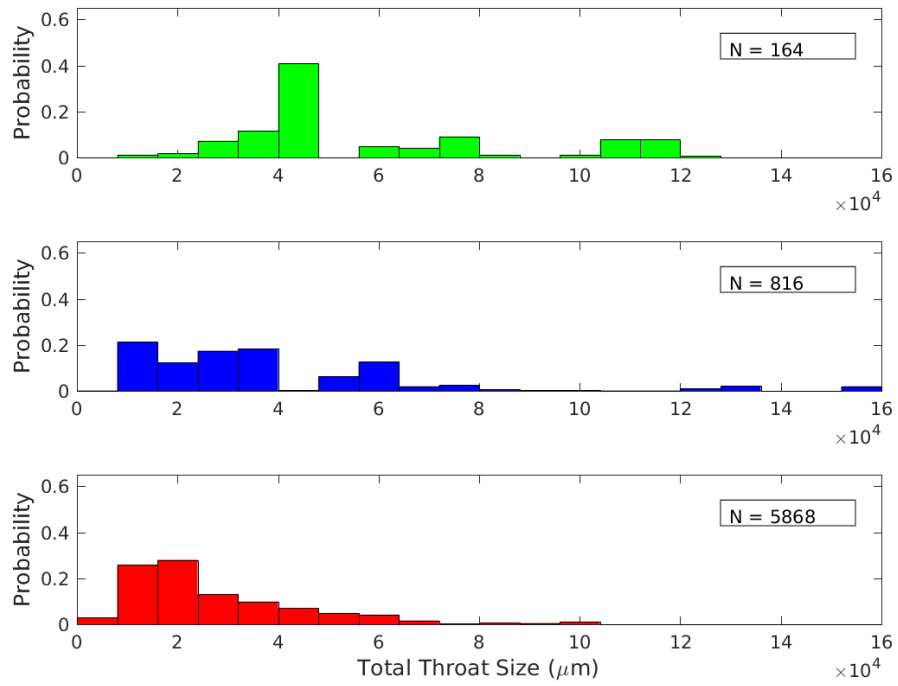


(b) $1,500 \leq r_f < 5,250 \mu\text{m}$

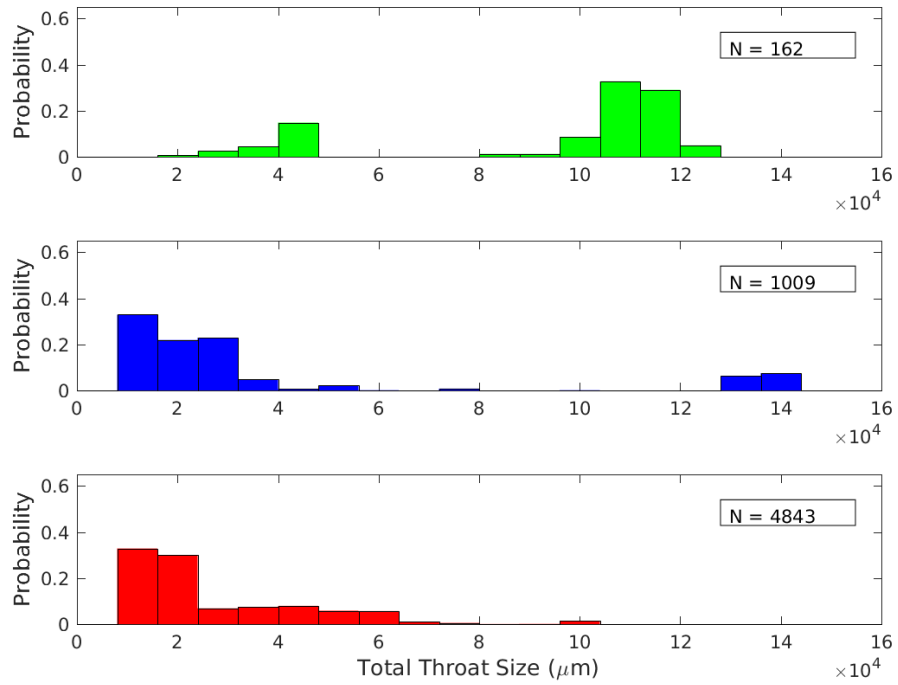


(c) $r_f \geq 52,500 \mu\text{m}$

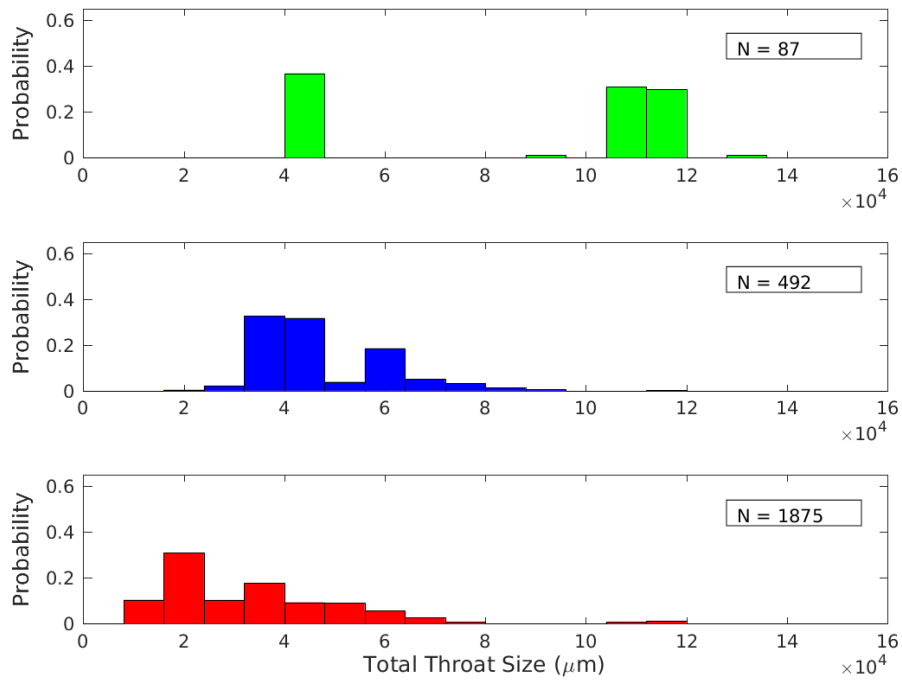
Figure D.3: Probability distribution of r^{max} of paths connecting the top to the bottom for all brine channels in the Butter Point ice core. Only paths greater than 50 steps, or $750 \mu\text{m}$ were considered. Panels a, b, and c represent channels where $r_f < 1,500 \mu\text{m}$, $1,500 \leq r_f < 5,250 \mu\text{m}$, and $r_f \geq 52,500 \mu\text{m}$, respectively. For all three panels, the colors red, blue, and green represent channels where $r_1 < 1,500 \mu\text{m}$, $1,500 \leq r_1 < 5,250 \mu\text{m}$, and $r_1 \geq 52,500 \mu\text{m}$, respectively.



(a) $r_f < 1,500 \mu\text{m}$



(b) $1,500 \leq r_f < 5,250 \mu\text{m}$



(c) $r_f \geq 52,500 \mu\text{m}$

Figure D.4: Probability distribution of summed throat size of paths connecting the top to the bottom for all brine channels in the Butter Point ice core. Only paths greater than 50 steps, or $750 \mu\text{m}$ were considered. Panels a, b, and c represent channels where $r_f < 1,500 \mu\text{m}$, $1,500 \leq r_f < 5,250 \mu\text{m}$, and $r_f \geq 52,500 \mu\text{m}$, respectively. For all three panels, the colors red, blue, and green represent channels where $r_1 < 1,500 \mu\text{m}$, $1,500 \leq r_1 < 5,250 \mu\text{m}$, and $r_1 \geq 52,500 \mu\text{m}$, respectively.

LITERATURE CITED

- Abbatt, J. P. D., Thomas, J. L., Abrahamsson, K., Boxe, C., Granfors, A., Jones, A. E., King, M. D., Saiz-Lopez, A., Shepson, P. B., Sodeau, J., Toohey, D. W., Toubin, C., von Glasow, R., Wren, S. N., and Yang, X.: Halogen Activation Via Interactions With Environmental Ice and Snow in the Polar Lower Troposphere and Other Regions, *Atmos. Chem. Phys.*, 12, 6237–6271, doi:10.5194/acp-12-6237-2012, 2012.
- Adams, J. W., Holmes, N. S., and Crowley, J. N.: Uptake and Reactions of HOBr on Frozen and Dry NaCl/NaBr Surface Between 253 and 233 K, *Atmos. Chem. Phys.*, 2, 79–91, 2002.
- Albert, M. R., Grannas, A. M., Bottenheim, J., Shepson, P. B., and Perron, F. E.: Processes and Properties of Snow-Air Transfer in the High Arctic with Application to Interstitial Ozone at Alert, Canada, *Atmos. Environ.*, 36, 2779–2787, 2002.
- Angelis, M. D., Morel-Fourcade, M.-C., Barnola, J.-M., Susini, J., and Duval, P.: Brine Micro-Droplets and Solid Inclusions in Accreted Ice from Lake Vostok (East Antarctica), *Geophys. Res. Lett.*, 32, 2005.
- Arrigo, K. R., Worthen, D. L., Lizotte, M. P., Dixon, P., and Dieckmann, G.: Primary Production in Antarctic Sea Ice, *Science*, 276, 394–397, doi:10.1126/science.276.5311.394, 1997.
- Assur, A.: Composition of Sea Ice and its Tensile Strength, in: *Arctic Sea Ice*, vol. 598, pp. 106–138, US National Academy of Sciences, National Research Council, Easton, MD, 1958.
- Backstrom, L. G. E. and Eicken, H.: Capacitance Probe Measurements of Brine Volume and Bulk Salinity in First-Year Sea Ice, *Cold Reg. Sci. Tech.*, 46, 167–180, 2006.
- Baker, I., Liu, F., Jia, K., Hu, X., Cullen, D., and Dudley, M.: Dynamic Observations of Dislocation/Grain-Boundary Interactions in Ice, *Ann. Glaciol.*, 31, 236–240, 2000.
- Barrie, L. A., Bottenheim, J. W., Schnell, R. C., Crutzen, P. J., and Rasmussen, R. A.: Ozone Destruction and Photochemical-Reactions at Polar Sunrise in the Lower Arctic Atmosphere, *Nature*, 334, 138–141, 1988.
- Batenburg, K. J. and Sijbers, J.: Optimal threshold Selection for Tomogram Segmentation by Projection Distance Minimization, *IEEE T. Med. Imaging*, 28, 676–686, 2009.
- Baveye, P. C., Laba, M., w. Otten, Bouckaert, L., Sterpaio, P. D., Goswami, R. R., Grinev, D., Houston, A., Yaoping, Y., Liu, J., Mooney, S., Pajor, R., Sleutel, S., Tarquis, A., Wang, W., Wei, Q., and Sezgin, M.: Observer-Dependent Variability of the Thresholding Step in the Quantitative Analysis of Soil Images and X-Ray Microtomography Data, *Geoderma*, 157, 51–63, 2010.
- Bragg, W. H.: The Crystal Structure of Ice, *P. Phys. Soc. Lond.*, 34, 98, 1921.
- Burrows, J. P., Weber, M., Buchwitz, M., Rozanov, V., Ladstätter-Weissenmayer, A., Richter, A., DeBeek, R., Hoogen, R., Bramstedt, K., Eichmann, K., and Eisinger, M.: The Global Ozone Monitoring Experiment (GOME): Mission Concept and First Scientific Results, *J. Atmos. Sci.*, 56, 151–175, 1999.

- Campbell, H. R. B. G. M., Klinck, R. J., MacNeil, J. A., and Boyd, S. K.: Automatic Segmentation of Cortical and Trabecular Compartments Based on a Dual Threshold Technique for In Vivo Micro-CT Bone Analysis, *Bone*, 41, 505–515, 2007.
- Chen, S. and Baker, I.: Evolution of Individual Snowflakes during Metamorphism, *J. Geophys. Res.*, 115, 2010.
- Cibin, G., Marcelli, A., Maggi, V., Sala, M., Marino, F., Delmonte, B., Albani, S., and Pignotti, S.: First Combined Total Reflection X-Ray Fluorescence and Grazing Incidence X-Ray Absorption Spectroscopy Characterization of Aeolian Dust Archived in Antarctica and Alpine Deep Ice Cores, *Spectrochim. Acta B*, 63, 1503–1510, 2008.
- Colbeck, S. C.: Model of Wind Pumping for Layered Snow, *J. Glaciol.*, 43, 60–65, 1997.
- Corley, J.: Best Practices in Establishing Detection and Quantification Limits for Pesticide Residues in Foods, in: *Handbook of Residue Analytical Methods for Agrochemicals*, edited by Lee, P. W., Aizawa, H., Barefoot, A. C., and Murphy, J. J., vol. 1, Wiley & Sons, New York, NY, 2003.
- Costanza-Robinson, M. S., Harrold, K. H., and Lieb-Lappen, R. M.: X-Ray Microtomography Determination of Air-Water Interfacial Area-Water Saturation Relationships in Sandy Porous Media, *Environ. Sci. Technol.*, 42, 2949–2956, 2008.
- Costanza-Robinson, M. S., Estabrook, B. D., and Fouhey, D. F.: Representative Elementary Volume Estimation for Porosity, Moisture Saturation, and Air-Water Interfacial Areas in Unsaturated Porous Media: Data Quality Implications, *Water Resour. Res.*, 47, 2011.
- Cox, G. F. N. and Weeks, W. F.: Brine Drainage and Initial Salt Entrapment in Sodium Chloride Ice, *Tech. Rep. Research Report 345*, CRREL, Hanover, NH, 1975.
- Cox, G. F. N. and Weeks, W. F.: Equations for Determining the Gas and Brine Volumes In Sea-Ice Samples, *J. Glaciol.*, 29, 306–316, 1983.
- Delerue, J. F., Perrier, E., Timmerman, A., and Swennen, R.: 3D Soil Image Characterization Applied to Hydraulic Properties Computation, in: *Applications of X-ray Computed Tomography in the Geosciences*, edited by Mees, F., Swennen, R., Van Geet, M., and Jacobs, P., vol. 215, pp. 167–175, Geological Society Special Publications, London, 2003.
- Dijkstra, E. W.: A Note on Two Problems in Connexion with Graphs, *Numer. Math.*, 1, 269–271, 1959.
- Dominé, F. and Shepson, P. B.: Air-Snow Interactions and Atmospheric Chemistry, *Science*, 297, 1506–1510, 2002.
- Domine, F., Sparapani, R., Ianniello, A., and Beine, H. J.: The Origin of Sea Salt in Snow on Arctic Sea Ice and in Coastal Regions, *Atmos. Chem. Phys.*, 4, 2259–2271, 2004.
- Domine, F., Taillandier, A. S., Simpson, W. R., and Severin, K.: Specific Surface Area, Density and Microstructure of Frost Flowers, *Geophys. Res. Lett.*, 32, L13502, doi:10.1029/2005GL023245, 2005.

- Dong, H., Fjeldstad, S., Alberts, L., Roth, S., Bakke, S., and Øren, P.-E.: Pore Network Modelling on Carbonate: A Comparative Study of Different Micro-CT Network Extraction Methods, in: Soc. Core Anal. Int. Symp., UAE, 2008.
- Duce, R. A. and Woodcock, A. H.: Difference in Chemical Composition of Atmospheric Sea Salt Particles Produced in the Surf Zone and on the Open Sea in Hawaii, *Tellus*, 23, 427–435, 1971.
- Dwyer, R. A.: Maximal and Minimal Balls, *Comp. Geom.*, 3, 261–275, 1993.
- Eicken, H.: Salinity Profiles of Antarctic Sea Ice: Field Data and Model Results, *J. Geophys. Res.*, 97, 15,545–15,557, 1992.
- Eicken, H.: From the Microscopic, to the Macroscopic, to the Regional Scale: Growth, Microstructure and Properties of Sea Ice, in: *Sea Ice: An Introduction to its Physics, Chemistry, Biology and Geology*, edited by Thomas, D. N. and Dieckmann, G. S., Blackwell Publishing, Inc., 2003.
- Elam, W. T., Ravel, B. D., and Sieber, J. R.: A New Atomic Database for X-Ray Spectroscopic Calculations, *Radiat. Phys. Chem.*, 63, 121–128, 2002.
- Emery, K. O., Aubrey, D. G., and Jansa, L.: *Sea Levels, Land Levels, and Tide Gauges*, Springer, New York, 1991.
- Fan, S.-M. and Jacob, D. J.: Surface Ozone Depletion in Arctic Spring Sustained by Bromine Reactions on Aerosols, *Nature*, 359, 522–524, 1992.
- Farman, J. C., Gardiner, B. G., and Shanklin, J. D.: Large Losses of Total Ozone in Antarctica Reveal Seasonal ClO_x/NO_x Interaction, *Nature*, 315, 207–210, 1985.
- Feltham, D. L., Untersteiner, N., Wettlaufer, J. S., and Worster, M. G.: Sea Ice is a Mushy Layer, *Geophys. Res. Lett.*, 33, 2006.
- Fetterer, F., Knowles, K., Meier, W., and Savoie, M.: Sea Ice Index, 1980 to 2012, doi: <http://dx.doi.org/10.7265/N5QJ7F7W>, 2002, updated daily.
- Frankenstein, G. and Garner, R.: Equations for Determining the Brine Volume of Sea Ice from –0.5 C to –22.9 C, *J. Glaciol.*, 6, 943–944, 1967.
- Freitag, J. and Eicken, H.: Meltwater Circulation and Permeability of Arctic Summer Sea Ice Derived from Hydrological Field Experiments, *J. Glaciol.*, 49, 349–358, 2003.
- Freitag, J., Wilhelms, F., and Kipfstuhl, S.: Microstructure-Dependent Densification of Polar Firn Derived from X-Ray Microtomography, *J. Glaciol.*, 50, 243–250, 2004.
- Frieß, U., Hollwedel, J., König-Langlo, G., Wagner, T., and Platt, U.: Dynamics and Chemistry of Tropospheric Bromine Explosion Events in the Antarctic Coastal Region, *J. Geophys. Res.*, 109, D06305, doi:10.1029/2003JD004133, 2004.
- Frieß, U., Sihler, H., Sander, R., Pohler, D., Yilmaz, S., and Platt, U.: The Vertical Distribution of BrO and Aerosols in the Arctic: Measurements by Active and Passive Differential Optical Absorption Spectroscopy, *J. Geophys. Res.*, 116, D00R04, doi:10.1029/2011JD015938, 2011.

- Galloway, J. N., Dentener, F. J., Capone, D. G., Boyer, E. W., Howarth, R. W., Seitzinger, S. P., Asner, G. P., Cleveland, C. C., Green, P. A., Holland, E. A., Karl, D. M., Michaels, A. F., Porter, J. H., Townsend, A. R., and Vorosmarty, C. J.: Nitrogen Cycles: Past, Present, and Future, *Biogeochemistry*, 70, 153–226, doi:10.1007/s10533-004-0370-0, 2004.
- Gladich, I., Shepson, P. B., Carignano, M. A., and Szleifer, I.: Halide Affinity for the Water- Air Interface in Aqueous Solutions of Mixtures of Sodium Salts, *J. Phys. Chem. A*, 115, 5895–5899, 2011.
- Golden, K. M., Ackley, S. F., and Lytle, V. I.: The Percolation Phase Transition in Sea Ice, *Science*, 282, 2238–2241, 1998.
- Golden, K. M., Eicken, H., Heaton, A. L., Miner, J., Pringle, D. J., and Zhu, J.: Thermal Evolution of Permeability and Microstructure in Sea Ice, *Geophys. Res. Lett.*, 34, 2007.
- Gordon, L. I., Codispoti, L. A., Jennings Jr., J. C., Millero, F. J., Morrison, J. M., and Sweeney, C.: Seasonal Evolution of Hydrographic Properties in the Ross Sea, Antarctica, 1996-1997, *Deep-Sea Res. II*, 47, 3095–3117, 2000.
- Gow, W. F. W. A. J.: Preferred Crystal Orientations in the Fast Ice Along the Margins of the Arctic Ocean, *J. Geophys. Res.*, 83, 5105–5121, 1978.
- Graham, J. E. and Hogg, R. V.: *Studies in Statistics*, Mathematical Association of America, Washington D. C., 1978.
- Grannas, A. M., Jones, A. E., Dibb, J., Ammann, M., Anastasio, C., Beine, H. J., Bergin, M., Bottenheim, J., Boxe, C. S., Carver, G., Chen, G., Crawford, J. H., Domine, F., Frey, M. M., Guzman, M. I., Heard, D. E., Helmig, D., Hoffmann, M. R., Honrath, R. E., Huey, L. G., Hutterli, M., Jacobi, H. W., Klan, P., Lefer, B., McConnell, J., Plane, J., Sander, R., Savarino, J., Shepson, P. B., Simpson, W. R., Sodeau, J. R., von Glasow, R., Weller, R., Wolff, E. W., and Zhu, T.: An Overview of Snow Photochemistry: Evidence, Mechanisms, and Impacts, *Atmos. Chem. Phys.*, 7, 4329–4373, 2007.
- Gregory, S. A., Albert, M. R., and Baker, I.: Impact of Physical Properties and Accumulation Rate on Pore Close-Off in Layered Firn, *Cryosphere*, 8, 91–105, 2014.
- Grenfell, T. C.: A Theoretical Model of the Optical Properties of Sea Ice in the Visible and Near Infrared, *J. Geophys. Res.*, 88, 9723–9735, 1983.
- Grenfell, T. C. and Perovich, D. K.: Spectral Albedos of Sea Ice and Incident Solar Irradiance in the Southern Beaufort Sea, *J. Geophys. Res.*, 89, 3573–3580, 1984.
- Grenfell, T. C. and Perovich, D. K.: Seasonal and Spatial Evolution of Albedo in a Snow-Ice-Land-Ocean Environment, *J. Geophys. Res.*, 109, C01001, doi:10.1029/2003JC001866, 2004.
- Grimmett, G.: *What is Percolation?*, Springer-Verlag, Berlin, Germany, 2 edn., 1999.
- Halfacre, J. W., Knepp, T. N., Shepson, P. B., Thompson, C. R., Pratt, K. A., Li, B., Peterson, P. K., Walsh, S. J., Simpson, W. R., Matrai, P. A., Bottenheim, J. W., Netcheva, S., Perovich, D. K., and Richter, A.: Temporal and Spatial Characteristics of Ozone Depletion Events from Measurements in the Arctic, *Atmos. Chem. Phys.*, 14, 4875–4894, doi:10.5194/acp-14-4875-2014, 2014.

- Hallet, J.: Experimental Studies of the Crystallization of Supercooled Water, *J. Atmos. Sci.*, 21, 671–682, 1964.
- Harrison, J. D. and Tiller, W. A.: Controlled Freezing of Water, in: *Ice and Snow - Processes, Properties, and Applications*, edited by Kingery, W. D., pp. 215–225, MIT Press, Cambridge, MA, 1963.
- Heijmans, H. J. A. M. and Roerdink, J. B. T. M.: *Mathematical Morphology and its Applications to Image and Signal Processing*, Kluwer Academic Publishers, Dordrecht, Netherlands, 1998.
- Helmig, D., Boylan, P., Johnson, B., Oltmans, S., Fairall, C., Staebler, R., Weinheimer, A., Orlando, J., Knapp, D. J., Montzka, D. D., Flocke, F., Frieß, U., Sihler, H., and Shepson, P. B.: Ozone Dynamics and Snow-Atmosphere Exchanges During Ozone Depletion Events at Barrow, Alaska, *J. Geophys. Res.*, 117, D20303, doi:10.1029/2012JD017531, 2012.
- Hobbs, P. V.: *Ice Physics*, Clarendon Press, Oxford, 1974.
- Hubbell, J. H. and Seltzer, S. M.: *Tables of X-Ray Mass Attenuation Coefficients and Mass Energy-Absorption Coefficients 1 keV to 20 MeV for Elements Z= 1 to 92 and 48 Additional Substances of Dosimetric Interest*, Tech. rep., National Inst. of Standards and Technology-PL, Ionizing Radiation Div., Gaithersburg, MD, 1995.
- Huff, A. K. and Abbatt, J. P. D.: Kinetics and Product Yields in the Heterogeneous Reactions of HOBr with Simulated Sea-Ice Surfaces, *J. Phys. Chem. A.*, 106, 5279–5287, 2002.
- Hutchings, J. K., Heil, P., Lecomte, O., Stevens, R., Steer, A., and Lieser, J. L.: Comparing Methods of Measuring Sea-Ice Density in the East Antarctic, *Ann. Glaciol.*, 56, 77, 2015.
- Hutterli, M. A., Huthwelker, T., Miedaner, M. M., Enzmann, F., Ammann, M., Schneebeli, M., Maus, S., Stampanoni, M., Jones, A. E., and Wolff, E. W.: A 3D X-Ray Micro Computer Tomography Perspective of Sea Ice, Frost Flowers and Snow as Sources of Reactive Halogens, in: *Geophysical Research Abstracts*, vol. 10, pp. EGU2008–A–04 181, EGU, EGU General Assembly, 2008.
- Jacobi, H. W., Voisin, D., Jaffrezo, J. L., Cozic, J., and Douglas, T. A.: Chemical Composition of the Snowpack During the OASIS Spring Campaign 2009 at Barrow, Alaska, *J. Geophys. Res.*, 117, doi:10.1029/2011JD016654, 2012.
- Jeffries, M. O., Shaw, R. A., Raymond, A., Morris, K., Veazey, A. L., and Krouse, H. R.: Crystal Structure, Stable Isotopes ($\delta^{18}\text{O}$), and Development of Sea Ice in the Ross, Amundsen, and Bellingshausen Seas, Antarctica, *J. Geophys. Res.*, 99, 985–995, 1994.
- Jones, A. E., Anderson, P. S., Begoin, M., Brough, N., Hutterli, M. A., Marshall, G. J., Richter, A., Roscoe, H. K., and Wolff, E. W.: BrO, Blizzards, and Drivers of Polar Tropospheric Ozone Depletion Events, *Atmos. Chem. Phys.*, 9, 4639–4652, 2009.
- Jones, A. E., Anderson, P. S., Wolff, E. W., Roscoe, H. K., Marshall, G. J., Richter, A., Brough, N., and Colwell, S. R.: Vertical Structure of Antarctic Tropospheric Ozone Depletion Events: Characteristics and Broader Implications, *Atmos. Chem. Phys.*, 10, 7775–7794, doi:10.5194/acp-10-7775-2010, 2010.

- Jungwirth, P., Finlayson-Pitts, B. J., and Tobias, D. J.: Introduction: Structure and Chemistry at Aqueous Interfaces, *Chem. Rev.*, 106, 1137–1139, 2006.
- Kaleschke, L., Richter, A., Burrows, J., Afe, O., Heygster, G., Notholt, J., Rankin, A. M., Roscoe, H. K., Hollwedel, J., Wagner, T., and Jacobi, H.-W.: Frost Flowers on Sea Ice as a Source of Sea Salt and Their Influence on Tropospheric Halogen Chemistry, *Geophys. Res. Lett.*, 31, L16114, doi:10.1029/2004GL020655, 2004.
- Kalnajs, L. E. and Avallone, L. M.: Frost Flower Influence on Springtime Boundary-Layer Ozone Depletion Events and Atmospheric Bromine Levels, *Geophys. Res. Lett.*, 33, L10810, doi:10.1029/2006GL025809, 2006.
- Ketcham, R. A. and Carlson, W. D.: Acquisition, Optimization and Interpretation of X-Ray Computed Tomographic Imagery: Applications to the Geosciences, *Comput. Geosci.*, 27, 381–400, 2001.
- Kovacs, A. and Morey, R. M.: Radar Anisotropy of Sea Ice Due to Preferred Azimuthal Orientation of the Horizontal c Axes of Ice Crystals, *J. Geophys. Res.*, 83, 6037–6046, 1978.
- Kreher, K., Johnston, P. V., Wood, S. W., Nardi, B., and Platt, U.: Ground-Based Measurements of Tropospheric and Stratospheric BrO at Arrival Heights, Antarctica, *Geophys. Res. Lett.*, 24, 3021–3024, 1997.
- Krnavek, L., Simpson, W. R., Carlson, D., Domine, F., Douglas, T. A., and Sturm, M.: The Chemical Composition of Surface Snow in the Arctic: Examining Marine, Terrestrial, and Atmospheric Influences, *Atmos. Environ.*, 50, 349–359, 2012.
- Landis, E. N. and Keane, D. T.: X-Ray Microtomography, *Mater. Charact.*, 61, 1305–1316, 2010.
- Lange, M. A., Ackley, S. F., Wadhams, P., Dieckmann, G. S., and Eicken, H.: Development of sea ice in the Weddel Sea, *Ann. Glaciol.*, 12, 92–96, 1989.
- Langhorne, P. J., Hughes, K. G., Gough, A. J., Smith, I. J., Williams, M. J. M., Robinson, N. J., Stevens, C. L., Rack, W., Price, D., Leonard, G. H., Mahoney, A. R., Haas, C., and Haskell, T. G.: Observed Platelet Ice Distributions in Antarctic Sea Ice: An Index for Ocean-Ice Shelf Heat Flux, *Geophys. Res. Lett.*, 42, 5442–5451, 2015.
- Lannuzel, D., Bowie, A. R., van der Merwe, P. C., Townsend, A. T., and Schoemann, V.: Distribution of Dissolved and Particulate Metals in Antarctic Sea Ice, *Mar. Chem.*, 124, 134–146, 2011.
- Liao, J., Huey, L. G., Tanner, D. J., Flocke, F. M., Orlando, J. J., Neuman, J. A., Nowak, J. B., Weinheimer, A. J., Hall, S. R., Smith, J. N., Fried, A., Staebler, R. M., Wang, Y., Koo, J.-H., Cantrell, C. A., Weibring, P., Walega, J., Knapp, D. J., Shepson, P. B., and Stephens, C. R.: Observations of Inorganic Bromine (HOBr, BrO, and Br₂) Speciation at Barrow, Alaska, in Spring 2009, *J. Geophys. Res.*, 117, D00R16, doi:10.1029/2011JD016641, 2012.
- Light, B., Maykut, G. A., and Grenfell, T. C.: Effects of Temperature on the Microstructure of First-Year Arctic Sea Ice, *J. Geophys. Res.*, 108, 3051, doi:10.1029/2001JC000887, 2003.

- Lindberg, S. E., Brooks, S., Lin, C. J., Scott, K., Meyers, T., Chambers, L., Landis, M., and Stevens, R.: Formation of Reactive Gaseous Mercury in the Arctic: Evidence of Oxidation of Hg to Gas-Phase Hg-II Compounds After Arctic Sunrise, *Water Air Soil Poll.*, 1, 295–302, 2001.
- Lindberg, S. E., Brooks, S., Lin, C., Scott, K. J., Landis, M. S., Stevens, R. K., Goodsite, M., and Richter, A.: Dynamic Oxidation of Gaseous Mercury in the Arctic Troposphere at Polar Sunrise, *Environ. Sci. Technol.*, 36, 1245–1256, 2002.
- Lizotte, M. P.: The Contributions of Sea Ice Algae to Antarctic Marine Primary Production, *Am. Zool.*, 41, 57–73, 2001.
- Lomonaco, R. W., Baker, I., and Chen, S.: Preliminary Results on the Characterization of Firn using SEM and Micro CT, in: 65th Eastern Snow Conference, pp. 28–30, Fairlee, VT, 2008.
- Lonsdale, D. K.: The Structure of Ice, *P. Roy. Soc. Lond. A Mat.*, 247, 424–434, 1958.
- Lu, J. Y., Schroeder, W. H., Barrie, L. A., Steffen, A., Welch, H. E., Martin, K., Lockhart, L., Hunt, R. V., Boila, G., and Richter, A.: Magnification of Atmospheric Mercury Deposition to Polar Regions in Springtime: The Link to Tropospheric Ozone Depletion Chemistry, *Geophys. Res. Lett.*, 28, 3219–3222, 2001.
- Malliaris, A. and Turner, D. T.: Influence of Particle Size on the Electrical Resistivity of Compacted Mixtures of Polymeric and Metallic Powders, *J. App. Phys.*, 42, 614–618, 1971.
- Martin, S. and Kauffman, P.: A field and laboratory study of wave damping by grease ice, *J. Glaciol.*, 27, 283–313, 1981.
- Massey, F. J.: The Kolmogorov-Smirnov Test for Goodness of Fit, *J. Am. Stat. Assoc.*, 46, 68–78, 1951.
- Massom, R. A., Eicken, H., Haas, C., Jeffries, M. O., Drinkwater, M. R., Sturm, M., Worby, A. P., Wu, X., Lytle, V. I., Ushio, S., Morris, K., Reid, P. A., and Allison, S. G. W. I.: Snow on Antarctic Sea Ice, *Rev. Geophys.*, 39, 413–445, 2001.
- Mauldin, III, R. L., Eisele, F. L., Tanner, D. J., Kosciuch, E., Shetter, R., Lefer, B., Hall, S. R., Nowak, J. B., Buhr, M., Chen, G., Wang, P., and Davis, D.: Measurements of OH, H₂SO₄, and MSA at the South Pole during ISCAT, *Geophys. Res. Lett.*, 28, 3629–3632, 2001.
- Maus, S., Huthwelker, T., Enzmann, F., Miedaner, M., Stampanoni, M., Marone, F., Hutterli, M. A., Hintermuller, C., and Kersten, M.: Synchrotron-Based X-Ray Tomography: Insights into Sea Ice Microstructure, in: *Rep. Ser. Geophys.*, edited by Lepparanta, M., vol. 61, pp. 28–45, University of Helsinki, 2009.
- Maus, S., Leisinger, S., Matzl, M., Schneebeli, M., and Wiegmann, A.: Modeling Oil Entrapment in Sea Ice on the Basis of 3D Micro-Tomographic Images, in: *Proc. Int. Conf. Port Ocean Eng. Arct. Cond.*, vol. 22, Espoco, Finland, 2013.
- Maykut, G. A.: An Introduction to Ice in the Polar Oceans, *Tech. Rep. APL-UW-8510*, Department Atmospheric Sciences, University of Washington, 1985.

- McConnell, J. C., Henderson, G. S., Barrie, L. A., Bottenheim, J. W., Niki, H., Langford, C. H., and Templeton, E. M. J.: Photochemical Bromine Production Implicated in Arctic Boundary-Layer Ozone Depletion, *Nature*, 355, 150–152, doi:10.1038/355150a0, 1992.
- Molina, M. J. and Rowland, F. S.: Stratospheric Sink for Chlorofluoromethanes: Chlorine Atom-Catalysed Destruction of Ozone, *Nature*, 249, 810–812, 1974.
- Morin, S., Marion, G. M., von Glasow, R., Voisin, D., Bouchez, J., and Savarino, J.: Precipitation of Salts in Freezing Seawater and Ozone Depletion Events: A Status Report, *Atmos. Chem. Phys.*, 8, 7317–7324, 2008.
- Morris, A. W. and Riley, J. P.: The bromide/chlorinity and sulphate/chlorinity ratio in sea water, *Deep-Sea Res.*, 13, 699–705, doi:10.1016/0011-7471(66)90601-2, 1966.
- Naik, N. N., Jupe, A. C., Stock, S. R., Wilkinson, A. P., Lee, P. L., and Kurtis, K. E.: Sulfate Attack Monitored by MicroCT and EDXRD: Influence of Cement Type, Water-to-Cement Ratio, and Aggregate, *Cement Concrete Res.*, 36, 144–159, 2006.
- Nakawo, M. and Sinha, N. K.: A Note on Brine Layer Spacing of First-Year Sea Ice, *Atmos. Ocean*, 22, 193–206, 1984.
- Nemoto, M. and Nishimura, K.: Numerical Simulation of Snow Saltation and Suspension in a Turbulent Boundary Layer, *J. Geophys. Res.*, 109, D18206, doi:10.1029/2004JD004657, 2004.
- Newman, M. E. J.: *Networks: An Introduction*, Oxford University Press, New York, 2011.
- Newville, M.: *Fundamentals of XAFS*, Tech. Rep. Revision 1.7, Consortium for Advanced Radiation Sources, University of Chicago, 2004.
- Notz, D.: *Thermodynamic and Fluid-Dynamical Processes in Sea Ice*, Ph.D. thesis, University of Cambridge, 2005.
- Obbard, R. W., Roscoe, H. K., Wolff, E. W., and Atkinson, H. M.: Frost Flower Surface Area and Chemistry as a Function of Salinity and Temperature, *J. Geophys. Res.*, 114, D20305, doi:10.1029/2009JD012481, 2009a.
- Obbard, R. W., Troderman, G., and Baker, I.: Imaging Brine and Air Inclusions in Sea Ice Using Micro-X-Ray Computed Tomography, *J. Glaciol.*, 55, 1113–1115, 2009b.
- Oldridge, N. W. and Abbatt, J. P. D.: Formation of Gas-Phase Bromine from Interaction of Ozone with Frozen and Liquid NaCl/Br Solutions: Quantitative Separation of Surficial Chemistry from Bulk-Phase Reaction, *J. Phys. Chem. A*, 115, 2590–2598, doi:10.1021/jp200074u, 2011.
- Otsu, N.: A Threshold Selection Method from Gray-Level Histograms, *IEEE T. Syst. Man Cyb.*, 9, 62–66, 1979.
- Oum, K. W., Lakin, M. J., DeHaan, D. O., Brauers, T., and Finlayson-Pitts, B. J.: Formation of Molecular Chlorine from the Photolysis of Ozone and Aqueous Sea-Salt Particles, *Science*, 279, 74–76, 1998.
- Owston, P. G.: The Structure of Ice-I, as Determined by X-Ray and Neutron Diffraction Analysis, *Adv. Phys.*, 7, 171–188, 1958.

- Perovich, D. K. and Richter-Menge, J. A.: Surface Characteristics of Lead Ice, *J. Geophys. Res.*, 99, 16,341–16,350, 1994.
- Perovich, D. K. and Richter-Menge, J. A.: Loss of Sea Ice in the Arctic, *Ann. Rev. Mar. Sci.*, 1, 417–441, 2009.
- Peterson, P. K., Simpson, W. R., Rivers, M. L., and Trainor, T. P.: Observations of Brine on Ice Using X-ray Absorption Edge Computed Microtomography, *Cryosphere*, 9, 2015.
- Petrich, C., Langhorne, P. J., and Sun, Z. F.: Modelling the Interrelationships Between Permeability, Effective Porosity and Total Porosity in Sea Ice, *Cold Reg. Sci. Technol.*, 44, 131–144, 2006.
- Pierret, A., Capowicz, Y., Belzunces, L., and Moran, C. J.: 3D Reconstruction and Quantification of Macropores using X-Ray Computed Tomography and Image Analysis, *Geoderma*, 106, 247–271, 2002.
- Piot, M. and von Glasow, R.: The Potential Importance of Frost Flowers, Recycling on Snow, and Open Leads for Ozone Depletion Events, *Atmos. Chem. Phys.*, 8, 2437–2467, 2008.
- Pomeroy, J. W. and Brun, E.: Physical Properties of Snow, in: *Snow Ecology: An Interdisciplinary Examination of Snow-Covered Ecosystems*, edited by Jones, H. G., Pomeroy, J. W., Walker, D. A., and Hoham, R. W., pp. 45–126, Cambridge University Press, Cambridge, UK, 2001.
- Pratt, K. A., Custard, K. D., Shepson, P. B., Douglas, T. A., Pohler, D., General, S., Zielcke, J., Simpson, W. R., Platt, U., Tanner, D. J., Huey, L. G., Carlsen, M., and Stirm, B. H.: Photochemical Production of Molecular Bromine in Arctic Surface Snowpacks, *Nat. Geosci.*, 6, 351–356, doi:10.1038/NGEO1779, 2013.
- Pringle, D. J., Miner, J. E., Eicken, H., and Golden, K. M.: Pore Space Percolation in Sea Ice Single Crystals, *J. Geophys. Res.*, 114, 2009.
- Rankin, A. M. and Wolff, E. W.: A Year-Long Record of Size-Segregated Aerosol Composition at Halley, Antarctica, *J. Geophys. Res.*, 108, 4775, doi:10.1029/2003JD003993, 2003.
- Rankin, A. M., Auld, V., and Wolff, E. W.: Frost Flowers as a Source of Fractionated Sea Salt Aerosol in the Polar Regions, *Geophys. Res. Lett.*, 27, 3469–3472, 2000.
- Rankin, A. M., Wolff, E. W., and Martin, S.: Frost Flowers: Implications for Tropospheric Chemistry and Ice Core Interpretation, *J. Geophys. Res.*, 107, 4683, doi:10.1029/2002JD002492, 2002.
- Roscoe, H. K., Brooks, B., Jackson, A. V., Smith, M. H., Walker, S. J., Obbard, R. W., and Wolff, E. W.: Frost Flowers in the Laboratory: Growth, Characteristics, Aerosol, and the Underlying Sea Ice, *J. Geophys. Res.*, 116, D12301, doi:10.1029/2010JD015144, 2011.
- Sahimi, M.: *Flow and Transport in Porous Media and Fractured Rock*, Wiley-VCH, Weinheim, Germany, 2011.
- Sander, R., Keene, W. C., Pszenny, A. A. P., Arimoto, R., Ayers, G. P., Baboukas, E., Caine, J. M., Crutzen, P. J., Duce, R. A., Honninger, G., Huebert, B. J., Maenhaut, W., Mihalopoulos, N., Turekian, V. C., and Dingenen, R. V.: Inorganic Bromine in the Marine Boundary Layer: A Critical Review, *Atmos. Chem. Phys.*, 3, 1301–1336, 2003.

- Santiago, E., Velasco-Hernández, J. X., and Romero-Salcedo, M.: A Methodology for the Characterization of Flow Conductivity through the Identification of Communities in Samples of Fractured Rocks, *Expert Syst. Appl.*, 41, 811–820, 2014.
- Schneebeli, M. and Sokratov, S. A.: Tomography of Temperature Gradient Metamorphism of Snow and Associated Changes in Heat Conductivity, *Hydrol. Processes*, 18, 3655–3665, 2004.
- Schulson, E. M.: The Structure and Mechanical Behavior of Ice, *JOM-J. Min. Met. Mat. S.*, 51, 21–27, 1999.
- Silin, D. and Patzek, T.: Pore Space Morphology Analysis using Maximal Inscribed Spheres, *Physica A*, 371, 336–360, 2006.
- Simpson, W. R., Alvarez-Alviles, L., Douglas, T. A., Sturm, M., and Domine, F.: Halogens in the Coastal Snow Pack Near Barrow, Alaska: Evidence for Active Bromine Air-Snow Chemistry During Springtime, *Geophys. Res. Lett.*, 32, L04811, doi:10.1029/2004GL021748, 2005.
- Simpson, W. R., Carlson, D., Honninger, G., Douglas, T. A., Sturm, M., Perovich, D., and Platt, U.: First-Year Sea-Ice Contact Predicts Bromine Monoxide (BrO) Levels at Barrow, Alaska Better Than Potential Frost Flower Contact, *Atmos. Chem. Phys.*, 7, 621–627, 2007a.
- Simpson, W. R., von Glasow, R., Riedel, K., Anderson, P., Ariya, P., Bottenheim, J., Burrows, J., Carpenter, L. J., Friess, U., Goodsite, M. E., Heard, D., Hutterli, M., Jacobi, H.-W., Kaleschke, L., Neff, B., Plane, J., Platt, U., Richter, A., Roscoe, H., Sander, R., Shepson, P., Sodeau, J., Steffen, A., Wagner, T., and Wolff, E.: Halogens and Their Role in Polar Boundary-Layer Ozone Depletion, *Atmos. Chem. Phys.*, 7, 4375–4418, 2007b.
- Small, H., Stevens, T. S., and Bauman, W. C.: Novel Ion Exchange Chromatographic Method Using Conductimetric Detection, *Anal. Chem.*, 47, 1801–1809, 1975.
- Stauffer, D. and Aharony, A.: Introduction to percolation Theory, CRC press, 2nd edn., 1994.
- Steffen, A., Douglas, T., Amyot, M., Ariya, P., Aspmo, K., Berg, T., Bottenheim, J., Brooks, S., Cobbett, F., Dastoor, A., Dommergue, A., Ebinghaus, R., Ferrari, C., Gardfeldt, K., Goodsite, M. E., Lean, D., Poulain, A. J., Scherz, C., Skov, H., Sommar, J., and Temme, C.: A Synthesis of Atmospheric Mercury Depletion Event Chemistry in the Atmosphere and Snow, *Atmospheric Chemistry and Physics*, 8, 1445–1482, 2008.
- Stock, S. R.: Recent Advances in X-Ray Microtomography Applied to Materials, *Int. Mater. Rev.*, 53, 129–181, 2008.
- Stroeve, J., Holland, M. M., Meier, W., Scambos, T., and Serreze, M.: Arctic Sea Ice Decline: Faster than Forecast, *Geophys. Res. Lett.*, 34, 2007.
- Stroeve, J., Serreze, M., Holland, M. M., Kay, J. E., Malanik, J., and Barrett, A. P.: The Arctic's Rapidly Shrinking Sea Ice Cover: A Research Synthesis, *Clim. Chang.*, 110, 1005–1027, 2012.
- Tarquis, A. M., Heck, R. J., Andina, D., Alvarez, A., and Anton, J. M.: Pore Network Complexity and Thresholding of 3D Soil Images, *Ecol. Complex.*, 6, 230–239, 2009.

- Theys, N., Roozendael, M. V., Hendrick, F., Yang, X., Smedt, I. D., Richter, A., Begoin, M., Errera, Q., Johnston, P. V., Kreher, K., and Maziere, M. D.: Global Observations of Tropospheric BrO Columns Using GOME-2 Satellite Data, *Atmos. Chem. and Phys.*, 11, 1791, 2011.
- Thomas, D. N. and Dieckmann, G. S.: *Sea Ice*, Wiley-Blackwell, Hoboken, NJ, 2009.
- Tiller, W. A.: Effect of Grain Boundaries on Solute Partitioning during Progressive Solidification, *J. App. Phys.*, 33, 3106–3107, 1962.
- Timco, G. W. and Frederking, R. M. W.: A Review of Sea Ice Density, *Cold Reg. Sci. Technol.*, 24, 1–6, 1996.
- Toyota, K., McConnell, J. C., Lupu, A., Neary, L., McLinden, C. A., Richter, A., Kwok, R., Semeniuk, K., Kaminski, J. W., Gong, S.-L., Jarosz, J., Chipperfield, M. P., and Sioris, C. E.: Analysis of Reactive Bromine Production and Ozone Depletion in the Arctic Boundary Layer Using 3-D Simulations with GEM-AQ: Inference From Synoptic-Scale Patterns, *Atmos. Chem. Phys.*, 11, 3949–3979, doi:10.5194/acp-11-3949-2011, 2011.
- Varshney, D. B., Elliott, J. A., Gatlin, L. A., Kumar, S., Suryanarayanan, R., and Shalaev, E. Y.: Synchrotron X-Ray Diffraction Investigation of the Anomalous Behavior of Ice During Freezing of Aqueous Systems, *J. Phys. Chem. B*, 113, 6177–6182, 2009.
- Vogt, R., Crutzen, P. J., and Sander, R.: A Mechanism for Halogen Release From Sea-Salt Aerosol in the Remote Marine Boundary Layer, *Nature*, 383, 327–330, 1996.
- von Glasow, R. and Crutzen, P. J.: Tropospheric Halogen Chemistry, in: *Treatise on Geochemistry*, vol. 4.02, pp. 1–67, Elsevier Pergamon, 2007.
- Wadhams, P., Lange, M. A., and Ackley, S. F.: The Ice Thickness Distribution Across the Atlantic Sector of the Antarctic Ocean in Midwinter, *J. Geophys. Res.*, 92, 14 535–14 552, 1987.
- Wagenbach, D., Ducroz, F., Mulvaney, R., Keck, L., Minikin, A., Legrand, M., Hall, J. S., and Wolff, E. W.: Sea-Salt Aerosol in Coastal Antarctic Regions, *J. Geophys. Res.*, 103, 10,961–10,974, 1998.
- Wagner, T., Leue, C., Wenig, M., Pfeilsticker, K., and Platt, U.: Spatial and Temporal Distribution of Enhanced Boundary Layer BrO Concentrations Measured by the GOME Instrument Aboard ERS-2, *J. Geophys. Res.*, 106, 24 225–24 235, 2001.
- Wang, X. and Baker, I.: Observation of the Microstructural Evolution of Snow under Uniaxial Compression using X-Ray Computed Microtomography, *J. Geophys. Res.*, 118, 12–371, 2013.
- Weast, R. C.: *Handbook of Chemistry and Physics*, Chemical Rubber Co., Cleveland, OH, 1969.
- Weeks, W. F. and Ackley, S. F.: *The Growth, Structure, and Properties of Sea Ice*, Tech. Rep. Monograph 82-1, CRREL, Hanover, NH, 1982.
- Weeks, W. F. and Wettlaufer, J. S.: Crystal Orientations in Floating Ice Sheets, in: *The Johannes Weertman Symposium*, edited by Arsenault, R. J., Cole, D., Gross, T., Kostorz, G., Liaw, P. K., Parameswaran, S., and Sizek, H., pp. 337–350, The Minerals, Metals and Materials Society, Warrendale, PA, 1996.

- Wessel, S., Aoki, A., Winkler, P., Weller, R., Herber, A., Gernandt, H., and Schrems, O.: Tropospheric Ozone Depletion in Polar Regions: A Comparison of Observations in the Arctic and Antarctic, *Tellus B*, 50, 34–50, 1998.
- West, D. B.: *Introduction to Graph Theory*, Prentice Hall, Upper Saddle River, NJ, 2001.
- Wettlaufer, J. S., Worster, M., and Huppert, H. E.: Natural Convection During Solidification of an Alloy from Above with Application to the Evolution of Sea Ice, *J. Fluid Mech.*, 344, 291–316, 1997.
- Wofsy, S. C., McElroy, M. B., and Yung, Y. L.: The Chemistry of Atmospheric Bromine, *Geophys. Res. Lett.*, 2, 215–218, 1975.
- Wren, S. N., Donaldson, D. J., and Abbatt, J. P. D.: Photochemical Chlorine and Bromine Activation from Artificial Saline Snow, *Atmos. Chem. Phys.*, 13, 9789–9800, doi:10.5194/acp-13-9789-2013, 2013.
- Yang, G., Myer, L. R., Brown, S. R., and Cook, N. G. W.: Microscopic Analysis of Macroscopic Transport Properties of Single Natural Fractures Using Graph Theory Algorithms, *Geophys. Res. Lett.*, 22, 1429–1432, 1995.
- Yang, X., Cox, R. A., Warwick, N. J., Pyle, J. A., Carver, G. D., O'Connor, F. M., and Savage, N. H.: Tropospheric Bromine Chemistry and its Impacts on Ozone: A Model Study, *J. Geophys. Res.*, 110, doi:10.1029/2005JD006244, 2005.
- Yang, X., Pyle, J. A., and Cox, R. A.: Sea Salt Aerosol Production and Bromine Release: Role of Snow on Sea Ice, *Geophys. Res. Lett.*, 35, L16815, doi:10.1029/2008GL034536, 2008.
- Yang, X., Pyle, J. A., Cox, R. A., Theys, N., and Roozendaal, M. V.: Snow-Sourced Bromine and Its Implications for Polar Tropospheric Ozone, *Atmos. Chem. Phys.*, 10, 7763–7773, doi:10.5194/acp-10-7763-2010, 2010.
- Zhou, X., Beine, H. J., Honrath, R. E., Fuentes, J. D., Simpson, W., Shepson, P. B., and Bottenheim, J. W.: Snowpack Photochemical Production of HONO: A Major Source of OH in the Arctic Boundary Layer in Springtime, *Geophys. Res. Lett.*, 28, 4087–4090, 2001.